Winter 12-15-2017

Mechanics of the Developing Brain: From Smooth-walled Tube to the Folded Cortex

Kara Ellspermann Garcia
Washington University in St. Louis

Washington University in St. Louis

School of Engineering and Applied Science

Department of Biomedical Engineering

Dissertation Examination Committee:
Larry A. Taber, Chair
Philip V. Bayly
Ruth J. Okamoto
Jin-Yu Shao
David C. Van Essen

Mechanics of the Developing Brain:

From Smooth-walled Tube to the Folded Cortex

by

Kara E. Garcia

A dissertation presented to
The Graduate School
of Washington University in
partial fulfillment of the
requirements for the degree
of Doctor of Philosophy

December 2017
Saint Louis, Missouri

Contents

List of Tables . . . . . **vi**

List of Figures . . . . . **vii**

Acknowledgments . . . . . **ix**

Abstract . . . . . **xii**

Preface . . . . . **xiv**

1 Introduction **1**
1.1 Brain development, from conception to birth 1
1.2 Mechanics in morphogenesis 7
1.2.1 Biomechanics of growth 7
1.2.2 Mechanobiology in growth 10
1.2.3 Stress and strain energy minimization 13
1.3 Research Significance 14
1.4 Synopsis of dissertation 16
1.4.1 Segmentation, inflation, and bending of the forebrain 16
1.4.2 Emergence of the right and left hemispheres 17
1.4.3 Patterns of growth during cortical folding in human 18

2 Contraction and stress-dependent growth shape the forebrain of the early chicken embryo **19**
2.1 Introduction 20
2.2 Methods 23
2.2.1 Embryo culture and perturbation 23
2.2.2 Morphological imaging and analysis 24
2.2.3 Actin imaging and analysis 25
2.2.4 Statistics 26
2.2.5 Computational modeling 26
2.3 Results 33
2.3.1 Contraction is necessary for AIS and OS formation 35
2.3.2 Actin is circumferentially aligned at forebrain constrictions 36
2.3.3 Contraction initiates forebrain segmentation 38

2.3.4 Lumen pressure drives forebrain expansion via inflation and growth . 41
2.3.5 Stress-dependent growth can generate realistic brain tube morphology at later stages . . . 43
2.4 Discussion . . . 48
2.4.1 Organized actomyosin as initiator of brain constrictions . . . 48
2.4.2 Stress-dependent growth as a mechanism of vesicle maintenance during brain expansion . . . 50
2.4.3 Mechanical constraint by the notochord predicts bending and realistic growth patterns . . . 52
2.4.4 Limitations . . . 53
2.4.5 A mechanistic model informs accurate patterning of the forebrain . . 54
2.5 Addendum . . . 57

3 Molecular and mechanical signals are required to shape cerebral hemispheres in the chicken embryo . . . 59
3.1 Introduction . . . 59
3.2 Results . . . 63
3.2.1 Hemisphere division coincides with decreased proliferation at the roof plate. . . . 64
3.2.2 Hemisphere size and division depend on eCSF pressure. . . . 66
3.2.3 Neuroepithelial growth is modulated by mechanical feedback. . . . 69
3.2.4 A chemomechanical feedback law describes growth in the embryonic brain. . . . 72
3.2.5 Growth model based on morphogens and mechanical feedback predicts normal hemisphere morphogenesis. . . . 75
3.2.6 Mechanical feedback explains hemisphere morphologies under altered eCSF pressure. . . . 80
3.3 Discussion . . . 87
3.3.1 Mechanical feedback as a key regulator of hemisphere morphogenesis 87
3.3.2 Clinical relevance: holoprosencephaly, microcephaly, and megalencephaly 89
3.3.3 Limitations and future work . . . 91
3.4 Materials and Methods . . . 93
3.4.1 Embryo culture, perturbation, and imaging . . . 93
3.4.2 Fluorescent labeling and quantification. . . . 95
3.4.3 Measuring growth and deformation . . . 96
3.4.4 Computational methods . . . 97
3.4.5 Pressure measurement . . . 99
3.4.6 Statistics . . . 100
3.5 Addendum . . . 100

4 Dynamic patterns of cortical expansion during folding of the preterm human brain . . . 102

4.1 Introduction . . . 103
4.2 Results . . . 106
4.2.1 aMSM produces accurate point correspondence and smooth growth estimation across the cortex of individual subjects . . . 106
4.2.2 Spatial patterns of preterm growth are consistent across subjects and correspond to folding regions . . . 108
4.2.3 Cortical growth changes regionally and dynamically during folding . . 110
4.2.4 Local growth estimation detects abnormalities associated with preterm injury . . . 111
4.3 Discussion . . . 114
4.4 Methods . . . 118
4.4.1 Recruitment, MRI acquisition and surface generation . . . 118
4.4.2 Longitudinal surface alignment and theory . . . 119
4.4.3 Group statistics . . . 120
4.5 Addendum . . . 121

5 Conclusions . . . 126

Appendix A Supplemental data on embryonic brain development . . . 130
A.1 Measurement of normal growth . . . 130
A.2 Experiments to rule out other factors . . . 132
A.3 Notochord tension . . . 133
A.4 Early measures of normal pressure . . . 134
A.5 Optic vesicle effects on brain tube morphogenesis . . . 135

Appendix B Strain energy minimization with aMSM . . . 137
B.1 Anatomical mesh regularization . . . 137
B.1.1 Strain energy density as an improved, higher-order regularization penalty 138
B.1.2 Proposed form meets requirements of a hyperelastic material. . . . 141
B.1.3 Using projection to minimize anatomical deformations within a spherical framework . . . 144
B.2 aMSM validation . . . 145
B.3 aMSM implementation details . . . 149
B.4 Minimizing directional registration bias for accurate growth measurements . 153
B.5 Effect of strain energy minimization on quality of alignment . . . 156
B.6 Growth estimates for short and long time steps . . . 158
B.7 Atlas generation with aMSM . . . 159

Appendix C Codes . . . 161
C.1 Discrete orientation fields and stress-dependent growth in ABAQUS . . . 161
C.2 Strain energy minimization in MATLAB . . . 185

Vita **217**

List of Tables

2.1 Model dimensions and sources 57
2.2 Model parameters and sources 57

4.1 Statistical improvements due to aMSM alignment 121
4.2 Linear fits for locations 1-10 122
4.3 Demographic information for studied cohort 123
4.4 Postmenstrual ages and time steps for individuals 124

List of Figures

1.1 Developmental timeline from conception to birth in human 2
1.2 Neurulation of the forebrain 3
1.3 Major brain compartments in human and chick 4
1.4 Mechanics of brain folding 6
1.5 Mechanics of growth 8
1.6 Mechanical feedback in growth 12

2.1 Forebrain development in chick embryo 21
2.2 Effects of actomyosin contraction on early forebrain morphogenesis (HH11–12) 34
2.3 Actin patterns in HH12 brain tube 37
2.4 Finite element models of initial forebrain subdivision (HH11–12) 39
2.5 Effects of eCSF pressure on forebrain development (HH12–17) 42
2.6 Finite element model of brain tube morphogenesis including flexure and stress-dependent growth (HH12–17) 44
2.7 Comparison of stress-dependent and uniform growth models 47
2.8 Forebrain regionalization in terms of columnar, prosomeric, and mechanistic subdivisions 55
2.9 Effects of free parameter (α), notochord, and stress-dependent growth on final BT shape 58

3.1 Normal development of the telencephalic hemispheres in the chicken embryo 60
3.2 Cell proliferation in the SP 65
3.3 Altering eCSF pressure in the embryonic brain 68
3.4 Effect of eCSF pressure on growth 70
3.5 Computational model for hemisphere division 76
3.6 Comparison of model and experimental growth 77
3.7 Comparison of model and experimental patterns of wall stress 79
3.8 Effects of external tissues 81
3.9 Comparison of numerical and experimental results for perturbed eCSF pressure 83
3.10 Effects of early pressure elevation on hemisphere morphogenesis 85
3.11 Proliferation is only decreased in the telencephalic roof plate at HH21 101

4.1 Global measures of cortical surface area and folding increase over time. . . . 104
4.2 Longitudinal (intra-subject) registration with aMSM 107
4.3 Gradients of cortical expansion are evident in individual brains 108

4.4 Gradients of cortical expansion and folding are consistent across subjects . . 109
4.5 Regions of highest cortical expansion change over time 112
4.6 Growth rate decreases in initially fast-growing cortical areas 113
4.7 Trajectory of preterm growth may continue after term 117

A.1 Change in lumen size during development 131
A.2 Experiments to rule out external factors 132
A.3 Notochord tension supports constrained growth model of flexure 134
A.4 Lumen pressure measurements in vivo 134
A.5 Removal of OVs has minimal effect on late stage BT morphogenesis 136

B.1 aMSM parameter effects on simple undulating geometry 148
B.2 aMSM optimized for complex, variable geometries 152
B.3 Averaging forward and reverse registrations to eliminate bias 155
B.4 Strain energy minimization does not adversely affect alignment of folds . . . 157
B.5 Effect of time interval between scans 159
B.6 Atlas generation and aMSM improvement (reduction in 3D dispersion) . . . 160

Acknowledgments

First and foremost, I would like to thank my advisor, Dr. Larry Taber. I am extremely grateful for all you have taught me in the past five years. Your rigorous approach has drastically improved my engineering, research, and communication skills. Thank you for your patience through our MANY rounds of edits! I have truly appreciated your mentorship, and I could not have asked for a more understanding advisor.

I would also like to thank Dr. Phil Bayly, who served as a secondary advisor and mentor throughout my PhD. I cannot express my gratitude for your guidance on both PhD and post-PhD work, and I look forward to working together in my post-graduate career. To the rest of my committee: Dr. Ruth Okamoto, thank you for valuable insights on experiments, modeling, and statistical analysis throughout the past five years – and for leading Biomechanics Journal Club, one of the most enjoyable classes of my PhD. Dr. Jin-Yu Shao, thank you for providing my foundation on continuum mechanics and offering advice throughout my PhD. Dr. David Van Essen, thank you for sharing your expertise in neuroscience and brain mapping, and for sparking collaborations essential to the success of my third project.

To my collaborators in the Washington University Neonatal Development Research group, especially Jim Alexopoulos, Dr. Chris Smyser, Dr. Cynthia Rogers, Dr. Cindy Ortinau, Dr. Jeff Neil, and Dr. Terrie Inder: thank you for not only providing valuable data but also welcoming me into your lab. I have truly appreciated this glimpse into the world of clinical research. I would also like to thank Donna Dierker, Matt Glasser, and Tim Coalson of the

Van Essen Lab. Finally, a very special thanks to Emma Robinson at Kings College London, for using her computer science genius to turn our ideas into a reality.

To my Taber lab mates: thank you for your friendship and help along the way. Alina Oltean and Gaby Espinosa taught me everything I know about working in the lab. It has been a pleasure to work with you both, as well as Hadi Hosseini, Yunfei Shi, Matt Wyzalkowski, Zi Chen, and my undergraduates Haley Nichols and Doren Lan. To my predecessors, Ben Filas and Andy Knutsen, thank you for paving the way for my doctoral research and offering your advice. To Wade Stewart and Jason Gleghorn at the University of Delaware, thank you for providing valuable (and challenging to obtain) data.

Lastly, I would like to thank my family. Mom, you have been a source of motivation and confidence as I pursued engineering, graduate school, and now my career. Dad, your support and outside perspective has helped me take an often-needed step back. Lauren, I would not have started this academic path without the example you set from an early age. Carrie, Jim, Laura, Grace, Caleb, and Luke: I couldn't have asked for better "bonus" family. Ed and Mako, thank you for raising a wonderful son, and especially for encouraging him to pamper his wife during this stressful time. And last but not least, thank you Marcel! After 10 years (and 7 degrees) together, I cannot imagine a better companion. Thank you for being my biggest supporter in every aspect of life, and especially for keeping me sane this past year.

Kara E. Garcia

Washington University in Saint Louis

December 2017

Dedicated to my family.

ABSTRACT OF THE DISSERTATION

Mechanics of the Developing Brain:

From Smooth-walled Tube to the Folded Cortex

by

Kara E. Garcia

Doctor of Philosophy in Biomedical Engineering

Washington University in St. Louis, December 2017

Research Advisor: Professor Larry A. Taber

Over the course of human development, the brain undergoes dramatic physical changes to achieve its final, convoluted shape. However, the forces underlying every cinch, bulge, and fold remain poorly understood. This doctoral research focuses on the mechanical processes responsible for early (embryonic) and late (preterm) brain development.

First, we examine early brain development in the chicken embryo, which is similar to human at these stages. Research has primarily focused on molecular signals to describe morphogenesis, but mechanical analysis can also provide important insights. Using a combination of experiments and finite element modeling, we find that actomyosin contraction is responsible for initial segmentation of the forebrain. By considering mechanical forces from the internal and external environment, we propose a role for mechanical feedback in maintaining these segments during subsequent inflation and bending. Next, we extend our analysis to division of right and left cerebral hemispheres. In this case, we discover that morphogen signals and mechanical feedback act synergistically to shape the hemispheres.

In human, cerebral hemispheres go on to form complex folds through a mechanical process that involves rapid expansion of the cortical surface. However, the spatiotemporal dynamics of cortical growth remain unknown in human. Here, we develop a novel strain energy minimization approach to measure regional growth in complex surfaces. By considering brain surfaces of preterm subjects, reconstructed from magnetic resonance imaging (MRI), this analysis reveals distinct patterns of cortical growth that evolve over the third trimester. This information provides a comprehensive view of cortical growth and folding, connecting what is known about patterns of development at the cellular and folding scales.

Abnormal brain morphogenesis can lead to serious structural defects and neurological disorders such as epilepsy and autism. By integrating mechanics, biology, and neuroimaging, we gain a more complete understanding of brain development. By studying physical changes from the simple, microscopic embryo to the macroscopic, folded cortex, we gain insight into relevant biological and physical mechanisms across developmental stages.

Preface

> Cell and tissue, shell and bone, leaf and flower, are so many portions of matter, and it is in obedience to the laws of physics that their particles have been moved, moulded and conformed. They are no exceptions to the rule that 'God always geometrizes.' Their problems of form are in the first instance mathematical problems, their problems of growth are essentially physical problems, and the morphologist is, *ipso facto*, a student of physical science.
> – D'Arcy Thompson, *On Growth and Form* (1917)

Exactly a century ago, D'Arcy Thompson published his famous book *On Growth and Form*, highlighting the role of physical laws, math, and mechanics in the development of living structures (Thompson et al., 1942). At a time when Darwinian evolution had emerged as the "explanation" for everything, Thompson called for engineering principles to explain not just *why* but *how* these morphologies came to be.

For the next half century, embryologists focused on physical changes, and mathematicians offered equations to explain morphogenesis (e.g., Turing patterns). However, with the discovery of DNA, genetics again took the center stage. Genetic and molecular perturbations have undoubtedly provided valuable insights into development and disease. Still, studies tend to report "interesting" or "peculiar" changes in morphology without a clear understanding of *how* these morphologies occur. In thousands of cases, the question remains: what are the physical mechanisms underlying morpohogenesis?

In this dissertation, we will address three of these cases, specific to brain development, by analyzing the mechanical forces responsible for morphogenesis.

Chapter 1

Introduction

The human brain is a physically complex organ with structure closely linked to function. The most primitive brain structures emerge shortly after conception and increase in complexity through the first years of human life. Malformations at early stages can lead to lethal brain defects (Lowery and Sive, 2009; Fernandes et al., 2007), while abnormal development at later stages can lead to serious neurological disorders (Lin et al., 2006; Li et al., 2016; Hardan et al., 2004). In this thesis, we examine the morphological changes responsible for shaping the early neural tube into the intricately folded structure we associate with human cognition. By studying the mechanics of brain development, we gain insight into how brain malformations occur. Furthermore, lessons from the brain may prove useful for a diverse range of biological applications, including development of other organs and tissue engineering.

1.1 Brain development, from conception to birth

As shown in Fig. 1.1, development of the embryonic brain begins shortly after conception. First, the single cell zygote divides to form a multicellular morula, which then becomes a

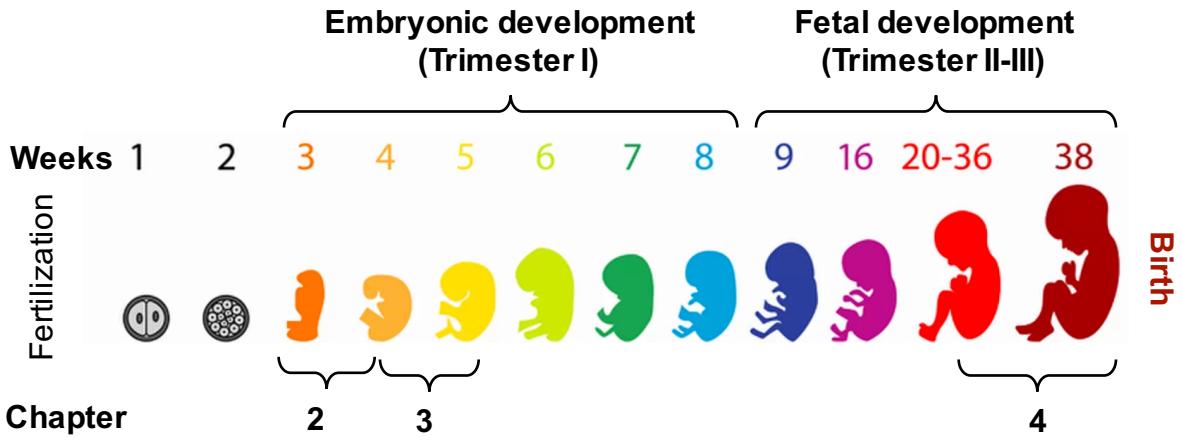

Figure 1.1: Developmental timeline from conception to birth in human. In Chapters 2-3, we model embryonic brain development that occurs during the first trimester (3-5 weeks gestational age) in human. In Chapter 4, we will examine fetal brain folding that occurs during the third trimester (28-38 weeks gestational age) and beyond in human. Image credit: Dragana Gerasimoski, Shutterstock.

blastula with inner and outer layers (Hall, 2012). Finally, gastrulation leads to the three distinct germ layers: ectoderm, mesoderm, and endoderm. From the flat ectoderm layer, the neural plate emerges as a thick, pseudostratified neuroepithelium (Fig. 1.2) (Ray and Niswander, 2012). Even at this early stage, morphogen signals begin to encode which cells will become brain, eye, or spinal cord (Puelles et al., 2012).

In avian and mammalian species, the neural tube forms through the well-studied physical process of neurulation (Ray and Niswander, 2012; Nonomura et al., 2013). First, acto-myosin contraction at the floor plate causes the neural plate to hinge and form a "V" shape (Fig. 1.2A-B). Next, lateral hinges form on the sides of this "V", bringing lateral edges together to fuse at the roof plate (Fig. 1.2C-D), forming a *neural tube*. Eventually, the anterior and posterior ends (anterior and posterior neuropores) also seal, and neuroepithelial cells begin to secrete embryonic cerebrospinal fluid (eCSF) that inflates the lumen (Jelinek and Pexieder, 1968; Desmond et al., 2005). The anterior portion of the neural tube becomes the

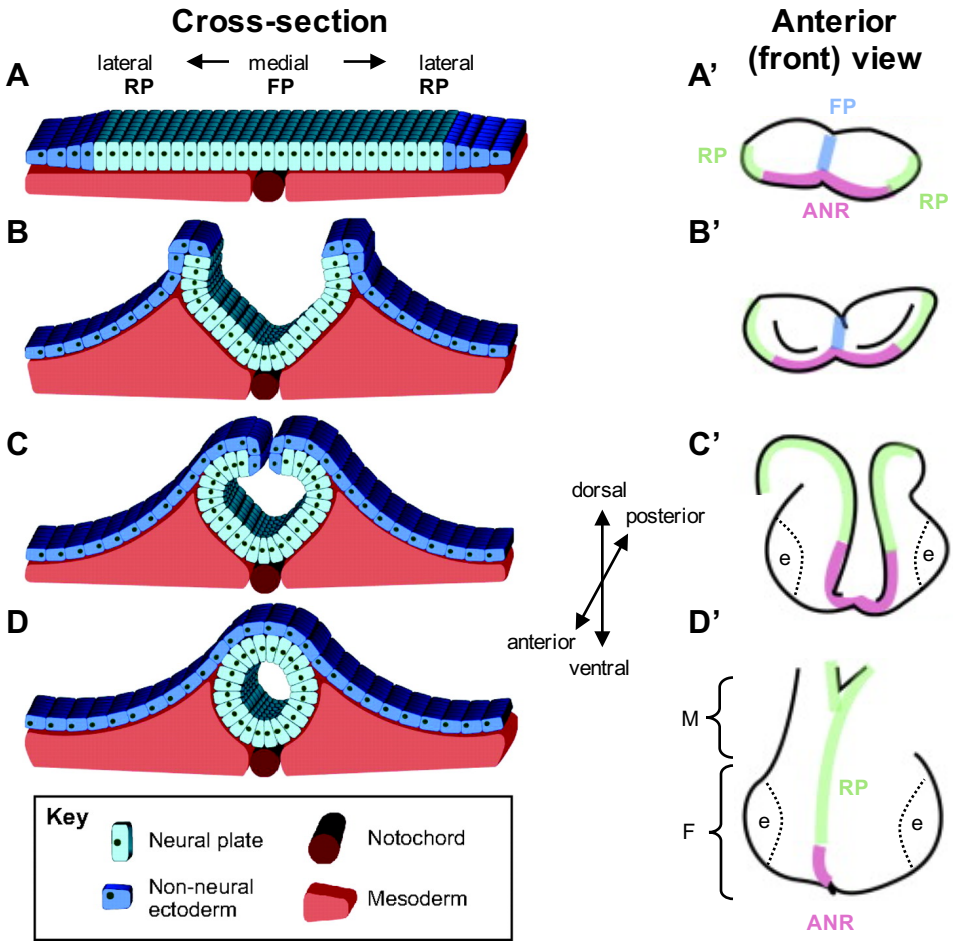

Figure 1.2: Neurulation of the forebrain. (A-D) Steps of neurulation in a cross-section of the neural tube, image modified from Ray and Niswander (2012). (A'-D') Front view of neurulation in the mammalian forebrain, modified from Nonomura et al. (2013). FP=floor plate, RP=roof plate, ANR=anterior neural ridge, F=forebrain, M=midbrain, e=eye field.

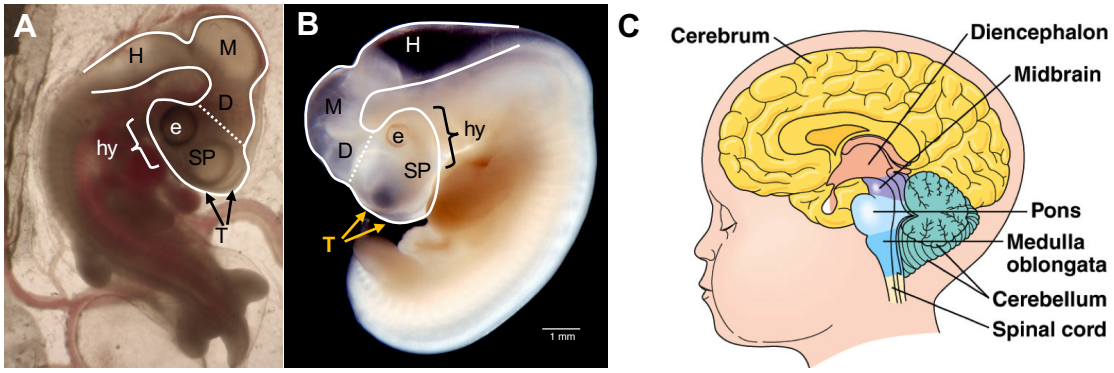

Figure 1.3: Major brain compartments in human and chick. (A) Bright field image of chicken embryo at latest stage considered. At this time, local constrictions visibly separate the hindbrain (H) from midbrain (M), midbrain from diencephalon (D), and diencephalon from secondary prosencephalon (denoted with dotted line). The secondary prosencephalon (SP) is subdivided into right and left telencephalic hemispheres (T, arrows), hypothalamus (hy), and prospective eyes (e). (B) The same brain regions and similar brain shape are observed in human at comparable stages (from embryo.soad.umich.edu). (C) The telencephalic (cerebral) hemispheres comprise the majority of the adult human brain, shown in yellow. Meanwhile, the hindbrain (pons, cerebellum) and midbrain make up the brainstem. Image modified from Pearson Education, Inc. (copyright).

brain (or brain tube), while the posterior portion becomes the spinal cord. Notably, the anterior neuropore (or anterior neural ridge, ANR, see Fig. 1.2A'-D'), roof plate (RP), and floor plate (FP) become important signaling centers in later development of the cerebral hemispheres (Nonomura et al., 2013; Puelles et al., 2012; Fernandes et al., 2007).

In parallel to the processes of neurulation and inflation, the brain tube segments along its length into three primary vesicles: the forebrain (prosencephalon), midbrain (mesencephalon), and hindbrain (rhombencephalon) (Lowery and Sive, 2009). Several studies have suggested that the constrictions between these regions are also initiated by a type of actomyosin contraction (Filas et al., 2012; Gutzman et al., 2008). The midbrain and hindbrain go on to make up the brain stem (midbrain, pons, and cerebellum), while the forebrain segments further into diencephalon and secondary prosencephalon (Fig. 1.3) (Puelles et al.,

2012). From the secondary prosencephalon, the ventral portion (closest to the floor plate, Fig. 1.2A'-D') becomes the hypothalamus, lateral portions evaginate into optic vesicles (future eyes), and dorsal portions evaginate into telencephalic hemispheres (Puelles et al., 2012). These telencephalic hemispheres become the adult cerebral hemispheres (cerebrum), which comprise the majority of the human brain volume (Fig. 1.3C). As all of these regions become morphologically distinct, they also expand rapidly. This expansion is facilitated by eCSF, which mechanically inflates each compartment and stimulates growth (Desmond and Jacobson, 1977; Desmond et al., 2014). Gradually, embryonic CSF transitions to adult CSF, fluid-filled lumens become brain ventricles, and neuroepithelium differentiates into neurons and glia (Lowery and Sive, 2009).

During early stages, embryos look nearly identical between many vertebrate species (Fig. 1.3A-B). Here, we use the chicken embryo (Fig. 1.3A) as an experimental model of early forebrain morphogenesis. Beyond this embryonic stage, however, brain morphologies diverge drastically between species (Fig. 1.4). In small animals (such as chicken and mouse), cerebral hemispheres tend to remain smooth, or lissencephalic, through adulthood (Tallinen et al., 2014; Chenn and Walsh, 2002). By contrast, the brains of humans and many large mammals develop cortical folds (Smart and McSherry, 1986; Wang et al., 2017). The first folds to emerge are fairly consistent across species and individuals, while secondary folds observed in human are more complex and variable between individuals. In humans, most folding occurs during the third trimester, with additional growth and deepening of folds through the first years of life (Dubois et al., 2007; Hill et al., 2010b).

Increasing mechanical evidence suggests that folding results from differential growth: the outer gray matter of the cortex grows faster than inner white matter, leading to mechanical buckling or creasing (Toro and Burnod, 2005; Bayly et al., 2013; Xu et al., 2010b; Tallinen

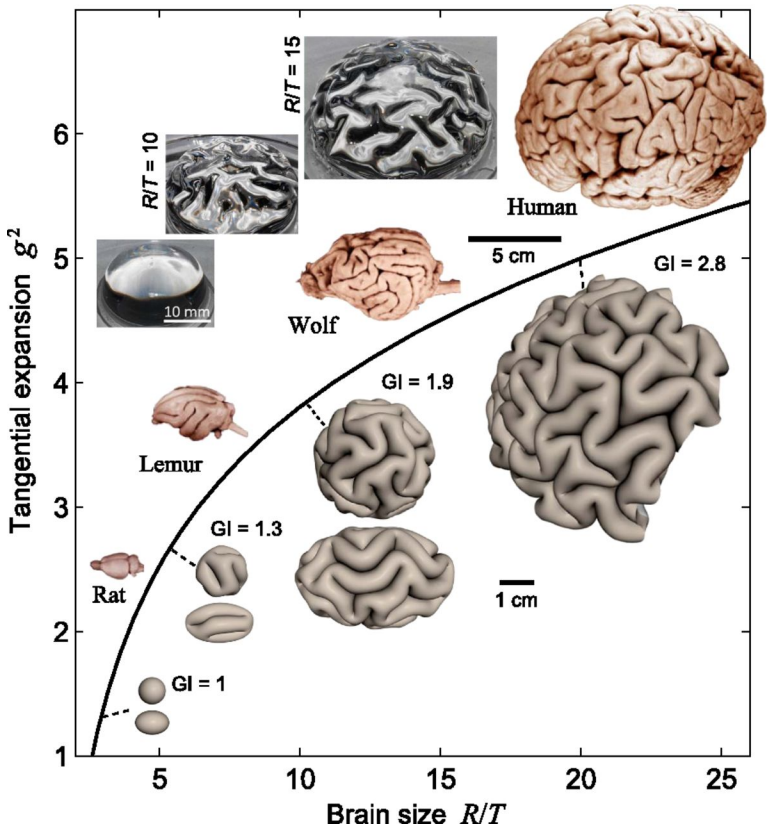

Figure 1.4: Mechanical models of cortical folding describe trends in brain folding. From (Tallinen et al., 2014), the degree of cortical folding (gyrification index, GI) can be explained by mechanical instability and physical scale. Rats (and similarly, chickens) do not have folded brains, but folding in larger mammals (lemur, wolf, human) generally increases with brain size. Top insets: Physical gel model of folding, where the outer layer of gel expands faster than the inner layer to produce mechanical instability. Bottom insets: Computational model of folding, which predicts folding trends as a function of both size and shape.

et al., 2014). However, other factors (e.g., brain geometry, regional growth differences, intracortical connections) likely influence these specific folding patterns (Toro and Burnod, 2005; Weickenmeier et al., 2016; Van Essen, 1997). While computational models have considered the effects of geometry (Tallinen et al., 2016), much remains unknown regarding the dynamic and spatial patterns of physical growth in the human brain.

1.2 Mechanics in morphogenesis

To understand the mechanical forces involved in brain morphogenesis, it is useful to first discuss some simple examples of growth theory, as well as their prior application in other organ systems. We start with examples of *biomechanics*, defined here as a biological process that exerts mechanical force to cause deformation or stress. Then, we move on to *mechanobiology*, the influence of mechanical force on a biological process.

1.2.1 Biomechanics of growth

As previously described, the embryonic brain is made up of tightly connected (neuro)epithelial cells that form a pseudostratified monolayer. Similarly, we consider one-dimensional growth of a bar with length L_0, made up of a single row of connected cells. In Fig. 1.5A, simple multiplication of these cells (proliferation) results in growth along a single line, such that the new length of the bar becomes L, and growth can be defined with the ratio $G = L/L_0$. In the absence of any external forces, the total deformation (stretch ratio) of this bar is equal to its growth, such that $\lambda = G = L/L_0$ and no stresses develop.

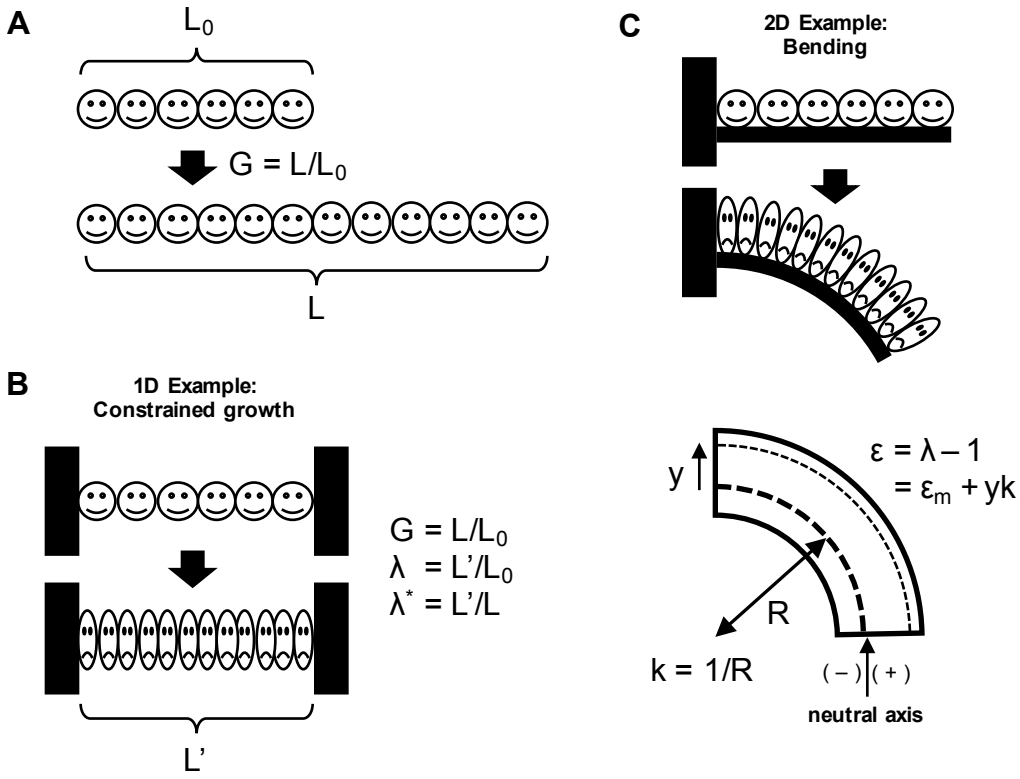

Figure 1.5: Mechanics of growth. (A) In the current framework, we model tissue growth (e.g., proliferation) as change in the unloaded geometry. For a single row of cells (circular faces, length L_0), one round of cell division (doubling the number of cells) could lead to a new length of $L = 2L_0$. (B) In the presence of physical constraints (black blocks represent fixed walls), the observed deformation (λ) is a combination of tissue growth (G) and elastic deformation (λ^*). In the above case where $G = L/L_0 = 2$ and $\lambda = L'/L = 1$, an elastic deformation of $\lambda^* = L'/L = 1/2$ is necessary to represent compression of the tissue. (L' represents the observed final length, in this case $L' = L$.) (C) Extending this example to 2D, we consider the same row of proliferating cells, this time attached to a flexible but non-growing bar along the bottom edge. In this case, growth can lead to complex deformations: To accommodate lengthening of the top layer only, but maintain connection between the growing and nongrowing layers bend, both structures must bend. The resulting shape and stresses can be predicted using mechanical theory.

In the real world, however, external constraints often exist that restrict deformation (Taber, 2009). In Fig. 1.5 we imagine the same bar, now constrained between two rigid walls (Fig. 1.5B). In this case growth has not changed ($G = L/L_0$), but the bar is mechanically compressed to a final length $L' = L_0$. Accordingly, we define total deformation as the combination of growth ($G = L/L_0$, due to biological processes) and elastic deformation ($\lambda^* = L'/L$, due to mechanical forces) such that

$$\lambda = \lambda^* G = L'/L_0. \tag{1.1}$$

In 3D, total deformation can be denoted similarly as

$$\mathbf{F} = \mathbf{F}^* \cdot \mathbf{G} \tag{1.2}$$

where $\mathbf{G}$ represents the 3D growth tensor and $\mathbf{F}^*$ represents the 3D elastic deformation gradient tensor (Rodriguez et al., 1994).

With this framework, we can begin to consider shape changes due to the mechanical "force", or stress, exerted by biological growth. For instance, a bilayer beam in which one layer grows more can produce bending of a structure (Fig. 1.5C). This effect has been previously studied in the embryonic heart tube (Shi et al., 2014) and optic cup (Oltean et al., 2016), and it has been hypothesized to play a role in bending of the brain tube (Takamatsu and Fujita, 1987). Contraction of an inner layer ($G < 1$) can also produce bending. For example, apical actomyosin contracts to form hinge points during neurulation (Ray and Niswander, 2012) (Fig. 1.2), as well as local constriction at the midbrain-hindbrain boundary (Filas et al., 2012). For the latter case, Filas et al. (2012) demonstrated that a bias in the direction of actomyosin contraction can lead to specific morphological shapes in 3D.

The process of cortical folding, in which the outer gray matter is thought to grow faster than the underlying white matter, offers a complex scenario of constrained growth and bending (Fig 1.4). In this case, the growing gray matter is constrained in both tangential directions (Fig. 1.5B) by surrounding tissue, and the underlying white matter represents a deformable substrate (Bayly et al., 2013; Tallinen et al., 2016). As the gray matter grows, the tissue becomes compressed, storing mechanical strain energy. Beyond a certain threshold, however, it becomes more energetically favorable for the gray matter to buckle or crease, resulting in curvature and bending (Fig. 1.4).

In Fig. 1.5C, note that a neutral axis (neutral surface in 3D) can be defined where strains due to bending are zero ($y = 0$). For $y > 0$ (toward the outer curvature) the bending strain $\epsilon_b = yk$ is positive ($\lambda > 1$), and for $y < 0$ (toward the inner curvature) the total bending strain is negative, where $k = 1/R$ represents curvature of the midthickness surface and $R =$ radius (Ventsel and Krauthammer, 2001). If the neutral axis undergoes additional growth, contraction, stretch, or compression, it is convenient to separate total strain into membrane (ϵ_m) and bending (ϵ_b) components. Under the assumption of small strain, $\epsilon = \lambda - 1 = \epsilon_m + \epsilon_b$. In Chapter 4 we consider membrane strain analysis, which omits bending strains and can be useful for analysis of surface reconstructions in which thickness information is not available.

1.2.2 Mechanobiology in growth

Up to this point, we have considered physical changes that occur due to growth. However, mechanical feedback is also known to induce biological effects. In adult physiology, stresses cause remodeling of bone, cardiovascular tissues, and tendons (Wang and Thampatty, 2006). In early brain development, mechanical feedback has been shown to produce changes in

actomyosin contractility and, therefore, tissue stiffness (Filas et al., 2011). Evidence also suggests that mechanical feedback can influence proliferation in a variety of tissues and developmental processes (Mammoto and Ingber, 2010).

In 1D, we consider the effect of mechanical stress on proliferation, or growth (G), according to the general law (Taber, 2009)

$$\dot{G} = (g_0 + g_\sigma \sigma)G \tag{1.3}$$

where g_0 is the baseline growth rate, g_σ is the stress-dependent growth constant, and dot denotes differentiation with respect to time t. Stress, σ, depends on elastic deformation (λ^*) and material properties, such that $\sigma > 0$ represents mechanical tension ($\lambda^* > 1$) and $\sigma < 0$ represents compression ($\lambda^* < 1$).

In the absence of mechanical feedback ($g_\sigma = 0$ or $\sigma = 0$), this differential equation can be solved as the standard equation for exponential growth, $G = e^{g_0 t}$. However, by allowing growth rate to depend on tension and compression, we obtain interesting behaviors in line with observations in a variety of epithelial tissues. For example, stretch (tension) has been shown to promote cell proliferation in pulmonary and vascular epithelium (Chaturvedi et al., 2007; Lehoux et al., 2005). This behavior can be achieved by setting $g_\sigma > 0$ (Taber, 2009), such that tension ($\sigma > 0$) increases the growth rate and compression ($\sigma < 0$) decreases the growth rate.

In carefully controlled experiments using epithelial monolayers (Wyatt et al., 2015; Streichan et al., 2014), stretch-induced cell divisions eventually stopped, restoring initial cell shapes at equilibrium (Wyatt et al., 2015). To understand this effect, we return to our 1D bar, attaching it to two rigid walls spaced such that $L' > L_0$ (Fig. 1.6A, top). At the initial time point, $L = L_0$ and $\lambda^* = L'/L_0 > 1$. This stretch leads to $\sigma > 0$, such that Eq. 1.3 ($g_\sigma > 0$)

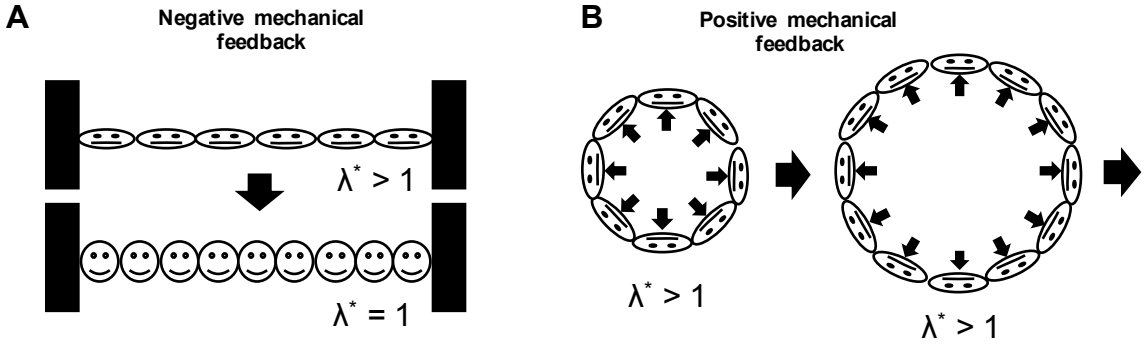

Figure 1.6: Mechanical feedback in growth (for simple cases of $g_\sigma > 0$, $g_0 = 0$). (A) For a predefined elastic stretch ($\lambda^* > 1$), mechanical tension can induce cell proliferation. As cells are produced to fill the space, tension decreases. This results in less proliferation, and so forth, until a stable equilibrium is reached. (B) By contrast, consider a ring of connected cells, with stretch induced by a constant pressure, p (denoted by small arrows). As these cells proliferate (increasing the ring's radius but not thickness), tension and proliferation continue to increase. In this case (a positive feedback loop), the structure will continue to grow and no equilibrium will be reached.

predicts an increase in proliferation (Fig. 1.6A, bottom). Furthermore, once the cells are sufficiently compressed ($\sigma_0 = -g_0/g_\sigma$), we expect growth to stop completely. A similar effect has been observed in *Drosophila* wing, where surrounding tissue causes compression and regional growth reduction during morphogenesis (Hufnagel et al., 2007; Aegerter-Wilmsen et al., 2007).

In Fig. 1.6A, stress serves as a negative feedback factor to ensure equilibrium. (Note that $g_0 > 0$ will lead to compression at equilibrium, $g_0 < 0$ will lead to tension at equilibrium, and $g_0 = 0$ will lead to zero stress at equilibrium.) However, the same growth law can produce positive feedback under different circumstances (Fig. 1.6B).

In a wide range of biological systems, fluid exerts pressure to elastically stretch tissues or organs. Examples include blood in the vessels or heart, fluid in the developing lung buds, and eCSF in the brain. For thin-walled vessels, hoop stress due to pressure can be approximated

by Laplace's Law,

$$\sigma = pr/h \tag{1.4}$$

where p is the internal pressure, r is the cross-sectional radius, and h is the wall thickness.

For a vessel under pressure, our growth law (assuming $g_\sigma > 0$) predicts increased proliferation due to the initial stretch of wall cells. However, growth does not succeed in reducing stress. Instead, circumferential growth causes an increase in radius and, therefore, a further increase in wall tension. This scenario leads to positive feedback, driving the structure to grow dramatically (Fig. 1.6B) until some external force or change in the growth law is applied. Similarly, altering eCSF pressure can drastically affect size of the early brain (Desmond and Jacobson, 1977; Alonso et al., 1998) despite extremely low pressures (Jelinek and Pexieder, 1968).

1.2.3 Stress and strain energy minimization

In 3D continuum mechanics, Cauchy stress is defined by the tensor (Taber, 2004)

$$\boldsymbol{\sigma} = J^{*-1}\mathbf{F}^* \cdot \frac{\partial W}{\partial \mathbf{F}^{*T}} \tag{1.5}$$

where $J^* = \det \mathbf{F}^*$ is the elastic volume ratio, T denotes the transpose, and $W = W(\mathbf{F}^*)$ is the elastic strain energy density function that describes material behavior.

In the simple, 1D analysis above (Fig. 1.6A), the goal of feedback was to minimize a mechanical quantity. Whether that quantity is truly Cauchy stress ($\boldsymbol{\sigma}$), strain energy density (W), or some other function of elastic deformation ($\mathbf{F}^*$) remains subject to debate. However, all roughly seek to minimize physical energy, a common concept in nature.

In Chapter 4, we seek a realistic solution for the deformation between younger (initial) and older (final) cortical surfaces. However, the elastic and growth components of deformation cannot be practically separated. For this problem, we take a step back from cellular mechanisms that may drive stress-dependent growth, instead thinking of growth as another energetic quantity to be minimized. Since both elastic stretch and tissue growth require energy, we assume nature will seek to minimize both to efficiently achieve the observed final structure. (This convoluted structure, which cannot be altered in our analysis, may in turn represent the most efficient shape for compact wiring (Van Essen, 1997) and/or differential growth between cortical layers (Toro and Burnod, 2005; Xu et al., 2010b; Tallinen et al., 2014).) Thus, we minimize the total surface strain energy, now defined as $W = W(\mathbf{F})$.

1.3 Research Significance

By considering both the mechanical effects of biological factors (biomechanics) and the biological effects of mechanical factors (mechanobiology), this dissertation provides insights into normal and abnormal brain development. Furthermore, the general approaches and theories developed here may be applied to future studies of brain development, other organ systems, or tissue engineering.

Notably, incomplete hemisphere division represents the most common brain malformation in human, occurring in 1 out of every 250 human pregnancies (Matsunaga and Shiota, 1977). Though most embryos do not survive to birth, the cases that do (1 in 10,000 live births) often present with neurological disorders (Leoncini et al., 2008; Barkovich et al., 2012). Furthermore, too little or too much growth can lead to microcephaly (small brain) or megalencephaly (oversized brain), respectively. Microcephaly is generally rare, but it is more

commonly observed with holoprosencephaly (Fernandes et al., 2007). By contrast, megalencephaly occurs in 2% of the general adult population and has been linked to neurological disorders including epilepsy and autism (Barkovich et al., 2012). Using mechanical analysis, we find that even subtle alterations in mechanical forces (eCSF pressure) may play a role in these morphologies.

In a broader sense, these embryonic studies explore the response of biological tissue to mechanical loading. Because the brain is comprised of simple epithelium at the stages considered, our observations may translate to other biological systems. The mechanisms, mechanical feedback laws, and modeling techniques described in this research may prove useful in future studies of organ or tissue development.

Beyond the embryonic phase, abnormal cortical folding has been linked to neural disorders including autism, epilepsy, and schizophrenia (Lin et al., 2006; Li et al., 2016; Hardan et al., 2004). In some cases the effect is global: too many small folds (microgyria), too few shallow folds (pachygyria), or possibly a brain that is too large or small (Fig. 1.4). Locally, abnormal folding can occur through injury including hydrocephalus (overinflated ventricles press on the brain), intraventricular hemorrhage, and brain lesions. Preterm infants are at special risk for these injuries.

For fetal and neonatal brain development, magnetic resonance imaging (MRI) offers a safe, noninvasive tool to record brain geometry, material properties, and functional activity (Shimony et al., 2016; Ball et al., 2014; Mukherjee et al., 2005; Glasser et al., 2016a). However, clinical researchers have been unable to obtain accurate, precise measures of physical growth during this period. By considering the mechanical concept of strain energy minimization, we develop a novel technique for measuring brain growth from structural MRI data. We illustrate its clinical application in preterm infants, providing unprecedented detail on the

dynamics of cortical growth and folding. By incorporating this mechanical theory into a free analysis tool already used by neuroscientists and clinical researchers (Robinson et al., 2014), our approach may be applied to a wide range of future clinical and animal studies.

1.4 Synopsis of dissertation

This dissertation can be divided into three distinct phases of brain development (Fig. 1.1), as outlined below.[1]

1.4.1 Segmentation, inflation, and bending of the forebrain

In Chapter 2, we describe the physical processes that partition the forebrain into the diencephalon, telencephalon, and optic vesicles. Furthermore, we explain how constrictions between these regions may be maintained (and exaggerated) during subsequent inflation, growth and bending. In experiments on chicken embryos, chemical perturbations of contractility and patterns of F-actin indicate a major role for actomyosin contraction in the creation of initial constrictions. However, the same experiments suggest that this effect is short-lived.

We propose a mechanical feedback mechanism to maintain and deepen these constrictions at later stages, such that growth is influenced by stresses from actomyosin contraction. This idea was examined by including stress-dependent growth in a model with eCSF pressure and bending (cephalic flexure). Model results are in close agreement with morphological changes observed under normal and reduced eCSF pressure, as well as previously published

[1]These chapters include co-authored work (first-author Kara E. Garcia). Contributions of co-authors are denoted at the beginning of each chapter.

patterns of cell proliferation. Taken together, our results support a biphasic mechanism for forebrain morphogenesis, initiated by differential contractility and propagated stress-dependent growth.

1.4.2 Emergence of the right and left hemispheres

In Chapter 3, we extend our mechanical feedback model to the next major change in brain morphology: division of the telencephalon into right and left cerebral hemispheres. From previous studies, we acquire a wealth of information regarding morphogen signals involved in this phenomenon. While it is widely accepted that these signals influence growth, and that these signals are necessary to cleave the hemispheres, no studies have analyzed whether differential growth is able to physically shape the cerebral hemispheres.

Unlike the processes in Chapter 2, disruption of embryonic hemisphere morphogenesis relates to several clinically-observed conditions, including holoprosencephaly, microcephaly, and megalencephaly. Some of these cases, particularly those associated with genetic or teratogenic factors, can be explained by aforementioned signals, but not all. In this study, we show that even subtle alterations in mechanical feedback (eCSF pressure) provide a morphogen-independent route to these morphologies.

1.4.3 Patterns of growth during cortical folding in human

In Chapter 4, we move directly from chicken to human, measuring surface expansion during the complex process of cortical folding. We consider surface reconstructions from preterm infants, imaged several times over the course of the third trimester, to quantify and understand the dynamics of brain growth and folding.

In a multidisciplinary, collaborative effort, we developed a new tool called anatomically-constrained Multimodal Surface Matching (aMSM). This approach merges current brain mapping techniques with mechanical theory to estimate physical deformation between younger and older time points. Our results suggest a pattern of cortical expansion consistent with what is known regarding regional maturation and the timing of new folds. We also detect injury in individual subjects, suggesting that this technique could be used to explore clinical conditions associated with abnormal growth due to genetics, injury, or other environmental variables.

Chapter 2

Contraction and stress-dependent growth shape the forebrain of the early chicken embryo[2]

Summary During early vertebrate development, local constrictions, or sulci, form to divide the forebrain into the diencephalon, telencephalon, and optic vesicles. These partitions are maintained and exaggerated as the brain tube inflates, grows, and bends. Combining quantitative experiments on chick embryos with computational modeling, we investigated the biophysical mechanisms that drive these changes in brain shape. Chemical perturbations of contractility indicated that actomyosin contraction plays a major role in the creation of initial constrictions (Hamburger-Hamilton stages HH11–12), and fluorescent staining revealed that F-actin is circumferentially aligned at all constrictions. A finite element model based on these findings shows that the observed shape changes are consistent with circumferential contraction in these regions. To explain why sulci continue to deepen as the forebrain

[2]Based on published manuscript: K. E. Garcia, R. J. Okamoto, P. V. Bayly, and L. A. Taber. Contraction and stress-dependent growth shape the forebrain of the early chicken embryo. *Journal of the mechanical behavior of biomedical materials*, 65:383397, 2017. https://doi.org/10.1016/j.jmbbm.2016.08.010. Larry Taber, Ruth Okamoto, and Philip Bayly helped design the experiments and edited the manuscript.

expands (HH12–20), we speculate that growth depends on wall stress. This idea was examined by including stress-dependent growth in a model with cerebrospinal fluid pressure and bending (cephalic flexure). The results given by the model agree with observed morphological changes that occur in the brain tube under normal and reduced eCSF pressure, quantitative measurements of relative sulcal depth versus time, and previously published patterns of cell proliferation. Taken together, our results support a biphasic mechanism for forebrain morphogenesis consisting of differential contractility (early) and stress-dependent growth (late).

2.1 Introduction

The embryonic brain emerges through a series of complex physical processes. Following neurulation, the anterior end of the neural tube expands to create the primitive brain, and circumferential constrictions, or sulci, divide the brain tube (BT) into three primary vesicles called the forebrain, midbrain, and hindbrain (Lowery and Sive, 2009). In the forebrain, additional constrictions form to separate the telencephalon, diencephalon, and the optic vesicles (Fig. 2.1). Meanwhile embryonic cerebrospinal fluid (eCSF) accumulates in the lumen, and the brain undergoes a period of rapid expansion and flexure. During these stages, insufficient growth of the forebrain can result in microcephaly (small brain) (Cox et al., 2006), and abnormal shaping has been linked to a range of neurodevelopmental disorders (Lowery and Sive, 2009).

This paper aims to explain secondary morphogenesis of the forebrain. On the dorsal side of the embryonic brain tube (Fig. 2.1A,B) the telencephalon and diencephalon are physically delineated by a constriction called the anterior intraencephalic sulcus, or AIS (Folgueira

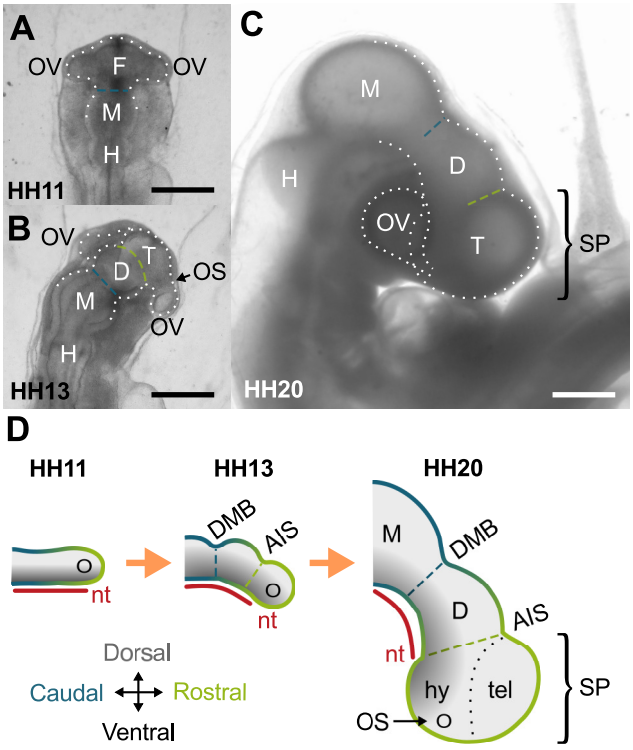

Figure 2.1: Forebrain development in chick embryo. (**A**–**C**) Bright-field images of extracted embryos. (**A**) At HH11 (dorsal view), the brain tube (BT) is divided into three primary vesicles: forebrain (F), midbrain (M) and hindbrain (H). Optic vesicles (OVs) protrude bilaterally from the forebrain. (**B**) By HH13, the forebrain has further divided into diencephalon (D) and the telencephalon-hypothalamus complex (T). On each side the optic stalk (OS) has also constricted to separate OVs from T. (**C**) By HH20, a 90 degree rotation at the level of the spinal cord (not shown) results in a lateral instead of dorsal view of the BT. All sulci persist as the BT bends and expands. Scale bars: 500 μm. (**D**) Schematic of forebrain development (lateral view). The notochord (nt) and caudal-rostral axis (blue-to-green gradient) of the BT are relatively straight initially. As the BT grows, the notochord and BT bend ventrally, maintaining dorsal-ventral signaling (black-to-gray gradient) along the new curvature. Together the OVs, telencephalon (tel), and hypothalamus (hy) comprise the secondary prosencephalon (SP). DMB, diencephalon-midbrain boundary sulcus (blue dashed line); AIS, anterior intraencephalic sulcus (green dashed line).

et al., 2012). On the ventral side, however, bending and bulging of the forebrain make subdivisions more difficult to interpret. As shown in Fig. 2.1C,D (right lateral view), the hypothalamus later appears as a ventral bulge in the curved forebrain. Optic vesicles also protrude from left and right sides of the forebrain to create the primitive eyes. Based on signaling patterns and fate-mapping, Puelles et al. (2012) propose that the telencephalon, hypothalamus, and optic vesicles all emerge from the rostral tip of the brain tube, a region named the secondary prosencephalon (SP). As shown in Fig. 2.1, the SP is morphologically distinct from the diencephalon and follows a dorsoventral pattern similar to the other brain vesicles.

The mechanisms responsible for secondary forebrain division remain poorly understood (Puelles et al., 2012). In the chick embryo, Filas et al. (2012) showed that actomyosin contraction likely creates the sulci between primary vesicles. A similar contractile mechanism is plausible within the forebrain, where actin is concentrated at the apical surface (Filas et al., 2012) and actin-binding proteins have been reported at sulci (Nicholson-Flynn et al., 1996). Yet evidence also suggests alternative or supplementary roles for pressure and growth (Gutzman and Sive, 2010; Lowery and Sive, 2009). Pressure from the eCSF inflates the brain tube viscoelastically and increases growth of the neuroepithelium (Desmond and Jacobson, 1977; Desmond et al., 2014; Alonso et al., 1998; Goodrum and Jacobson, 1981). Studies have also revealed increased proliferation in vesicles and dorsal regions of the normal embryonic chick brain (Layer and Sporns, 1987; Weikert et al., 1990; Takamatsu and Fujita, 1987).

This study focuses on the origin of the constrictions that separate the telencephalon-hypothalamus complex (T), diencephalon (D), and optic vesicles (OVs). Using the chick embryo as an experimental model, we determined the effects of actomyosin contraction and eCSF pressure on

brain shape. Computational models incorporating experimentally measured F-actin alignment verify that a contractile mechanism is sufficient to initiate forebrain subdivision. However, our results suggest that an additional mechanism is needed to maintain and deepen sulci during subsequent brain inflation and bending (cephalic flexure). We propose that mechanical feedback, through the interaction of wall stress and growth, is instrumental in forebrain expansion and sulcal maintenance. To evaluate this hypothesis, we compare new experimental data with a model that includes contraction, eCSF pressure, bending, and stress-dependent growth. Our results highlight how the interplay of several common morphogenetic mechanisms can generate the complex structure of the early embryonic brain.

2.2 Methods

2.2.1 Embryo culture and perturbation

Fertilized white Leghorn chicken eggs were incubated at 37° C (90% humidity), and embryos were extracted using a filter paper carrier as described in Chapman et al. (2001). Embryos were staged according to the system of Hamburger and Hamilton (1951) (denoted HHxx) and cultured in Dulbecco's Modified Eagle's Medium (Sigma) with 10% chick serum (Sigma), 1% penicillin/streptomycin/neomycin (Invitrogen). During culture embryos were submerged under a thin layer of fluid and superfused with a mixture of 95% oxygen and 5% carbon dioxide (Voronov and Taber, 2002). All embryos were examined over the course of development under a Leica MZ8 microscope.

Altering actomyosin contractility To alter contractility during initial forebrain subdivision, embryos were extracted at 40–42 h incubation (HH11) and cultured with blebbistatin (60 μM, Sigma) or calyculin A (30 nM, Sigma). Blebbistatin decreases contraction by inhibiting myosin II adenosine triphosphatase, while calyculin A enhances contraction by inhibiting myosin II phosphatase (Filas et al., 2012). As an alternate method of increasing contraction, several embryos were treated in media containing 5 mM adenosine triphosphate (ATP, Sigma) and 0.05% Triton-X 100 for 3 h. To rule out the effects of external forces, external mesenchyme and membranes were removed from several samples, which were then cultured for 6 h in control media or media containing calyculin A (30 nM). To observe effects at later stages, calyculin A was also added to culture medium of embryos after 50–60 h incubation (HH14–17) at concentrations of 30 nM or 100 nM.

Altering eCSF pressure To relieve pressure during later stages of brain expansion, normal embryos (HH12) were intubated at the anterior neuropore with an open pulled glass micropipette (inner diameter = 40–60 μm) and cultured in media for 24 h (Desmond and Jacobson, 1977). Only embryos in which the tube remained intact and unblocked were used for subsequent analysis. In control embryos, pressure was similarly relieved at the equivalent end stage (HH17) using a glass capillary tube (inner diameter = 150 μm).

2.2.2 Morphological imaging and analysis

For quantitative analysis, optical coherence tomography (OCT) was used to record three-dimensional (3D) geometries in living embryos at multiple time points. With Fiji/ImageJ software, image stacks were oriented to yield cross sections along the axis of the BT (see Fig. A.1 for details) (Schindelin et al., 2012). The perimeter δ of the lumen was traced and

recorded for each cross section, and the average inner radius was computed as $R = \delta/2\pi$. The average circumferential stretch ratio is given by $\lambda_\Theta = r/R$, where R and r are the average radii in the initial and final configurations, respectively.

Relative constriction is defined as the ratio of vesicle radius to adjacent sulcus radius. Ratios are denoted by T/AIS (r_T/r_{AIS}), D/DMB (r_D/r_{DMB}), and M/DMB (r_M/r_{DMB}). According to this notation, a sulcus forms when the corresponding ratio is greater than unity, and the sulcus deepens as the ratio increases.

2.2.3 Actin imaging and analysis

To visualize F-actin on the apical surfaces, embryos were fixed with 3.7% formaldehyde, cut into dorsal and ventral halves, and stained with phalloidin (Filas et al., 2012). Three-dimensional images of the apical surface were recorded using a Zeiss LSM 710 confocal microscope with a 20x objective lens.

Fiji/ImageJ was used to divide image stacks into 50 μm by 50 μm squares, with the view angle reoriented manually to ensure images tangent to the apical surface. This method was designed to minimize tissue distortion associated with previous flat-mount techniques (Filas et al., 2012). For each square, the angular distribution of actin was calculated from its Fourier power spectrum using the directionality function in Fiji/ImageJ (Liu, 1991). The resulting histogram of actin directionality (N=90 bins spanning 0° to 180°) was converted into circumferential (0°) and longitudinal (90°) components, S_Θ and S_Z, respectively, as

defined by the relations

$$S_\Theta = \int_0^\pi \mid \xi(\gamma)\cos\gamma \mid d\gamma \approx \sum_{n=1}^{N} \mid \xi_n \cos\gamma_n \mid$$
$$S_Z = \int_0^\pi \mid \xi(\gamma)\sin\gamma \mid d\gamma \approx \sum_{n=1}^{N} \mid \xi_n \sin\gamma_n \mid . \tag{2.1}$$

Here γ is the fiber angle relative to the circumferential direction, and ξ is the angular distribution normalized to $\int_0^\pi \xi(\gamma)d\gamma = \sum_{n=1}^{N} \xi_n = 1$ (Marquez, 2006). The total area fraction of actin was estimated by the number of bright pixels divided by total number of pixels in the image. Since actin generally outlines apical cell borders, cell density was also estimated as the number of cells in an image divided by the total image area.

2.2.4 Statistics

Statistical significance was evaluated between groups using SigmaPlot (Systat Software, San Jose, CA). Analysis of Variance (ANOVA) with post-hoc Tukey test was used to compare data between multiple groups. Student t-test was used to compare data between two groups where applicable. For all tests, $P<0.05$ was considered to be significant. All error bars denote standard deviation unless otherwise indicated.

2.2.5 Computational modeling

Geometry and boundary conditions To simulate forebrain morphogenesis, finite element models were created using ABAQUS Standard (v6.10, SIMULIA, Providence, RI).

Initial three-dimensional geometries were based on dimensions from OCT images at HH11, before forebrain constriction.

We considered two idealized models for development from HH11 to HH12. The first model considers the main BT as a cylinder of length $L = 0.5$ mm, wall thickness $h = 50$ μm, and inner radius $R = 0.1$ mm, including a hemispherical cap for the forebrain but omitting optic vesicles (Fig. 2.4A, top). The second model considers only the SP (Fig. 2.4A, bottom), consisting of a middle spherical shell (telencephalon-hypothalamus complex) with inner radius $R_T = 0.15$ mm, optic vesicles with inner radius $R_{OV} = 0.08$ mm, wall thickness $h = 50$ μm, and total distance $W = 0.6$ mm between tips of the optic vesicles. In both models only the left half of the brain was simulated, using symmetry conditions at the cutting plane to reduce computation time. The open (midbrain) end of the BT model is constrained by roller boundary conditions, and the SP model assumes rostral-caudal symmetry. Walls are five elements thick and composed of C3D20R elements (20-node hexagonal elements with reduced integration). To capture full model behavior, 7115 elements are used in the BT model, and 3810 elements are used in the SP model.

A third, modified BT model was used to simulate morphogenesis beyond HH12 (omitting OVs), as the BT undergoes significant bending and growth. Flexure has been attributed in part to the notochord, which is a relatively stiff, rod-like structure attached along the ventral side of the BT (Fig. 2.1D) (Adams et al., 1990; Zhou et al., 2009; Agero et al., 2010). As the brain grows longer, the length of the notochord changes relatively little, which could cause the tube to bend (Takamatsu and Fujita, 1987; Fujita, 1986). Here the notochord is represented by a stiff, non-growing region on the ventral side of the BT with a shear modulus that decays from 100μ at the ventral midline to μ at its dorsal and lateral edges (Fig. 2.6A). This continuous representation, as opposed to a separate notochord, was

implemented to minimize stress concentrations and improve convergence for models that include stress-dependent growth. Notably, bending requires a fully 3D analysis.

To simulate the one-cell-thick neuroepithelium, the walls of all models consist of an outer layer of passive, growing tissue and a relatively thin inner layer of contractile tissue (20% of the initial wall thickness) to represent the network of actomyosin fibers located at cell apices. In addition, a uniform pressure $p = 30$ Pa (Jelinek and Pexieder, 1968) is applied to the inner surface of each model. Pressure is ramped to its final value after contraction (HH12$^-$ to HH12$^+$), then held constant for all subsequent development up to HH20, in agreement with data of Desmond et al. (2005), who measured relative changes in eCSF pressure from HH12–26. For simplicity, stress-dependent growth is applied only after contraction and pressure have reached their final, maintained values (HH12$^+$).

Kinematics Contraction and growth were simulated in ABAQUS using a custom user subroutine based on the UMAT-generator of Young et al. (2010) for large deformations. Modifying the theory for volumetric growth (Rodriguez et al., 1994), we decompose the total deformation gradient tensor in the form

$$\mathbf{F} = \mathbf{F}^* \cdot \mathbf{C} \cdot \mathbf{G}, \tag{2.2}$$

where $\mathbf{G}$, $\mathbf{C}$, and $\mathbf{F}^*$ are growth, contraction, and elastic deformation gradient tensors, respectively. With rigid-body rotation absorbed into $\mathbf{F}^*$, $\mathbf{G} = \mathbf{I}$ corresponds to no net growth and $\mathbf{C} = \mathbf{I}$ corresponds to passive tissue, where $\mathbf{I}$ is the identity tensor. Relative to the zero-stress configuration, the Lagrangian strain tensor is $\mathbf{E}^* = \frac{1}{2}(\mathbf{F}^{*T} \cdot \mathbf{F}^* - \mathbf{I})$.

Since the wall thickness of the early BT remains relatively unchanged throughout the stages considered here (Fig. A.1D), we do not include contraction or growth in the radial (transverse normal) direction. We also assume that growth is transversely isotropic relative to the radial direction. For cylindrical geometry, these stipulations lead to the relations

$$\begin{aligned}\mathbf{C} &= \mathbf{e}_R\mathbf{e}_R + C_\Theta\,\mathbf{e}_\Theta\mathbf{e}_\Theta + C_Z\,\mathbf{e}_Z\mathbf{e}_Z \\ \mathbf{G} &= \mathbf{e}_R\mathbf{e}_R + G\,\mathbf{e}_\Theta\mathbf{e}_\Theta + G\,\mathbf{e}_Z\mathbf{e}_Z.\end{aligned} \tag{2.3}$$

Contraction is simulated by taking $0 < C_\Theta < 1$ and $0 < C_Z < 1$ ($C_\Theta = C_Z = 1$ for passive tissue), and $G > 1$ gives positive growth. For spherical and toroidal geometries, the Z direction is replaced by the more general meridional direction Φ.

Constitutive relations In all models, the passive outer layer is taken as isotropic (Xu et al., 2010a), while the contractile inner layer is represented by an active orthotropic material consisting of aligned fibers within an isotropic meshwork (cell membrane and disordered actomyosin fibers) (Murrell et al., 2015). To account for the relatively small volumes of water that enter or exit the tissue during deformation, both layers are assumed to be composed of nearly incompressible pseudoelastic materials (Xu et al., 2010a).

The Cauchy stress tensor is given by (Taber and Perucchio, 2000)

$$\boldsymbol{\sigma} = J^{*-1}\mathbf{F}^* \cdot \mathbf{S} \cdot \mathbf{F}^{*^T} \tag{2.4}$$

where Eq. (2.2) gives $\mathbf{F}^* = \mathbf{F} \cdot \mathbf{G}^{-1} \cdot \mathbf{C}^{-1}$, and

$$\mathbf{S} = \varphi_{iso} \frac{\partial W_{iso}}{\partial \mathbf{E}^*} + \varphi_\Theta \frac{\partial W_f}{\partial E^*_{\Theta\Theta}} \mathbf{e}_\Theta \mathbf{e}_\Theta + \varphi_Z \frac{\partial W_f}{\partial E^*_{ZZ}} \mathbf{e}_Z \mathbf{e}_Z \tag{2.5}$$

is the second Piola-Kirchhoff stress tensor. Here, $W_{iso}(\mathbf{E}^*)$ and $W_f(E^*_{\Theta\Theta}, E^*_{ZZ})$ represent strain-energy density functions for isotropic constituents and aligned contractile fibers, respectively. In addition, $J^* = \det \mathbf{F}^*$ is the elastic volume ratio, the $\mathbf{e}_i$ are unit base vectors in the initial configuration, and T denotes the transpose. The φ_k are volume fractions that satisfy the condition

$$\varphi_{iso} + \varphi_\Theta + \varphi_Z = 1. \tag{2.6}$$

In the passive outer layer, $\mathbf{C} = \mathbf{I}$, $\varphi_{iso} = 1$, and $\varphi_\Theta = \varphi_Z = 0$.

For these early stages in the chick embryo, neuroepithelial tissue is relatively linear and can be treated as a modified neo-Hookean material (Xu et al., 2010a). Here, we take

$$\begin{aligned} W_{iso} &= \tfrac{\mu}{2}(\bar{I}^*_1 - 3) + \kappa \left[\tfrac{1}{2}(J^{*2} - 1) - \ln J^*\right] \\ W_f &= \tfrac{1}{2}\left(\mu_\Theta E^{*2}_{\Theta\Theta} + \mu_Z E^{*2}_{ZZ}\right), \end{aligned} \tag{2.7}$$

where $\bar{I}^*_1 = J^{*-2/3}\ \mathrm{tr}(\mathbf{I} + 2\mathbf{E}^*)$ is the first strain invariant; μ, μ_Θ, and μ_Z are shear moduli; and κ is the bulk modulus. Using the measurements of Xu et al. (2010a) for the embryonic chick brain (HH11–13), we set $\mu = 200$ Pa and $\kappa = 100\mu$ for both layers. Values for the other moduli and volume fractions are discussed below.

Contraction parameters To estimate the values of C_Θ and C_Z (or C_Φ), we modified the method of Filas et al. (2012), who modeled morphogenesis of the midbrain and hindbrain vesicles. Accordingly, contractile strength C is characterized by the relative change in apical

surface area of the cells as given by

$$C = C_\Theta C_Z = C_\Theta C_\Phi. \tag{2.8}$$

As C decreases from unity, strength of contraction increases. For normal development, we let $C = 0.5$ at peak contraction, consistent with measurements of Nakajima and Tanoue (2010) for mammalian epithelial cells. To check for consistency, model results were compared to the experimentally measured stretch ratio λ_Θ in the diencephalon. To calibrate contraction for the hypercontracted brain, C was decreased until λ_Θ reached the average value measured for embryos cultured in 30 nM calyculin A, corresponding to $C = 0.3$ for our case. In other systems undergoing apical constriction, such as during Drosophila gastrulation and avian lung budding, the relative change in area has been reported as low as 0.25 (Martin et al., 2009; Kim et al., 2013). We assume uniform C throughout the inner layer of our models, where colocalization of F-actin and phosphorylated myosin light chain (pMLC) has been reported previously (Filas et al., 2012).

Filas et al. (2012) assumed that contractile anisotropy is related to changes in cell shape. Here, however, we estimate anisotropy from our actin alignment data through the relations

$$C_\Theta = \frac{S_Z}{S_\Theta}\sqrt{C}, \quad C_Z = \frac{S_\Theta}{S_Z}\sqrt{C}, \tag{2.9}$$

which satisfy Eq. (2.8). As defined by Eqs. (2.1), S_Θ and S_Z represent the net fiber components oriented in the circumferential and longitudinal directions, respectively. According to these relationships, greater circumferential fiber content (increased S_Θ) corresponds to increased circumferential contractility (decreased C_Θ), and vice versa. This relationship is

consistent with published findings that contractile force increases with fiber alignment in vascular smooth muscle cells and cardiomyocytes (Alford et al., 2011; Feinberg et al., 2012).

Actomyosin fibers also stiffen as they contract, due in part to the addition of myosin crosslinks (Stricker et al., 2010; Salbreux et al., 2012). To include this effect we assume that the fiber shear modulus increases with contraction (decreased C_Θ, C_Z) through the relations

$$\mu_\Theta = \mu C_\Theta^{-\alpha}, \qquad \mu_Z = \mu C_Z^{-\alpha} \tag{2.10}$$

where $\alpha > 0$. Here we consider $\alpha = 4$. For control embryos this relationship gives $\mu_\Theta = \mu_Z \approx 4\mu$ in isotropic regions but $\mu_\Theta \approx 13\mu$ and $\mu_Z \approx 1.2\mu$ in aligned regions (for $S_\Theta/S_Z \approx 1.3$). For hypercontracted brains these relations yield $\mu_\Theta = \mu_Z \approx 11\mu$ in isotropic regions. Such increases are consistent with previously reported stiffening of the BT under contraction (Filas et al., 2011), as well as direct measurement of actin fiber stiffening in living endothelial cells (Lu et al., 2008). All values fall within the range of previously reported actin-fiber stiffness data (Stricker et al., 2010; Salbreux et al., 2012).

Since S_Θ and S_Z also represent fractional sums of all fiber components oriented in the Θ and Z directions, we use these quantities to estimate volume fractions in the relatively thin contractile layer. Actin image analysis indicates that fibers comprise about 50% of the apical surface area. To satisfy Eq. (2.6), we take $\varphi_{iso} = 0.5$ and

$$\varphi_\Theta = \frac{0.5 S_\Theta}{S_\Theta + S_Z}, \quad \varphi_Z = \frac{0.5 S_Z}{S_\Theta + S_Z}. \tag{2.11}$$

Growth law In the BT model for HH12–20, growth is included in the outer, passive layer through a rate equation of the form

$$\dot{G} = (g_0 + g_\sigma \bar{\sigma})G \tag{2.12}$$

where $g_0 \geq 0$ is the baseline growth rate and $g_\sigma \geq 0$ is a coefficient for stress-dependent growth (Taber, 2009). In this equation, the nondimensionalized average stress is defined as

$$\bar{\sigma} = \frac{1}{2\mu}(\sigma_{\Theta\Theta} + \sigma_{ZZ}). \tag{2.13}$$

Here we assume stress-dependent growth is triggered by tension only ($g_\sigma = 0$ for $\bar{\sigma} \leq 0$). As described in the Results section, values of the growth parameters were determined by fitting model results to experimental measurements of embryos cultured under control and zero-pressure conditions.

2.3 Results

Stage-dependent results are based on the system of Hamburger and Hamilton (1951), who divided the 21-day incubation period of the chick embryo into 46 stages based on morphological characteristics. Stage is a nonlinear function of time that depends on environmental and other factors. Thus, developmental stage in the following models is related to average midbrain radius (r_M) measured in chick embryos.

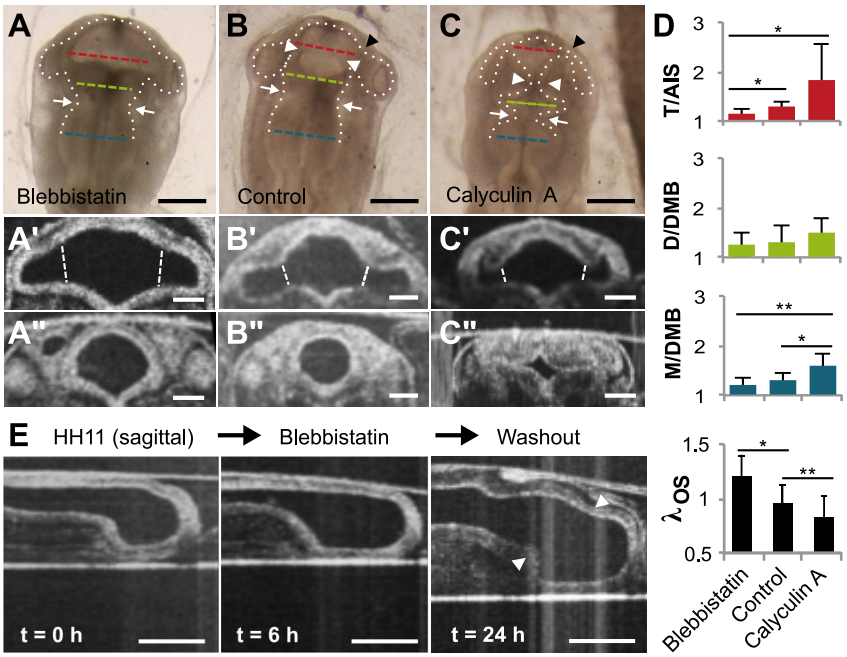

Figure 2.2: Effects of actomyosin contraction on early forebrain morphogenesis (HH11–12). Stage HH11 embryos were cultured 6 h in media containing blebbistatin or calyculin A to inhibit or enhance contractility, respectively (control n=9, blebbistatin n=15, calyculin A n=12). (**A**–**C**) Bright-field images reveal altered BT morphology under each condition (dorsal view). White arrowheads indicate AIS, black arrowheads indicate the optic stalk (OS), and white arrows highlight previously formed DMB. Dashed lines indicate locations used to compute average radii for T (red), D (green) and M (blue). Scale bars: 200 μm. (**A'**–**C'**) Representative OCT cross sections of SP for each case. Dashed white lines indicate locations used to compute average radii for the OS, and the average radius of T was calculated considering lumen area between the optic stalks. Scale bars: 100 μm. (**A"**–**C"**) Representative AIS cross sections for each case. Scale bars: 100μm. (**D**) Relative constrictions based on average radii at locations indicated in (A–C), as well as relative OS stretch ratio λ_{OS} based on locations indicated in (A'–C'). *P<0.05, **P<0.001 (**E**) Representative sagittal cross sections before and after 6 h in blebbistatin, followed by washout (n=6). White arrowheads indicate AIS. Scale bars: 200 μm.

2.3.1 Contraction is necessary for AIS and OS formation

In the early chick embryo, the apical (inner) surface of the BT is lined with actin and myosin, which have been implicated in shaping the primary vesicles (Filas et al., 2012). To determine whether actomyosin contraction also partitions the forebrain (AIS and OS formation), embryos were cultured from HH11 to HH12 in control media (n=9), blebbistatin to reduce contractility (n=15), or calyculin A to increase contractility (n=12) (Fig. 2.2A–C). Morphological changes were measured from OCT cross sections (Fig. 2.2A'–C', A"–C"). To rule out the influences of external factors, additional experiments were also conducted as outlined in Supplementary Data (Fig. A.2). These include exposure to ATP (n=5), culture of isolated brain tubes in control media (n=3) or calyculin A (n=5), reduced eCSF pressure during boundary formation (n=3), and staining for cell death (n=21).

Exposure to blebbistatin significantly reduced relative AIS constriction (T/AIS) (P=0.001, Fig. 2.2D), which resumed after subsequent washout (n=6, Fig. 2.2E). Blebbistatin had relatively little effect on the DMB, which formed prior to HH11, suggesting that constriction may be at least partially irreversible (Filas et al., 2012). Due to the complex shape of the optic vesicle (see Fig. 2.1C), OS constriction could not be measured relative to the primitive eye. However, comparison of circumferential stretch, λ_{OS}, revealed that the optic stalk expanded when cultured in blebbistatin (Fig. 2.2A'–B').

Exposure to calyculin A increased relative constriction of the DMB (M/DMB, P<0.001) and AIS (T/AIS, P=0.058) and caused significant shrinkage of the OS (λ_{OS}, P<0.001). The effect of calyculin A on T/AIS showed largest variability, with the AIS sometimes appearing similar to controls and other times almost entirely closing off the boundary. Because even embryos of the same stage show slight differences, we speculate that the embryos most

affected by calyculin A were at an optimal point in development to allow hypercontraction. "Hinge-points" were also observed at the dorsal, ventral, and lateral corners of the AIS in hypercontracted embryos (Fig. 2.2C"), similar to those described in other regions by Filas et al. (2011). For simplicity our measures reflect only the change in total boundary circumference.

Embryos cultured with ATP showed hyperconstriction that was qualitatively similar to those cultured in calyculin A (Fig. A.2A). Isolated BTs constricted slightly more than those of intact embryos in control media (Fig. A.2B), but isolated BTs constricted drastically in calyculin A (Fig. A.2C). Constrictions were observed even for embryos in which the neural tube failed to close, ruling out a need for eCSF pressure in sulcus initiation (Fig. A.2D). Furthermore, no cell death was observed during early or late sulcus formation (Fig. A.2E). These results suggest that the observed changes in morphology are likely caused by altered contractility within the neuroepithelium; external forces are not necessary for initial forebrain subdivision.

2.3.2 Actin is circumferentially aligned at forebrain constrictions

The importance of myosin II in forebrain subdivision motivated a closer look at its structural counterpart, F-actin. Staining for F-actin at the time of AIS formation (HH12, n=15) revealed localization at the apical surface throughout the forebrain (Fig. 2.3A–C). This appears similar to the midbrain and hindbrain, where colocalized F-actin and phosphorylated myosin light chain (pMLC) were found along the apical surface (Filas et al., 2012). Confocal imaging of the apical surface (Fig. 2.3A'–C') revealed distinct patterns of actin alignment and three statistically significant groups (ANOVA $P<0.001$, n=5–6 per group). Actin fibers were

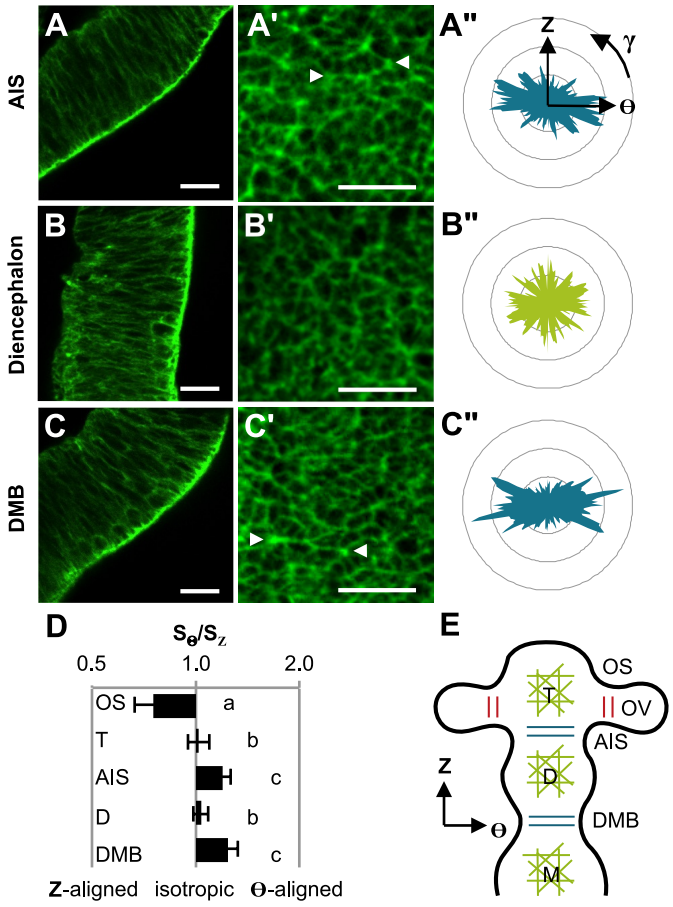

Figure 2.3: Actin patterns in HH12 brain tube. (**A**–**C**) Phalloidin staining revealed F-actin concentrated along the entire apical surface of the forebrain vesicles and sulci. Representative images are shown for the wall of the AIS, D, and DMB, respectively. (**A'**–**C'**) The inner, apical surface of the forebrain was recorded and divided into 50 μm x 50 μm squares for analysis. Representative squares are shown for the AIS, D, and DMB, respectively. Arrowheads indicate actin cables that span multiple cells. (**A"**–**C"**) Histograms of fiber orientation for squares in (A'–C'). (**D**) Each histogram was decomposed into circumferential and longitudinal components, S_Θ and S_Z, relative to the BT. Fiber orientation, defined by S_Θ/S_Z, is compared across major regions (log scale). $S_\Theta/S_Z = 1$ indicates isotropic fiber organization, $S_\Theta/S_Z > 1$ indicates circumferentially aligned fibers, and $S_\Theta/S_Z < 1$ indicates longitudinally aligned fibers. One-way ANOVA (P<0.001) with post-hoc Tukey test revealed three statistically different groups denoted by a, b and c (n≥5 per region, P<0.05). (**E**) Schematic summarizing observed fiber orientations. Isotropic fiber organization for the midbrain (M) has been previously described (Filas et al., 2012). Scale bars: 20 μm.

circumferentially oriented ($S_\Theta/S_Z > 1$) in circumferentially constricted regions (DMB and AIS), longitudinally oriented ($S_\Theta/S_Z < 1$) on the dorsal side of the OS, and isotropically oriented ($S_\Theta/S_Z \approx 1$) elsewhere (D, T, and ventral OS). With the exception of the OS, no significant differences were observed between dorsal, ventral, and lateral sides of the BT. These patterns are summarized in Fig. 2.3E, and detailed distributions are shown in Fig. 2.4C.

Since the OS is essentially a small cylinder protruding perpendicularly from the BT, the longitudinal direction relative to the BT is circumferential relative to the OS. As such, actin fibers are consistently oriented in the direction of maximum curvature at all constrictions. With this interpretation, the estimated alignment in the local circumferential direction is similar for the DMB, AIS and OS (Fig. 2.3D). As in Filas et al. (2012), actin is circumferentially aligned at persistent brain constrictions (MHB, DMB, AIS, OS), while it is relatively isotropic in brain vesicles (H, M, D, T).

2.3.3 Contraction initiates forebrain segmentation

To examine whether measured actin patterns could produce observed morphology, we simulated contraction in finite element models for the HH11–12 BT (without OVs) and SP (including OVs). Initial model geometries are based on OCT measurements (Fig. 2.4A, see Table 2.1 for parameter values). Material properties, eCSF pressure p, and contractile strength C were taken from published data (Xu et al., 2010a; Jelinek and Pexieder, 1968; Nakajima and Tanoue, 2010), and directional contractilities were calculated from actin orientation using Eq. (2.9) (Fig. 2.4C,D). The resulting model contained only one free parameter, α, which determines how fiber shear modulus varies with C (see Eq. (2.10), calibration

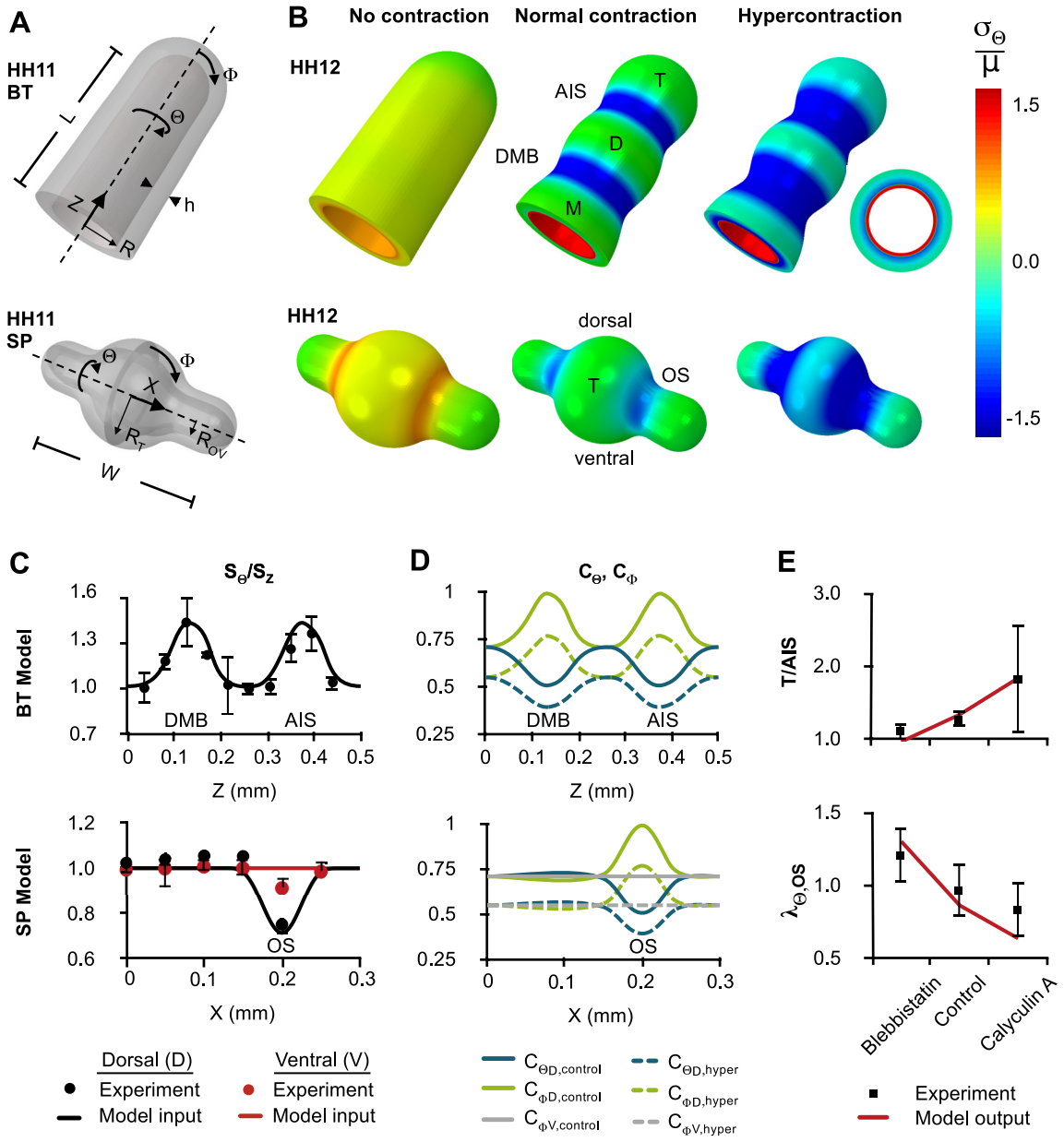

Figure 2.4: (Continued on the following page.)

Figure 2.4: Finite element models of initial forebrain subdivision (HH11–12). (**A**) Initial geometries approximate HH11 BT (omitting OVs, top) and SP (bottom). A thin contractile layer covers the inner surface (red in B, right) (**B**) Deformed geometry with normalized circumferential stress distributions for the cases of no contraction (blebbistatin), normal contraction (control), and hypercontraction (calyculin A). Representative cross section is shown at right. (**C**) Experimental actin alignment patterns were used as model input. Top: Patterns along the Z-axis of the BT indicate circumferential alignment at DMB ($Z \approx 0.13$ mm) and AIS ($Z \approx 0.37$ mm). Experimental data are shown for the dorsal midline, but no significant differences were observed between dorsal and ventral sides. Bottom: Patterns along the X-axis of the SP indicate circumferential alignment at dorsal but not ventral OS ($X \approx 0.2$ mm). Bars represent standard error of the mean. (**D**) Resulting circumferential (C_Θ) and longitudinal (C_Φ) contraction tensor components plotted along the Z and X-axes for normal ($C = 0.5$) and hypercontracted ($C = 0.3$) cases. (**E**) Relative AIS depth (T/AIS) and OS stretch ($\lambda_{\Theta,OS}$) plotted for model and experimentally measured values.

in Fig. 2.9). Since the size of the BT changes relatively little from HH11–12, growth was neglected during this step.

For $\alpha = 4$, our BT model produced a shape resembling morphology of the HH12 BT (compare Fig. 2.4B to Fig. 2.2A–C). Relative constriction of the AIS agrees well with quantitative measurements under reduced, normal, and enhanced contraction (Fig. 2.4E, top). Using the same contraction parameters, the SP model gives similarly accurate results for OS constriction (Fig. 2.4E, bottom).

At these stages, wall stress is determined by a combination of lumen pressure, which produces tension, and apical contraction, which produces tension in the inner, contractile layer and compression in the outer, passive layer. Under normal contraction, the passive layer experiences circumferential compression at the sulci but minimal wall stress in the vesicles (Fig. 2.4B). As contraction increases, compression of the passive layer increases. Note that, while both model geometries are initially axisymmetric, differences between ventral and dorsal actin orientation at the OS produce slight asymmetry in final shape and stresses

of the SP. (As shown in Fig. 2.1C, the OVs becomes quite asymmetric at later stages of SP development.)

For a pressurized tube, compliance generally increases with the ratio of radius to wall thickness. This ratio is relatively small at HH12; eCSF pressure causes elastic deformation of only $\lambda^*_\Theta = 1.1 \pm 0.1$ in control embryos (vesicle radii measured from OCT before and after deflation, n=7). In embryos exposed to blebbistatin, however, the walls of the BT and SP are abnormally compliant. Similarly, in BT and SP models with no contraction, the active layer fails to stiffen and we see overexpansion. Our SP model reveals that the OS is particularly susceptible to overexpansion (Fig. 2.4B), consistent with experimental observations (Fig. 2.2A').

2.3.4 Lumen pressure drives forebrain expansion via inflation and growth

The BT undergoes significant expansion in subsequent stages of normal development, with vesicle radii more than doubling from HH12–17. To separate the relative contributions of eCSF pressure and growth, we measured lumen radii across the BT for three cases: (1) embryos cultured from HH12 to HH17 with no pressure (n=6 intubated; Fig. 2.5B–C); (2) embryos cultured from HH12 to HH17 with normal pressure (n=8 control; Fig. 2.5E); and (3) control embryos immediately after deflation at HH17 (n=8; Fig. 2.5D). The relationships between each case are depicted schematically in Fig. 2.5A.

As shown in Fig. 2.5F, vesicle radii increased slightly during culture of intubated BTs, indicating low baseline growth in the absence of pressure (P=0.25, 0.02, and 0.13 for M, D,

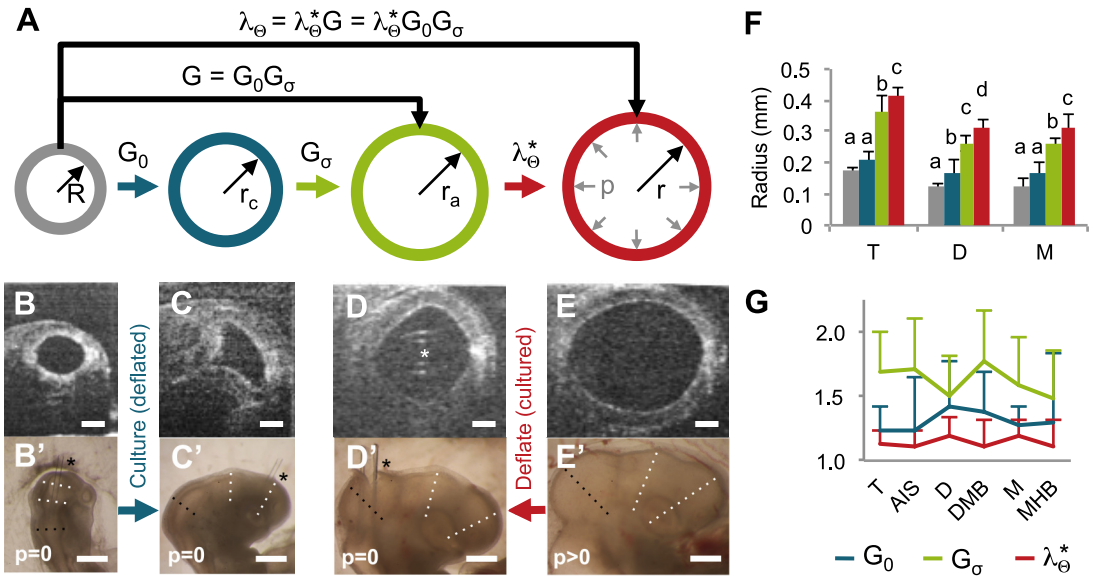

Figure 2.5: Effects of eCSF pressure on forebrain development (HH12–17). (**A**) Schematic depicting analysis of growth and elastic deformation. Radius for each cross section was determined from images of brains shown below each section. These radii were used to compute baseline growth ($G_0 = r_c/R$), pressure-dependent growth ($G_\sigma = r_a/r_c$), and elastic stretch ratio ($\lambda^*_\Theta = r/r_a$). (**B**–**C**) To determine baseline growth, embryos were intubated at HH12 (B) and cultured to HH17 (C, n=6). (**D**–**E**) To determine elastic stretch due to pressure, HH17 control embryos were imaged immediately before (E) and after intubation (D, n=8). Representative OCT cross sections shown for midbrain are shown (B'–E'). Bright field images (lateral view) for sections shown in B–E. Dotted lines indicate locations used to compute average radii for M (black), D and T (white); asterisks indicate location of tube insertion. (**F**) Measured radii for each case, where colors of each bar correspond to radii shown in (A). For each vesicle, one-way ANOVA ($P<0.001$) with post-hoc Tukey test revealed 3–4 statistically different groups denoted by a, b, c and d ($P<0.05$). (**G**) Estimated contributions of baseline growth G_0, stress-dependent growth G_σ, and elastic stretch (λ^*_Θ) to total expansion from HH12 to HH17. No statistically significant differences were detected between regions. Scale bars: 0.1 mm for (B–E) and 0.5 mm for (B'–E').

and T). However, these radii were significantly less than equivalent controls, indicating additional growth driven by eCSF pressure (P<0.001 for all vesicles). Circumferential stretch and growth ratios were estimated from these radius measurements. As illustrated in Fig. 2.5A, we assume that the total stretch ratio $\lambda_\Theta = r/R$ can be decomposed into the following components: baseline growth $G_0 = r_c/R$ for $p = 0$; pressure- or stress-dependent growth $G_\sigma = r_a/r_c$ for $p > 0$; and elastic deformation $\lambda^*_\Theta = r/r_a$ due to pressure. These quantities are related by $\lambda_\Theta = G\lambda^*_\Theta$, where the total growth is $G = G_0 G_\sigma$. As shown in Fig. 2.5G, elastic inflation ($\lambda^*_\Theta \approx 1.1$) contributed considerably less than total growth ($G \approx 2.1$) to BT expansion. Pressure-dependent growth ($G_\sigma \approx 1.6$) contributed considerably more to the total growth than baseline growth ($G_0 \approx 1.3$), suggesting that pressure-dependent growth accounts for most brain expansion during stages HH12–17.

2.3.5 Stress-dependent growth can generate realistic brain tube morphology at later stages

To determine whether the observed effects can be explained by mechanical feedback, we extended the BT model for HH12–20 to include stress-dependent growth, as well as a stiff notochord to account for bending (Fig. 2.6A). Intubated and control conditions were simulated by running the model with $p = 0$ Pa and $p = 30$ Pa, respectively.

The growth parameters in Eq. (2.12) were determined by approximately matching model predictions to the data in Fig. 2.5. To produce the growth ratio observed under intubated conditions (G_0), the baseline growth rate was calculated as $g_0 = 0.02$ hr^{-1}. To produce growth and inflation observed under normal conditions (λ_Θ), the stress-dependent rate constant was $g_\sigma = 5g_0$ (Fig. 2.6B–C). With these values, circumferential deformations in our

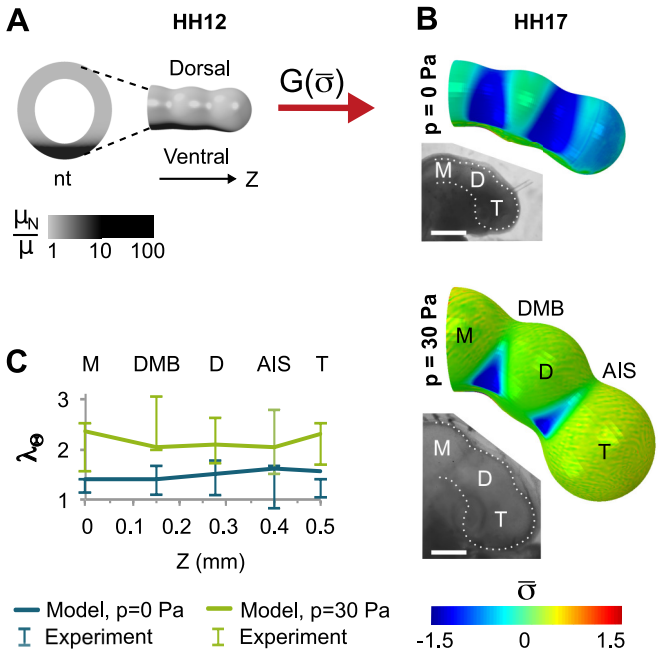

Figure 2.6: Finite element model of brain tube morphogenesis including flexure and stress-dependent growth (HH12–17). (**A**) Model geometry at HH12. A relatively stiff notochord (nt, modulus $\mu_N \geq 10\mu$) is added to the model shown in Fig. 2.4A. The BT subsequently undergoes stress-dependent growth, but the notochord (black) does not grow or contract. (**B**) As the BT grows, both structures bend ventrally. For p=0, the passive outer layer remains compressed ($\bar{\sigma} < 0$) due to contraction of the actin layer, resulting in negligible stress-dependent growth throughout the brain. When pressure is included ($p = 30$ Pa), tension induces stress-dependent growth, particularly in the vesicles. Colors represent normalized average tangential stress ($\bar{\sigma}$). Insets: Bright field images of intubated and control HH17 embryos shown for comparison (scale bar = 0.5 mm). (**C**) Model and experimentally measured circumferential stretch ratio (λ_Θ) in five regions of intubated ($p = 0$) and control ($p = 30$ Pa) BTs cultured from HH12 to HH17. As discussed in the text, these data were used to determine the growth-rate coefficients g_0 and g_σ, respectively.

model fall within experimentally measured ranges, except for a slight overestimation for the intubated telencephalon.

For both zero and normal eCSF pressure, the calibrated model yields morphology similar to experimental observations, including realistic differences in flexure (Fig. 2.6B). From OCT measurements of control embryos, we found that the dorsal length of the BT (measured from M to T) was approximately 1.8 times the ventral length at HH17 (n=8), slightly more than the value given by our model (≈ 1.5). As notochord stiffness is increased in our model, this flexure increases but model convergence suffers (Fig. 2.9). In the absence of pressure, our model predicts a decrease in bending (13%) comparable to that observed in intubated embryos (16%, n=6).

Since wall stresses in a pressurized vessel increase with radius, circumferential and longitudinal stresses increase as the BT grows. Wall stress is also higher in the vesicles than in the sulci, and cephalic flexure adds tension on the dorsal side of the BT while subtracting tension on the ventral side (Fig. 2.6B). Patterns of growth follow these stress distributions, leading to more growth and greater vesicle bulging on the dorsal side (Fig. 2.7A), in agreement with previous measurements of proliferation in chick embryos (Layer and Sporns, 1987; Weikert et al., 1990; Takamatsu and Fujita, 1987; Gutzman and Sive, 2010). Confocal imaging of late-stage embryos (HH17–18) also revealed increased cell density in dorsal vesicles (n=14) compared to sulci (n=10, P=0.02) (Fig. 2.7C), consistent with increased proliferation.

In our model, an important consequence of differential growth is that the AIS and DMB become more defined after HH16, similar to experimental measurements. Prior to this time, wall stress remains low as a result of initial contraction, and stress-dependent growth is inhibited. After HH16, pressure-induced tension starts to dominate and vesicle growth accelerates.

This growth increases the ratios T/AIS and M/DMB, but D/DMB remains relatively constant (Fig. 2.7D). In our model, the closely spaced DMB and AIS constrain diencephalon expansion, keeping tension low and inhibiting growth.

For comparison we also ran our model without stress-dependent growth ($g_\sigma = 0$) and increased the baseline growth rate ($g_0 = 0.03\ \mathrm{hr}^{-1}$). In contrast to the deepening sulci produced by stress-dependent growth, relative sulcal depth remains low in the uniform growth model, contrary to our data (Fig. 2.7B,D). These results suggest that stress-dependent growth contributes to both size and shape of the early embryonic brain.

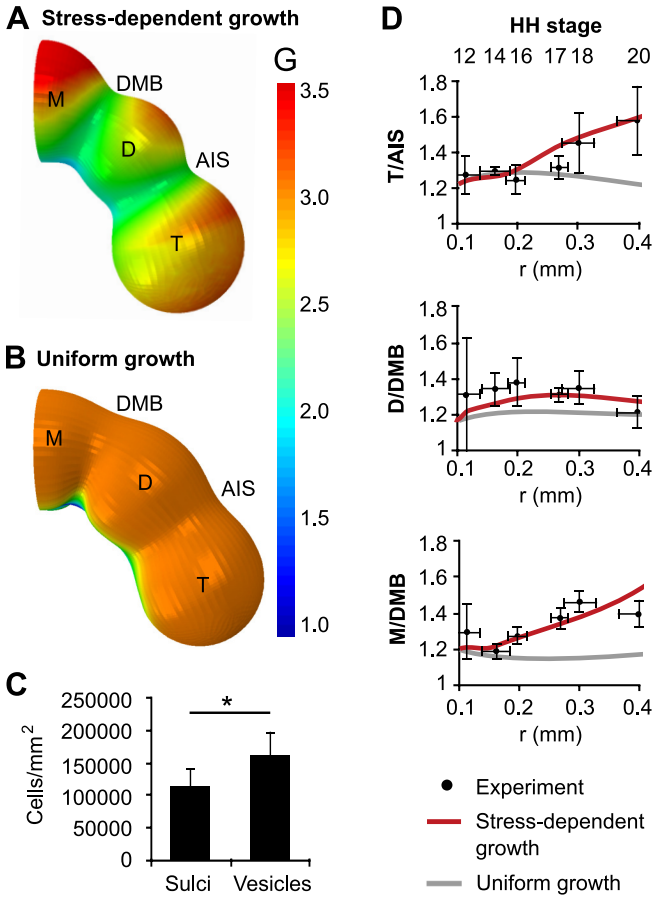

Figure 2.7: Comparison of stress-dependent and uniform growth models. (**A**) Growth pattern from stress-dependent growth model at HH20 ($g_\sigma > 0$) (**B**) Growth pattern from uniform growth model at HH20 ($g_\sigma = 0$, g_0 chosen so midbrain radius is same as in (A)). (**C**) Based on F-actin staining (HH17–18), apical cell density was significantly higher in vesicles compared to sulci. (**D**) Relative constrictions, plotted as functions of midbrain radius with corresponding stages shown. Stress-dependent growth (red) predicts experimentally observed increases in relative constriction, or sulcal depth. Conversely, sulcal depths change relatively little for uniform growth (gray).

2.4 Discussion

Much is now known concerning the biophysical mechanisms that create the neural tube (Colas and Schoenwolf, 2001; Brodland and Clausi, 1995; Davidson and Keller, 1999) and those that drive cortical folding (Richman et al., 1975; Tallinen et al., 2016). However, processes that shape the brain between these two phases of neural development have received relatively little attention. The present study focuses on development of the early embryonic forebrain, finding that: (1) differential patterns of actomyosin contraction initiate constrictions between the telencephalon-hypothalamus complex, diencephalon, and optic vesicles (HH11–12); (2) stress-dependent growth can maintain and deepen sulci during subsequent expansion and flexure of the BT (HH12–20); and (3) regionally constrained growth likely produces cephalic flexure and contributes to dorsoventral growth patterns (HH12–20).

2.4.1 Organized actomyosin as initiator of brain constrictions

This study extends an earlier investigation of boundary formation, which found that differential contraction of apical actomyosin creates the constriction dividing the midbrain and hindbrain of the chick embryo (Filas et al., 2012). Results here suggest that similar patterns initiate segmentation of the forebrain. Together these studies support the notion that regional circumferential contraction forms sulci in the early BT, with the exception of the transient rhombomere boundaries of the hindbrain that have relatively smaller radii and may require a different contractile mechanism (Filas et al., 2012).

Our findings are backed by three main pieces of evidence. First, chemical perturbations that inhibit myosin-II activity (blebbistatin) prevent the formation of constrictions, whereas

exposure to chemicals that enhance contractility (calyculin A, ATP) lead to deeper constrictions (Fig. 2.2). Second, apical actin exhibits predominately circumferential alignment in constricted regions, consistent with circumferential contraction, and relatively isotropic orientation elsewhere (Fig. 2.3). Third, computational models based on realistic parameters agree with quantitative measurements of both normal and hypercontracted BTs (Fig. 2.4).

Our results for F-actin orientation are similar to previous observations in the MHB (Filas et al., 2012), where both F-actin and cell shape were circumferentially oriented. Strikingly, all regions of aligned actin (MHB, DMB, AIS, OS) match regions of high molecular weight tropomyosin expression reported in the embryonic rat (Nicholson-Flynn et al., 1996). Tropomyosin stabilizes actin to form long, straight filaments (Gunning et al., 2005) similar to the long, circumferential filaments we observed at forebrain constrictions (Fig. 2.3A', C'). Reports also suggest that binding of tropomyosin can increase actin bundle stiffness (Fujime and Ishiwata, 1971). This behavior is captured by Eqs. (2.9) and (2.10) in our models. In cultured epithelial cells, actin fibers have been shown to align in the direction of maximum curvature (Yevick et al., 2015; Svitkina et al., 1995), suggesting that circumferential alignment may occur naturally in situations where long, stable filaments of actin are allowed to form.

As shown in Fig. 2.4, circumferential contraction effectively minimizes circumferential tension in the BT and SP. Indeed, similar contractile mechanisms have been observed in embryonic wound healing (Bement et al., 1993) and gut morphogenesis (Burgess, 1982). In the zebrafish, Gutzman et al. (2008) found that basal constriction helps to form the MHB. However, important morphological differences between zebrafish and chick (or mammal) suggest that mechanisms may be species dependent (Filas et al., 2012).

2.4.2 Stress-dependent growth as a mechanism of vesicle maintenance during brain expansion

In cultured embryos, forebrain sulci continue to deepen after HH12 as the BT expands (Fig. 2.1B,C). This behavior contradicts our computational model with prescribed *uniform* growth, in which lumen pressure causes the DMB and AIS to become more shallow as the brain grows (Fig. 2.7B). The result may seem counterintuitive, since Laplace's law predicts greater circumferential expansion in regions of larger radius, i.e., in the vesicles between constrictions. On the other hand, Laplace's law also predicts longitudinal tension for a capped vessel such as the BT. This force tends to unbend the sulcal folds and dominate the relatively small difference in circumferential stretch. Cephalic flexure of the BT only exacerbates this behavior, further increasing longitudinal tension on the dorsal side of the brain tube.

One potential mechanism to counteract unfolding would be to increase contraction in sulci. However, our experiments do not support this possibility since exposure to calyculin A had no noticeable effect beyond stage HH14 (n=6 at 30 nM, n=5 at 100 nM; Fig. A.2). We also note that uniform growth is not consistent with previously documented proliferation patterns (Layer and Sporns, 1987; Weikert et al., 1990; Takamatsu and Fujita, 1987; Gutzman and Sive, 2010), and predefined growth (uniform or patterned) does not predict documented increases in cell proliferation due to pressure (Desmond et al., 2005; Desmond and Jacobson, 1977; Desmond et al., 2014).

Accordingly, we speculate that mechanical feedback, in the form of stress-dependent growth, is required to deepen sulci as the BT expands during HH12–20 and beyond. Elevated tension in vesicles relative to sulci (due to initial contraction, see Fig. 2.4B) would induce relatively

higher growth rates in vesicles, deepening the sulci. As vesicles expand, increased wall stress (via Laplace's law) would further accelerate their growth, causing sulci to deepen further. This idea is supported by multiple studies showing growth of the BT depends on eCSF pressure: Eliminating lumen pressure via intubation slows growth considerably (Desmond and Jacobson, 1977) (Fig. 2.5), and abnormally high pressure increases proliferation (Alonso et al., 1998; Desmond et al., 2014). Cell proliferation has been shown to increase with the degree of mechanical tension in tissues such as blood vessels and epithelia (Lehoux et al., 2005; Wyatt et al., 2015).

With a growth rate that depends linearly on average in-plane stress (Eq. (2.12)), our model yields morphology similar to that of experimental BTs for both $p = 0$ Pa and $p = 30$ Pa (Fig. 2.6B). In contrast to the uniform growth model, our stress-dependent growth model predicts temporal increases in relative AIS and DMB depth that are in remarkable agreement with experimental measurements for control embryos during stages HH12–20 (Fig. 2.7D). This model predicts differential growth patterns consistent with observations in both chick and zebrafish, which found higher proliferation in vesicles than sulci (Layer and Sporns, 1987; Weikert et al., 1990; Gutzman and Sive, 2010) and reduced proliferation in the ventral neuroepithelium during stages of flexure (Takamatsu and Fujita, 1987; Layer and Sporns, 1987).

At the molecular level, mechanical feedback may be regulated by focal adhesion kinases (FAKs), which act as mechanotransducers in vascular and epithelial systems (Lehoux et al., 2005; Chaturvedi et al., 2007). In Xenopus, Hens and DeSimone (1995) found FAK transcripts localized in the forebrain, midbrain, hindbrain, and optic vesicle. In the chick embryo, Desmond et al. (2014) showed that FAK and cell proliferation were upregulated and activated

by eCSF pressure. The stress and growth patterns predicted by our model are consistent with these data (Figs. 2.6B and 2.7A).

2.4.3 Mechanical constraint by the notochord predicts bending and realistic growth patterns

For decades, researchers have speculated that differential growth drives flexure of the BT (Goodrum and Jacobson, 1981). Others have suggested that an external structure on the ventral side of the BT, e.g., the notochord or foregut, may constrain longitudinal growth and cause the tube to bend (Takamatsu and Fujita, 1987; Pikalow et al., 1994). None, however, have offered conclusive physical evidence for their theories.

Our model for stages HH12–20 includes a relatively stiff, non-growing notochord along the ventral side of the BT extending from midbrain to the telencephalon-hypothalamus complex (Fig. 2.6A). With a stiffness in the range of published data (Adams et al., 1990; Zhou et al., 2009), this structure provides sufficient constraint to force realistic bending of the BT as it grows (Fig. 2.6B). Since growth depends on stress, bending is slightly reduced in our model without lumen pressure (Fig. 2.6), similar to experimental observations. The notochord also springs apart when cut experimentally, indicating that it is under tension as predicted by our model (Fig. A.3). In this model, stress and growth near the notochord decrease due to bending, which could explain previous reports of decreased proliferation on the ventral side of the BT (Takamatsu and Fujita, 1987; Layer and Sporns, 1987).

2.4.4 Limitations

While our stress-dependent growth model yields realistic trends, we cannot rule out other forms for the growth law (2.12). For example, we assume that growth is triggered by tension but reduced to baseline levels under compression. The first part of this assumption is supported by studies showing that proliferation in the BT increases with eCSF pressure (Desmond and Jacobson, 1977; Desmond et al., 2014; Alonso et al., 1998; Goodrum and Jacobson, 1981). We did not observe any indications of cell death ($G < 1$) in compressed regions (Fig. A.2), but it is possible that cells in compression could proliferate at a further reduced rate. Future studies are warranted to address this issue. It is also plausible that growth depends on a different mechanical quantity, such as strain or strain rate (Cowin, 1996).

For simplicity, our model assumes that growth is transversely isotropic (isotropic tangent to the surface) and depends on the average in-plane stress. Future studies could determine whether differences exist in the circumferential and longitudinal directions, similar to previous studies of proliferation in epithelial tissue (Wyatt et al., 2015; Kim et al., 2013). Our model also assumes no changes in wall thickness due to growth or contraction. For growth, this choice is supported by minimal change in tissue thickness over time (Fig. A.1D). For contraction, this implies no change in actin layer thickness as fibers are pulled toward and between each other, such that fluid which once occupied space between fibers is pushed out of the actin layer and into the cell body. While a multiscale model would ultimately be necessary to describe the interactions of actin, myosin, and fluid in the cell, here we have proposed a continuum approximation to describe critical aspects of the system.

Finally, our model does not consider additional subdivisions of the diencephalon and secondary prosencephalon that begin to emerge during the final stages of our analysis (HH18–20), and our model is limited to the physical mechanisms responsible for morphogenesis. While countless reports have revealed regionalizing effects of molecular signals such as Sonic hedgehog (SHH) and fibroblast growth factors (FGF8) (Puelles et al., 2012), their influences are outside the scope of the present study. Future work may consider how such signals apply to these or subsequent subdivisions.

2.4.5 A mechanistic model informs accurate patterning of the forebrain

Historically, researchers have described the forebrain using columnar subdivisons first proposed by Herrick (1910) (Fig. 2.8A), which attributed the hypothalamus and optic vesicles to the diencephalon region. However, recent advances in fate-mapping have modified our understanding of brain organization (Puelles and Rubenstein, 2015; Folgueira et al., 2012), leading Puelles et al. (2012) to propose updated functional prosomeric subdivisions in the forebrain (or prosencephalon), as shown in Fig. 2.8B (Puelles et al., 2012; Puelles and Rubenstein, 2015). Comparing our model to the prosomeric subdivisions, regional morphogenesis emerges naturally from stress-dependent growth and bending (Fig. 2.8C), with prosomeres (p1–3, hp1–2) corresponding neatly to equally spaced regions in the HH11 BT.

While discrepancies between anatomical subdivisions may seem trivial, they can become critical when attempting to understand physical morphogenesis. For example, if we assume all brain vesicles are roughly partitioned by a contractile ring, the outdated columnar subdivisions would lead us to expect circumferentially aligned actin between the telencephalon and

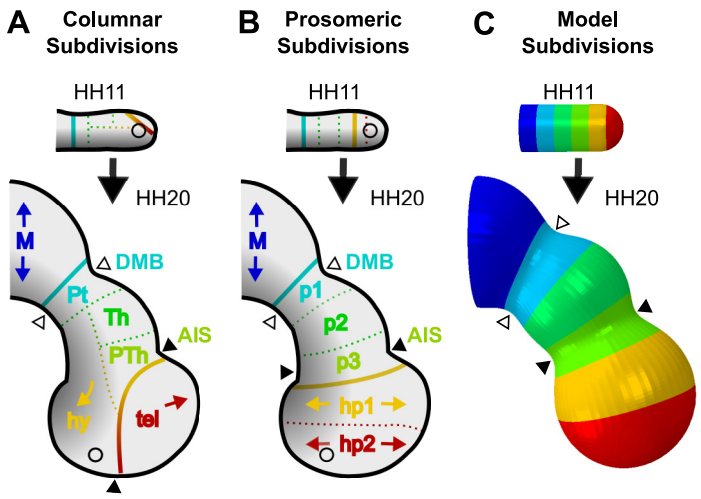

Figure 2.8: Forebrain regionalization in terms of columnar, prosomeric, and mechanistic subdivisions. (**A**–**B**) Proposed functional regions drawn onto forebrain tracings at HH11 and HH20. Black-to-gray gradient represents approximate ventral-to-dorsal signaling (Puelles et al., 2012), regions are denoted by color. Solid lines denote proposed functional boundaries between the diencephalon (middle) and adjacent vesicles, while dotted lines separate regions within each vesicle. Historically accepted columnar subdivisions are shown in (A) (Herrick, 1910), and prosomeric subdivisions (based on signaling patterns and fate mapping) are shown in (B) (Puelles and Rubenstein, 2015). Arrowheads represent expected bounds of physical sulci (black = AIS, white = DMB) for each. (**C**) Finite element model based on physical observations. Colors represent equally-spaced sections along the rostral-caudal axis at HH11. In this mechanistic model, physical sulci form in regions of circumferentially aligned actin, matching prosomeric regions p1 and p3. Bending of the BT and bulging of the hypothalamus result from constrained growth (constrained by the notochord). Vesicle inflation results from eCSF pressure and stress-dependent growth. M=midbrain, p1=Pt=pretectum, tel=telencephalon, hy=hypothalamus, Th=thalamus, PTh=prethalamus, hy=hypothalamus, p1–p3=diencephalon (prosomeric), hp1–hp2=secondary prosencephalon (SP, prosmeric). Circles represent location of optic stalk.

hypothalamus. Alternatively, researchers might conclude that complicated, region-specific mechanisms are necessary to obtain the secondary forebrain shape (Goodrum and Jacobson, 1981). Instead, our analysis finds actin is circumferentially aligned along prosomere p3 to form the AIS, consistent with alignment along p1 to form the DMB. By considering the updated definitions of secondary prosencephalon, diencephalon, and their subdivisions (Puelles et al., 2012), we obtain a physical understanding of development that complements functional anatomic regions.

In this study, we have proposed a mechanistic model for early forebrain morphogenesis that is consistent with both structural and functional partitioning. In conjunction with experiments, our model provides new insight into how complex morphology can arise from simple mechanisms.

2.5 Addendum

Dimension	Source	Measured Value	Model Value	Figure
R	OCT (R_M)	0.11 ± 0.02 mm	0.1 mm	2.4A (top)
L	OCT	0.46 ± 0.02 mm	0.5 mm	2.4A (top)
R_T	OCT	0.14 ± 0.02 mm	0.15 mm	2.4A (bottom)
R_{OV}	OCT	0.06 ± 0.01 mm	0.08 mm	2.4A (bottom)
W	OCT	0.56 ± 0.07 mm	0.06 mm	2.4A (bottom)
h	OCT	54 ± 5 μm	50 μm	2.4A
$^*X_{OS}$	Confocal	0.20 mm	0.20 mm	2.4C, 2.6
$^*Z_{DMB}$	Confocal	0.13 mm	0.13 mm	2.4C, 2.6
$^*Z_{AIS}$	Confocal	0.38 mm	0.38 mm	2.4C, 2.6

Table 2.1: Model dimensions and sources. All OCT dimensions were measured at HH11. Items marked with * denote peaks of S_Θ/S_Z, which were not measured until HH12. For the BT model, the spacing between constrictions was adjusted to a total length L to account for longitudinal growth from HH11 to HH12. For the SP model, W did not change substantially from HH11 to HH12.

Parameter	Source	Model Value	Equation
ψ_{iso}	Confocal (Fig. 2.3A"-C")	0.5	Eq. 2.5, 2.6
ψ_Θ, ψ_Z	S_Θ, S_Z (Eq. 2.1, Fig. 2.3, 2.4C)	Eq. 2.11	Eq. 2.5, 2.6
μ	Xu et al. (2010a)	200 Pa	Eq. 2.7
κ	Xu et al. (2010a)	20,000 Pa	Eq. 2.7
μ_Θ, μ_Z	S_Θ, S_Z (Eq. 2.1, Fig. 2.3, 2.4C)	Eq. 2.10	Eq. 2.7
C (normal)	Nakajima and Tanoue (2010)	0.5	Eq. 2.8
C (hyper)	$\lambda_{\Theta,D}$	0.3	Eq. 2.8
α	free parameter	4	Eq. 2.10
g_0	G_0	0.02 h^{-1}	Eq. 2.12
g_σ	G/G_0	$5g_0$	Eq. 2.12
$(\frac{\mu_N}{\mu})_{max}$	Adams et al. (1990); Agero et al. (2010)	100	$\frac{\mu_N}{\mu} = 100e^{\frac{-10(Y+R+h)}{(R+h)}}$

Table 2.2: Model parameters and sources. With the exception of one free parameter, α, all parameters were taken from literature or calculated/calibrated from experimental measurements.

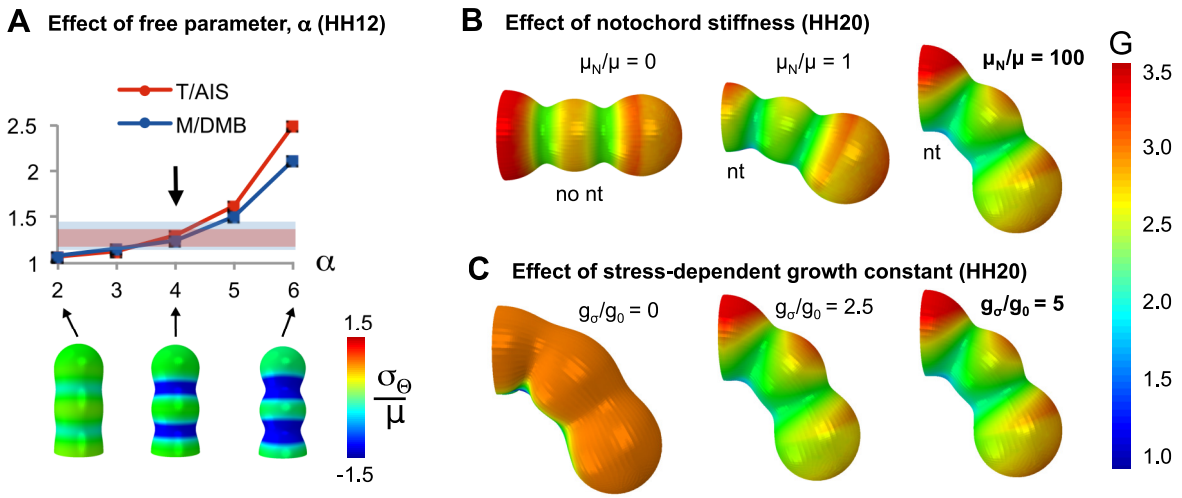

Figure 2.9: Effects of free parameter (α), notochord, and stress-dependent growth on final BT shape. (**A**) As contraction parameter α increases (see Eq. 10), actin stiffness and relative sulcal depth increase. Red box represents the range of T/AIS and blue box represents range of M/DMB measured experimentally at HH12 (mean $\pm$ standard deviation). For the control case (C=0.5), $\alpha = 4$ (arrow) produces T/AIS and M/DMB within the correct ranges. (**B**) Bending increases as notochord (nt) modulus μ_N increases. (**C**) As the stress-dependent growth rate parameter (g_σ) increases relative to the constant growth rate parameter (g_0), sulci become more distinct. Final model values for (B–C), based on measurement or calibration, are shown in bold.

Chapter 3

Molecular and mechanical signals are required to shape cerebral hemispheres in the chicken embryo[3]

3.1 Introduction

In humans, the cerebral hemispheres account for the majority of adult brain volume, and incomplete hemisphere division, or holoprosencephaly, represents the most common brain malformation (1 in 250 human pregnancies; 1 in 10,000 live births) (Matsunaga and Shiota, 1977; Leoncini et al., 2008). Furthermore, abnormally small (microcephalic) or large (megalencephalic) cerebral hemispheres have been associated with disorders including epilepsy, cerebral palsy, and autism (Barkovich et al., 2012). Still, the physical and cellular mechanisms responsible for hemisphere morphogenesis remain unclear from a mechanical perspective (Gupta and Sen, 2016).

[3]Experiments to measure pressure were conducted by Wade Stewart and Jason Gleghorn, and section 3.4.5 was drafted by Wade Stewart. Cryostat sectioning was conducted by M. Gabriela Espinosa. Larry Taber helped design the experiments and edited the manuscript.

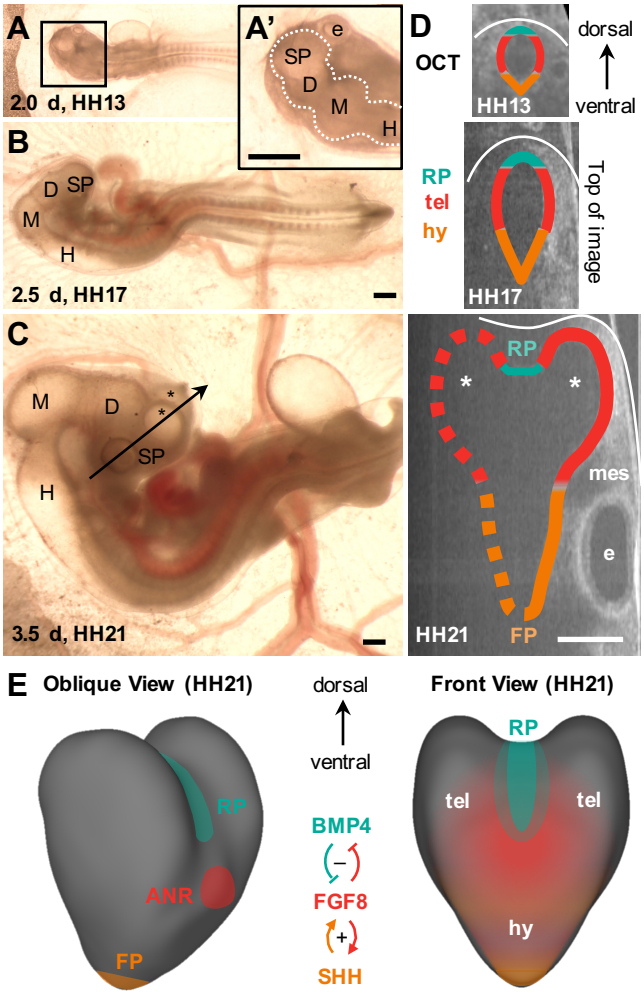

Figure 3.1: (Continued on the following page.)

Figure 3.1: Normal development of the telencephalic hemispheres in the chicken embryo. (A-C) Bright field images at Hamburger and Hamilton (HH) stages 13, 17, and 21, all images shown to same scale. (A') Magnified view of boxed region in (A), with white dotted line to denote embryonic brain tube. Local constrictions visibly separate the secondary prosencephalon (SP), diencephalon (D), midbrain (M), and hindbrain (H). (D) OCT images of cross sections through the SP containing telencephalon (tel) and hypothalamus (hy). Location of cross section is denoted by black line in (C), where arrowhead indicates the dorsal end of the SP. During days 2-3, all brain structures can be imaged clearly; at 3.5 days only the topmost (right) hemisphere can be imaged clearly. Space between surface ectoderm (white line) and neuroepithelial wall (multicolored line) is filled with loose mesenchymal tissue (mes) and external structures such as the prospective eyes (e). (E) Three-dimensional reconstruction from OCT images (HH21), illustrating molecular signals in hemisphere morphogenesis. BMP4 produced at the roof plate (RP, blue) inhibits FGF8 production, and vice versa, while SHH produced at the floor plate (FP, orange) promotes FGF8, which is also produced at the anterior neural ridge (ANR). Scale bars are 500 microns; all images in (D) shown to same scale. Asterisks (*) denote telencephalic hemispheres.

After neurulation, local constrictions produce distinct vesicles along the length of the early brain tube (Lowery and Sive, 2009; Filas et al., 2012). These primary vesicles are the forebrain (prosencephalon), midbrain (mesencephalon), and hindbrain (rhombencephalon) (Lowery and Sive, 2009). The forebrain further segments into the diencephalon and secondary prosencephalon, and all vesicles undergo dramatic, pressurized expansion during subsequent development (Puelles et al., 2012; Garcia et al., 2017) (Fig. 3.1A-C). In this study, we focus on the rostral-most vesicle, the secondary prosencephalon (SP), from which right and left cerebral hemispheres emerge (Fig. 3.1D-E) Puelles et al. (2012). As shown in Fig. 3.1D, hemispheres grow from the dorsal portion (telencephalon), while the ventral portion (hypothalamus) remains relatively small and conical.

Throughout the early neural tube, Sonic hedgehog (SHH) is secreted by the ventral floor plate, and bone morphogenetic proteins (BMP4) are secreted by the dorsal roof plate (Monuki, 2007) (Fig. 3.1D). At the rostral end of the early brain tube, the anterior neural ridge also secretes fibroblast growth factors (FGF8) (Monuki, 2007; Toyoda et al., 2010),

which form a positive feedback loop with SHH (Fig. 3.1E). This combination is thought to promote proliferation and cell survival of ventral and lateral neuroepithelium (Monuki, 2007). In contrast, BMP4 reduces proliferation at the roof plate and forms a generally negative feedback loop with FGF8 (Ohkubo et al., 2002).

Studies in mouse and chicken have shown that hemisphere division may be impeded by altering these chemical morphogens. Reducing SHH, reducing FGF8, or increasing BMP4 leads to underdeveloped ventral and lateral structures, similar to cases of *classic* holoprosencephaly in human (Fernandes et al., 2007; Furuta et al., 1997; Storm et al., 2006; Ohkubo et al., 2002; Huang et al., 2007b). By contrast, midline interhemispheric (MIH) holoprosencephaly, a phenotype in which the dorsal midline fails to develop, can be induced by decreasing BMP4 or increasing SHH (Fernandes et al., 2007; Huang et al., 2007a). While such studies suggest a morphogen-dependent gradient of growth, a more quantitative, mechanical approach is needed to understand these structural alterations.

Mechanical loads and mechanical feedback have also emerged as important factors in early brain morphogenesis (Jelinek and Pexieder, 1968; Lowery and Sive, 2009; Garcia et al., 2017). After the brain tube seals (Fig. 3.1A), it fills with embryonic cerebrospinal fluid (eCSF) that exerts pressure on the walls of the early brain (Jelinek and Pexieder, 1968; Desmond et al., 2005; Garcia et al., 2017). This pressure stretches the neuroepithelium mechanically and stimulates growth (Alonso et al., 1998; Desmond et al., 2014; Jelinek and Pexieder, 1968; Desmond and Jacobson, 1977), suggesting a role for mechanical feedback, similar to other systems: In pulmonary and vascular epithelia, tissue stretch has been shown to induce cell proliferation (Chaturvedi et al., 2007; Lehoux et al., 2005). In epithelial monolayers derived from canine kidney, stretch-induced cell divisions tend to dissipate stress and restore isotropic cell shape (Wyatt et al., 2015). By including mechanical feedback in models of

growth, previous studies have accurately predicted morphogenesis of the wing in *Drosophila* (Hufnagel et al., 2007; Aegerter-Wilmsen et al., 2007).

In this study, we examine the role of mechanics in hemisphere morphogenesis in chicken embryos (*Gallus gallus*). We hypothesize that hemisphere division depends on differential cell proliferation, regulated by a combination of morphogen gradients and mechanical feedback. We confirm regional differences in growth by quantifying cell proliferation during normal hemisphere division. To determine the role of mechanical signals on growth, we use live optical coherence tomography (OCT) to measure morphological changes over time under different mechanical loads. Finally, we create a computational model to test whether proposed mechanisms (morphogen gradients, external loads, and mechanical feedback) are sufficient to explain observed hemisphere morphologies. By elucidating the role of mechanical forces and chemomechanical feedback in hemisphere morphogenesis, our results offer new insights into clinically-observed malformations such as microcephaly, megalencephaly, and holoprosencephaly.

3.2 Results

To understand the mechanics of initial hemisphere cleavage and growth, we focused on three specific stages in chicken embryo development according to the Hamburger and Hamilton staging system (denoted HHx) (Hamburger and Hamilton, 1951). At HH13, after 2 days of development *in ovo* (Fig. 3.1A-A'), the neural tube has sealed, and eCSF begins to accumulate in the lumen. At this stage, the brain is also visibly segmented into secondary prosencephalon (SP), diencephalon (D), midbrain (M), and hindbrain (H) (Puelles et al., 2012). By HH17, (2.5 days, Fig. 3.1B), all brain regions have expanded, and the prospective

eyes are connected to the rostral hypothalamus via narrow optic stalks. Meanwhile, the brain has bent and rotated 90° at the level of the presumptive spinal cord. By HH21 (3.5 days, Fig. 3.1C), all vesicles have further expanded, and telencephalic hemispheres are clearly separated. Throughout these stages, the ventral hypothalamus is surrounded by mesenchyme and external structures, including large prospective eyes on each side (Fig. 3.1D).

In the results below, embryos were grouped by incubation time (2 days, 2.5 days, 3.5 days), resulting in subtle stage variation. For simplicity, we refer to these ranges as HH13 (HH12-14), HH17 (HH16-18), and HH21 (HH20-22), respectively.

3.2.1 Hemisphere division coincides with decreased proliferation at the roof plate.

To observe proliferation patterns before and after hemisphere division, cells undergoing DNA synthesis were labeled with EdU (5-ethynyl-2-deoxyuridine) (Warren et al., 2009). At HH17 (before hemisphere division), proliferation was visible throughout the secondary prosencephalon. At HH21 (after hemisphere division), proliferation had dissipated at the roof plate by HH21 (Fig. 3.2A-B). To quantify this effect regionally, we defined proliferation fraction as the number of EdU-labeled nuclei divided by the total number of (Hoescht 33342-labeled) nuclei for roof plate and hemisphere regions. No regional differences were detected at HH17, but roof plate proliferation was significantly lower at HH21 (Fig. 3.2C, n=5 per group). The latter results are consistent with previous reports of BMP4 and reduced proliferation at the hemisphere midline (Furuta et al., 1997; Gupta and Sen, 2015). Furthermore, the dynamic shift in proliferation is consistent with molecular signaling dynamics in chicken, where the territory of *Bmp4* expression remains fairly small until HH18 (Crossley et al., 2001).

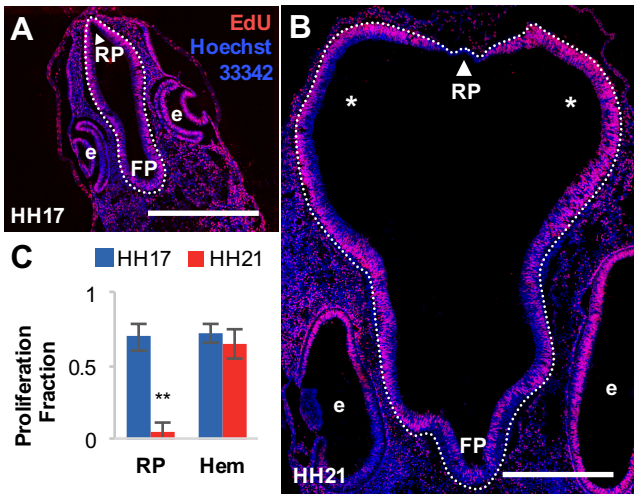

Figure 3.2: Cell proliferation in the SP. (A-B) Cross-sections through the secondary prosencephalon showing EdU-labeled nuclei (red) and all nuclei (blue). At HH17, proliferating cells (red nuclei) are visible throughout the neuroepithelial wall (outer surface denoted with white dotted line). At HH21, proliferation appears to be reduced in the roof plate (RP, white arrowheads). (C) Proliferation fraction (number of EdU-labeled nuclei divided by total number of nuclei) is significantly decreased in the RP of HH21 embryos relative to the RP at HH17, and relative to hemispheres (Hem) at either stage (n=5 in each group, **$p<0.01$). Scale bars are 500 microns. Asterisks (*) in (B) denote right and left hemispheres, e=prospective eye.

To obtain a comprehensive view of proliferation throughout the forebrain, a subset of embryos were cryosectioned and analyzed at 4 levels in the forebrain: rostral SP, middle SP, caudal SP, and diencephalon (Supplemental Fig. 3.11). Proliferation appeared relatively uniform throughout the forebrain of HH17 embryos (n=3) at all levels. By contrast, proliferation fraction dropped sharply to zero at the SP roof plate of HH21 embryos (n=2) but not the diencephalon roof plate, consistent with reported patterns of BMP4 (Shimogori et al., 2004; Furuta et al., 1997).

Taken together, these results confirm that neuroepithelial proliferation is inhibited at the roof plate during hemisphere division but not earlier stages. Furthermore, this inhibition is limited to the roof plate between telencephalic hemispheres, not the roof plate of more caudal regions (i.e., diencephalon) where cleavage does not occur.

3.2.2 Hemisphere size and division depend on eCSF pressure.

We hypothesized that neuroepithelial growth depends not only on morphogen patterning, but also on mechanical stress. Numerous studies have noted the effect of eCSF pressure on tissue volume (Jelinek and Pexieder, 1968; Desmond and Jacobson, 1977; Alonso et al., 1998) and proliferation (Desmond et al., 2005; Desmond and Jacobson, 1977; Desmond et al., 2014) in the developing brain, but none have considered the telencephalic hemispheres in detail.

To address this issue, we quantified the effects of eCSF pressure on hemisphere size, measured with live OCT imaging during the period of telencephalic hemisphere division (Fig. 3.3). To reduce pressure in HH17 embryos, an open glass tube was inserted into the midbrain (intubated), similar to past studies (Desmond and Jacobson, 1977). This alleviated existing

eCSF pressure and prevented the accumulation of additional eCSF over a 24h culture period (Fig. 3.3A,A'). To control for wounding effects (Jelinek and Pexieder, 1968; Desmond and Jacobson, 1977), closed glass tubes were also inserted into the midbrain of sham embryos (Fig. 3.3B,B'). This caused initial deflation but was followed by rapid reinflation and total growth similar to the control group (Fig. 3.3C,C). Lastly, to determine the effect of increased pressure on hemisphere size, pressure was osmotically increased during culture with β-D-xyloside (BDX, Fig. 3.3D,D') (Alonso et al., 1998; Desmond et al., 2014).

Figure 3.3A'-D' shows representative OCT cross-sections of the telencephalic hemispheres under each experimental case. For each embryo, normalized hemisphere arclength was measured, defined as end hemisphere arclength (HH21) divided by initial arclength (HH17). As shown in Fig. 3.3E, hemispheres under increased eCSF pressure were significantly larger than controls (BDX n=9; control n=13), and hemispheres under zero pressure were significantly smaller than those of sham and control embryos (intubated n=13; sham n=10). Furthermore, hemispheres failed to divide in intubated embryos (n=13) despite normal reductions in roof plate proliferation (n=4, Fig. 3.11). Since no significant differences were detected between sham and control embryos, these results are grouped as "normal pressure" in subsequent analysis.

Past measurements of eCSF pressure in chicken embryos have spanned several orders of magnitude: 25 ± 9 Pa (Jelinek and Pexieder, 1968), 350 ± 40 Pa (Desmond et al., 2005), and 3700 ± 150 Pa (Alonso et al., 1998). To obtain an accurate, definitive value, we measured pressure in control embryos as described in Materials and Methods. We found an average eCSF pressure of 15.4±3.8 Pa (n=7) at HH17 and 15.4±2.5 Pa (n=5) at HH21. These results are closest to those reported by Jelinek and Pexieder (1968), though slightly lower and more precise. The constant pressure observed between HH17 and HH21 matches dynamic trends

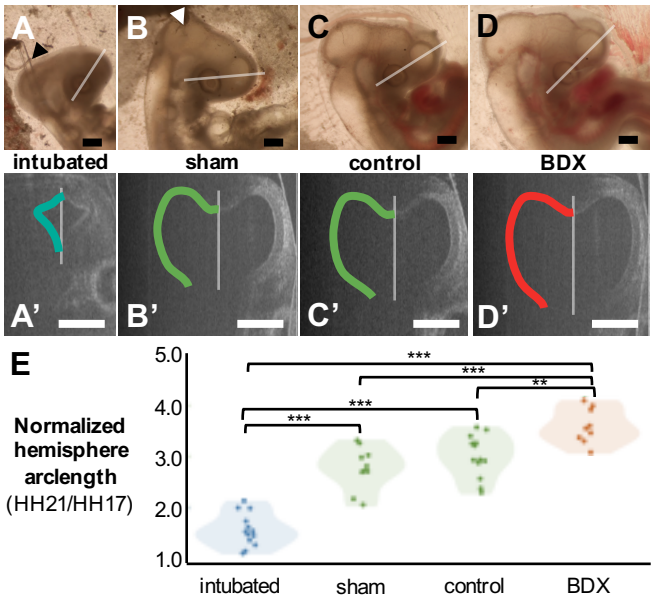

Figure 3.3: Altering eCSF pressure in the embryonic brain. (A-D) Bright field images of HH21 embryos cultured for 24h from HH17 under one of four conditions: (A) To reduce eCSF pressure, an open glass tube (black arrowhead) was inserted into the midbrain (n=15 intubated). (B) To control for injury but allow approximately normal eCSF pressure, a closed glass rod (white arrowhead) was inserted into the midbrain (n=10 sham). (C) Control embryos were cultured without perturbation (n=13). (D) To osmotically increase pressure, embryos were cultured in media containing beta-D-xyloside (BDX, n=14). (A'-D') Representative OCT cross-sections through telencephalon (white lines in A-D). Colored lines represent hemisphere arclength, traced on right hemisphere and flipped to left for visualization. (E) Normalized hemisphere arclength (HH21/HH17) was significantly higher under increased pressure (BDX) and significantly lower under decreased pressure (intubated), with no significant differences between sham and control groups. Scale bars are 500 microns. ***$p<0.0001$, **$p<0.01$.

reported by Jelinek and Pexieder (1968) and Desmond et al. (2005), who considered a range from HH13 to HH26.

Together, these results suggest that eCSF pressure remains fairly constant during the period of hemisphere division, but the magnitude of eCSF pressure serves as a key regulator of cerebral hemisphere size. Reducing pressure (via surgical manipulation) produced small hemispheres without clear separation, while increasing pressure (via osmotic manipulation) produced significantly larger hemispheres.

3.2.3 Neuroepithelial growth is modulated by mechanical feedback.

Change in hemisphere size, as reported in Fig. 3.3E, involves a combination of both growth and elastic stretch due to eCSF pressure. Therefore, to quantify tissue growth under normal and high pressure cases, we cannot simply consider the initial and final geometries. (Although eCSF pressure remains constant from HH17 to HH21, wall stress and elastic stretch due to pressure may change with geometry according to Laplace's Law.) To address this issue, we estimated tissue growth as the difference between initial and final *deflated* geometries (Fig. 3.4A).

To quantify elastic deformation and growth, we consider the diencephalon-midbrain boundary (DMB) as a representative region for the entire brain tube (Fig. 3.4). This landmark is easily distinguished across all stages considered and is free of large structures (i.e., prospective eyes) that can partially obscure the secondary prosencephalon and diencephalon in OCT images (Fig. 3.1D). As described below, the simple, roughly cylindrical geometry of the DMB

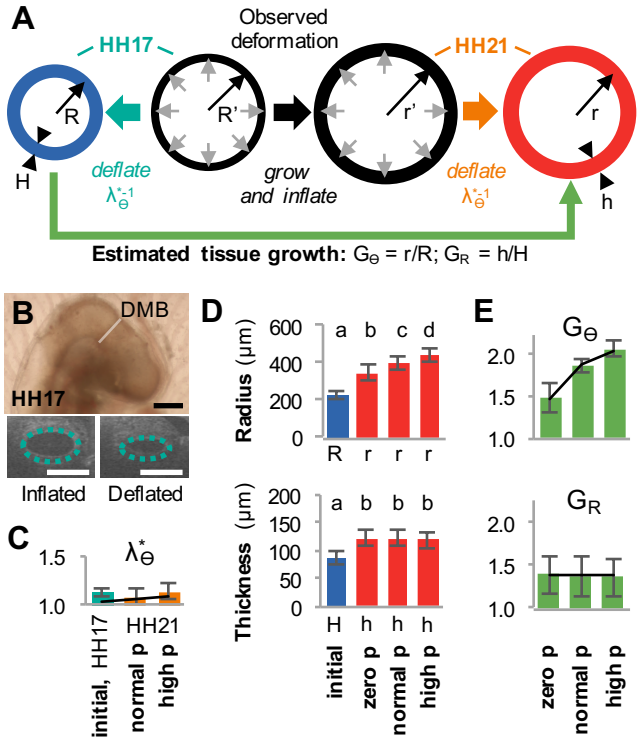

Figure 3.4: Effect of eCSF pressure on growth. (A) Expansion of the embryonic brain depends on elastic inflation due to eCSF pressure and tissue growth. To determine circumferential elastic stretch ratio, λ^*_Θ, change in cross-sectional geometry was measured before and after deflation at HH17 and HH21. ($\lambda^*_\Theta = R'/R$ at HH17 and $\lambda^*_\Theta = r'/r$ at HH21.) Circumferential and radial growth from HH17 to HH21 were estimated from deflated brains ($G_\Theta = r/R$, $G_R = h/H$). (B) Measurements were made at the diencephalon-midbrain boundary (DMB, white line on bright field image). (C) Elastic stretch ratio was relatively small ($\approx 10\%$) at both HH17 (blue) and HH21 (orange). (D) Deflated radius and thickness increased significantly from HH17 (R, H) to HH21 (r, h). Deflated radius at HH21 was significantly larger after culture under high pressure (p) and significantly smaller after culture under zero pressure, suggesting that circumferential growth depends on wall stress. (Left to right: n=19,15,17,14; statistically different groups denoted by a-d.) (E) Circumferentail and radial growth were estimated for each group. Black lines denote results given by theoretical model (see text for details). Scale bars are 500 microns.

also allows for a relatively simple mathematical analysis to determine growth parameters for a stress-based feedback law.

Measurements in deflated brains revealed a significant increase in radius between HH17 (R) and HH21 (r) (Fig. 3.4D). Furthermore, the deflated radius r was significantly higher in embryos cultured with high eCSF pressure (n=14) and lower in embryos cultured with zero eCSF pressure (n=15) compared to controls (n=17). Wall thickness also increased between HH17 (H) and HH21 (h) but was not significantly affected by pressure (Fig 3.4D). Note that R and H represent measures from intubated and sham embryos (n=19), since only these experimental groups could undergo initial deflation without affecting subsequent measurements. However, since no significant differences existed in inflated geometries at HH17 (R' and H'), we assume the same R and H across all groups.

The total (observed) circumferential stretch ratio is defined as $\lambda_\Theta = r'/R'$, where R' and r' are the *inflated* radii at initial (HH17) and final (HH21) time points, respectively (Fig. 3.4A). This quantity can be decomposed as $\lambda_\Theta = \lambda^*_\Theta G_\Theta$, where λ^*_Θ represents the elastic stretch ratio and $G_\Theta = r/R$ is the circumferential growth ratio ($G_\Theta > 1$ indicates positive growth, see Taber (2009)). With measurements of radius giving λ_Θ and G_Θ (Fig. 3.4E), we compute $\lambda^*_\Theta = \lambda_\Theta/G_\Theta$ (Fig. 3.4C). As a fraction of total brain expansion, the contribution of elastic stretch ($\lambda_\Theta \approx 1.1$, or 10% strain) to total expansion is considerably smaller than that due to growth during these stages.

Furthermore, our results indicate that circumferential growth ($G_\Theta = r/R$) depends on pressure but radial growth ($G_R = h/H$) does not (Fig. 3.4E). This finding supports the idea that neuroepithelial lengthening and thickening represent different biological mechanisms, i.e., proliferation leads to primarily tangential growth (G_Θ), while differentiation causes thickening (Fish et al., 2008).

In summary, these results suggest that expansion of the brain tube during stages HH17 to HH21 is driven mainly by growth modulated by eCSF pressure. Elastic inflation contributes relatively little to the total expansion, in agreement with previous studies (Garcia et al., 2017).

3.2.4 A chemomechanical feedback law describes growth in the embryonic brain.

Using the above results, we developed a mathematical growth law that depends on both morphogen concentration and mechanical feedback. Here, Θ and Φ denote the circumferential and longitudinal coordinates, respectively, in the brain tube. As in Garcia et al. (2017), we assume that growth is transversely isotropic (isotropic parallel to the wall) such that $G \equiv G_\Theta = G_\Phi$ is the tangential growth ratio. This assumption is based on the observation that, in simple epithelial monolayers, large strains (30% or greater) are required to bias cell divisions in the direction of maximum stretch (Wyatt et al., 2015) (approximately 10% in this study, Fig. 3.4).

We consider a growth law of the form

$$\dot{G} = \alpha(g_0 + g_\sigma \bar{\sigma})G, \quad \dot{G}_R = \alpha g_{0r} G_R, \tag{3.1}$$

where

$$\bar{\sigma} = \frac{1}{2\mu}(\sigma_\Theta + \sigma_\Phi) \tag{3.2}$$

is the nondimensional average tangential stress with $\mu = 300$ Pa being the shear modulus of neuroepithelium in chick (Xu et al., 2010a). In addition, g_0 and g_{0r} represent baseline

growth rates for zero eCSF pressure ($\bar{\sigma} = 0$), α and g_σ are non-negative growth coefficients, and dot denotes differentiation with respect to time t. Notably, Eqs. (3.1) are consistent with our findings that tangential growth increases with pressure-induced wall stress, while radial growth is independent of stress.

Concentrations of BMP4 and FGF8 are normalized by their maximum values such that $0 \leq C_{BMP}, C_{FGF} \leq 1$. Consistent with evidence that BMP4 inhibits growth of the forebrain wall (Ohkubo et al., 2002), we take

$$\alpha = 1 - C_{BMP}. \tag{3.3}$$

We also assume that mechanical stress is a prerequisite for growth factor-dependent effects, as previously described for certain FAK-dependent pathways to cell proliferation (Walker et al., 2005). Since the presence of the growth factor FGF8 increases growth, we set

$$g_\sigma = a + bC_{FGF}, \tag{3.4}$$

where a and b are constants.

To summarize, growth rates are assumed to depend locally on wall stress and morphogen concentration. With α and g_σ given by Eqs. (3.3) and (3.4), the proposed growth law (3.1) contains four unknown growth parameters (g_0, g_{0r}, a, b) to be found using experimental data from the DMB.

Since the DMB is far from the territories of high BMP4 and FGF8, we set $C_{FGF} = C_{BMP} = 0$, and Eqs. (3.1) become

$$\dot{G} = (g_0 + a\bar{\sigma})G, \quad \dot{G}_R = g_{0r}G_R. \tag{3.5}$$

To compute $\bar{\sigma}$, the DMB region is approximated by a thin-walled cylindrical tube with closed ends to maintain an internal pressure p. According to Laplace's law, the tangential wall stresses are $\sigma_\Theta = pr/h$ and $\sigma_\Phi = pr/2h$. If we neglect the relatively small elastic deformation, growth alone defines the evolving geometry, giving $r = G_\Theta R = GR$ and $h = G_R H$. Substitution of these relations into Eq. (3.2) yields

$$\bar{\sigma} = \bar{\sigma}_0 G/G_R \tag{3.6}$$

in which

$$\bar{\sigma}_0 = \frac{3pR}{4\mu H} \tag{3.7}$$

is the average tangential stress at the initial time (HH17), i.e., before growth when $G = G_R = 1$. Inserting this relation into Eq. $(3.5)_1$ gives the nonlinear differential equation

$$\dot{G} - g_0 G = a\bar{\sigma}_0 G^2/G_R. \tag{3.8}$$

Equations $(3.5)_2$ and (3.8) can be solved for $G_R(t)$ and $G(t)$ with initial conditions $G_R(0) = G(0) = 1$. In the absence of mechanical feedback ($a = 0$), the solution is

$$G = e^{g_0 t}, \quad G_R = e^{g_{0r} t}, \tag{3.9}$$

which are the usual relations for exponential growth. When mechanical feedback is included ($a \neq 0$), the radial growth does not change, and, after substituting $G_R(t)$ from $(3.9)_2$ into (3.8), we obtain the closed-form solution

$$G(t) = e^{g_0 t}\left[1 + \frac{a\bar{\sigma}_0}{g_0 - g_{0r}}\left(1 - e^{(g_0 - g_{0r})t}\right)\right]^{-1}. \tag{3.10}$$

The growth parameters were determined as follows:

1. With the measured values $G = G_\Theta = 1.48 \pm 0.17$ and $G_R = 1.38 \pm 0.02$ at HH21 ($t = 1$ d) at zero pressure (Fig. 3.4), Eqs. (3.9) give $g_0 = 0.39$ d^{-1} and $g_{0r} = 0.32$ d^{-1}. These values characterize baseline growth in intubated brains.

2. For normal pressure of $p = 15$ Pa, shear modulus $\mu = 300$ Pa (Xu et al., 2010a), initial radius $R = 235$ μm and initial wall thickness $H = 88$ μm (Fig. 3.4D), Eq. (3.7) gives $\bar{\sigma}_0 = 0.10$. Then, with $G = G_\Theta = 1.87 \pm 0.08$ over $t = 1$ d in control brains (Fig. 3.4), Eq. (3.10) yields $a = 2.0$ d^{-1}.

3. Set $b = 6a = 12$ d^{-1} based on FGF8 immunofluorescence gradients (arbitrary units) reported in citetoyoda2010fgf8.

These parameter values were determined for normal brains. To test the predictive ability of the proposed growth law, we simulated BDX experiments by increasing pressure without changing the parameters. For an estimated 40% increase in p during culture with BDX (Alonso et al., 1998), Eq. (3.10) yields $G_\Theta = 2.09$, in close agreement with experimentally measured values for BDX-treated brains ($G_\Theta = 2.07 \pm 0.10$, Fig. 3.4E).

3.2.5 Growth model based on morphogens and mechanical feedback predicts normal hemisphere morphogenesis.

Next, we considered the more complex scenario of hemisphere morphogenesis. To determine whether our assumptions are sufficient to predict realistic hemisphere shapes, we created a three-dimensional computational model of the SP including realistic morphogen gradients and mechanical loads.

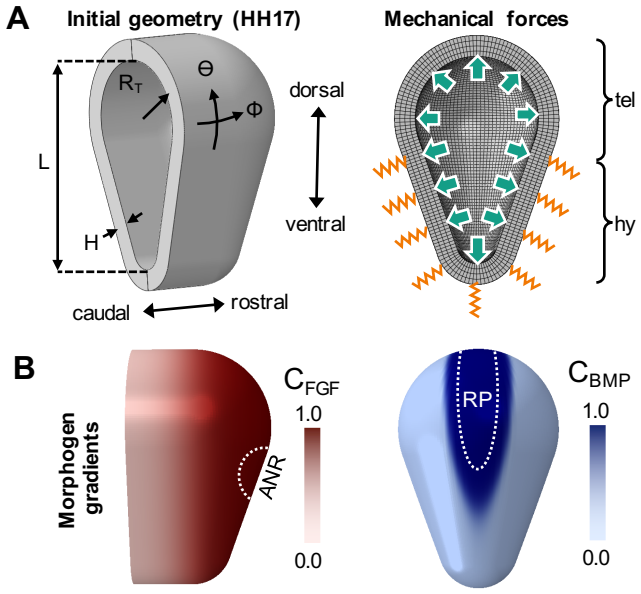

Figure 3.5: Computational model for hemisphere division. (A) Left: Initial geometry for the secondary prosencephalon including telencephalon (tel) and hypothalamus (hy). Right: eCSF pressure was applied along the inner wall (blue arrows), and ventral reinforcement from surrounding tissue is represented by an elastic foundation (orange springs). (B) Normalized morphogen gradients (C_{BMP} and C_{FGF}) approximate BMP4 and FGF8 diffusion from the roof plate (RP) and anterior neural ridge (ANR), respectively.

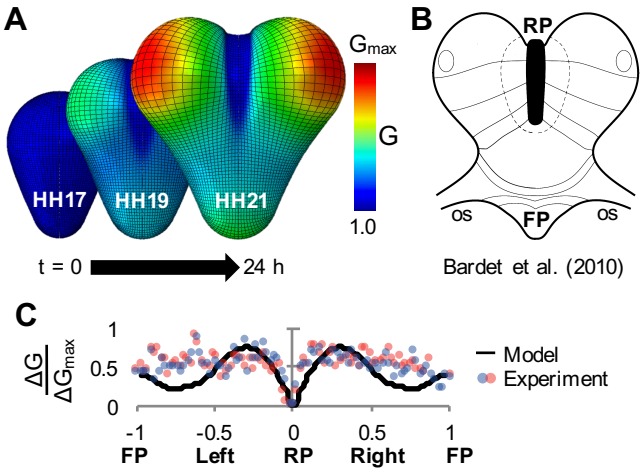

Figure 3.6: Comparison of model and experimental growth. (A) Over 24 h (HH17 to HH21), the computational model grows and develops realistically-shaped left and right hemispheres (rostral view). Colors represent tangential growth, G. (B) Modified drawing from (Bardet et al., 2010) illustrates qualitative comparison between model and commonly observed morphology. Thin lines divide functional areas of the SP, following contours similar to those of the deformed mesh. In model, the optic stalk (os) is lumped into elastic foundation constraint. (C) Comparison of model-predicted growth fraction (black line, $\Delta G/\Delta G_{max} = (G-1)/(G_{max}-1)$) and measured proliferation fraction (dots) along the neuroepithalial wall. Each dot represents the average for a 60μm-long region of wall at HH21 (n=2 samples, denoted by pink and blue color). Location along the wall (x) is normalized so that $x = 0$ at the roof plate (RP), $x = \pm 1$ at the floor plate (FP). Scale bar represents 500 microns.

The initial, unloaded geometry is based on dimensions of the deflated SP at HH17, and a constant eCSF pressure was applied on the inner wall (Fig. 3.5A). Since the hypothalamus is surrounded by external tissues (including prospective eyes and mesenchyme) that may reinforce or constrain this region, a relatively soft elastic foundation is applied on the outer conical surface, as denoted by springs (Fig. 3.5A, right). Normalized morphogen gradients were generated such that BMP4 concentration (C_{BMP}) is highest at the roof plate and FGF8 concentration (C_{FGF}) is highest at the anterior neural ridge (Fig. 3.5B). Stress-dependent growth at all points is governed by Eqs. (3.1)-(3.4) with the parameter values provided in Sec. 3.4. (See Methods for material properties and additional details.)

Figure 3.6A shows progression of the model over 24 hours. The resulting growth produces two distinct hemispheres of reasonable morphology. Figure 3.6B depicts normal SP geometry and functional subdivisions reported by (Bardet et al., 2010). In the initial configuration ($t = 0$), our model can be divided along the dorsal-ventral axis (Θ-direction, horizontal lines in Fig. 3.6A) and medial-lateral axis (Φ-direction, vertical lines). As shape evolves over time, these horizontal lines (representing different dorsal-ventral levels at $t = 0$) reorient to mirror contours between functional subdivisions of the cortex (black lines in Fig. 3.6B).

Normal growth and proliferation. To compare proliferation between model and experiment, proliferation fraction was calculated along the circumference of the wall in EdU-stained cross-sections (Fig. 3.2B) and equivalent model cross-sections (see Fig. 3.9A). Total circumference was normalized so that $x = 0$ at the roof plate and $x = \pm 1$ at the floor plate ($x > 0$ for right hemisphere, $x < 0$ for left hemisphere). As shown in Fig. 3.6C, proliferation drops sharply to zero at the roof plate of HH21 embryos (n=2, pink and blue dots). Furthermore, a subtle decrease in proliferation is visible from the hemispheres ($0.1 < |x| < 0.5$) to the hypothalamus ($|x| > 0.5$; see Fig. 3.6C). Tangential growth from the stress-dependent model (black line) predicts spatial trends similar to those observed experimentally, but with a more exaggerated decrease at the hypothalamus.

Apical stresses and cell shape Using a computational model that includes mechanical feedback, Wyatt et al. (2015) showed that cell divisions tend to reduce stress and encourage isotropic cell shapes in epithelial monolayers. If the same is true in the neuroepithelium, we should also see reduced stress and isotropic cell shapes in regions where stress-dependent growth is significant. By contrast, areas where stress-dependent growth is inhibited (high BMP4 as defined in Fig. 3.5B) may be subject to high stresses and anisotropic cell stretch.

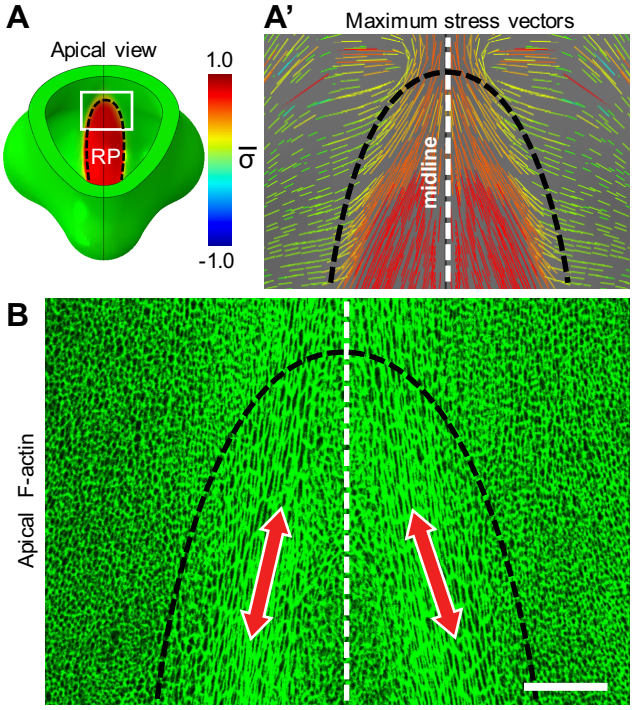

Figure 3.7: Comparison of model and experimental patterns of wall stress. (A) HH21 model reveals high in-plane tension, $\bar{\sigma} = (\sigma_\Theta + \sigma_\Phi)/(2\mu)$, along the apical (inner) RP, where stress-dependent growth is turned off. (A') Magnified view of white box region in (A), where lines represent the direction of maximum stress and color represents magnitude. (B) Staining for F-actin in the same RP region (enclosed by black dashed lines, midline denoted with white dashed line) reveals cells that are dramatically stretched in the direction of maximum stress (n=5, red arrows). Conversely, regions of stress-dependent growth (hemispheres, shown on right and left edges) maintain relatively small, round cells (isotropic cell shape, n=5 for hemisphere and hypothalamus regions). Scale bar represents 40 microns.

As shown in Fig. 3.7A, our model predicts low stress in areas of stress-dependent growth (outside of RP, green where $\bar{\sigma} \approx 0$) but high stress in the roof plate where growth is inhibited by BMP4 (region denoted by black dashed line). Experimentally, we note isotropic (round) cells in the same regions of low stress (Fig. 3.7B), as illustrated by apical F-actin that outlines each cell. By contrast, the non-proliferative roof plate contains drastically stretched cells (Fig. 3.7B), and the direction of maximum stretch matches that predicted by our model (Fig. 3.7A').

Effects of external forces. As described above, the observed drop in roof plate proliferation depends on a predefined morphogen gradient, C_{BMP}, such that even high stresses may not induce significant growth. However, for growth outside the roof plate, stress gradients should result in proliferation gradients. This idea is supported by our model, where tissues surrounding the hypothalamus (represented by an elastic foundation) prevent the development of high stresses (Fig. 3.8C, left), resulting in slightly lower growth (G) in this region (Fig. 3.6C). Conversely, a model without this support predicts maximal $\bar{\sigma}$ in the conical hypothalamus (Fig. 3.8C, right), leading to overexpansion of this region. To test this prediction, we dissected the surrounding tissues from five HH13 embryos and allowed them to develop to HH21 (Fig. 3.8A-A"). In agreement with our model, the absence of prospective eyes (no elastic foundation) produced a wider hypothalamus compared to controls (n=5 per group, Fig. 3.8B-C).

Taken together, these results support our 3D model based on morphogen gradients, external loads, and mechanical feedback. For the case of normal hemisphere development, our model is able to link and explain several experimental observations: (1) In the hypothalamus, reduced proliferation is caused by reduced mechanical stresses due to constraints from external tissues; (2) In the roof plate, elongated apical cell shapes are caused by very high stress due to inhibited proliferation in this region.

3.2.6 Mechanical feedback explains hemisphere morphologies under altered eCSF pressure.

After testing our model against normal development (Figs. 3.6 and 3.7), we examined its ability to predict abnormal hemisphere morphologies observed under altered eCSF pressure.

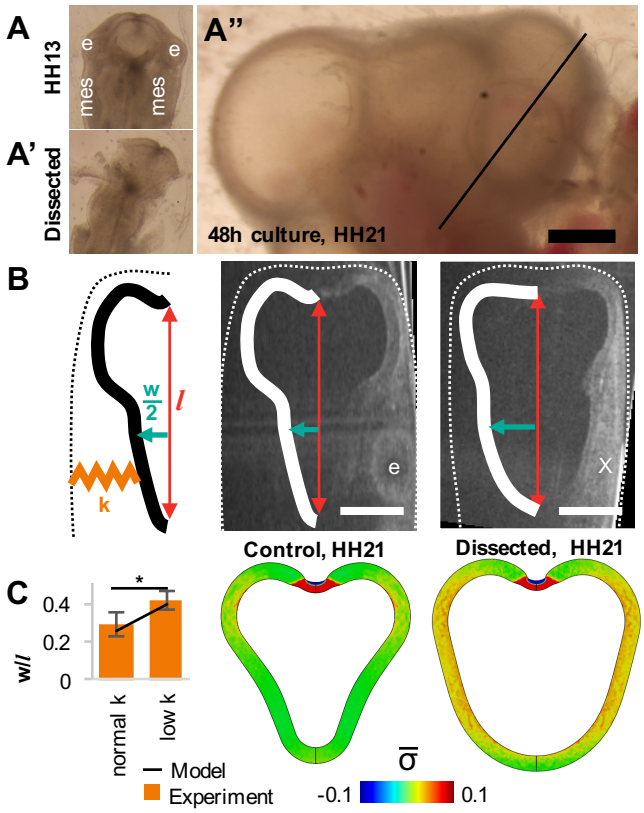

Figure 3.8: Effects of external tissues. (A-A") Prospective eyes (e) and lateral mesenchyme (mes) were dissected from the rostral brain at HH13, and embryos were cultured to HH21. Scale bar is 500 microns, all bright field images shown to same scale. (B) OCT images of the secondary prosencephalon in control (n=5) and dissected embryos (n=5). In dissected embryos, loose mesenchyme repopulated the dissected area, but prospective eyes did not regenerate. Ratio of hypothalamus width (w) to secondary prosencephalon length (l) was higher (hypothalamus was wider) in dissected embryos. (C) Model results with and without external constraint of elastic foundation (normal and negligible stiffness, k). Consistent with experimental trends, the conical hypothalamus experienced high stresses and expanded more without external constraint. *$p<0.05$.

We also considered a model without feedback, in which a set growth pattern (growth produced under normal pressure, Fig. 3.6) was subjected to no pressure ($p = 0$), normal pressure ($p = 15$ Pa), and high pressure ($p = 21$ Pa).

Reduced eCSF pressure (HH17-21) produces classic holoprosencephalic morphology. In the experimental case of embryos cultured without eCSF pressure (HH17-21), hemispheres failed to grow or separate (Fig. 3.9A). To quantify this effect, hemisphere growth was estimated from OCT images as previously described in Figs. 3.3 and 3.4, and analysis revealed significant differences under growth for each pressure case (ANOVA $p<0.0001$, n=10 zero pressure, n=15 normal pressure, n=7 high pressure). With mechanical feedback, our model results agree reasonably well with our experimental measurements in intubated and control brains (Fig. 3.9B).

For each pressure case, we also measured relative RP invagination depth, defined as the vertical distance from hemisphere peak to roof plate valley (Fig. 3.9B), normalized by the total hemisphere arclength (Fig. 3.3A'-D'). In our feedback model, reduced growth was insufficient to produce hemisphere separation at HH21, as illustrated by a significant (70%) reduction in relative RP depth ($p<0.0001$, Fig. 3.9). This microcephalic, holoprosencephalic morphology (classic holoprosencephaly) has been previously reported due to FGF8 reduction (Storm et al., 2006; Ohkubo et al., 2002) or BMP4 increase (Fernandes et al., 2007; Furuta et al., 1997), roughly equivalent to $g_0 \to 0$ or $\alpha \to 1$ in our model. By contrast, reducing pressure for the "no feedback" model increases RP depth (Fig. 3.9B).

Increased eCSF pressure (HH17-21) produces megalencephalic but not holoprosencephalic morphology. Under high pressure (HH17-21), no decreases in RP depth were

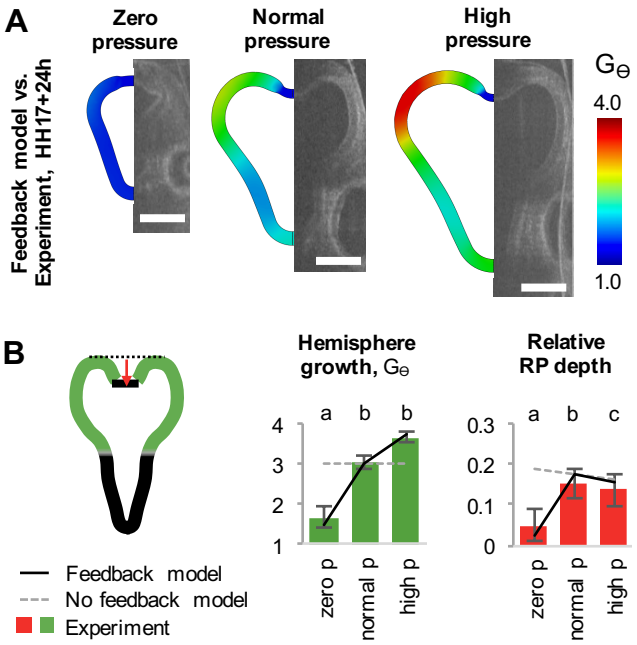

Figure 3.9: Comparison of numerical and experimental results for perturbed eCSF pressure. (A) Comparable HH21 cross-sections through model (left) and representative embryos (right, OCT images) after 24h culture under zero, normal, and high pressure. (B) Growth of the telencephalic hemispheres (green arclength) was estimated as described in Fig. 3.4. Hemisphere division was quantified by measuring depth of the RP relative to maximum hemisphere height (red arrows). To normalize this depth with respect to size, it was divided by the final, inflated hemisphere arclength. Experimentally measured hemisphere growth and RP depth (bars) are accurately predicted by the stress-dependent growth model (feedback model, black lines). For comparison, results from a model without mechanical feedback are also shown (dashed gray lines). Mechanical feedback is necessary to produce the measured differences. (Left to right: n=10,15,7 for G_Θ; n=13,23,9 for relative RP depth; statistically different groups denoted by a-c.) Scale bars are 500 microns.

observed experimentally or in the feedback model (Fig. 3.9B). However, hemisphere growth did increase significantly under high pressure relative to the normal pressure case (Fig. 3.9A), corresponding to a megalencephalic (abnormally large) hemisphere morphology.

As illustrated by the "no feedback" model, eCSF pressure produces elastic deformations that tend to push the RP outward (decreasing RP depth, Fig. 3.9B). For this reason, one might also expect a holoprosencephalic morphology under the condition of increased pressure, especially as wall stresses increase with growth, G (see Eq. 3.6). However, since RP proliferation is inhibited during this period (Fig. 3.2), hemisphere growth also serves to increase *differential* growth, the driving force for hemisphere division. In this way, mechanical feedback counteracts the outward push of higher pressures to maintain relatively normal RP depth.

Increased eCSF pressure (HH13-17) produces MIH holoprosencephalic morphology. Interestingly, we also observed one scenario where high pressure led to significantly reduced RP depth. As previously reported via perturbation of molecular signaling (Fernandes et al., 2007; Huang et al., 2007a), overproliferation in the roof plate has been shown to produce holoprosencephalic morphologies. Since the onset of eCSF pressure occurs at HH13 in chick, at least 12 hours before roof plate proliferation is inhibited by BMP4 ($\geq$HH18) (Crossley et al., 2001), we hypothesized that increased pressure may also increase growth of the roof plate at earlier stages, reducing the ability of the RP to descend.

To test this hypothesis, we cultured HH13 embryos with BDX or control media for 36h (Fig. 3.10A-B). Measuring RP width relative to hemisphere arclength, we found that the roof plate was significantly wider after culture under high eCSF pressure compared to controls ($p=0.026$, $n=6$ per group). By contrast, high pressure at later stages (HH17-21) only increased growth in the hemispheres, such that relative RP width was unchanged (n=7 high

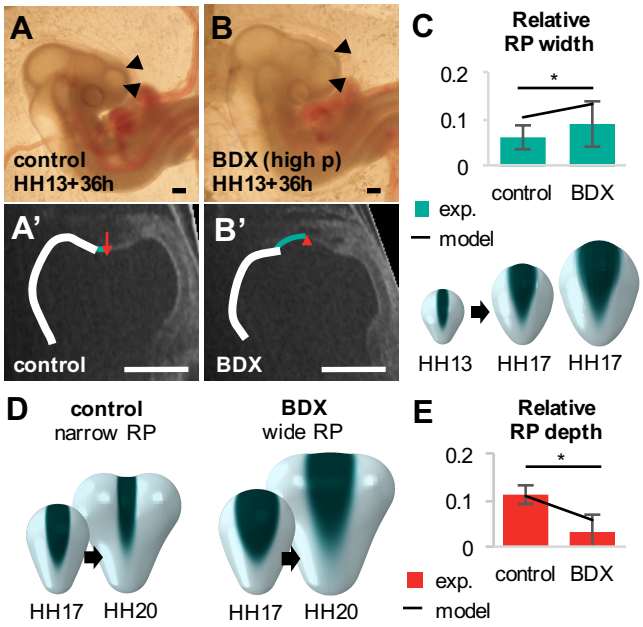

Figure 3.10: Effects of early pressure elevation on hemisphere morphogenesis. (A-B) Bright field images of embryos cultured 36h with control media (n=6) or BDX (n=6) starting from HH13. Since embryos *in vitro* developed slightly slower than *in ovo*, they were slightly smaller than embryos cultured for 24h from HH17, reaching an average stage of HH20. (A'-B;) OCT cross-sections reveal overexpansion of the RP (teal outline) and laterally-displaced hemispheres (white outline, black arrowheads in A-B). Relative RP invagination (red arrow) was also reduced, as the expanded midline remained relatively flat (n=3) or even convex (n=3). (C) Relative RP width (RP arclength divided by total SP circumference at HH17) revealed a significant increase for embryos cultured with BDX from HH13. Bottom: A model of growth from HH13 to HH17, with adjusted initial geometry (HH13) and stress-dependent growth at the RP, accurately predicts RP widening effect. (D) Model of growth between HH17 and HH21, considering the effect of RP width (region of no growth). Dark colored regions in (D-E) denote RP domain where BMP4 inhibits growth at later stages ($C_{BMP} \approx 1$). (E) For the model in (D), increasing RP width led to reduced RP depth, as observed with early application of BDX. Scale bars are 500 microns. *p<0.05.

pressure, n=15 normal pressure; p=0.95). To consider stress-dependent growth of the roof plate during early stages (prior to growth inhibition by BMP4), we created a new model with initial geometry based on HH13, C_{FGF} similar to Fig. 3.5, and $C_{BMP} = 0$ everywhere. We also defined the RP to be thinner, as observed experimentally (Fig. 3.2A). Without inhibition of growth at the roof plate, and with development of high tension at the roof plate, our mechanical feedback model predicts similar increases in RP width under high pressure (Fig. 3.10C).

As in other cases of roof plate overproliferation (Fernandes et al., 2007; Huang et al., 2007a), embryos subjected to high eCSF pressure also displayed reduced RP depth compared to controls (n=6 per group), sometimes with a roof plate that bulges outward (Fig. 3.10B'). To determine whether a relatively wide roof plate could produce this effect mechanically, we also considered a model of hemisphere division (HH17-21) with expanded roof plate region (geometry, loads, and C_{FGF} from Fig. 3.5, region of $C_{BMP} = 1$ expanded 50% based on results in Fig. 3.10C). In this model, a widened roof plate does reduce RP depth (Fig. 3.10E). In fact, a widened roof plate was sufficient to reduce invagination under normal pressure, suggesting that even a short period of increased pressure, during the specific window of RP proliferation, is capable of producing mild holoprosencephalic morphologies.

Taken together, these results support a role for mechanical feedback in hemisphere development. In our model, feedback is necessary to predict not only hemisphere size, but also whether or not hemisphere division will occur under specific eCSF pressures. Moreover, we note that short periods of both decreased and increased pressure impaired hemisphere division, suggesting new mechanisms by which holoprosencephalic morphologies may occur.

3.3 Discussion

In this study, we hypothesized that hemisphere morphogenesis is driven by differential growth, controlled by both chemical and mechanical signals. To test this hypothesis, we used a combination of experimental and computational approaches. First, we quantified cell proliferation and morphology under normal and altered loading conditions. Next, we proposed a novel chemomechanical growth law to reconcile the effects of morphogens and mechanical stress on growth, with mathematical form and parameters determined by experimental measures. Through computational modeling, we confirmed that differential growth is sufficient to induce hemisphere division, and we propose that measured proliferation patterns may be explained in part by mechanical feedback. For the first time, this study demonstrates how a range of abnormal hemisphere morphologies – typically attributed to morphogen signaling – can be produced by alterations in eCSF pressure and predicted by models with mechanical feedback.

3.3.1 Mechanical feedback as a key regulator of hemisphere morphogenesis

Mechanical feedback has been largely overlooked in the context of hemisphere development. For decades, researchers have known that eCSF pressure influences growth in the early brain tube (Desmond and Jacobson, 1977; Alonso et al., 1998; Desmond et al., 2005). However, the mechanism by which eCSF pressure affects morphogenesis is not understood. Though mechanical tension has been hypothesized as a driver of cerebral growth (Van Essen, 1997), no prior studies have reported effects in this region.

The results of the present study show that pressure-induced wall stresses influence both the size and shape of the cerebral hemispheres in the early chick embryo. Compared to controls, hemispheres grew more under osmotically increased pressure and less under mechanically reduced pressure (Fig. 3.3 and 3.9). These trends are consistent with growth modulation observed at the DMB (Fig. 3.4) and at the SP during earlier stages (Garcia et al., 2017). At a more global level, similar effects had been reported in terms of total brain tissue volume and proliferation rate in chick (Alonso et al., 1998; Desmond and Jacobson, 1977; Desmond et al., 2005, 2014). Regionally, we found that proliferation rates were higher in the hemispheres than the ventral hypothalamus (Fig. 3.6). While this gradient is not predicted by chemical morphogen gradients (ventral FGF8 is as high if not higher than in dorsal regions, Fig. 3.1E), it can be explained by mechanical feedback. Through experiments and computational modeling, we confirmed that ventral tissues, particularly the prospective eyes, constrain deformation of the hypothalamus, leading to lower tension and less growth (Fig. 3.8).

Notably, we found that tangential growth, but not radial growth, varied with pressure (Fig. 3.4), supporting the notion that tangential and radial growth are caused by different biological processes (Fish et al., 2008). At early stages of development, the wall of the brain is a (pseudostratified) monolayer, and tangential growth may represent planar, or symmetric, cell divisions. In neural development, these *symmetric* divisions (in which each new cell acquires both apical and basal cell processes) increase the pool of apical progenitor cells that can continue to proliferate, ultimately determining brain size (Fish et al., 2008; Konno et al., 2008). For epithelial monolayers, symmetric cell divisions have been shown to increase with planar stretch (Wyatt et al., 2015; Streichan et al., 2014), in agreement with our observation of mechanically-induced tangential growth. Conversely, asymmetric cell divisions are linked to differentiation and radial growth (thickening) of the neuroepithelium (Fish et al., 2008).

The details of mechanical feedback in growth are just beginning to be uncovered. Desmond et al. (2014) recently reported focal adhesion kinase (FAK) as a mechanotransducer in the embryonic brain, finding that its expression was upregulated with increasing eCSF pressure. This mechanotransducer may be present throughout the early brain tube (Hens and DeSimone, 1995; Desmond et al., 2014) and has been implicated in stretch-induced proliferation of other systems (Chaturvedi et al., 2007; Lehoux et al., 2005; Walker et al., 2005). In determining the form of our proposed stress-dependent growth law, we therefore turned to existing studies of other, similar systems. For example, it remains unclear whether cells respond to mechanical feedback at a specific stage of the cell cycle, or if mechanical feedback is accumulated over one or more cell cycles. In monolayers derived from canine kidney epithelium, Streichan et al. (2014) found that proliferation depends on mechanical feedback specifically between G1- and S-phases of the cell cycle and has no memory of stretch from past phases. In our model, we therefore consider the current, instantaneous stress rather than stress accumulated over a set period. We also assume transversely isotropic growth, based on the additional observation that in-plane stretch direction did not bias the direction cell division at low levels ($< 30\%$ strain) (Streichan et al., 2014).

3.3.2 Clinical relevance: holoprosencephaly, microcephaly, and megalencephaly

Here we considered a novel mechanism – dysregulation of eCSF pressure – to account for a range of abnormal hemisphere morphologies without altered molecular signaling. Holoprosencephaly represents a diverse group of conditions, many of which have been attributed to altered morphogen signaling (Fernandes et al., 2007). While some cases have been directly

linked to genetic markers, external factors including alcohol, retinoic acid, and maternal diabetes have also been implicated in animal models (Petryk et al., 2015).

In Fig. 3.9, we found that decreasing eCSF pressure during the period of normal hemisphere division (HH17-21) produces hemispheres that are both holoprosencephalic and microcephalic. Though microcephaly had been reported for chicken embryos intubated at earlier stages (Desmond and Jacobson, 1977; Garcia et al., 2017), as well as chicken and rat embryos cultured under osmotically decreased eCSF pressure (Ramasubramanian et al., 2013; Morriss-Kay et al., 1986; Alonso et al., 2000), the report of holoprosencephaly is novel to this paper. By incorporating chemomechanical feedback into a realistic model of hemisphere morphogenesis, we show that division fails as a result of insufficient growth of ventral and lateral structures (classic holoprosencephaly). In this respect, holoprosencephaly induced by low pressure is similar to cases produced by low FGF8, low SHH, or high BMP4 (Furuta et al., 1997; Storm et al., 2006; Ohkubo et al., 2002; Huang et al., 2007b).

In chicken embryos, we were also able to explore the effect of increased eCSF pressure *before* proliferation is inhibited at the roof plate (Fig. 3.2). In this case, mechanical feedback disproportionately increased growth of the thin, unsupported roof plate (Fig. 3.10). Though no molecular signals were altered, results were strikingly similar to MIH holoprosencephaly phenotypes produced by decreasing BMP4 or increasing SHH (Fernandes et al., 2007; Huang et al., 2007a). While the neural tube closes later in mouse and human compared to chicken, which could result in a shorter window for pressure-induced overproliferation of the roof plate, future studies should keep this mechanism in mind.

After roof plate growth had been inhibited (HH17-21), we found that increasing pressure neither reduced nor increased hemisphere division (Fig. 3.9A). However, it did produce megalencephaly (Fig. 3.9B), a condition reported in 2% of the general population that has

been linked to delayed development, epilepsy, and corticospinal dysfunction (Barkovich et al., 2012).

Because regulation of eCSF pressure represents a complex process in itself, alterations could occur during natural brain development. In zebrafish, genetic mutations related to Na^+K^+ATPase have induced dysregulation of eCSF pressure (Lowery and Sive, 2005; Doğanlı et al., 2013). In chicken embryos, pressure can be altered by overproduction or break down of osmotically active components (e.g. chondroitin sulfate) (Alonso et al., 1998; Ramasubramanian et al., 2013; Morriss-Kay et al., 1986; Alonso et al., 2000), or increase in external osmolarity (Chen et al., 2014). In mammalian systems, hyperglycemia has been proposed to explain increased incidence of holoprosencephaly in maternal diabetes (Petryk et al., 2015) – a feasible hypothesis in the context of osmotic changes.

3.3.3 Limitations and future work

Using assumptions and initial conditions based on experimental evidence, our chemomechanical feedback model was able to accurately predict complex and abnormal morphologies during hemisphere division. However, it is worth noting several biological observations not considered in our model.

For simplicity and convergence, our model of hemisphere division (HH17-21) considered uniform thickness at $t = 0$. However, the true roof plate is noticeably thinner than other areas of the brain wall by HH17. In our model for earlier stages (HH13-17), thinning contributes significantly to mechanical feedback: a thinner roof plate leads to higher tension and therefore greater tissue expansion (Fig. 3.10). However, since this effect is inhibited at later stages,

we assume this variation in thickness has a minimal impact on our model of hemisphere division.

As an approximation, we also assumed uniform, isotropic material properties across the brain wall. This assumption contradicts evidence that actomyosin is more concentrated on the apical surface, which may correspond to tissue stiffening or contraction (Filas et al., 2012; Garcia et al., 2017; Filas et al., 2011). While actomyosin contraction plays a role in earlier brain morphogenesis (Filas et al., 2012; Garcia et al., 2017)), no effect was observed for the stages considered in this paper (Garcia et al., 2017). We did, however, stiffen the caudal boundary of our model (separating secondary prosencephalon from diencephalon) to compensate for the increased stiffness and decreased tension that may exist in this region (Garcia et al., 2017).

In this study, we approximated morphogen gradients based on existing literature. Though we did not measure morphogen concentrations or effects directly, a wealth of studies have reported the territories and effects of BMP4, SHH, and FGF8 in the early telencephalon (Furuta et al., 1997; Monuki, 2007; Bardet et al., 2010; Toyoda et al., 2010). For simplicity, our model consolidated these positive and negative feedback effects (Fig. 3.1E) into one BMP4 gradient and one FGF8 gradient defined at $t = 0$ (Fig. 3.5B) to approximate diffusion of these signals (Toyoda et al., 2010). Future studies should consider dynamic morphogen behavior, though additional work is needed to quantify diffusion coefficients and chemical interaction in this context.

Lastly, our model roughly approximates the effect of ventral tissues using an elastic foundation. This approximation was necessary for computational time, since full incorporation would require contact between separate structures to represent mesenchyme, prospective

eyes, and surface ectoderm. While our approach does not capture the details of these structures, we find it sufficient to capture basic effects on our structure of interest. For the hypothalamus, we discovered that external tissues, particularly the prospective eyes, play an important role in restricting growth (Fig. 3.8). This complements a previous study, where we proposed external tissues as a factor in bending and growth reduction of the ventral brain tube (Garcia et al., 2017).

At later stages of hemisphere morphogenesis, Choe et al. (2014) reported the necessity of external mesenchyme, which migrates into the space between cortical hemispheres, for hemisphere division. Authors speculated that mesenchyme may provide a source of critical roof plate signaling. Alternately, Gupta and Sen (2015) proposed that mesenchyme may exert a downward force to assist invagination. Notably, our model did not require downward force from the dorsal mesenchyme to initiate hemisphere division (Fig. 3.5). However, we did observe dramatic stretch of the roof plate region (Fig. 3.7), which must form delicate choroid plexus projections at later stages (Choe et al., 2014). Like ventral tissues that reinforce the hypothalamus, it is possible that mesenchyme serves to reinforce the roof plate at later stages. Studies of later development should consider the role of mesenchyme in subsequent roof plate morphogenesis.

3.4 Materials and Methods

3.4.1 Embryo culture, perturbation, and imaging

Fertilized white Leghorn chicken eggs were incubated at 38°C (90% humidity), and embryos were extracted at 48 or 60 hours (HH13 or HH17, respectively) using a filter paper carrier

(Chapman et al., 2001). Embryos were cultured on 0.3% agar-albumen gels in 35mm culture dishes (Chapman et al., 2001), with a 200μL layer of culture media on top. Unless otherwise stated, culture media contained Dulbecco's Modified Eagle's Medium (Sigma) with 10% chick serum (Sigma) and 1% penicillin/streptomycin/neomycin (Invitrogen). To ensure adequate oxygen delivery during culture under media, embryos were superfused with a mixture of 95% oxygen and 5% carbon dioxide (Voronov and Taber, 2002).

To increase eCSF pressure during development, 100μL of media was replaced with media containing 4mM β-D-xyloside (BDX, Sigma), which increases osmolarity of the eCSF, increasing the pressure required for osmotic-pressure equilibrium (Alonso et al., 1998; Desmond et al., 2014). To reduce eCSF pressure during development, an open glass capillary tube (inner diameter=150μm) was inserted into the midbrain. For sham embryos, a closed glass rod was used instead. Only embryos in which the tube remained intact for the full 24h culture were used for subsequent analysis. To reduce the influence of external tissues, prospective eyes and lateral mesenchyme were dissected from the HH13 forebrain, and embryos were cultured for 48h (allotting an additional 12 hours for healing and slower culture *in vitro*). To measure deflated final geometries, a small incision was made in the midbrain.

All embryos were examined over the course of development using optical coherence tomography (Thorlabs) and a Leica MZ8 microscope. To measure changes due to growth, geometries were recorded before and after culture. To measure geometric changes due to inflation, geometries were also recorded immediately before and after deflation where applicable.

3.4.2 Fluorescent labeling and quantification.

To quantify cell proliferation, EdU (5-ethynyl-2'-deoxyuridine) was incorporated into cells undergoing DNA synthesis using the Click-iT EdU assay (Invitrogen). Based on previous optimization for chicken embryos (Warren et al., 2009), 400μL of 1 mM EdU was pipetted directly on top of embryos (HH17 or HH21), which were then cultured 4h and immediately fixed in 3.7% formaldehyde. Embryos were manually cut through the secondary prosencephalon (n=2 HH17, n=3 HH21) or cryosectioned (n=3 HH17, n=2 HH21) before permeabilizing for one hour in 1% bovine serum albumin (Sigma) and 0.1% Triton X-100 (Sigma). The Click-iT EdU reaction was applied according to the manufacturer protocol. To protect the integrity of cryosectioned tissues, embryos were soaked in 30% sucrose prior to freezing. To label all nuclei (DNA stain), samples were then incubated 30 minutes in 5μg/mL Hoechst 33342. To visualize apical F-actin on the inner surface of the brain, additional embryos were fixed with 3.7% formaldehyde, manually cut through the secondary prosencephalon (HH17 or HH21), permeabilized, and stained with phalloidin as described in (Garcia et al., 2017).

Fixed fluorescent samples were imaged using a Zeiss LSM 710 confocal microscope at 20x magnification. For large sections, FIJI/ImageJ (Schneider et al., 2012) was used to stitch multiple 20x z-stacks (Preibisch et al., 2009), then z-stacks were transformed to maximum intensity z-projections (see Fig. 3.2A-B). To minimize bias when determining proliferation fraction, nuclei were semi-automatically counted as follows: First, EdU maximum intensity projections were run through a 3D Gaussian blur filter of 0.5μm x 0.5μm x 0.5μm, followed by a CLAHE (contrast-limited adaptive histogram equalization) algorithm to optimize local contrast for each channel. For continuous quantification along the wall of the brain tube (Figs. 3.6C and 3.11), the neuroepithelium was traced and straightened (Kocsis et al., 1991)

such that the x-dimension represented distance from the RP. Finally, local maxima (representing EdU-labeled or Hoechst33342-labeled nuclei) were counted, using a 1-pixel ($36\mu m^2$) Gaussian filter to avoid labeling noise as nuclei. Images were checked manually to ensure accurate capture of nuclei. Due to variability in image quality, some images required an additional round of Gaussian blur (1 pixel $\approx 36\mu m^2$) after z-projection and CLAHE. For a given region, proliferation fraction was calculated as the number of EdU-labeled nuclei (undergoing S-phase during the 4-hour labeling window) divided by the total number of Hoechst 33342-labeled nuclei. For Figs. 3.6C and 3.11, each data point represents a 60 μm-long segment along the circumference of the wall.

3.4.3 Measuring growth and deformation

OCT image stacks were reoriented in ImageJ/FIJI (Schneider et al., 2012) to yield cross sections through the DMB or SP as shown in Figs. 3.4B and 3.1D, respectively. For measures at the DMB, the wall perimeter δ was traced for each cross section, and average radius was computed as $\delta/(2\pi)$. For intubated and sham embryos, initial radius (HH17) was recorded before deflation (R') and after deflation (R), while only the initial inflated radius (R') could be recorded for control and BDX cases (Fig. 3.3). For all cases, final radius (HH21) was recorded before deflation (r') and after deflation (r). Elastic stretch was calculated as the ratio of inflated to deflated radius at each stage, $\lambda^*_{\Theta,i} = R'/R$ at HH17 and $\lambda^*_{\Theta,f} = r'/r$ at HH21. Using the average value of $\bar{\lambda}^*_{\Theta,i}$ to represent all experimental groups (before perturbation), circumferential growth was estimated as $G_\Theta = r/R \approx \bar{\lambda}_{\Theta,i}(r/R')$. (Overbar denotes group average.) These relationships are further described in Fig. 3.4.

Deflated wall thickness (H at HH17, h at HH21) was also measured in the lateral DMB (top of OCT image in Figs. 3.4), where image quality was maintained at late stages. Since elastic deformation was too small to be detected in the thickness direction, average radial growth was estimated as $\bar{G}_R = \bar{h}/\bar{H}$. To estimate hemisphere growth, the same technique was applied, replacing DMB radius with equivalent hemisphere radius, calculated from arclengths shown in Fig. 3.3.

3.4.4 Computational methods

Finite element models were created in ABAQUS Standard (v6.10, SIMULIA, Providence, RI) using C3D20R elements (20-node hexagonal elements with reduced integration). For models of hemisphere division, the initial, unloaded geometry was based on OCT images of the deflated secondary prosencephalon at HH17. As shown in Fig. 3.5A, this consists of a spherical telencephalon of inner radius $R_T = 3H$, a conical hypothalamus defined such that the total dorsal-ventral length $L = 4R_T$, and a caudal portion extending straight ($3H$ long) to represent the boundary connecting secondary prosencephalon to diencephalon. To reduce computational time, only the left half of the brain was simulated, with symmetry conditions applied at the midline, and the caudal end was constrained with a roller boundary condition. The model contained 4 elements across the thickness, for a total of 12448 elements.

A normal eCSF pressure of $p = 15$ Pa was applied along the inner wall based on measured results. BDX cases were modeled by applying a 40% increase in pressure ($p = 21$ Pa) according to (Alonso et al., 1998), and intubated cases were modeled without pressure ($p = 0$ Pa). The conical hypothalamus and its caudal extension are constrained by an external elastic foundation. Here we assumed a spring stiffness per unit area of $k/A = 1.7$ Pa/micron

(for a 300μm-thick layer of external tissue, $\mu_{ext} \approx 0.35\mu$). This value is reasonable if we consider surrounding tissues as a composite, with prospective eye neuroepithelium (μ similar to that of the brain tube (Oltean et al., 2016)) filling approximately one third of the space (Fig. 3.1D) and mesenchyme (extremely low μ) filling the rest. Shear modulus of other tissues, such as the myocardium and cardiac jelly of the developing heart, have been reported as low as 0.34μ and 0.07μ, respectively (Zamir et al., 2003).

To simulate growth in ABAQUS, we implemented a custom user subroutine based on the UMAT generator developed by Young et al. (2010). Based on the theory for volumetric growth (Rodriguez et al., 1994), we decompose the 3D deformation gradient tensor into $\mathbf{F} = \mathbf{F}^* \cdot \mathbf{G}$, where $\mathbf{G}$ represents the 3D growth tensor and $\mathbf{F}^*$ represents the 3D elastic deformation gradient tensor. We assume transversely isotropic growth such that

$$\mathbf{G} = G_R \mathbf{e}_R \mathbf{e}_R + G\mathbf{e}_\Theta \mathbf{e}_\Theta + G\mathbf{e}_\Phi \mathbf{e}_\Phi \tag{3.11}$$

where $\mathbf{e}_i$ represent unit base vectors in the initial configuration. The Cauchy stress tensor, $\boldsymbol{\sigma}$ depends on $\mathbf{F}^*$ according to

$$\boldsymbol{\sigma} = J^{*-1}\mathbf{F}^* \cdot \frac{\partial W}{\partial \mathbf{F}^{*T}} \tag{3.12}$$

where $J^* = \det \mathbf{F}^*$ is the elastic volume ratio and T denotes the transpose. Morphogen- and stress-dependent growth was defined according to Eq. 3.1.

Based on past measurements in the chick brain tube (Xu et al., 2010a), we define the neuroepithelial wall as a nearly incompressible hyperelastic material with with shear modulus, $\mu = 300$ Pa, and bulk modulus, $\kappa = 100\mu$. Here we use a modified neo Hookean strain

energy density of the form

$$W = \frac{\mu}{2}(\bar{I}_1^* - 3) + \kappa \left[\frac{1}{2}(J^{*2} - 1) - \ln J^*\right] \tag{3.13}$$

where $\bar{I}_1^* = J^{*-2/3}\ \mathrm{tr}(\mathbf{F}^{*T} \cdot \mathbf{F}^*)$ is the first strain invariant. To approximate observed constriction between secondary prosencephalon and diencephalon and improve model convergence, the caudal end was stiffened such that $\mu = 1.8$ kPa.

3.4.5 Pressure measurement

Lumen pressure was measured with a micropipette connected to a pressure transducer adapted from Jelinek and Pexieder (1968). Briefly, borosilicate glass micropipettes were pulled to an internal diameter greater than 80μm with a 30° beveled tip and connected via polyethylene tubing (BD; 427440) to a differential pressure transducer (Honeywell; CPCL04DFC). A signal conditioner (Omega; DMD4059-DC) was used to amplify the transducer signal and a data acquisition module (National Instruments; USB-6009) and a custom LabVIEW program was used to record voltage over time. The transducer was calibrated using a water manometer and all data was processed in MATLAB.

At HH17 or 21, chicken embryos were extracted and transferred to a phosphate buffered saline (PBS) filled petri dish. Micropipettes and tubing were backfilled with PBS to match the osmolality of chick cerebrospinal fluid (Alonso et al., 1998). A baseline voltage was recorded for at least 5 minutes and then the micropipette was inserted into the hindbrain and data was recorded for at least 5 minutes before being removed. Pressure values were calculated as the mean pressure over at least the first 3 minutes after insertion.

3.4.6 Statistics

Analysis of Variance (ANOVA) with post hoc Tukey test was used to compare data between more than two groups, and student t-test was used to compare data between two groups. Ratio data was log transformed to ensure normal distributions. For all tests, $p<0.05$ was considered to be significant. All error bars denote standard deviation.

3.5 Addendum

Additional computational methods: HH13–HH17 model For models of earlier telencephalon growth (HH13 to HH17), geometry was adjusted to $L = 3R_T$ and a caudal extension $2H$ long. Furthermore, initial roof plate thickness was decreased by half to better approximate true roof plate thickness. To account for the relatively large prospective eyes at this stage, which cover a greater extent of the secondary prosencephalon, elastic foundation was also applied to the lower portion of the spherical telencephalon in the younger model. This HH13-17 model contained 5 elements across the thickness, for a total of 10875 elements.

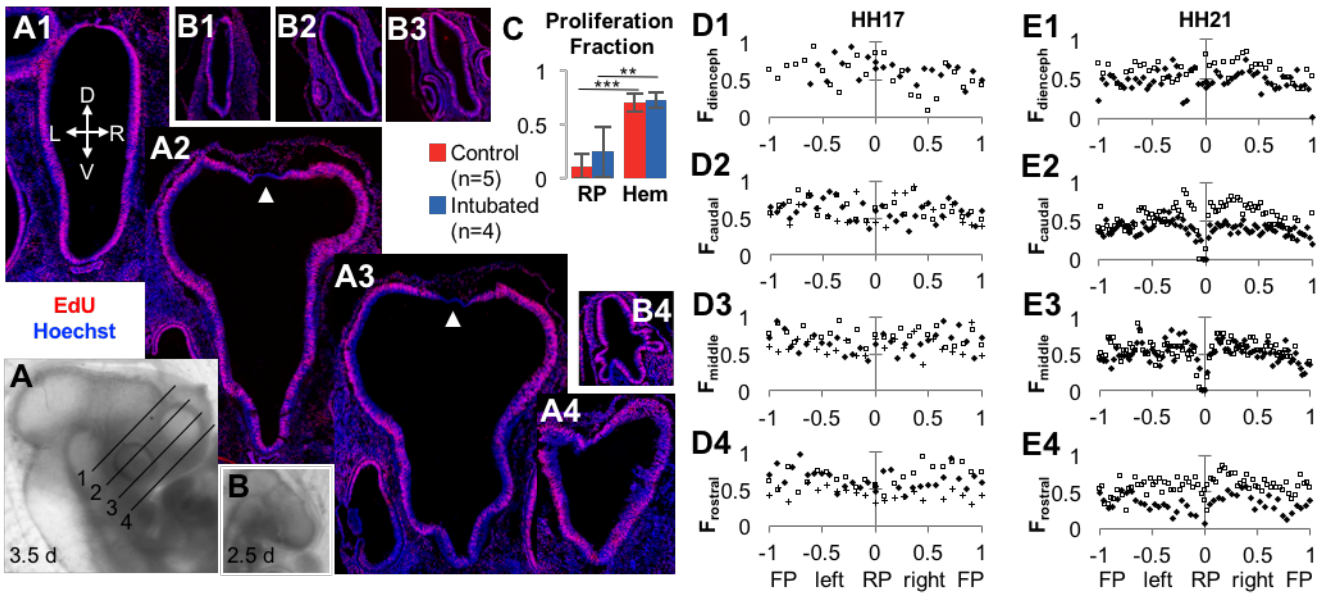

Figure 3.11: Proliferation is only decreased in the telencephalic roof plate at HH21. (A) At 3.5 days of development (HH21), hemispheres are clearly visible in the chick telencephalon. (A1-A4) Cross-sections are shown from rostral to caudal end of the telencephalon, corresponding to slices 1-4 in (A). Proliferating nuclei (red) were labeled with EdU (cells undergoing S-phase during a 4-hour pulse), and all nuclei were labeled with Hoechst33342 (blue). White arrowheads denote roof plate (RP) region with decreased proliferation. (B) For comparison, hemispheres are note yet visible at 2.5 days (HH17). (B1-B4) Cross-sections corresponding to slices 1-4 at 2.5 days. Note that proliferation remains high throughout the RP during these stages. (C) Quantitative comparison of proliferation fraction in the RP and lateral hemisphere at 3.5d for control (n=5) and intubated (n=4) embryos. (D1-D4) At 2.5 days, the fraction of proliferating cells is approximately uniform across the neuroepithelial wall for all slices analyzed. Each data point represents the fraction of proliferating cells in a region covering 60 microns along the circumference of the wall. (E1-E4) At 3.5 days, the fraction of proliferating cells decreases sharply at the RP in caudal (E2), middle (E3) and rostral (E4) regions. Diamond denotes measurement from sample shown in (A1-B4), square denotes measurement from second sample, and '+' denotes measurement from third sample if applicable. Total circumference is normalized for each sample such that the RP corresponds to x=0, moving clockwise to the right hemisphere corresponds to x¿0, moving counter-clockwise to the left hemisphere corresponds to x<0, and x=1 or x=-1 corresponds to the floor plate (FP). All images to scale, scale bar is 500 microns.

Chapter 4

Dynamic patterns of cortical expansion during folding of the preterm human brain[4]

Summary During the third trimester of human brain development, the cerebral cortex undergoes dramatic surface expansion and folding. Physical models suggest that relatively rapid growth of the cortical gray matter helps drive this folding, and structural data suggests that growth may vary in both space (by region on the cortical surface) and time. In this study, we propose a new method to estimate local growth from sequential cortical reconstructions. Using anatomically-constrained Multimodal Surface Matching (aMSM), we obtain accurate, physically-guided point correspondence between younger and older cortical reconstructions of the same individual. From each pair of surfaces, we calculate continuous, smooth maps of cortical expansion with unprecedented precision. By considering 30 preterm infants scanned

[4]Magnetic resonance imaging data in this study was collected, processed, and reconstructed by the Washington University Neonatal Development Research group, and section 4.4.1 was drafted by Dimitrios Alexopoulos, Christopher Smyser, and Cynthia Rogers. Philip Bayly helped design the experiments. Philip Bayly, Emma Robinson, Larry Taber, Donna Dierker, Matt Glasser, Tim Coalson, and Daniel Rueckert contributed to methods. Christopher Smyser, Cynthia Rogers, Cynthia Ortinau, and David Van Essen helped interpret results. All edited the manuscript.

2-4 times during the period of rapid cortical expansion (28 to 38 weeks postmenstrual age), we observe significant regional differences in growth across the cortical surface that are consistent with the emergence of new folds. Furthermore, these growth patterns shift over the course of development, with non-injured subjects following a highly consistent trajectory. This information provides a detailed picture of dynamic changes in cortical growth, connecting what is known about patterns of development at the microscopic (cellular) and macroscopic (folding) scales. Since our method provides specific growth maps for individual brains, we are also able to detect alterations due to injury. This fully-automated surface analysis, based on tools freely available to the brain mapping community, may also serve as a useful approach for future studies of abnormal growth due to genetic disorders, injury, or other environmental variables.

4.1 Introduction

During the final weeks of fetal or preterm development, the human brain undergoes crucial changes in connectivity and cellular maturation (Ball et al., 2014; Mukherjee et al., 2005). The cerebral cortex also rapidly increases in surface area, coinciding with the formation of complex folds (Fig. 4.1). Physical simulations suggest that cortical folding may result from mechanical instability, as the outer gray matter grows faster than underlying white matter (Bayly et al., 2013; Tallinen et al., 2016). Such models accurately predict stress patterns within folds and explain abnormal folding conditions such as polymicrogyria and pachygyria. However, even recent models that consider uniform cortical growth on a realistic brain geometry do not accurately reproduce the conserved (primary) patterns of folding observed in the human brain (Tallinen et al., 2016). This discrepancy suggests a role for

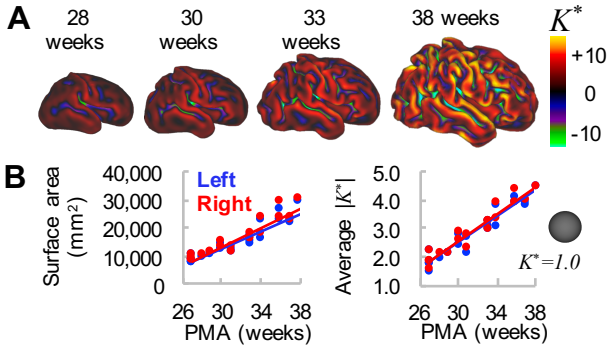

Figure 4.1: Global measures of cortical surface area and folding increase over time. (A) Cortical mid-thickness surfaces for individual hemisphere at 28, 30, 33, and 38 weeks PMA. Color overlay represents non-dimensional curvature, K^*, a useful metric of the degree of folding. (B) Total cortical surface area (left) and average magnitude of K^* (right) increase with time. However, these global measures do not provide information about regional variations in maturation and morphology.

other hypothesized factors such as axon tension in white matter (Van Essen, 1997), regional differences in material properties, or regional differences in growth (Toro and Burnod, 2005).

Advances in magnetic resonance imaging (MRI) and cortical reconstruction have enabled detailed quantification of brain structure and connectivity during brain development (Dubois et al., 2007; Shimony et al., 2016; Glasser et al., 2016a). Nonetheless, measuring patterns of physical growth over time presents a unique challenge, requiring precise identification of corresponding points between multiple scans. To date, clinical studies often rely on global measures of shape or total surface expansion (Shimony et al., 2016) despite evidence of important regional differences (Hill et al., 2010b). Primary sensory and motor regions exhibit earlier maturation and folding than other areas (Mukherjee et al., 2005; Dubois et al., 2007). Furthermore, even subtle or localized abnormalities in folding have been linked to disorders such as epilepsy, autism, and schizophrenia (Lin et al., 2006; Li et al., 2016; Hardan et al., 2004).

To attain more detailed measures of cortical growth, several groups have segmented the brain into user-delineated regions of interest (ROIs) for analysis (Moeskops et al., 2015; Lyall et al., 2014; Wang et al., 2017). However, manual definition of ROIs may introduce bias or error and typically requires labor-intensive editing. *A priori* parcellation can also lead to skewed or weakened conclusions if the true effect does not fall neatly within the assumed area.

In this study, we employ an ROI-independent approach to estimate spatiotemporal patterns of cortical growth over the course of human brain folding. Harnessing recent developments in *anatomical* Multimodal Surface Matching (aMSM) (Robinson et al., 2014, 2017), we achieve physically-guided point correspondence between cortical surfaces of the same individual across multiple time points. This was accomplished by automatically matching common features (gyri and sulci) within a spherical framework and penalizing physically unlikely (energy-expensive) deformations on the anatomical surface, an approach first described in ferret models (Knutsen et al., 2010, 2012). While alternative methods have been proposed to match anatomical surfaces (Orasanu et al., 2016; Durrleman et al., 2014), none provide MSM's flexibility in terms of data matching (Robinson et al., 2014) or utilize penalties inspired by physical behavior of brain tissue (Knutsen et al., 2010). Our approach produces smooth, regionally-varying maps of surface expansion for each subject analyzed. By considering right and left hemispheres from 30 preterm subjects, scanned at different intervals from approximately 28 to 38 weeks postmenstrual age (PMA), we observe consistent, meaningful patterns of differential growth that change over time.

This study provides a comprehensive, quantitative analysis of cortical expansion dynamics during human brain folding. We report statistically significant regional differences consistent with established patterns of cellular maturation and the emergence of new folds. These findings, which suggest that prenatal cortical growth is not uniform, may guide future studies

of regional maturation and more accurate simulations of cortical folding. Furthermore, since our tools are freely available to the neuroscience community Robinson et al. (2014); Marcus et al. (2011); Winkler et al. (2014); Glasser et al. (2016a), the approach presented here can be widely applied to future studies of development and disease progression.

4.2 Results

To visualize changes in cortical growth over the course of brain folding, we analyzed right and left hemispheres from 30 very preterm infants (born <30 weeks PMA, 15 male, 15 female) scanned 2-4 times leading up to term-equivalent (36-40 weeks PMA). Six subjects were excluded from group analysis due to injury (see Materials and Methods for criteria), but all were analyzed longitudinally for individual growth patterns.

4.2.1 aMSM produces accurate point correspondence and smooth growth estimation across the cortex of individual subjects

Multimodal Surface Matching uses a flexible spherical framework to align surfaces based on a range of available surface data (Robinson et al., 2014). As shown in Fig. 4.2, anatomical surfaces (Fig. 4.2*A*) and corresponding data (e.g., univariate patterns of curvature, Fig. 4.1*A*) are projected to a spherical surface to provide a simpler mathematical framework for registration (Fig. 4.2*B*). Spherical registration shifts points on the input sphere until data is optimally aligned with that of the reference sphere (Fig. 4.2*C*), such that reprojection onto the input anatomical surface reveals accurate point correspondence with the reference surface (Fig. 4.2*D*).

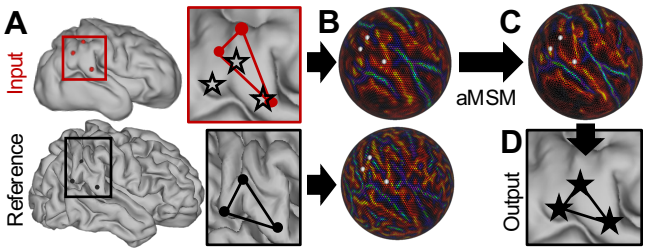

Figure 4.2: Longitudinal (intra-subject) registration with aMSM. (A) Cortical mid-thickness surfaces (ordered sets of vertices in 3D) were generated at multiple time points for each individual. After resampling to a standard mesh, vertices on the input surface (red dots) do not correspond to the same locations on the reference surface (black dots). Red and black boxes outline a region of interest, in which black stars represent plausible locations for point correspondence. (B) Mean curvatures (generated from original topologies, Fig. 4.1A), along with deformations (generated from area-normalized input and reference anatomical surfaces), are projected to a spherical framework to drive registration. (C) aMSM moves points on the input sphere in order to (1) optimize curvature matching and (2) minimize deformations between the anatomical surfaces. (D) Projection of shifted vertices reveals new anatomical locations with plausible alignment and reduced deformations.

In this study, we use mean surface curvature (K), calculated at the cortical mid-thickness, to drive initial matching. To reduce unrealistic distortions induced by both curvature matching and spherical projection, we further refine our registration to minimize physical strain energy (Eq. 4.1) between the input and reference anatomical surfaces (Robinson et al., 2017). Unlike other spherical registration methods, which reduce distortions on the sphere, this allows us to explicitly minimize deformations that are energetically unfavorable (and thus unlikely), greatly reducing artifacts associated with the spherical projection process. (See *SI Text* for examples and validation.) Local expansion can then be estimated for each individual mesh face as the ratio of older to younger surface area.

Using aMSM, we were able to obtain physically justified point correspondence and smooth maps of cortical expansion at the individual level. Figure 4.3 shows results for a representative subject at multiple developmental periods: 27 to 31 weeks, 31 to 33 weeks, 33 to 37 weeks, and directly from 31 to 37 weeks PMA. Qualitatively, plotting the same color map

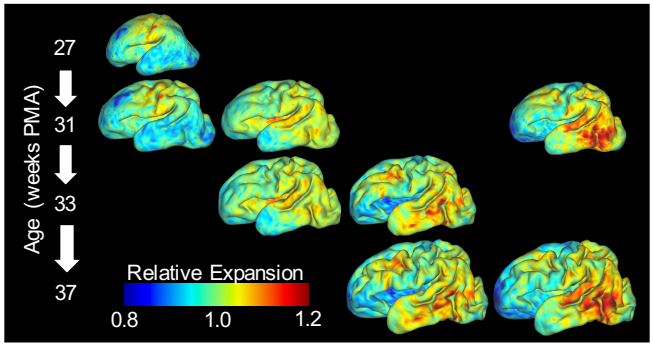

Figure 4.3: Gradients of cortical expansion are evident in individual brains. Relative cortical expansion (local surface expansion normalized by total hemisphere expansion) is shown for each developmental period. For each column, the same map is overlaid on younger (top) and older (bottom) surface to visualize point correspondence after longitudinal registration. From left to right, relative expansion is estimated for growth from 27 to 31 weeks PMA, 31 to 33 weeks PMA, 33 to 37 weeks PMA. Far right: Direct registration from 31 to 37 weeks PMA, as considered for group analysis in Fig. 4.4. True cortical expansion is equal to relative expansion (plotted) multiplied by global cortical expansion of 1.26, 1.37, 1.70, and 2.33, respectively.

on registered younger (top) and older (bottom) geometries reveals accurate point correspondence for each time period. Quantitative analysis confirmed significant improvements in curvature correlation and strain energy due to aMSM registration (Table 4.1). As illustrated in Fig. 4.3, direct registration from 31 to 37 weeks was also similar to registration from 31 to 33 then 33 to 37 weeks. (See Fig. B.5 for group-wise comparison.)

4.2.2 Spatial patterns of preterm growth are consistent across subjects and correspond to folding regions

For statistical comparisons, individuals were also registered to a 30-week atlas generated from our cohort (Fig. 4.4*A*, see *SI Text* for details). Since folding patterns (primary sulci) are similar across individuals at 30 weeks PMA (Dubois et al., 2007), and because most

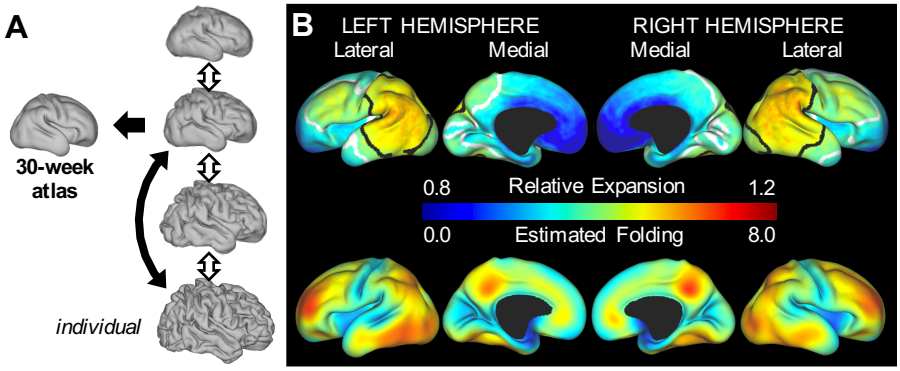

Figure 4.4: Gradients of cortical expansion and folding are consistent across subjects. (A) Correspondence between individual surfaces (closest to 30-weeks, black arrow) and the 30-week atlas was determined by aMSM registration. Using intra-subject correspondence from aMSM (double arrows), individual growth patterns from each period are registered to the 30-week atlas for inter-subject statistics. (B) For the period from 30 to 38 weeks PMA (black double arrow in A), relative area expansion (top) and regional folding (bottom) were highest in the lateral parietal-temporal-occipital region and lateral frontal lobe (n=20). Black and white contours enclose regions where relative expansion is significantly higher and lower than the global average.

subjects were scanned near 30 weeks PMA, this atlas served as an appropriate reference for group analyses. Once registration was established between 30-week individual surfaces and the 30-week atlas (inter-subject registration, black arrow in Fig. 4.4A), individual growth metrics determined by intra-subject registration were transformed to the atlas, facilitating statistical analysis across individuals and time points.

To determine whether regional differences in cortical expansion are conserved across individuals, we first considered the period from 30±1 to 38±2 weeks PMA (n=20 subjects without significant injury). Permutation Analysis of Linear Models (PALM) with threshold-free cluster enhancement (Winkler et al., 2014) revealed significantly higher cortical expansion in the lateral parietal, occipital, and temporal regions and significantly lower cortical expansion in medial and insular regions (Fig. 4.4B, top). These patterns were consistent across right and left hemispheres.

At the individual level, we observed highest cortical expansion in areas undergoing the most dramatic folding (Fig. 4.3), consistent with previous reports in ferret (Knutsen et al., 2012; Reillo et al., 2010; Kriegstein et al., 2006; Smart and McSherry, 1986). To quantify change in preterm folding, we analyzed non-dimensional mean curvature, defined as $K^* = KL$ where $L = \sqrt{SA/4\pi}$ and SA = total cortical surface area (Knutsen et al., 2012). As shown in Fig. 4.1B (right), $K^* = 1$ across a spherical surface, and the global average of $|K^*|$ increases for more convoluted surfaces. Local folding was estimated as the difference between $|K^*|$ on the older and younger surfaces after one iteration of Gaussian kernel smoothing ($\sigma = 4$ mm) on the atlas. As shown in Fig. 4.4B, regions of highest cortical folding were similar, but not identical, to those of highest cortical expansion (Pearson's correlation = 0.46 and 0.42 for left and right hemispheres).

4.2.3 Cortical growth changes regionally and dynamically during folding

From individuals with scans less than 6 weeks apart (n=27 measurements from 15 subjects), we also investigated temporal variations in regional growth. As shown in Fig. 4.5A, relative expansion initially appears highest in the early motor, somatosensory, and visual cortices, as well as the insula, but lower near term-equivalent (n=4 with four sequential scans). By contrast, relative growth appears to increase with age in lateral parietal, temporal, and frontal regions. To determine whether these dynamic shifts were statistically significant, we considered the effect of midpoint PMA (midpoint between younger and older scan PMAs) as a covariate. PALM revealed mean spatial patterns (Fig. 4.5B left, mean PMA=33 weeks) similar to those for 30 to 38 weeks (Fig. 4.4B, mean PMA=34 weeks). Importantly, temporal analysis revealed significant decreases in relative expansion of the insula and early motor,

somatosensory, and visual cortices (initially fast-expanding regions slow over time relative to other regions), as well as increases in the lateral temporal lobe (Fig. 4.5*B*).

We also examined dynamic changes in terms of *growth rate*, defined as local percent increase in cortical area per week. By plotting vertex values versus midpoint PMA (Fig. 4.6*A*), we quantified the rate and acceleration of cortical growth at specific locations over time. For non-injured individuals (blue and red dots), growth rates were generally higher at younger ages. Note that growth decelerates significantly (p¡0.05) in the initially fast-growing primary cortices (3, 8, 9) and insula (7), but it remains fairly constant in frontal (1-2, 10), temporal (6) and lateral parietal-occipital (4-5) vertices. Linear fit and statistics are available in Table 4.2.

4.2.4 Local growth estimation detects abnormalities associated with preterm injury

Since our technique produces continuous estimates of cortical growth for individual subjects, we also analyzed cortical surfaces of infants identified to have grade III/IV IVH and/or ventriculomegaly during their Neonatal Intensive Care Unit course (n=6). For illustration, Fig. 4.6*B* compares a subject with no injury (same subject as Fig. 4.3) to one diagnosed with bilateral grade III/IV IVH. Reduction in growth rate is particularly evident in the temporal and occipital lobes of the subject with IVH (Fig. 4.6*B*, middle). We also note that growth rate 'recovered' to near non-injured levels during the period from 34 to 38 weeks PMA in this individual (Fig. 4.6*B*, bottom, and black open stars in Fig. 4.6*A*).

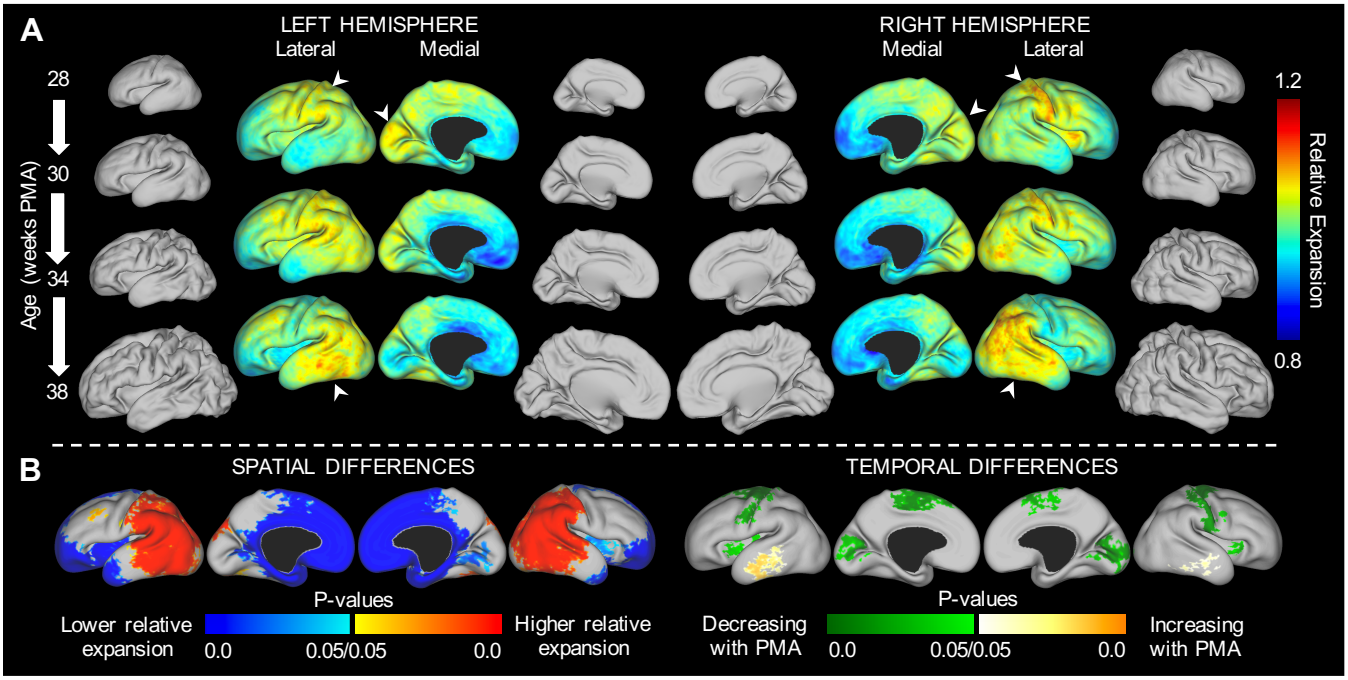

Figure 4.5: **Regions of highest cortical expansion change over time.** (*A*) Maps of average relative expansion are shown for brief windows of development, denoted on left. For subjects in which three distinct periods of growth could be measured (n=4), regions of maximum expansion (white arrowheads) appear to shift over time. For illustration, average mid-thickness surfaces are also shown to scale for each time point. (*B*) Regions of statistically significant differences relative to global growth were observed based on 27 growth measurements (15 subjects) over the third trimester equivalent (temporal resolution <6 weeks, mean PMA=33 weeks). Left: Relative expansion is higher in the lateral parietal, temporal, occipital and frontal regions (red) and lower in the medial frontal and insular regions (blue). Right: Relative expansion in the primary motor, sensory, and visual cortices, as well as in the insula, decreases over time (green). By contrast, relative expansion increases in the temporal lobe over time (yellow).

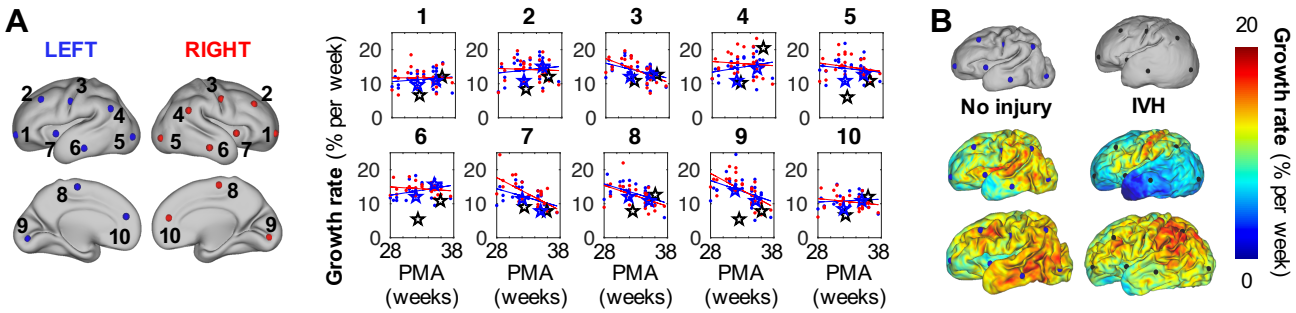

Figure 4.6: Growth rate decreases in initially fast-growing cortical areas. (*A*) To quantify changes over time, local growth rates (n=27 measurements from 15 non-injured subjects) are plotted against midpoint PMA at ten vertices on left (blue) and right (red) hemispheres. Growth rate decreases with PMA at vertices 3, 8, and 9 (early motor, somatosensory, and visual cortices) and 7 (insula). By contrast, vertices 1-2, 4-6 and 10 remain relatively constant. (*B*) Individual growth rates were also compared between a non-injured subject (left) and a subject with bilateral grade III/IV intraventricular hemorrhage (IVH, right). From top to bottom, surfaces are shown at approximately 30 weeks, 34 weeks, and 38 weeks PMA. Growth rate from 30 to 34 weeks is plotted on the 34-week surface, and growth rate from 34 to 38 weeks is plotted on 38-week surface. For the subject with IVH, growth rate is initially reduced in occipital (5, 9) and temporal (6) lobes, but later recovers to near non-injured levels. Rates at locations 1-10 in these specific individuals are denoted in (*A*) by blue stars (no injury) or black stars (IVH).

4.3 Discussion

In this work, we implemented an automated, quantitative method for analyzing regional growth in longitudinal studies of cortical maturation. Individual registration with aMSM not only produced accurate alignment of gyri and sulci, but it also effectively minimized distortions on the cortical surface (Fig. 4.3, Table 4.1). This shift in focus – regularizing the physical anatomical mesh instead of the abstract spherical mesh – offers a significant improvement for longitudinal registration using spherical techniques, which have been plagued by artifactual deformations that obscure real trends and limit interpretation of cortical growth maps (Robinson et al., 2017). Furthermore, our mechanics-inspired regularization penalty (strain energy density, Eq. 4.1) is physically justified for longitudinal registration and has been shown to outperform other mathematical approaches (Robinson et al., 2017).

Other registration techniques have been proposed to control distortion via spectral matching or varifolds (Orasanu et al., 2016; Durrleman et al., 2014), but they have not been integrated into widely-used analysis pipelines Glasser et al. (2013, 2016b,a) or produced smooth, meaningful maps of cortical surface expansion. By contrast, spherical registration provides an efficient, versatile framework for inter- and intra-subject analysis based on a variety of imaging modalities Robinson et al. (2014); Tong et al. (2017). While this study matched curvatures, an intrinsic feature of any cortical reconstruction, MSM allows registration based on multimodal data, which may further improve the accuracy of registration (Glasser et al., 2016a). Future studies may exploit additional data, such as myelin content and fMRI contrasts, to establish or improve correspondence.

The current approach provides continuous maps of local expansion for each individual, enabling continuous statistical analysis across the surface. Without the limitations of ROIs

(Moeskops et al., 2015; Lyall et al., 2014; Wang et al., 2017), spatiotemporal trends presented here offer new insight into the trajectory of cortical growth and maturation. In many respects, these patterns are consistent with past literature: Diffusion tensor imaging and histological analyses have reported mature dendritic branching in the primary motor and sensory cortices before the visual cortex, which in turn matures earlier than the frontal cortex Mukherjee et al. (2005); Ball et al. (2014). Similar patterns have been reported for regional folding in the preterm brain Dubois et al. (2007). The dynamic measures of cortical surface expansion reported here offer a bridge between these metrics, supporting the idea that biological processes (neuronal migration and dendritic branching) contribute to physical expansion of the cortex (constrained regional growth), which leads to mechanical instability and folding in different areas at different times.

As shown in Fig. 4.7, the patterns we report for preterm growth (third trimester equivalent) may also link existing studies of cortical growth during the late second trimester and childhood. A volumetric study of fetal MRIs found maximum cortical growth at the central sulcus, which increased between 20-24 weeks and 24-28 weeks, as well as above-average growth near the insula, cingulate, and orbital sulcus (Rajagopalan et al., 2011). Similarly, we observe a trajectory in which the area of maximum growth migrates outward from the central sulcus at 28-30 weeks (Fig. 4.7A, top) toward the parietal then temporal and frontal lobes while dissipating from the medial occipital lobe (Fig. 4.7C). As shown in Fig. 4.7B, this is generally consistent with reported patterns of postnatal expansion (term to adult in human, also proposed for human evolution) (Hill et al., 2010b).

One limitation of our study is the use of preterm infant data rather than fetal scans. With the advent of improved motion correction tools (Kuklisova-Murgasova et al., 2012), fetal scans have become feasible and may reveal faster or different growth patterns Clouchoux et al.

(2012). Though our results appear consistent with second trimester and postnatal trends, future studies should assess potential differences in preterm versus healthy growth as *in utero* longitudinal scans become available with sufficient temporal resolution. Furthermore, the current approach may not fully characterize within-fold differences, such as gyri-specific growth (de Juan Romero et al., 2015); higher resolution matching data may be needed to resolve growth patterns at subgyral scales.

We also note some conflicting results with past studies using manually-defined ROIs. For example, a recent study of preterm infants (30 weeks PMA to term-equivalent) analyzed growth by dividing the brain into its major lobes (Moeskops et al., 2015). Authors reported high expansion in the parietal and occipital lobes, in agreement with our results, but low expansion in the temporal lobe. We speculate that this discrepancy stems from inclusion of the insula and medial temporal surface in their temporal lobe ROI. Relatively low expansion of these regions (Fig. 4.4*B*) may be sufficient to 'cancel out' the high expansion we observed in the lateral temporal region. Another recent study used ROIs to relate regional surface expansion and cellular maturation in the developing rhesus macaque brain (Wang et al., 2017). This ROI analysis did not reveal a clear relationship, whereas our current approach in human (Fig. 4.6) (Mukherjee et al., 2005; Ball et al., 2014) and ferret (Knutsen et al., 2012) suggests a connection between the two. We speculate that *a priori* definition of ROIs may diminish the ability to detect such relationships.

Finally, we note that, for infants with high-grade IVH and/or ventriculomegaly, our analysis was able to clearly detect alterations in local growth. Fig. 4.6*B* provides an example of grade III/IV IVH, where abnormal folding is evident at all time points. However, as illustrated in Fig. 4.4*B*, folding may not serve as a perfect representation of underlying growth. Our method revealed reduced growth rate in specific regions, followed by recovery

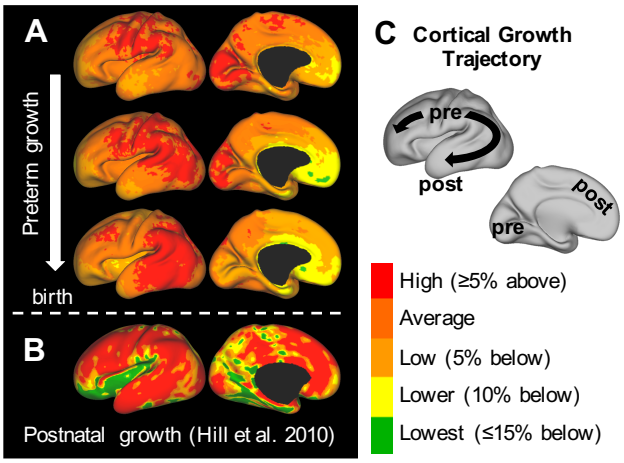

Figure 4.7: Trajectory of preterm growth may continue after term. (*A*) We observe that regions of highest expansion ('hot spots') migrate smoothly from the central sulcus and nearby regions (top) into parietal (middle) then, finally, frontal and temporal regions (bottom). Growth slows gradually in the primary visual cortex. (*B*) Reported postnatal trends appear to continue this trajectory, maintaining high growth in the parietal, temporal and frontal lobes (Hill et al., 2010b). Expansion is lowest in the insula and visual cortex after birth (though still a minimum of two-fold, adapted from Fig. 1 of ref. (Hill et al., 2010b)). (*C*) Schematic illustrating the trajectory of the maximum growth region from primary motor, sensory and visual cortices areas highly conserved across species and critical for basic survival into regions highly developed in humans, particularly after birth. pre = prenatal/preterm, post = postnatal.

to near-normal levels. These areas and effects would be difficult to pinpoint with global measures, or even local measures of folding. Just as we were able to detect subtle differences in preterm growth, future studies may apply this approach to detect differences related to specific injury mechanisms, genetic disorders, or environmental variables.

4.4 Methods

4.4.1 Recruitment, MRI acquisition and surface generation

Preterm infants in this study were born at <30 weeks gestation and were recruited from St Louis Childrens Hospital. The Washington University Institutional Review Board approved all procedures related to the study, and parents or legal guardians provided informed, written consent. Images were obtained using a turbo spin echo T2-weighted sequence (repetition time = 8,500 milliseconds; echo time = 160 milliseconds; voxel size = 1 x 1 x 1 mm^3) on a Siemens (Erlangen, Germany) 3T Trio scanner. T2-weighted images were processed, and cortical segmentations were generated at the mid-thickness of the cortex using previously documented methods (Hill et al., 2010a). These segmentations were then used to generate cortical surface reconstructions, including mid-thickness and spherical surfaces, for each hemisphere using methods previously reported (Hill et al., 2010a).

Preterm infants with moderate to severe cerebellar hemorrhage, grade III/IV IVH, cystic periventricular leukomalacia or ventriculomegaly on MRI were identified and analyzed separately (Inder et al., 2005; Kidokoro et al., 2014). Clinical and demographic information for included and excluded subjects can be found in Table 4.3. Three out of 26 included subjects exhibited non-cystic white matter injuries. These details, as well as PMA for each individual scan, can be found in Table 4.4.

4.4.2 Longitudinal surface alignment and theory

To obtain point correspondence across time, individual surfaces ('input' and 'reference') were projected to a sphere and registered with aMSM (Robinson et al., 2017) (Fig. 4.2). This tool systematically moves points on the input spherical surface in order to maximize similarity of a specified metric and minimize strain energy between the *anatomical* input and reference surfaces. Mean curvatures, generated in Connectome Workbench (Marcus et al., 2011), were used for matching data and cortical mid-thickness surfaces, rescaled to the same total surface area, were used as the anatomical input and reference surfaces.

Inspired by studies that have modeled brain tissue as a hyperelastic material (Bayly et al., 2013; Tallinen et al., 2016; Xu et al., 2010b; Toro and Burnod, 2005), we define surface strain energy as:

$$W = \frac{\mu}{2}(R + \frac{1}{R} - 2) + \frac{\kappa}{2}(J + \frac{1}{J} - 2), \tag{4.1}$$

where $R = \lambda_1/\lambda_2$ represents change in shape, $J = \lambda_1\lambda_2$ represents change in size, and λ_1 and λ_2 represent in-plane anatomical stretches in the maximum and minimum principal directions, respectively. This form corresponds to a modified, compressible Neo-hookean material in 2D, and here we define bulk modulus, κ, to be 10 times greater than shear modulus, μ. To prevent bias associated with the direction of registration (Reuter et al., 2012), average results were calculated for aMSM registration performed from both older to younger and younger to older surfaces (Fig. B.3). Additional details on theory and implementation of aMSM, as well as parameter effects of bulk-to-shear ratio, are described in *SI Text* and (Robinson et al., 2017). Other parameter effects have been described previously (Robinson et al., 2017, 2014).

4.4.3 Group statistics

To analyze trends in growth, individual metric maps were compared on the 30-week group atlas by applying point correspondences described in Fig. 4.4. Atlas generation details can be found in *SI Text*. Individual-to-atlas alignment was accomplished with aMSM, using one surface from each individual as input (time point closest to 30 weeks PMA). PALM was performed with threshold-free cluster enhancement (TFCE) (Winkler et al., 2014), using 1000 iterations and a medial wall mask. Single group t-tests were performed on the log transform of relative surface expansion to obtain a normally distributed metric centered at zero. Atlas mid-thickness surfaces and vertex areas were used for TFCE surface area computations.

Significance of correlations was assessed using Pearson's correlation coefficient, and total strain energy was calculated by integrating Eq. 4.1 with respect to cortical surface area (MATLAB, The MathWorks, Inc., Natick, MA) (Knutsen et al., 2010). Significant improvements due to aMSM were assessed by comparing total correlation and energy values before and after registration with paired t-tests (Table 4.1).

4.5 Addendum

Table 4.1: Statistical improvements due to aMSM alignment (n = 10 for each column)

Weeks (PMA):	28 to 30	30 to 34	34 to 38	30 to 38
P before (affine registration)	0.31 ± 0.09	0.32 ± 0.07	0.27 ± 0.13	0.14 ± 0.08
P after (aMSM registration)	0.70 ± 0.14	0.81 ± 0.06	0.87 ± 0.03	0.68 ± 0.08
$E/\mu A$ before (affine registration)	1.92 ± 0.45	1.83 ± 0.33	1.87 ± 0.37	3.70 ± 0.65
$E/\mu A$ after (aMSM registration)	0.59 ± 0.29	0.61 ± 0.26	0.60 ± 0.33	2.19 ± 0.58

For statistical analysis of aMSM performance, right and left hemisphere results are combined from 5 subjects scanned at all four time points (n=10 per group). This includes one injured subject (small focal hemorrhagic lesion) that was excluded from analysis of non-injured development in the main results (n=4 in Fig. 4.5A). P represents Pearson's correlation coefficient between curvatures, such that this value approaches 1 with improved alignment. $E = \int W(A)\,\mathrm{d}A$ represents total strain energy across the anatomical surface, here normalized by shear modulus (μ) and total surface area (A). Values reported as mean ± standard deviation.

Table 4.2: Linear fits for locations 1-10 in Fig. 4.6: growth rate ($\dot{g}$, % per week) versus PMA

	Description	$\dot{g}_{28,L}$	$\dot{g}_{28,R}$	$\ddot{g}_L$	$\ddot{g}_R$	P_L	P_R	p_L	p_R	L/R
1	Prefrontal (lateral)	11	12	0.14	0.00	0.15	0.00	0.449	0.995	/
2	Frontal (lateral)	13	14	0.20	-0.06	0.16	-0.05	0.436	0.806	/
3	S.-Motor (lateral)	16	17	-0.45	-0.71	-0.43	-0.57	0.026	0.002	*/**
4	Parietal (lateral)	13	17	0.31	-0.13	0.27	-0.09	0.174	0.646	/
5	Occipital (lateral)	15	16	-0.20	-0.25	-0.18	-0.22	0.377	0.275	/
6	Parietal (lateral)	12	15	0.30	-0.12	0.33	-0.18	0.088	0.376	/
7	Insula (lateral)	14	18	-0.53	-0.97	-0.50	-0.64	0.007	<0.001	**/**
8	S.-Motor (medial)	16	15	-0.57	-0.62	-0.53	-0.48	0.004	0.011	**/*
9	Visual (medial)	17	19	-0.63	-0.99	-0.41	-0.64	0.033	<0.001	*/**
10	Frontal (medial)	11	12	0.08	-0.19	0.10	-0.21	0.629	0.290	/

Labels 1-10 correspond to locations denoted in Figure 4.6B for left (L) and right (R) hemispheres. Values shown for 28-week intercept ($\dot{g}_{28}$), slope ($\ddot{g}$), Pearson's correlation coefficient, and p-value; Trend significance for L/R hemispheres denoted in rightmost column with *($p<0.05$) or **($p<0.01$).

Table 4.3: Demographic information for studied cohort (n = 30)

	No significant injury (n = 24)	Injured (n = 6)
Gestational age at birth (weeks)	27 ± 1	26 ± 2
Birth weight (g)	976 ± 226	898 ± 239
Head circumference at birth (cm)	25 ± 2	24 ± 2
Male	50% (12)	50% (3)
Caucasian	46% (11)	67% (4)
CRIB score (Bührer et al., 2000) at birth	10 ± 2	12 ± 3
Time on ventilator (hours)	24 (0-792)	1104 (24-1176)
Sepsis	16% (4)	50% (3)
Intrauterine growth restriction	13% (3)	0% (0)
Head circumference at final scan (cm)	33 ± 2	33 ± 2
PMA at final scan (weeks)	37 ± 1	37 ± 1

Above statistics are formatted to denote one of the following: mean ± standard deviation, % (n), or median (min–max). Subjects were excluded from group analysis due to: (1)* small grade IV IVH and focal cerebellar hemorrhage on left hemisphere, (2) grade IV IVH on right hemisphere, (3) grade II IVH and below average cortical surface area / delayed folding, (4)** bilateral grade IV IVH, (5) bilateral grade IV IVH, (6) left ventricular dilation. *Used in Table 4.1. **Used in Fig. 4.6*B*. (CRIB = Clinical Risk Index for Babies.)

Table 4.4: Postmenstrual age and time steps (weeks) for individual scans (n = 30)

	A	B	C	D	B-A	C-B	D-C	D-B
noninjured1	28	30	33	38	2.3	2.7	5.3	8.0
noninjured2	27	31	33	37	4.1	2.0	3.9	5.9
noninjured3	27	29	33	36	2.0	3.1	3.6	6.7
noninjured4'	27	30	34	36	2.9	4.1	2.1	6.3
noninjured5		29	32	37		3.0	5.0	8.0
noninjured6		31	33	37		2.0	4.1	6.1
noninjured7		30	34	38		4.1	3.7	7.9
noninjured8		29	33	36		4.1	2.9	7.0
noninjured9			33	37			4.7	
noninjured10			36	39			3.3	
noninjured11			35	40			4.6	
noninjured12			33	36			3.0	
noninjured13		32		39				7.0
noninjured14		29		38				8.9
noninjured15		30		38				8.4
noninjured16'		30		40				10.1
noninjured17		30		37				7.7
noninjured18		29		36				7.6
noninjured19		30		36				5.6
noninjured20		31		38				7.0
noninjured21'		29		37				8.3
noninjured22		30		35.9				5.1
noninjured23		30		40				10.0
noninjured24		32		37				4.9
injured1	27	31	34	37	3.3	3.4	3.4	6.9
injured2		31	34	38		3.4	3.6	7.0
injured3		29	33	38		4.9	4.3	9.1
injured4			35	37			2.0	

’ denotes non-cystic white matter injury in noninjured subject.

Chapter 5

Conclusions

Mechanical forces represent an often overlooked, but important, aspect of morphogenesis. Past studies have used mechanical analysis to elucidate gastrulation (Rauzi et al., 2015); heart tube formation and bending (Hosseini et al., 2017; Shi et al., 2014); gut morphogenesis (Savin et al., 2011); eye morphogenesis (Oltean et al., 2016); and lung bud formation (Kim et al., 2013). In the brain, neurulation (Chen and Brodland, 2008) and cortical folding (Toro and Burnod, 2005; Bayly et al., 2013) have also benefited from physical analysis and simulation.

In the study of cortical folding, computational models have gradually increased in sophistication (Richman et al., 1975; Toro and Burnod, 2005; Bayly et al., 2013; Tallinen et al., 2014, 2016). However, even the most complex models – starting from realistic 3D geometries of the human cortex – have failed to predict the expected folding patterns (Tallinen et al., 2016). In Chapter 4, we provide novel insights into the dynamics of human cortical growth. Since previous models only considered uniform growth across the gray matter, our finding of nonuniform growth may provide the (or, at least, one) missing link. To determine whether our measured growth patterns are sufficient to induce accurate folds, future studies should model regional growth gradients on realistic cortical geometries.

This scenario exemplifies the value of combining mechanical modeling with experimental results. For a complex case like cortical folding, multiple research groups and disciplines have worked together to (1) develop mechanical hypotheses (Richman et al., 1975; Van Essen, 1997) (2) gain insights from animal models (Reillo et al., 2010; Knutsen et al., 2010; Xu et al., 2010b; Wang et al., 2017) (3) develop simple models based on these insights (Toro and Burnod, 2005; Bayly et al., 2013; Tallinen et al., 2014), and (4) collect complex clinical data (Mukherjee et al., 2005; Shimony et al., 2016; Glasser et al., 2016a). Only by integrating all of this information can we create a model that explains normal and abnormal folding in the convoluted human brain. For the simpler cases described in Chapters 2-3, we gained valuable insights through experimental perturbations and measurements, considering the easily accessible chicken embryo as an approximation of human brain development. By iterating between models and experiments, we were able to develop and test novel hypotheses.

Building on previous research, which has suggested roles for pressure, actomyosin contraction, and differential growth in the embryonic brain, we highlighted the interplay of multiple mechanisms during embryonic morphogenesis. By analyzing initial segmentation of the forebrain into optic vesicles, diencephalon, and the telencephalon-hypothalamus complex, we discovered circumferential alignment of F-actin between segments, as well as shape changes that depends on actomyosin contraction. This discovery extended the work of Filas et al. (2012), who reported a similar mechanism between forebrain, midbrain, and hindbrain. However, by extending our analysis to HH20, we discovered the need for another mechanism, stress-dependent growth, to maintain constrictions between vesicles as the brain tube inflates and bends.

As illustrated in Fig. 2.8, understanding *how* the forebrain is shaped can inform *where* we delineate brain regions for other analyses. Similar to cell tracking or fate mapping studies,

computer simulation allows us to accurately predict the trajectory of a given cell (exposed to specific signaling patterns). This knowledge may clarify how regions develop into specific tissue types. With improvements in computational speed and 3D simulation, future studies could model development from the patterned neural plate all the way through hemisphere division. By applying a similar approach, based on physical laws and biological observations, such studies could predict other "peculiar" morphologies observed by biologists and clinicians (e.g., proboscis formation in cyclopia).

In Chapters 2-3, we highlighted the role of stress-dependent growth in the early forebrain. Past studies had suggested a role for eCSF, noting that overall brain size and proliferation are modulated by changes in pressure. Through physical and osmotic perturbations, we precisely quantified this change in growth due to pressure. By incorporating (chemo)mechanical feedback in our models, we accurately predicted normal and abnormal morphologies, including microcephaly and megalencephaly. For the first time, we also showed that low or high eCSF pressure can impede hemisphere formation, leading to morphologies like to classic or midline interhemispheric holoprosencephaly.

We also showed that, through mechanical feedback, a relatively small mechanical force can produce a large morphological change. By considering external tissues that surround the early brain tube, we offer an explanation for observed reductions in ventral proliferation. In turn, differential growth produces greater bending of the brain tube and relatively small ventral structures. By considering the compression produced by actomyosin contraction, stress-dependent growth also suggests a mechanism by which proliferation is reduced at boundaries. In turn, this differential growth deepens the sulci separating brain regions. Similar effects may exist in other organs or developmental stages. Tension has been shown to induce growth in a wide range of tissues (Wyatt et al., 2015; Streichan et al., 2014;

Chaturvedi et al., 2007; Lehoux et al., 2005; Walker et al., 2005), and mechanical feedback may even determine cell fate in some cases (Mammoto and Ingber, 2010).

> Make everything as simple as possible, but not simpler.
> – Albert Einstein

In morphogenesis, problems are inherently complicated. However, as scientists and engineers, we strive to find simple laws that may explain a range of different phenomena. In Chapter 1, we assumed a general law by which tissues can minimize stress or energy (Taber, 2009). In Chapters 2-3, we show that the same law may misguidedly increase stress under certain circumstances, producing dramatic changes in shape, i.e., morphogenesis. In Chapter 4, we used the simplified assumption of strain energy minimization (Knutsen et al., 2010) to obtain valuable estimates of differential growth in preterm infant brains. These concepts and tools may prove useful in a range future applications, including morphogenesis of other organ systems, tissue engineering, and quantification of surface growth in studies including brain development and degeneration.

Appendix A

Supplemental data on embryonic brain development

A.1 Measurement of normal growth

The embryonic BT steadily bends and grows during the stages following initial sulcus formation. To quantify regional growth over the course of development, we measured regional BT dimensions from stages HH11 to HH20 using OCT (Fig. A.1). By tracing the perimeter of the inner wall over the course of development (Fig. A.1A–B, n=6–9 embryos per group), we saw that average vesicle radii (T, D, M) increase approximately linearly with hours of development. The rate of radius increase was highest for the telencephalon-hypothalamus complex ($\dot{r}_T = 0.012$ mm/h, $R_T(40\text{h}) = 0.14 \pm 0.02$ mm), followed by the midbrain ($\dot{r}_M = 0.010$ mm/h, $R_M(40\text{h}) = 0.11 \pm 0.02$mm), and lastly the diencephalon ($\dot{r}_D = 0.008$ mm/h, $R_D(40\text{h}) = 0.12 \pm 0.01$mm). Linear correlation was highest for the midbrain region (Fig. A.1C, $R^2 = 0.95$), and for this reason the midbrain radius was used to compare growth models in subsequent analysis.

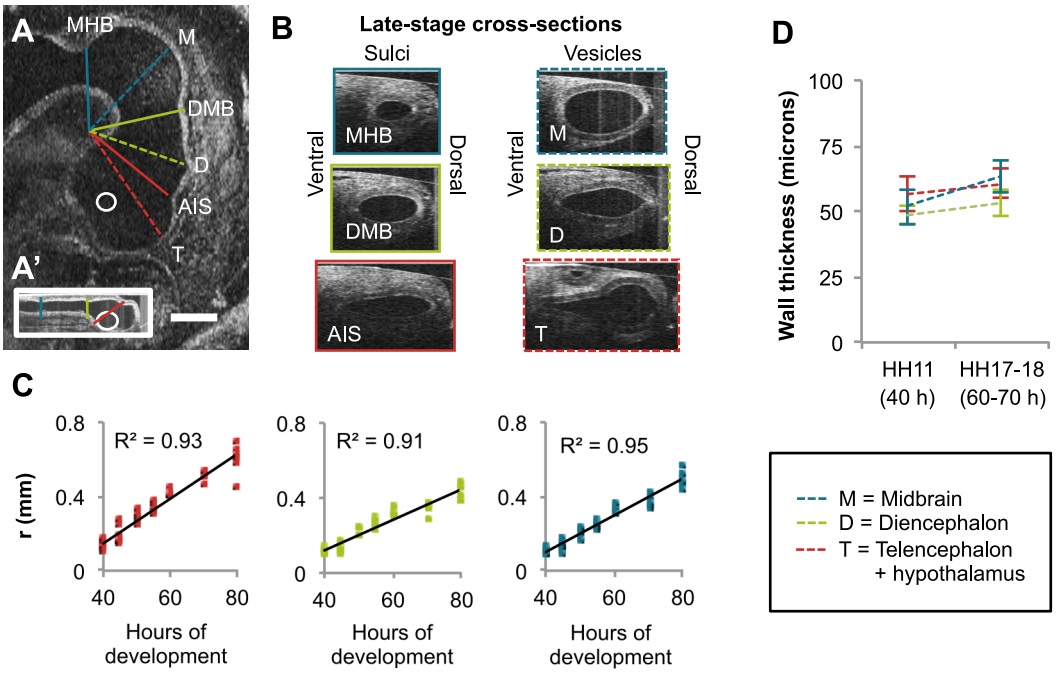

Figure A.1: Change in lumen size during development. (**A**) Sagittal OCT cross section of HH17 brain tube. Dashed lines cross through the middle of each vesicle, solid lines cross through sulci. (**A**) For comparison, sagittal cross section of a HH12 brain tube is shown to scale. (**B**) Sulci and vesicle cross sections corresponding to each line in A. (**C**) Average vesicle radius (perimeter/2π) versus time of development (HH11–20). (**D**) Average vesicle wall thickness (wall area/perimeter) at HH11 and HH17. T=telencephalon, D=diencephalon, M=midbrain, AIS=anterior intraencephalic sulcus, DMB=diencephalon-midbrain boundary sulcus, MHB=midbrain-hindbrain boundary sulcus, overlaid circle in A, A' denotes location of optic stalk. Scale bar: 0.5 mm, all images shown to scale.

Regional thickness was also estimated at HH11 (n=10) and HH17-18 (n=8). To obtain a single value for each cross section, average wall thickness was estimated as the wall area (bounded by outer and inner edges) divided by perimeter. We observe insignificant thickening of the forebrain regions (Fig. A.1D) but significant thickening of the midbrain ($P<0.001$), which could result in part from bending. Note that this increase is less than 40%, while circumference increases by 240% across the same stages.

A.2 Experiments to rule out other factors

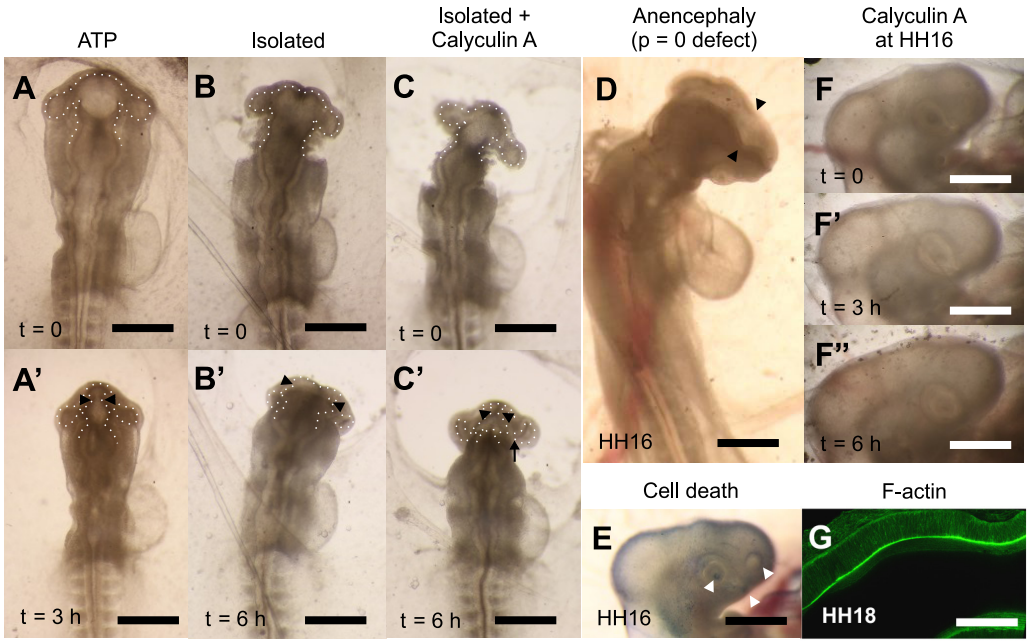

Figure A.2: Experiments to rule out external factors. (**A**–**A'**) Application of ATP produced hypercontraction after 3 h, similar to embryos cultured in calyculin A at similar stage. (**B**–**B'**) Removing external mesenchyme and membranes to isolate embryos (HH11–12) caused slight hypercontraction after 6 h culture in control media. (**C**–**C'**) However, those isolated and cultured 6 h in calyculin A exhibited strong hypercontraction (n=5), similar to non-isolated embryos. (**D**) In embryos for which the neural tube failed to close (during development in ovo), constrictions were still observed between all vesicles. (**E**) Staining for cell death (Nile blue) did not indicate cell death at brain sulci. White arrowheads indicate locations where stain is positive for cell death: lens, otic placode, and optic fissure. (**F**–**F"**) When embryos were cultured in calyculin A beyond HH14, no effect was observed, suggesting actomyosin contraction has relatively little effect on BT morphology at these stages. (**G**) F-actin remains concentrated on the apical surface of sulci and vesicles at late stages. Scale bars on brightfield images are 500 μm; scale bar on confocal image is 200 μm. Black arrowheads indicate AIS; black arrow points to maximally hyperconstricted optic stalk.

Several potential mechanisms of forebrain morphogenesis were ruled out through experiments. To consider contractile response at a shorter time scale, ATP was applied to permeabilized embryos at HH12 (n=5). To rule out effects of the surrounding mesenchyme,

several brain tubes were isolated and cultured in control media (n=3) or media containing calyculin A (n=5). Results in Fig. A.2A–C indicate that contraction is intrinsic to the neuroepithelium.

Upon extraction from the egg, we observed that brain tubes had failed to close in several embryos (n=3), producing exencephaly (open brain tube). The AIS, DMB, and MHB were still constricted in all cases, suggesting that pressure is not necessary for initial sulcus formation (Fig. A.2D). Furthermore, Nile blue stain did not indicate patterned cell death in vesicles or sulci (n=10 HH11–13 and n=11 HH16–18, Fig. A.2E). Late-stage embryos (HH14–17) were also cultured for 6 h in 30nM (n=6) or 100nM (n=5) calyculin A (Fig. A.2F–F"). No effect was observed, but confocal imaging revealed that F-actin was still present on the apical surface of sulci and vesicles at late stages (n=14 HH16–18, Fig. A.2G). These results suggest that actin structure remains intact but actomyosin contraction has little effect on BT shape at later stages.

A.3 Notochord tension

In our computational models that include cephalic flexure, the growing brain tube is constrained by a nongrowing notochord along the ventral midline. This quickly builds longitudinal tension in the notochord as it resists growth of the surrounding tissue (Fig. A.3A). To test whether this occurs in the embryo, the BT was isolated in embryos after the onset of bending (HH12–13, n=6) and the notochord was surgically cut. In all cases, the notochord sprang apart (Fig. A.3B), suggesting that it is in tension.

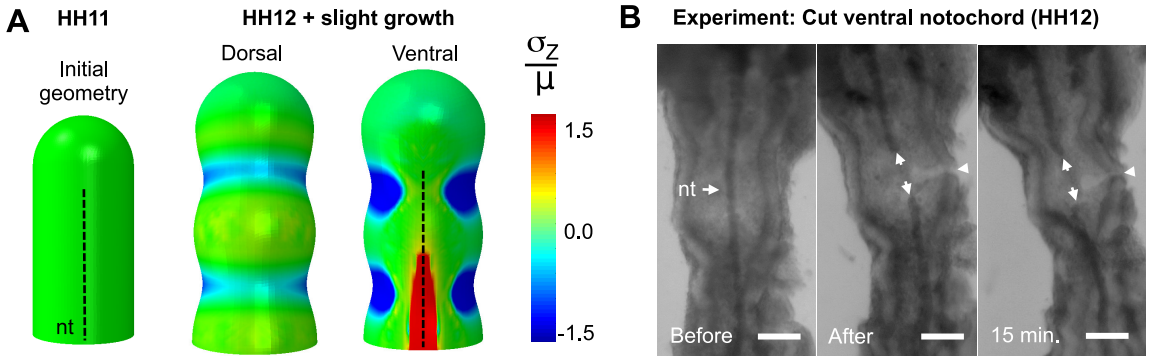

Figure A.3: Notochord tension supports constrained growth model of flexure. (**A**) When the BT model including ventral notochord (nt) is allowed to grow, longitudinal tension develops in the nongrowing notochord (HH12+). At early stages, dorsal and lateral regions are still under compression or near-zero longitudinal stress. (**B**) When the notochord is cut at similar stages, it springs apart suggesting tension (white arrows). Alternately, a cut in the lateral BT shows minimal change, suggesting relatively low stress (white arrowhead). Scale bars: 100 μm. Experimental images courtesy of Dr. Benjamen Filas.

A.4 Early measures of normal pressure

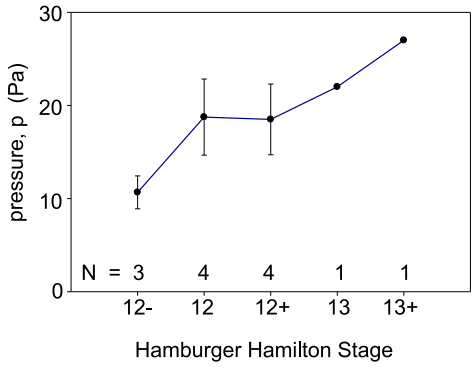

Figure A.4: Lumen pressure measurements in vivo (mean ± standard deviation). Data courtesy of Dr. Shuddahadeb Ray.

Embryonic CSF pressure was recorded using a servo-null micropressure system (model 5A, Instruments for Physiology and Medicine, San Diego, CA) as described by Chabert and Taber (2002). To measure pressure in the early brain tube (HH12–13), pipette tips were

inserted into the midbrain. Pressure measurements shown in Fig. A.4 fall within the range measured by Jelinek and Pexieder (1968).

A.5 Optic vesicle effects on brain tube morphogenesis

After initial contraction, the optic vesicles and optic stalks undergo complex morphogenesis that is outside the scope of this paper. To determine whether optic vesicles had an effect on the behavior of the BT at later stages, optic vesicles were surgically removed at the stalk (HH11–13), and the embryos were cultured for 18–24 h on a 0.3% agarose albumin gel as described by Chapman et al. (2001) for improved viability. After healing, the BT retained normal development with respect to the AIS and DMB (Fig. A.5). The hypothalamus was less compressed in these embryos (T more circular) and more closely resembled the shape of our BT model.

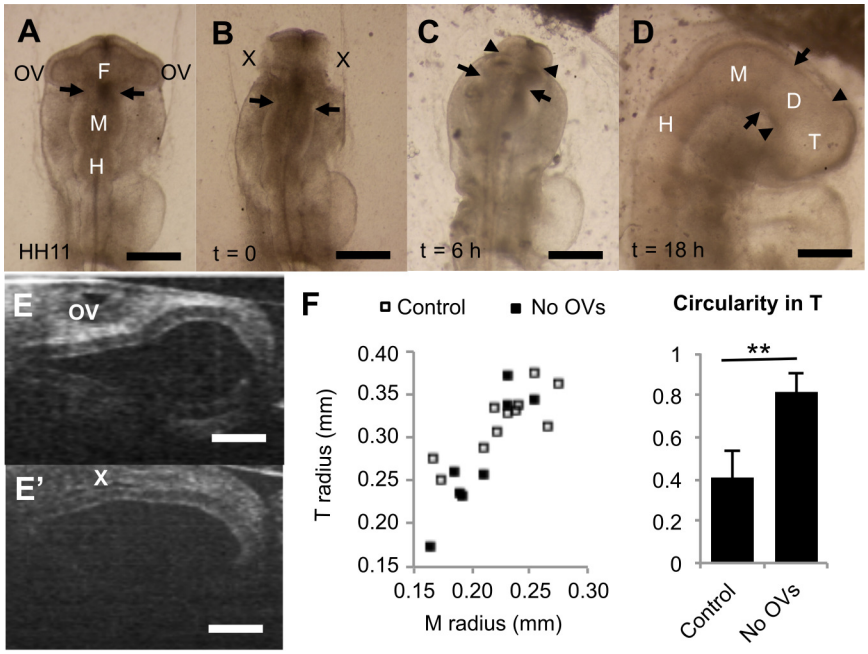

Figure A.5: Removal of OVs has minimal effect on late stage BT morphogenesis. (**A**–**D**) Representative bright field images comparing embryo before perturbation (A), after OV removal (B), after wound healing and AIS formation (C), and after BT expansion and bending (D, shown at HH15). (**E**) Representative OCT cross section of control telencephalon-hypothalamus complex (T) at HH17. (**E'**) Representative OCT cross section of T at HH17 for embryos in which OVs had been surgically removed. (**F**) Left: scatterplot of T radii versus midbrain (M) radii (HH15–17) for control (n=11, black) and experimental (n=8, white) embryos. Midbrain radius was chosen as the x-axis because it offered the closest linear correlation with stage (Fig. A.1). Right: Circularity of the lumen was significantly higher in T when the OVs were removed. A value of 1 corresponds to a perfect circle, similar to the circular cross section assumed in BT models. Scale bars: 300 μm for (A–D), 200 μm for (E). ** denotes P<0.001, X denotes absent OV.

Appendix B

Strain energy minimization with aMSM

B.1 Anatomical mesh regularization

In the original MSM algorithm (Robinson et al., 2014) flexible cortical surface registration is achieved via projection of convoluted brain surfaces to a sphere. This is a common simplification inherent to other popular spherical algorithms (e.g., FreeSurfer and Spherical Demons) (Yeo et al., 2010), and can be beneficial under some circumstances (e.g., removing the influence of cortical shape on cross subject alignments of brain function). For the case of longitudinal (intra-subject) registration, however, accurate quantification of physical distortion becomes vital. For this paper, we therefore propose anatomically-constrained MSM (aMSM, available at https://www.doc.ic.ac.uk/ ecr05/). In this modified algorithm, correspondences between surfaces are constrained by estimated distortions between the anatomical (mid-thickness) surfaces. With this process, we use the locations and spacing of anatomical

landmarks to obtain physically-reasonable deformation gradients. Though the mathematical details of our approach have been described in Robinson et al. (2017), a brief synopsis is provided below for convenience.

B.1.1 Strain energy density as an improved, higher-order regularization penalty

Soft materials like brain tissue are often modeled as hyperelastic (the relationship between loading and deformation is nonlinear) and slightly compressible (total volume can change under loading) (Knutsen et al., 2010; Chatelin et al., 2010; Bayly et al., 2013; Tallinen et al., 2016; Xu et al., 2010b). These properties can be described via a strain energy density function, such as Eq. 4.1 of the main text, which captures the effects of 2- or 3D deformations in a scalar quantity. Because strain energy density functions represent a clear physical concept (work done by deformation-producing loads), they often separate the energies produced by isochoric deformations (change in shape) and volumetric deformations (change in size). The relationship between deformation and energy for each component can be experimentally determined and associated with shear modulus (μ) and bulk modulus (κ'), for isochoric and volumetric deformations, respectively.

In this study, we seek to minimize energetically unfavorable (thus, unlikely) deformations via a physically-relevant strain energy density function, replacing the original scalar regularization penalty term in MSM. In 3D, one popular form used to describe biological soft tissues, including brain, is the classic compressible Neo-hookean model,

$$W_{3D} = \frac{\mu}{2}(\bar{I}_{1,3D} - 3) + \frac{\kappa'}{2}(J-1)^2 \tag{B.1}$$

where $I_{1,3D} = trace(\mathbf{F}_{3D}^T \cdot \mathbf{F}_{3D})$, $J = det(\mathbf{F}_{3D})$, and $\bar{I}_{1,3D} = I_{1,3D}/J^{2/3}$, and $\mathbf{F}_{3D}$ is the 3D deformation tensor. These terms are invariant with respect to coordinate transformation. $\bar{I}_{1,3D}$ can be also written in terms of the (invariant) principal stretches as $(\lambda_1^2 + \lambda_2^2 + \lambda_3^2)/(\lambda_1\lambda_2\lambda_3)$, and J_{3D} can be written as $J_{3D} = \lambda_1\lambda_2\lambda_3$.

Note that $\bar{I}_{1,3D} - 3$ is greater than zero for shape-changing ('shear') deformations but not changes in volume. Similarly, $(J_{3D} - 1)^2$ is greater than zero for size-changing ('bulk') deformations but not changes in shape. A limitation of the classic Neo-hookean form is that $(J_{3D} - 1)^2$ approaches infinity as volume increases ($J_{3D} \to \infty$) but just $\kappa'/2$ as volume decreases to zero ($J_{3D} \to 0$). To better match physical observations and improve numerical stability, this volumetric term is often modified to a form that also approaches infinity as volume decreases. Furthermore, for our surface analysis, modifications are necessary to approximate strain energy in 2D. To address both of these issues, we used the following modified, compressible 2D Neo-hookean form in our analysis:

$$W_{2D,mod} = \frac{\mu}{2}(\bar{I}_{1,2D} - 2) + \frac{\kappa}{2}(J + \frac{1}{J} - 2) \tag{B.2}$$

where $I_{1,2D} = trace(\mathbf{F}_{2D}^T \cdot \mathbf{F}_{2D})$, $J = det(\mathbf{F}_{2D}) = \lambda_1\lambda_2$, and $\bar{I}_{1,2D} = I_{1,2D}/J = (\lambda_1^2 + \lambda_2^2)/(\lambda_1\lambda_2)$. In the main text, we have rewritten $\bar{I}_{1,2D}$ as $\lambda_1/\lambda_2 + \lambda_2/\lambda_1 = R + 1/R$ for easier conceptualization. $R = \lambda_1/\lambda_2$ represents a new variable that conveniently describes change in 2D shape (e.g., aspect *R*atio). The new form of the right-hand side was chosen to (1) penalize area shrinkage and expansion similarly and (2) conceptually match the Neo-hookean function on the left-hand side (R and J are penalized using the same equation). The isochoric term, modulated by μ, now describes strain energy due to change in *surface shape*; and the volumetric term, modulated by κ, describes strain energy due to change in *surface area*.

In mechanical studies of actual brain tissue (3D), both gray and white matter have been found to behave as nearly incompressible materials ($\kappa' \geq 1000\mu$) (Chatelin et al., 2010). However, our 2D analysis requires adjustment of the 3D bulk modulus into a 2D *effective* bulk modulus (κ) based on assumptions of either 'plane stress' or 'plane strain' (Jasiuk et al., 1994). Under the assumption of plane strain, thickness of the cortex cannot deform due to in-plane forces ($\lambda_3 = 1$), and change in area relates directly to a change in volume ($\kappa \approx \kappa'$). Under the assumption of plane stress, thickness of the cortex must deform to ensure zero stress in the thickness direction; for $\kappa' \geq 1000\mu$, it can be shown that the 2D effective bulk modulus is $\kappa \approx 3\mu$ (Jasiuk et al., 1994). In reality, behavior of the cortical mid-thickness likely falls between these extremes: Cortical thickness is not rigidly constrained to prevent deformation, but cross-sectional models of folding also reveal developing stresses normal to the cortical surface (Bayly et al., 2013). Fig. B.1*B'* illustrates the effect of κ/μ on strain energy minimization throughout this range.

We also note that 2D strain energy minimization only involves in-plane surface distortions and displacements – it does not introduce changes in surface curvature or penalize bending. In shells, 3D strains are due to a combination of membrane strains (uniform across the shell thickness) and bending strains which vary across the thickness (higher on the outer curvature, lower on the inner curvature). Here, we have focused on membrane strain energy, considering the cortical mid-thickness as a rough approximation for the neutral surface (the surface at which bending strains are zero).

B.1.2 Proposed form meets requirements of a hyperelastic material.

As described in Darijani and Naghdabadi (2010), several conditions should be met for any isotropic hyperelastic material. For 2D, these requirements can be summarized - and satisfied by our proposed form - as follows:

The strain energy density function, W, must be greater than or equal to zero for all deformations. In the following proofs, it is convenient to consider the proposed strain energy density equation in terms of principal stretches. By definition, $\lambda_1 \geq \lambda_2 \geq 0$, so we must only consider $R^k \geq 0$ and $J^k \geq 0$. Since both anisotropic and areal terms in W employ the basic function, $f(x) = x + 1/x - 2$, we can simply take the first and second derivative to see that (for $x \geq 0$) the global minimum exists at $x = 1$ and $f(1) = 0$. Therefore, $W \geq 0$ for all $\lambda_1 \geq \lambda_2 \geq 0$.

The strain energy density function must be a function of either the stretch or strain invariants and invariant under all coordinate transformations. Since $J = det(\mathbf{F})$ is an invariant by definition, we must only prove that R is a function of other invariants. In 2D, recall that

$$\bar{I}_{1,2D} = trace(\mathbf{F}_{2D}^T \cdot \mathbf{F}_{2D})/J = \frac{\lambda_1}{\lambda_2} + \frac{\lambda_2}{\lambda_1} = R + \frac{1}{R} \tag{B.3}$$

By rearrangement, this can be written as $R^2 - \bar{I}_{1,2D}R + 1 = 0$. Using the quadratic formula, we see that

$$R = \frac{1}{2}(\bar{I}_{1,2D} \pm \sqrt{\bar{I}_{1,2D}^2 - 4}). \tag{B.4}$$

We take only the positive sign from $\pm$, enforcing the definition of $R = \lambda_1/\lambda_2 \geq 1$ rather than $R = \lambda_2/\lambda_1 \leq 1$.

The strain energy density function must be symmetrical with respect to the principal stretches λ_1, λ_2. The function is considered symmetrical if swapping λ_1 and λ_2 does not alter the value of W. For this and the following postulates, it is useful to rewrite $W_{2D,mod}$ in terms of principal stretches:

$$W_{2D,mod}(\lambda_1, \lambda_2) = \frac{\mu}{2}(\lambda_1^k \lambda_2^{-k} + \lambda_1^{-k}\lambda_2^k - 2) + \frac{\kappa}{2}(\lambda_1^k \lambda_2^k + \lambda_1^{-k}\lambda_2^{-k} - 2). \tag{B.5}$$

We can now see clearly that swapping λ_1 and λ_2 makes no difference (commutative property of multiplication).

The strain energy density function must equal zero at the undeformed state, $\lambda_1 = \lambda_2 = 1$.

$$W_{2D,mod}(1,1) = \frac{\mu}{2}(1+1-2) + \frac{\kappa}{2}(1+1-2) = 0 \tag{B.6}$$

To ensure a stress-free configuration at the undeformed state, the strain energy density function must be at minimum at $\lambda_1 = \lambda_2 = 1$. This is true if the following criteria are met at $\lambda_1 = \lambda_2 = 1$:

1. $\frac{\partial W}{\partial \lambda_i} = 0$

$$\frac{\partial W_{2D,mod}}{\partial \lambda_1}(\lambda_1, \lambda_2) = \frac{\mu}{2}\Big(k\lambda_1^{k-1}\lambda_2^{-k} - k\lambda_1^{-k-1}\lambda_2^k\Big) + \frac{\kappa}{2}\Big(k\lambda_1^{k-1}\lambda_2^k - k\lambda_1^{-k-1}\lambda_2^{-k}\Big) \tag{B.7}$$

$$\frac{\partial W_{2D,mod}}{\partial \lambda_1}(1,1) = \frac{\mu}{2}\Big(k-k\Big) + \frac{\kappa}{2}\Big(k-k\Big) = 0 \tag{B.8}$$

Same is true for λ_2.

2. $\frac{\partial^2 W}{\partial \lambda_i^2} > 0$

$$\frac{\partial^2 W_{2D,mod}}{\partial \lambda_1^2}(\lambda_1,\lambda_2) = \frac{\mu}{2}\Big(k(k-1)\lambda_1^{k-2}\lambda_2^{-k} + k(k+1)\lambda_1^{-k-2}\lambda_2^{k}\Big) + \frac{\kappa}{2}\Big(k(k-1)\lambda_1^{k-2}\lambda_2^{k} + k(k+1)\lambda_1^{-k-2}\lambda_2^{-k}\Big) \tag{B.9}$$

$$\frac{\partial^2 W_{2D,mod}}{\partial \lambda_1^2}(1,1) = \frac{\mu}{2}\Big(k^2-k+k^2+k\Big) + \frac{\kappa}{2}\Big(k^2-k+k^2+k\Big) = \frac{k^2}{2}(\mu+\kappa) > 0 \tag{B.10}$$

Same is true for λ_2.

3. $det(\frac{\partial^2 W}{\partial \lambda_i \partial \lambda_j}) > 0$

$$\frac{\partial^2 W_{2D,mod}}{\partial \lambda_1 \partial \lambda_1}(\lambda_1,\lambda_2) = \frac{\mu}{2}\Big(-k^2\lambda_1^{k-1}\lambda_2^{-k-1} - k^2\lambda_1^{-k-1}\lambda_2^{k-1}\Big) + \frac{\kappa}{2}\Big(k^2\lambda_1^{k-1}\lambda_2^{k-1} - k^2\lambda_1^{-k-1}\lambda_2^{-k-1}\Big) \tag{B.11}$$

$$\frac{\partial^2 W_{2D,mod}}{\partial \lambda_1 \partial \lambda_1}(1,1) = \frac{\mu}{2}\Big(-k^2-k^2\Big) + \frac{\kappa}{2}\Big(k^2+k^2\Big) = \frac{k^2}{2}(\kappa-\mu) \tag{B.12}$$

Combining the results from equations B.10 and B.12, we see that

$$det\Big(\frac{\partial^2 W_{2D,mod}}{\partial \lambda_i \partial \lambda_j}\Big)(1,1) = \frac{k^2}{2}\Big((\mu+\kappa)^2 - (\kappa-\mu)^2\Big) = k^2\mu\kappa > 0. \tag{B.13}$$

The strain energy density function must approach positive infinity as deformations approach infinity (very large λ_1 or λ_2), but also as deformations approach

the singularity case ($\lambda_1 = 0$ or $\lambda_2 = 0$).

$$\lim_{\lambda_1 \to \infty} W_{2D,mod}(\lambda_1, \lambda_2) \to \frac{\mu}{2}\Big(\infty + 0 - 2\Big) + \frac{\kappa}{2}\Big(\infty + 0 - 2\Big) \to \infty \tag{B.14}$$

$$\lim_{\lambda_1 \to 0} W_{2D,mod}(\lambda_1, \lambda_2) \to \frac{\mu}{2}\Big(0 + \infty - 2\Big) + \frac{\kappa}{2}\Big(0 + \infty - 2\Big) \to \infty \tag{B.15}$$

Same is true for λ_2.

B.1.3 Using projection to minimize anatomical deformations within a spherical framework

A procedure for minimizing anatomical deformations within a spherical framework was first described in (Knutsen et al., 2010). As in that study, here we describe 3D deformation between the younger and older anatomical surfaces with $\mathbf{F}_{3D} = \partial\mathbf{x}/\partial\mathbf{X}$, where $\mathbf{x}$ and $\mathbf{X}$ represent vertex coordinates on the older and younger anatomical surfaces, respectively. (Surface strain energy is calculated from $\mathbf{F}_{2D}$ by considering the in-plane deformation of each anatomical face.) Similarly, projection from the younger anatomical surface to its corresponding spherical surface can be described by $\mathbf{H}_{3D} = \partial\mathbf{Y}/\partial\mathbf{X}$, where $\mathbf{Y}$ represents vertex coordinates on the younger spherical surface. Projection from the older anatomical surface to its corresponding spherical surface can be described by $\mathbf{h}_{3D} = \partial\mathbf{y}/\partial\mathbf{x}$, where $\mathbf{y}$ represents vertex coordinates on the older spherical surface. Deformations on the sphere – which are typically considered in spherical registration algorithms – can be defined as $\mathbf{G}_{3D} = \partial\mathbf{y}/\partial\mathbf{Y}$. Note that a spherical deformation of $\mathbf{G}_{3D} = \mathbf{I}$ (the identity matrix, no deformation) will not correspond to $\mathbf{F}_{3D} = \mathbf{I}$ unless $\mathbf{x} = \mathbf{X}$ and $\mathbf{h}_{3D} = \mathbf{H}_{3D}$. Helpful

schematics and further mathematical description of this process are available in (Knutsen et al., 2010).

In Fig. 2 we defined the younger surface as the 'input': its vertices will be repositioned to obtain accurate point-correspondence with the older reference surface. Therefore, let us consider a second configuration, $\mathbf{Y}^*$, to represent a potential perturbation of the younger spherical surface. (Registration can also be performed in the opposite direction, which would simply reverse the terminology. We choose to denote the younger, initial surface using capital letters for consistency with standard notation of continuum mechanics.) Since $\mathbf{y}$, $\mathbf{Y}$, and $\mathbf{Y}^*$ represent coordinates on a sphere of a set radius, we switch from Cartesian coordinates (Y_1, Y_2, Y_3) to spherical coordinates (Θ, Φ, R), such that we only need to consider rotations in Θ and Φ directions ($r = R = R^*$). Shifted positions, $\Theta^* = \Theta + \Delta\Theta$ and $\Phi^* = \Phi + \Delta\Phi$, are projected as as new anatomical locations *constrained to the original anatomical surface geometry* ($\mathbf{X}^*$) using barycentric interpolation. For each potential perturbation of the spherical surface ($\mathbf{Y}^*$), an average surface strain penalty is calculated from the resulting in-plane *anatomical* deformations ($\mathbf{X}^*$ to $\mathbf{x}$) of the surrounding faces.

B.2 aMSM validation

To evaluate how aMSM performs under specific circumstances, we used simple geometries to test specific aspects of the registration technique. These served to validate aMSM under cases where the correct result is known and provided a starting point for optimization of more complex registration cases.

First, we validated the behavior of our strain energy minimization term (W) in the absence of data matching. For comparison to past work, we considered the same geometry as ref. Knutsen et al. (2010): a spherical surface that deforms into a 'pumpkin' shape according to

$$r = 1.1(R + 0.1sin(4\Theta)cos\Phi), \quad \phi = \Phi, \quad \theta = \Theta, \tag{B.16}$$

shown in Fig. B.1*A*. Note that, since curvature is uniform across the spherical surface, curvature matching is irrelevant in this example. However, the deformation produces strains that are not optimized (minimized) across the surface. Based on W, surface strains will be minimized differently depending on the input values for bulk (κ) and shear (μ) moduli.

Fig. B.1*B* (top) shows the areal (J) and shape (R) components of this initial deformation. If areal and shape changes are penalized equally in aMSM ($\kappa/\mu = 1$, bottom image), both J and R are reduced and smoothed slightly. Conversely, if areal changes are penalized more heavily ($\kappa/\mu = 10$, middle image), J becomes much smoother at the expense of higher R variability. Despite algorithmic differences between aMSM and previously described finite element approaches (Knutsen et al., 2010), both approaches produce similar results (Fig. B.1*B'*). In keeping evidence that $3 \gtrapprox \kappa/\mu \gtrapprox 1000$ in real brain tissues (Chatelin et al., 2010), we choose an intermediate value of $\kappa/\mu = 10$, which produces an intermediate behavior, throughout our analysis.

Next, we consider the efficacy of curvature matching with strain energy minimization as a regularizing term (weighted by MSM input parameter Λ) to accurately align undulations on our pumpkin surface. For this, we created a second pumpkin, shifting the deformation field in Eq. B.16 by $\Delta\Theta = \pi/8$. As illustrated in Fig. B.1*C*, this results in a surface with the same geometry as before but with misaligned vertices. The vertex denoted with a black star

is located on an outward fold ('gyrus') in the left surface but an inward fold ('sulcus') on the right surface.

As shown in Fig. B.1*E* (top), the initial configuration leads to nonzero values of strain energy density (W) and differences in curvature (Δk_{min}). For this simple case, we know that the difference between surfaces can be best described as a global affine rotation ($\Delta\Theta = \pi/8$), which results in no deformation ($W = 0$) and no differences in curvature ($\Delta k_{min} = 0$). However, since global rotation is insufficient for more complicated cases such as the folding brain, our discrete approach must be capable of producing the same alignment and deformations.

By setting regularization weight extremely high ($\Lambda \geq 10$), we approach the result of strain minimization alone (Fig. B.1E, second row). In this case, deformations and strain energy are drastically reduced, but points are not pushed toward the correct gyri and sulci (as illustrated by the remaining differences in k_{min}). Conversely, unconstrained curvature matching with very low regularization ($\Lambda \leq 0.001$) induces unrealistic deformations (Fig. B.1E, bottom row). A reasonable balance of curvature matching and strain energy minimization (optimal $\Lambda = 0.1$ for this case) achieves accurate alignment ($\Delta k_{min} = 0$, $\Delta K = 0$) and minimal distortion ($W = 0$, $J = 1$). An order of magnitude parameter sweep for the regularizing parameter, Λ, is shown in Fig. B.1*D*.

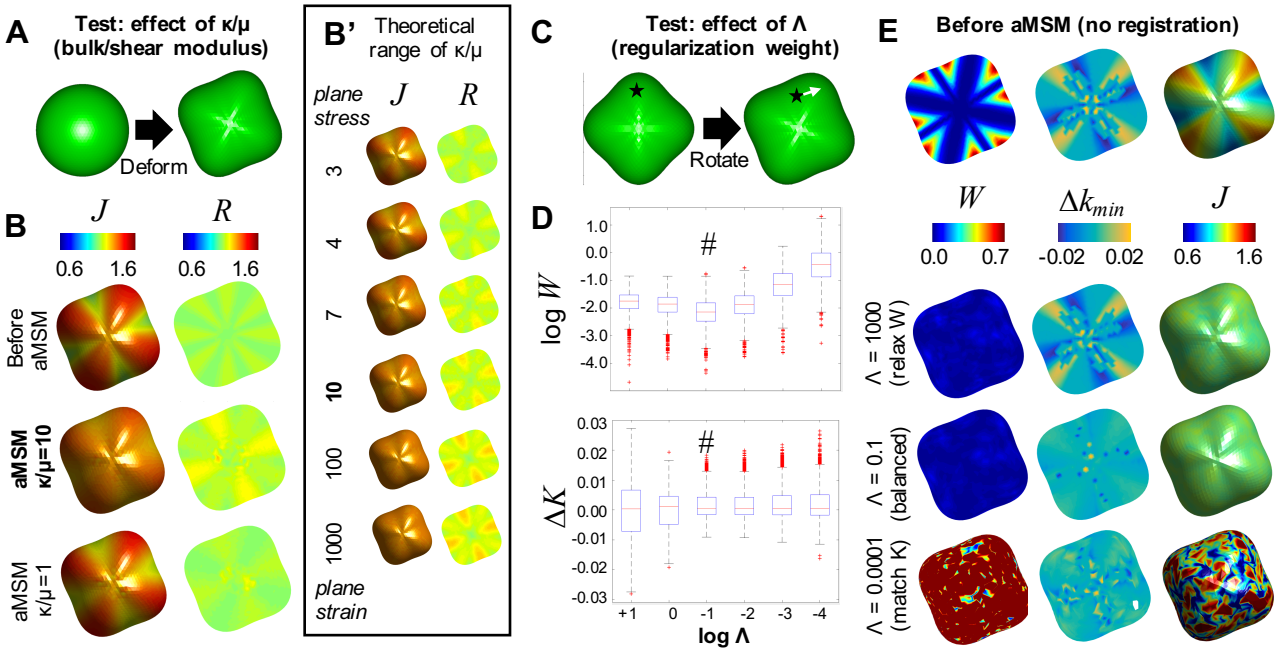

Figure B.1: aMSM parameter effects on simple undulating geometry. (A) Effect of bulk-shear ratio (κ/μ) was explored by minimizing surface strain energy between a sphere and 'pumpkin'. (B) Areal changes (J) and shape changes (R) are not minimized in the initial, mathematically-generated pumpkin shape (top). Using aMSM, equal values of κ and μ smooth both J and R moderately (bottom). By contrast, increasing κ reduces J at the expense of more variable R (top). (B') For comparison, J and R distributions for the full theoretical range of κ/μ were calculated using code modified from (Knutsen et al., 2010). (C) Effect of regularization weight (Λ) was explored by aligning a shape shifted by affine rotation. (D) Parameter sweep reveals an optimal range of Λ that minimizes both strain energy (W) and mean curvature differences (ΔK). For registration at each Λ, distribution of vertex values are represented by boxplots, with outliers denoted by red + symbols, optimal solution denoted by hashtag. (E) Distributions of strain energy, curvature differences, and J before (top) and after (bottom) registration. Solutions near the optimal Λ (middle) accurately moved points to approximate the true affine rotation solution ($W = 0$, $\Delta k_{min} = 0$, $J = 1$). Note: For illustration we show change in minimum curvature, k_{min}, which appeared most pronounced. Changes were similar for $K = 0.5(k_{min} + k_{max})$.

B.3 aMSM implementation details

For the simple case described above, we saw that an optimal value of the regularizer weight parameter, Λ, could be obtained through trial-and-error. However, optimal balance depends on both the magnitude of deformations and the magnitude of curvature differences between surfaces, which varies for different time spans and different subjects. Furthermore, in complex brain geometries, where different areas grow and fold at different rates, the optimal balance can vary spatially within each registration. This presents a new practical issue: too much regularization may prevent a subset of points from moving to the correct fold/position, but too little allows unrealistic deformations to develop.

For complex, variable geometries such as the brain, we modified our approach to perform two-step registration. First we applied the lowest acceptable regularization weight ($\Lambda = 0.01$) which consistently allows each point to reach the correct gyrus or sulcus for each time span considered in this study (such that the same parameters could be used for all time spans in this study). Then we applied a heavy regularization weight ($\Lambda = 10000$) to allow relaxation of unrealistic deformations, including those induced by spherical projection and over-alignment of curvatures. In (a)MSM, registration of complex surfaces also progresses in a coarse-to-fine fashion, as described in Fig. B.2, and Λ can be altered and optimized for each resolution level.

Since curvature matching was only considered to obtain general, initial alignment between gyri and sulci, we performed our two-step registration (balanced then high Λ) only at low resolution levels. At higher resolution levels, after qualitative alignment had been obtained between gyri and sulci, the emphasis was shifted to strain energy minimization only (high Λ). This successfully matched each gyrus and sulcus while providing robust, smooth deformation

maps at high resolution, as quantified in Table 4.1. Non-default configuration parameters used in this study are shown below. With these parameters, over half of registrations completed in less than 12 hours and 97% of registrations completed in less than 24 hours when run on a single processor:

–CPgrid=2,2,3,3,4,5 (see Fig. B.2)

–SGgrid=4,4,5,5,6,6 (see Fig. B.2)

–datagrid=4,4,5,5,6,6 (see Fig. B.2)

–lambda=0.01,10000, 0.01,10000,10000,10000 (see Fig. B.2)

–bulkmod=10 (see Fig. B.1*A,B*)

–shearmod=1 (see Fig. B.1*A,B*)

–regoption=3 (aMSM)

–IN (histogram matching)

–regexp=1 (exponent on W penalty)

–kexp=1 (exponent on R and J)

–dopt=HOCR (higher order clique reduction)

–rescaleL (rescaled grid options at each iteration)

–it=50,50,50,50,50,50*

*MSM stops running each level once it reaches convergence, usually between 10-20 iterations for registrations considered in this study. Here, we set an excessively high number of iterations to ensure consistent, fully-converged solutions, but future optimization could consider limiting each level to fewer iterations.

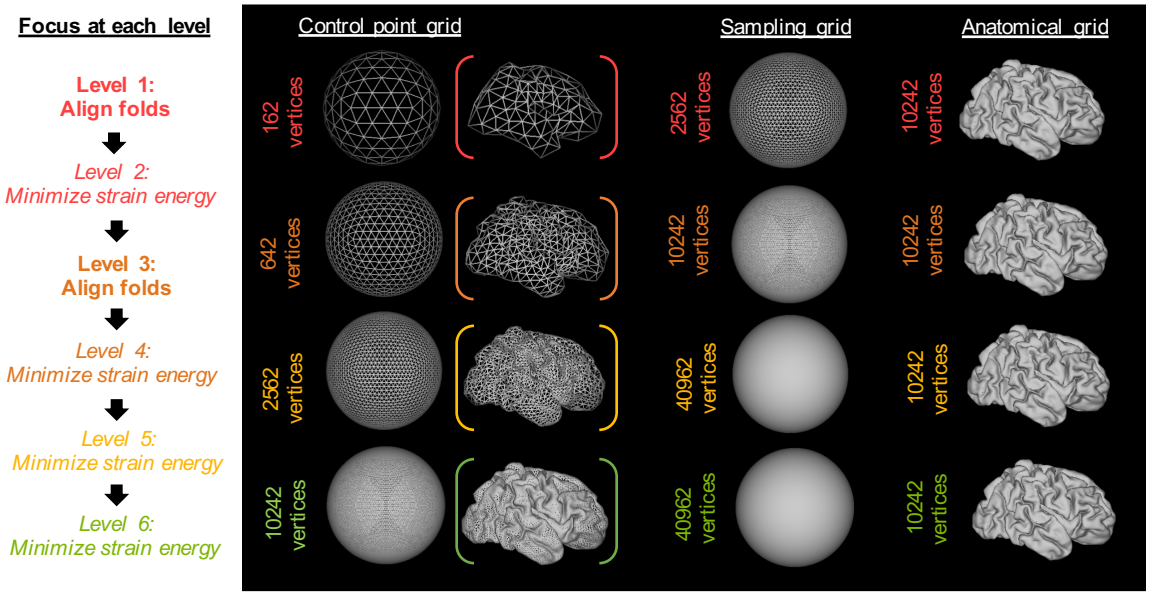

Figure B.2: aMSM optimized for complex, variable geometries. For speed and robustness, MSM aligns complex surfaces in 'levels', starting with a coarse (low resolution) representation of the input and reference surfaces, then progressively moving to higher resolutions. From left to right in black box: the internal control point grid (CPgrid, points to be moved/optimized) begins as a very basic representation of the cortex. Illustration of how this grid is distributed on a cortex shown in parentheses to right. The corresponding sampling grid (SGgrid, set of locations to which control points can move) is typically set to a higher resolution. For increased accuracy, anatomical strains were calculated at a default resolution (anatgrid) of 10,242 vertices, the maximum for our final CPgrid for all levels, for each level within aMSM optimization. Low resolutions were optimized twice: first with a 'balanced' $\Lambda = 0.01$, the highest value that consistently allowed each point to reach the correct gyri and sulci, then with a high $\Lambda = 10000$ to minimize unrealistic deformations after accurate alignment had been achieved.

B.4 Minimizing directional registration bias for accurate growth measurements

Lastly, we address the issue that the basic MSM algorithm produces a unidirectional registration of an input surface to a reference surface. As such, differences are likely to exist between a registration of a younger surface to an older surface (forward registration) versus registration of an older surface to a younger surface (reverse registration). To minimize any bias, we ran forward and reverse registrations for each longitudinal case. All growth maps reported in the main text represent the average of forward and reverse registrations, accomplished via a series of projections and averages in Connectome Workbench (Marcus et al., 2011) (http://www.humanconnectome.org/software/get-connectome-workbench). (Each direction of registration produces a deformed version of its input sphere. In order to average these relationships, the inverse of the reverse registration was applied to the reference sphere. The coordinates of this sphere's vertices were then averaged with the forward registration's deformed sphere, to reduce the directional bias of registration. The inverse-reverse registration was also used to resample the growth map – always calculated from younger to older – from reverse registration into the forward framework, where it was averaged with the growth map from forward registration. The opposite of this procedure can also be used to obtain averages in the reverse framework.)

Fig. B.3 quantifies observed differences between forward and reverse registrations for our largest subject group and longest time step: 30 to 38 weeks PMA (n=20). As in the main text, mean relative expansion maps are plotted for each, as well as regions of significantly higher (red) or lower (blue) expansion. As shown in Fig. B.3*A*-*B*, patterns were similar but not identical between forward and reverse aMSM registrations. Furthermore, discrepancies

appear to flip for right versus left hemisphere: e.g., relative expansion is high on the forward-registered left frontal lobe and the reverse-registered right frontal lobe. As shown in Fig. B.3*C*, a paired t-test in PALM (Winkler et al., 2014) (https://fsl.fmrib.ox.ac.uk/fsl/fslwiki/PALM) revealed significant trends in the difference between forward and reverse registrations. These differences also appear to roughly flip for right versus left hemisphere: reverse registration leads to higher relative expansion on the right lateral surface but the left medial surface. Note, however, that these differences largely cancel out when forward and reverse registrations are averaged, such that unbiased results for right and left hemispheres show nearly identical trends Fig. B.3*C*.

It is important to note that right and left hemispheres were analyzed independently throughout this study. Furthermore, lateral coordinates were consistently defined such that a positive value on the right hemisphere is negative on the left hemisphere. These differences may have introduced subtle biases during surface generation (Hill et al., 2010a), spherical projection, and/or optimization. As such, left and right hemispheres serve as a valuable check for consistency. Though general trends reported in this study are robust, studies which combine analysis of right and left hemispheres should carefully consider this issue and ensure proper validation.

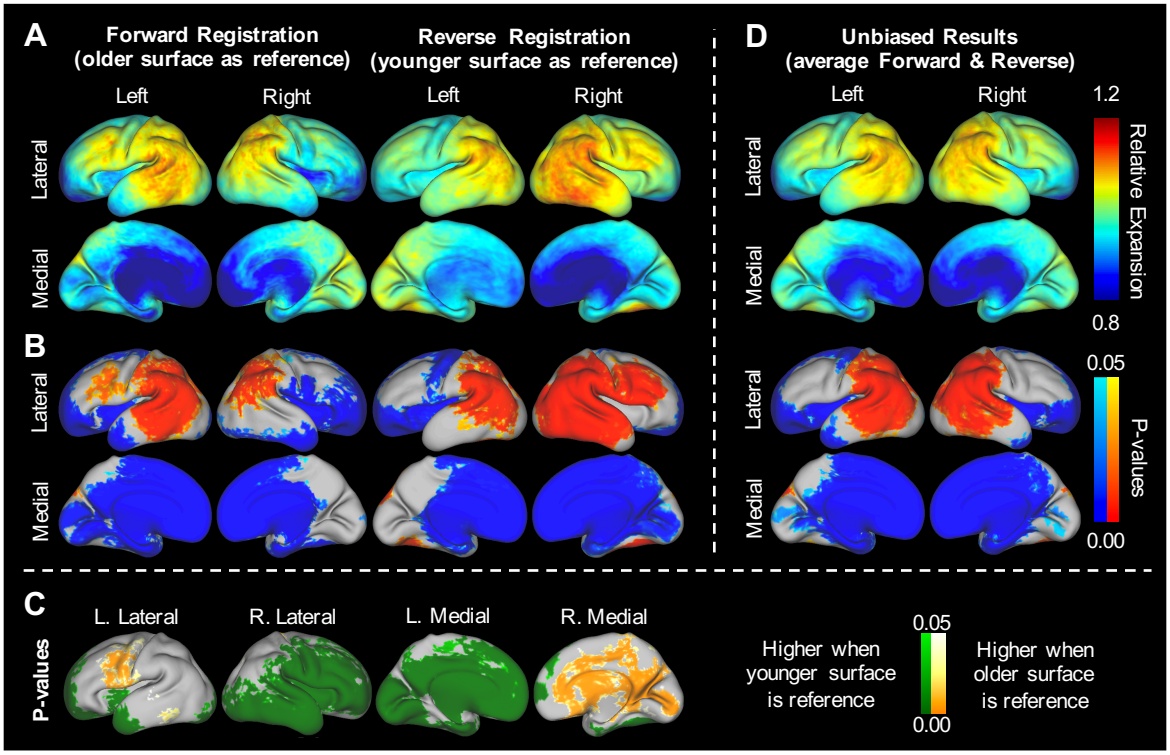

Figure B.3: Averaging forward and reverse registrations to eliminate bias. (A) For forward (left) and reverse (right) registration, map of mean relative expansion is shown for 30 weeks PMA to 38 weeks PMA (n=20). (B) Areas of statistical significance corresponding to the relative expansion maps shown in (A), where red is significantly higher than the global average and blue is significantly lower than the global average. Since here we are interested in the effects of registration, which includes registration of the non-cortical medial wall, the medial wall was not excluded from this statistical analysis. (C) Testing paired differences between forward (left) to reverse (right) registrations reveals significant regional differences. Note similarity between the right lateral and left medial walls, as well as dissimilarity between corresponding right and left regions. (D) Averaging forward and reverse registration effectively eliminates this bias, resulting in similar maps for right and left.

B.5 Effect of strain energy minimization on quality of alignment

Since the parameters for registration in this paper allow strong strain energy regularization, we performed additional tests to determine whether this could adversely affect the quality of alignment between folds. I.e., Can unconstrained minimization of strain energy (using $\kappa = 10\mu$) push initially-aligned points off of the correct fold? If so, will regional differences in surface expansion dissipate under the fully converged solution? To illustrate this theoretical issue, we considered strong, *regional* folding of a sphere defined by $r = 1.1(R + 0.2sin(7\Theta)cos\Phi)$ if $\Theta \geq 0$, else $r = 1.1R$ (Fig. B.4A). (In this case, the regional difference in relative surface expansion was designed to be on the order of results in Fig. 3.) By solving the problem via mechanical equations of motion, again using code modified from (Knutsen et al., 2010), we can see the solution approaches convergence as a function of time (Fig. B.4C). At $t = 70$ s, clear differences in relative expansion are still visible (Fig. B.4B, right). Despite large regional differences in expansion, we observe only a slight shift at the border between static and folding regions, and the distribution within each gyrus and sulcus remains reasonable (Fig. B.4D).

While these theoretical results are useful for conceptualization, they do not prove that alignment will be maintained in discrete optimization of more complex surfaces. To examine whether alignment is maintained on an actual set of mid-thickness surfaces using aMSM, we revisit the representative subject in Fig. 3. Specifically, we examine the large time period (representing a more drastic change in folding) from 31 to 37 weeks PMA (Fig. B.4E). Fig. B.4F plots mean curvature from the younger surface on the older surface after forward, reverse, and average aMSM registrations. In all cases, common sulci (blue) and gyri (orange)

remain correctly positioned despite strong strain energy regularization at levels 2, 4, 5 and 6.

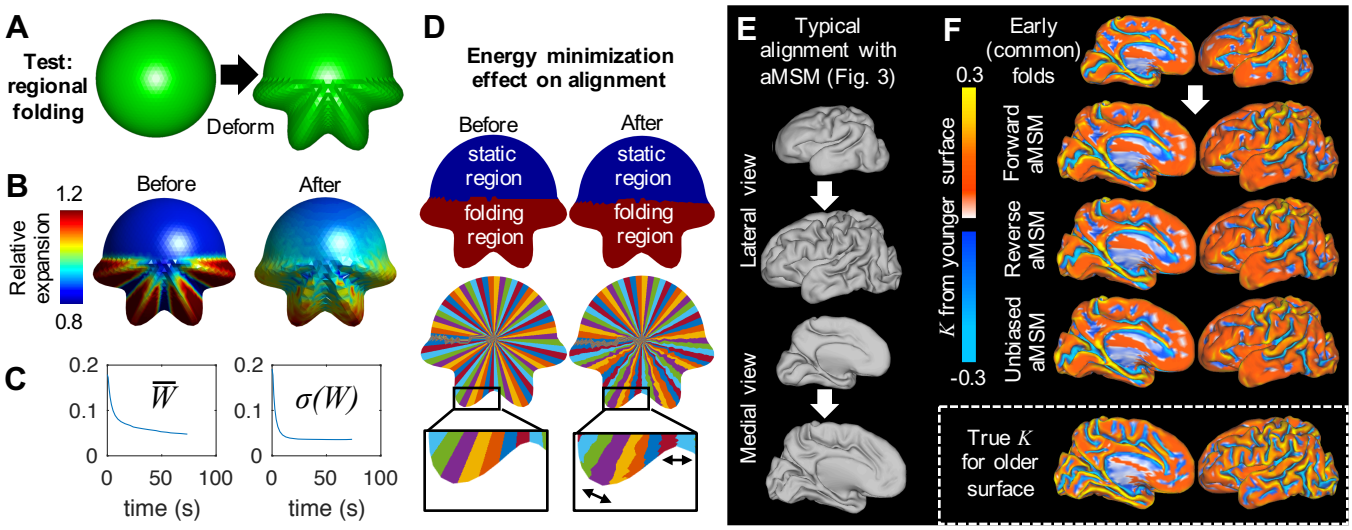

Figure B.4: Strain energy minimization does not adversely affect alignment of folds. (A) Effect of strain energy minimization on drift was explored by considering asymmetric (regional) folding of a sphere. (B-C) Strain energy minimization (using $\kappa = 10\mu$) approximates the converged solution at $t = 70$ s, shown in (B) as the average and standard deviation of strain energy density, $\bar{W}$ and $\sigma(W)$, approach a constant value. (D) Two artificial segmentations (based on original angle Φ) are shown for the aligned geometry before and after strain energy minimization to visualize the final locations of points. (E-F) Effects of aMSM strain energy minimization do not appear to impede qualitative alignment of folds. Regional expansion patterns for this subject are shown in Fig. 3. By plotting K for early folds, we see that reasonable alignment of these early folds is maintained on the corresponding older surface after aMSM including strong regularization (strain energy minimization). Inset: Older folding pattern is shown for reference.

Although strong regularization via strain energy minimization worked well for these surfaces, we recognize that this solution may not be ideal for all cases. In particular, cortical mid-thickness reconstructions in this study had undergone careful manual editing to remove topological 'holes' and other artifacts. The presence of artefactual irregularities could skew strain energy minimization and lead to unrealistic results. Furthermore, constraints on computational time may dictate the need for faster registration. These issues have been considered in ref. (Robinson et al., 2017), which obtained strikingly similar results from 30 weeks to term-equivalent using different parameters and fewer iterations. Consistency between these results, with different surface reconstruction methods and different regularization parameters, suggest that aMSM is a robust tool for longitudinal analysis of growth.

B.6 Growth estimates for short and long time steps

As shown in Table 4.4, subjects in this analysis were scanned at a variety of ages, with varying time steps between scans. To confirm that growth maps were accurate for larger time steps, we compared relative expansion maps from 30±1 to 38±2 weeks PMA with and without an intermediate registration time point (34±2 weeks PMA). As shown in Fig. B.5A, average expansion maps were qualitatively similar with and without the intermediate time points (n=8 per group). For the case with an intermediate step, relative expansion maps (30 to 34 weeks and 34 to 38 weeks) were multiplied. Therefore, the higher and lower peaks observed in this case may represent multiplication of "noise" in discrete registration, rather than true growth. Paired t-test in PALM revealed only small regions of statistically significant difference (Fig. B.5B).

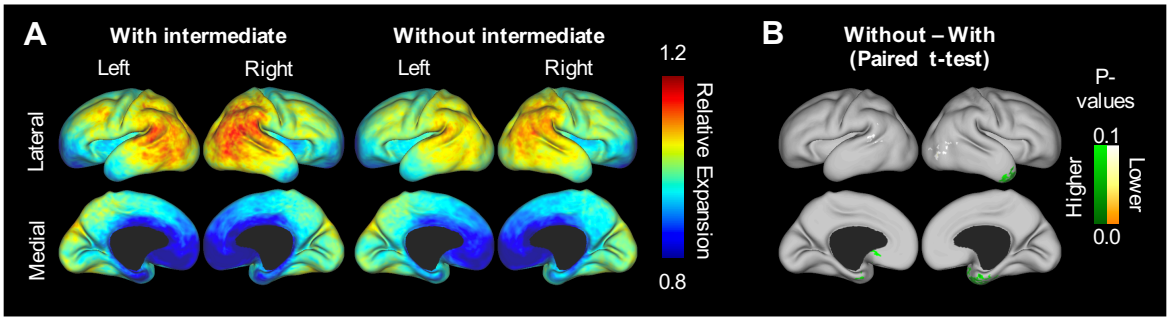

Figure B.5: **Effect of time interval between scans.** (*A*) For registration with (left) and without (right) an intermediate time point, maps of mean relative expansion are shown for 30±1 weeks PMA to 38±2 weeks PMA (n=8, noninjured1-8 in Table 4.4). (*B*) Testing paired differences with and without the intermediate step reveals only a few small areas of statistical significance. Green denotes areas where relative expansion was higher without an intermediate step, yellow denotes areas lower without an intermediate step. Note: To visualize small differences that do exist, and account for low sample size, the threshold for plotting has been raised to p=0.1. Only the dark green region of the right temporal lobe was significant with $p<0.05$.

B.7 Atlas generation with aMSM

For group analysis, a 30-week PMA group atlas was created through the following steps, as outlined in Fig. B.6: (*A*) Cortical surfaces from 18 non-injured subjects (30±1 weeks PMA) were affine-aligned at the anterior and posterior commissures and projected to a corresponding spherical surface using CARET (Van Essen et al., 2001). (*B*) Using Connectome Workbench (Marcus et al., 2011), cortical surfaces were resampled to a standard 40,962-vertex mesh and averaged to create a proto-atlas. (*C*) Individual surfaces were registered

to the proto-atlas with aMSM using the same parameters described above. (D) Registered surfaces were averaged in Connectome Workbench to create a final 30-week atlas. Note that this final atlas conserves greater anatomical detail and reduces 3D dispersion (minimizes standard deviation of the distance of subjects vertices to the mean 3D coordinate) (Fig. B.6E). For group analysis, all individual surfaces (time point closest to 30 weeks PMA) were registered to this final 30-week atlas.

All atlas registrations in this study used the individuals scan closest to 30 weeks, so that variability between age groups did not affect our individual-to-atlas registrations. At 30-weeks, variability was small between our subjects, as illustrated in Fig. B.6. In future studies using multiple or different subject groups, investigators should assess variability between groups when deciding whether to use this (or another existing) atlas, or whether to develop multiple group atlases for their specific research question.

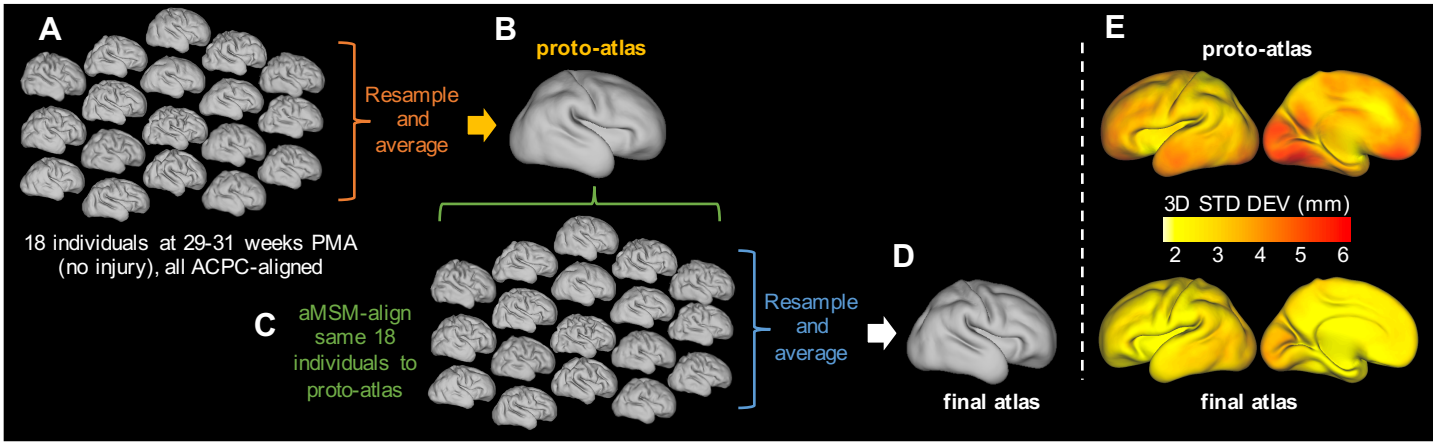

Figure B.6: .

Atlas generation and aMSM improvement (reduction in 3D dispersion)

Appendix C

Codes

C.1 Discrete orientation fields and stress-dependent growth in ABAQUS

The UMAT generator developed by Young et al. (2010) offers a useful tool to implement growth with nonlinear materials in ABAQUS. ABAQUS is especially useful for handling complex geometries and full, 3-dimensional analysis: offering a range of capabilities including spatially-varying loads and vector fields. In Chapters 2-3 of this dissertation, we considered complex 3D geometries that could not be defined using standard spherical or cylindrical coordinates (SP models).

To circumvent this issue, we defined discrete orientation fields in ABAQUS. However, the UMATs originally produced by the UMAT generator are not designed to handle pre-defined orientations. The following MATLAB code, UMAT modifications, and instructions offer one solution to this issue.

Note that this UMAT also reorients Cauchy stress to these discrete orientation directions to facilitate orthotropic stress-dependent growth in the original material directions. This required modification of the rotation tensors originally defined in the UMAT generator.

discreteA.m

```
% Written by Kara E. Garcia

% Converts Discrete Orientation Table (DiscOrient) from Abaqus input file
% to orthogonal base vectors (A11-A33) that can be used in a modified UMAT
% (Kara Garcia) based on the UMAT generator by Young et al. (2010)

% Note: DiscOrient must be copied into a separate text file
% eg. 'discorient12448.txt'
% Then, all references to the discrete orientation field in the input file
% should be deleted or commented out before use with UMAT described above.

T1T2 = load('discorient12448.txt');
element = T1T2(:,1);
T1 = T1T2(:,2:4);
T2 = T1T2(:,5:7);
N3 = cross(T1,T2);
A1A2A3 = [T1,T2,N3];
count = 1:100;

A1A2A3T = A1A2A3';

fileID = fopen('A_12448.f77','w');
for i=1:(max(element)-min(element)+1)
   fprintf(fileID,'      %4.3f,%4.3f,%4.3f,%4.3f,%4.3f,%4.3f,%4.3f,%4.3f,%4.3
f, \n',A1A2A3(i,1:9));
end
fclose(fileID);

fileID = fopen('A1_12448.f77','w');
for i=1:(max(element)-min(element)+1)
    fprintf(fileID,'      %16.15f,%16.15f,%16.15f, \n',A1A2A3(i,1:3));
end
fclose(fileID);

fileID = fopen('A2_12448.f77','w');
for i=1:(max(element)-min(element)+1)
    fprintf(fileID,'      %16.15f,%16.15f,%16.15f, \n',A1A2A3(i,4:6));
end
fclose(fileID);

fileID = fopen('A3_12448.f77','w');
for i=1:(max(element)-min(element)+1)
    fprintf(fileID,'      %16.15f,%16.15f,%16.15f, \n',A1A2A3(i,7:9));
end
fclose(fileID);

max(element)-min(element)+1
```

```
C
C
C ABAQUS/STANDARD UEXTERNALDB FROM MATHEMATICA
C
C Used to update the total rotation at the end of increment.
C
C Mathematica Routine Written by: Jonathan Young
C Modified by Kara Garcia to incorporate:
C (1) discrete orientation fields (ABAQUS CAE) to define complex material orientations
C (2) stress-dependent growth, using Cauchy stress in material (reference) orientations
C *This example also incorporates morphogen effects based on predefined distributions.
C **This UMAT considers a modified neo Hookean material, using UMAT generator by JY.
C
      SUBROUTINE UEXTERNALDB(LOP,LRESTART,TIME,DTIME,KSTEP,KINC)
C
      INCLUDE 'ABA_PARAM.INC'
C
      DIMENSION TIME(2)

C MUST INSERT TOTAL NUMBER OF ELEMENTS AS FIRST NUMBER IN KA1-3EL,RTOTAL,DROTINC
C     ALSO IN LINES TO IMPORT "A" DATA FILES, AND BEGINNING OF UMAT!!!
C FOR RTOTAL AND DROTINC, MULTIPLY TOTAL NUMBER OF ELEMENTS BY INTEGRATION POINTS
C     INTEGRATION POINTS = 8 FOR HEX (LINEAR C3D8, QUAD C3D20R [C3D20=27])
C     INTEGRATION POINTS = 4 FOR TET (LINEAR C3D4, QUAD C3D10)
C     ALSO IN LINES TO INITIALIZE ROTATION VARIABLES, AND BEGINNING OF UMAT

      REAL*8 KA1EL(10875,3)
      REAL*8 KA2EL(10875,3)
      REAL*8 KA3EL(10875,3)
      COMMON RTOTAL(10875*8,9)
      COMMON DROTINC(10875*8,9)
      COMMON KA1EL
      COMMON KA2EL
      COMMON KA3EL

      DIMENSION R0(3,3), DROT(3,3), R(3,3)

      CHARACTER(256) FILENAME
      CHARACTER(256) JOBDIR
C
C INITIALIZE COMMON ROTATION VARIABLES
C
C At the start of the analysis.
      IF(LOP.EQ.0) THEN
C For all integration points.
        DO K1=1,10875*8
          RTOTAL(K1,1) = 1.D0
          RTOTAL(K1,2) = 0.D0
          RTOTAL(K1,3) = 0.D0

          RTOTAL(K1,4) = 0.D0
          RTOTAL(K1,5) = 1.D0
          RTOTAL(K1,6) = 0.D0
```

```
        RTOTAL(K1,7) = 0.D0
        RTOTAL(K1,8) = 0.D0
        RTOTAL(K1,9) = 1.D0

        DROTINC(K1,1) = 1.D0
        DROTINC(K1,2) = 0.D0
        DROTINC(K1,3) = 0.D0

        DROTINC(K1,4) = 0.D0
        DROTINC(K1,5) = 1.D0
        DROTINC(K1,6) = 0.D0

        DROTINC(K1,7) = 0.D0
        DROTINC(K1,8) = 0.D0
        DROTINC(K1,9) = 1.D0

      END DO

      CALL GETOUTDIR(JOBDIR,LENJOBDIR)

        FILENAME=JOBDIR(:LENJOBDIR)//'\A1_10875.f77'
        OPEN(UNIT=111,FILE=FILENAME)
C AGAIN, MUST DEFINE TOTAL NUMBER OF ELEMENTS AS SECOND NUMBER!!!!
        DO K1=1,10875
           READ(111,*) (KA1EL(K1,K2),K2=1,3)
        END DO
        PRINT *,KA1EL(1,1:3)
        CLOSE(111)

        FILENAME=JOBDIR(:LENJOBDIR)//'\A2_10875.f77'
        OPEN(UNIT=112,FILE=FILENAME)
C AGAIN, MUST DEFINE TOTAL NUMBER OF ELEMENTS AS SECOND NUMBER!!!!
        DO K1=1,10875
           READ(112,*) (KA2EL(K1,K2),K2=1,3)
        END DO
        PRINT *,KA2EL(1,1:3)
        CLOSE(112)

        FILENAME=JOBDIR(:LENJOBDIR)//'\A3_10875.f77'
        OPEN(UNIT=113,FILE=FILENAME)
C AGAIN, MUST DEFINE TOTAL NUMBER OF ELEMENTS AS SECOND NUMBER!!!!
        DO K1=1,10875
           READ(113,*) (KA3EL(K1,K2),K2=1,3)
        END DO
        PRINT *,KA3EL(1,1:3)
        CLOSE(113)

    END IF

C
C UPDATE TOTAL ROTATION
C
```

```
C At the end of the current increment
      IF(LOP.EQ.2) THEN
C For all integration points
        DO K1=1,10875*8
          R0(1,1) = RTOTAL(K1,1)
          R0(2,1) = RTOTAL(K1,2)
          R0(3,1) = RTOTAL(K1,3)

          R0(1,2) = RTOTAL(K1,4)
          R0(2,2) = RTOTAL(K1,5)
          R0(3,2) = RTOTAL(K1,6)

          R0(1,3) = RTOTAL(K1,7)
          R0(2,3) = RTOTAL(K1,8)
          R0(3,3) = RTOTAL(K1,9)

          DROT(1,1) = DROTINC(K1,1)
          DROT(2,1) = DROTINC(K1,2)
          DROT(3,1) = DROTINC(K1,3)

          DROT(1,2) = DROTINC(K1,4)
          DROT(2,2) = DROTINC(K1,5)
          DROT(3,2) = DROTINC(K1,6)

          DROT(1,3) = DROTINC(K1,7)
          DROT(2,3) = DROTINC(K1,8)
          DROT(3,3) = DROTINC(K1,9)

C Update the total rotation
          CALL MULMAT(DROT,R0,R)

          RTOTAL(K1,1) = R(1,1)
          RTOTAL(K1,2) = R(2,1)
          RTOTAL(K1,3) = R(3,1)

          RTOTAL(K1,4) = R(1,2)
          RTOTAL(K1,5) = R(2,2)
          RTOTAL(K1,6) = R(3,2)

          RTOTAL(K1,7) = R(1,3)
          RTOTAL(K1,8) = R(2,3)
          RTOTAL(K1,9) = R(3,3)
        END DO
      END IF

      RETURN
      END

C
C
C ABAQUS/STANDARD UMAT GENERATED BY MATHEMATICA
C
C Mathematica routine written by:
```

```
C Jonathan M. Young (1*)
C
C With contribution from:
C Dr. Jiang Yao (1),
C Dr. Ashok Ramasubramanian (2),
C Dr. Larry A. Taber (3), and
C Dr. Renato Perucchio (1)
C
C (1) Dept. of Mechanical Engineering
C     University of Rochester
C     Rochester, NY 14627
C
C (2) Dept. of Mechanical Engineering
C     Union College
C     Schenectady, NY 12308
C
C (3) Dept. of Biomedical Engineering
C     Washington University
C     St. Louis, MO 63130
C
C * Address correspondence to:
C Jonathan M. Young
C jyoung@me.rochester.edu
C 01.585.275.8074
C
C Date: 5/12/2014
C
C
      SUBROUTINE UMAT(STRESS,STATEV,DDSDDE,SSE,SPD,SCD,
     1 RPL,DDSDDT,DRPLDE,DRPLDT,
     2 STRAN,DSTRAN,TIME,DTIME,TEMP,DTEMP,PREDEF,DPRED,CMNAME,
     3 NDI,NSHR,NTENS,NSTATV,PROPS,NPROPS,COORDS,DROT,PNEWDT,
     4 CELENT,DFGRD0,DFGRD1,NOEL,NPT,LAYER,KSPT,KSTEP,KINC)
C
      INCLUDE 'ABA_PARAM.INC'
C
      CHARACTER*8 CMNAME
      DIMENSION STRESS(NTENS),STATEV(NSTATV), !TEMP(28),
     1 DDSDDE(NTENS,NTENS),DDSDDT(NTENS),DRPLDE(NTENS),
     2 STRAN(NTENS),DSTRAN(NTENS),TIME(2),PREDEF(1),DPRED(1),
     3 PROPS(NPROPS),COORDS(3),DROT(3,3),DFGRD0(3,3),DFGRD1(3,3)

C ONCE AGAIN, UPDATE TOTAL NUMBER OF ELEMENTS FOR KAEL!
      REAL*8 KA1EL(10875,3)
      REAL*8 KA2EL(10875,3)
      REAL*8 KA3EL(10875,3)
      COMMON RTOTAL(10875*8,9)
      COMMON DROTINC(10875*8,9)
      COMMON KA1EL
      COMMON KA2EL
      COMMON KA3EL
      REAL*8 KH1, KH2, KH3, KSTEPG, KACONSTANT, KR1, KRATIO, KBCONSTANT
      REAL*8 KAG1T, KAG2T, KAG3T, KPI, KC1, KD1, KCN, KCA
```

```
      REAL*8 KBMP, KSHH, KFGF, KFP, KRP, KFPA, KRPA, KBEXP, KSEXP, KFEXP
      REAL*8 KGBASE, KSG1, KSG2, KSG3, KSMAX, KGMAX, KAIS

      DIMENSION CBAR1(3,3), CL1(3,3,3,3), CL2(3,3,3,3), C(3,3),
     1 DEVS(3,3), DI(3,3), DWDE(3,3), D2WDE2(3,3,3,3),
     2 FBAR1(3,3), FBAR1T(3,3), F1(3,3), F2(3,3), FE(3,3), FT(3,3),
     3 E1(3,3), E2(3,3), E3(3,3), FWC(3,3), FWCF1(3,3),
     4 GI(3,3), WC(3,3), A1A2A3(9), DROT1(3,3), DROT2(3,3), DROT3(3,3),
     5 R0(3,3), R(3,3), RT(3,3), RI(3,3), RIT(3,3), R0T(3,3),
     6 S1(3,3), S2(3,3), S3(3,3), S4(3,3), S4A(3,3), S5(3,3), S6(3,3),
     6 S4MX(3,3), S4MR(3,3), PS(3), AN(3,3),
     7 SOUT1(3,3), SOUT2(3,3), SYM(3,3,3,3)

C  DEFINED DISCRETE ORTHOGONAL BASE VECTORS (A11-A33 FOR EACH ELEMENT, A TRANSPOSE)

      A1A2A3(1)=KA1EL(NOEL,1)
      A1A2A3(2)=KA2EL(NOEL,1)
      A1A2A3(3)=KA3EL(NOEL,1)
      A1A2A3(4)=KA1EL(NOEL,2)
      A1A2A3(5)=KA2EL(NOEL,2)
      A1A2A3(6)=KA3EL(NOEL,2)
      A1A2A3(7)=KA1EL(NOEL,3)
      A1A2A3(8)=KA2EL(NOEL,3)
      A1A2A3(9)=KA3EL(NOEL,3)

C
C MATERIAL PROPERTIES
C
      b1111 = PROPS(1)
      b1122 = PROPS(2)
      b1133 = PROPS(3)
      b1112 = PROPS(4)
      b1113 = PROPS(5)
      b1123 = PROPS(6)
      b2222 = PROPS(7)
      b2233 = PROPS(8)
      b2212 = PROPS(9)
      b2213 = PROPS(10)
      b2223 = PROPS(11)
      b3333 = PROPS(12)
      b3312 = PROPS(13)
      b3313 = PROPS(14)
      b3323 = PROPS(15)
      b1212 = PROPS(16)
      b1213 = PROPS(17)
      b1223 = PROPS(18)
      b1313 = PROPS(19)
      b1323 = PROPS(20)
      b2323 = PROPS(21)
      C1 = PROPS(22)
      D1 = PROPS(23)
      T0 = 0.1
      TMAX = PROPS(25)
```

```
      AG1T = PROPS(26)
      AG2T = PROPS(27)
      AG3T = PROPS(28)
      A11 = A1A2A3(1)
      A21 = A1A2A3(2)
      A31 = A1A2A3(3)
      A12 = A1A2A3(4)
      A22 = A1A2A3(5)
      A32 = A1A2A3(6)
      A13 = A1A2A3(7)
      A23 = A1A2A3(8)
      A33 = A1A2A3(9)

      E = 2.718281828459046
      KPI = 3.141592654

      NLINE = 8*(NOEL - 1) + NPT

      CT = TIME(2) + DTIME

C DEFINE SPATIAL VARIATION GROWTH/CONTRACTION

      KH1 = 0.175 !TELENCEPHALON (MID)RADIUS
      KH2 = 0.1 !FLOORPLATE ADDITIONAL DISTANCE
      KH3 = 0.1 !BOUNDARY EDGE OF MODEL (AIS)
      KSTEPG = 1. !TIME TO START STRESS-DEPENDENT GROWTH LAW
      KACONSTANT = 2./2 * 6 !2.73*2 !STRESS-DEPENDENT
      KGBASE = 0.39
      KBCONSTANT = 0.38 !CONSTANT FOR THICKENING
      KRATIO = 0. !0.2 !RATIO OF THICKENING TAKEN FROM G1,G2 (0-1)
      KR1 = 0. !0.5 !RATIO OF G1,G2 REMOVED VENTRALLY
      KSEXP = 10. !EXPONENT FOR SHH DECAY IN D-V AXIS
      KFEXP = 2. !10. !EXPONENT FOR FGF DECAY IN R-C AXIS
      KBEXP = 5. !10. !EXPONENT FOR BMP/RP/FP DECAY
      KRPA = 0.05 ! 0.075 !MAX WIDTH OF BMP/RP BAND
      KFPA = 0.1 !MAX WIDTH OF FP BAND
      KCN = 0. !FLOORPLATE EXTRA STIFFNESS
      KCA = 5. !10. !BOUNDARY STIFFNESS
      KAIS = 1-1./6 !BOUNDARY FRACTION OF GROWTH *REMOVED*
      KENDG = 2.5 !STEP 2 TOTAL TIME (ACTUAL END OF MODEL=36h)

      IF (TIME(2).EQ.0.) THEN !RECORD COORDS AT T=0
        STATEV(15) = COORDS(1) !X (ROSTRAL X>0)
        STATEV(16) = COORDS(2) !Y (DORSAL Y>0)
        STATEV(17) = COORDS(3) !Z (LATERAL Z>0)
        STATEV(10) = ATAN2(COORDS(2),COORDS(1)) !PHI(0=R,PI/2=D,-PI/2=V)
        STATEV(11) = ATAN2(COORDS(2),COORDS(3)) !THETA (0=L,",")
      END IF

C     BMP GRADIENT, NO GROWTH HH17-END
      KBMP = 1/(1 + E**(KBEXP * ((STATEV(17)**2
     1 + ((STATEV(10)-KPI/5)*.125/KPI)**2) / (KRPA)**2 - 1)))
     2 * (1-1/(1 + E**(20 * (CT-KSTEPG - 2.*(KENDG-KSTEPG)/4)) )) !
```

```
C     FP (NO LONGER NEEDED)
      KFP = 1/(1 + E**(KBEXP * ((STATEV(17)**2
     1 + ((STATEV(10)+KPI*1.4)*.2/KPI/2)**2) / (KFPA)**2 - 1)))

C     RP (ABSOLUTELY NO THICKENING)
      KRP = 1/(1 + E**(KBEXP * ((STATEV(17)**2
     1 + ((STATEV(10)-KPI/5)*.125/KPI)**2) / (KRPA)**2 - 1)))

C     SHH GRADIENT (THICKENING/ASYMMETRIC SIPHONED FROM TANGENTIAL/SYMMETRIC)
c     KSHH = (-1*STATEV(16)+KH1+KH2+0.025)/(2*KH1+KH2+0.05)
      KSHH = 1.0 !instead, let thickening happen everywhere except RP

C     FGF GRADIENT (ROSTRAL-CAUDAL GROWTH)
c     KFGF = 1 - KAIS/(1 + E**(10 * ((STATEV(15)+KH3)/(KH3/2) - 1)))
      KFGF = 1 - KAIS/(1 + E**(KFEXP*((STATEV(15)+KH3/2)/(KH3/2) - 1)))

C     REGIONAL STIFFNESS (CAN BE INCREASED FOR BOUNDARY, VENTRAL MESENCHYME)
      KC1 = C1 + KCN*(1-COS(KSHH*KPI/2)**4)
     1 + KCA/(1 + E**(5 * ((STATEV(15)+KH3)/(KH3/2) - 1))) !STIFF AIS
      KD1 = D1/KC1

      KSGMAX = 1.0 !MAX STRESS FOR GROWTH LAW
      IF (STATEV(4).GT.KSGMAX) THEN
        KSG1 = KSGMAX
      ELSE
        KSG1 = STATEV(4)
      END IF
      IF (STATEV(5).GT.KSGMAX) THEN
        KSG2 = KSGMAX
      ELSE
        KSG2 = STATEV(5)
      END IF

      KSG3 = (STATEV(4) + STATEV(5)) / 2 !COULD DO ABOVE
      IF (KSG3.GT.KSGMAX) THEN
        KSG3 = KSGMAX
      END IF
C     ONLY USE FOLLOWING LINES FOR TRANSVERSELY ISOTROPIC GROWTH
      KSG1 = KSG3
      KSG2 = KSG3

C     PREDEFINED GROWTH IN STEP 1
      AG1T = 1.0  !INITIAL GROWTH IN MATERIAL DIRECTION 1
      AG2T = 1.0  !INITIAL GROWTH IN MATERIAL DIRECTION 2
      AG3T = 1.0 - 0.5*KRP !INITIAL GROWTH IN MATERIAL DIRECTION 3
c     ^ only thin for hh13 onward model
C
C INITIALIZE MATRICES
C
C DI = Identity matrix
      DO K1=1,3
        DO K2=1,3
```

```
          IF(K1.EQ.K2) THEN
            DI(K1,K2) = 1.D0
          ELSE
            DI(K1,K2) = 0.D0
          END IF
          DWDE(K1,K2) = 0.D0
          WC(K1,K2) = 0.D0
        END DO
      END DO

C Fourth order symmetric matrix
      DO K1=1,3
        DO K2=1,3
          DO K3=1,3
            DO K4=1,3
              SYM(K1,K2,K3,K4) = (DI(K1,K4)*DI(K2,K3)
     1 + DI(K1,K3)*DI(K2,K4))/2.D0
            END DO
          END DO
        END DO
      END DO

C
C MATERIAL ORIENTATION
C
      CALL SPRIND(STRESS,PS,AN,1,NDI,NSHR) !PRINCIPAL STRESSES = PS(3)

C     IF(TIME(2).LT.KSTEPG) THEN
        RI(1,1) = A11
        RI(2,1) = A21
        RI(3,1) = A31

        RI(1,2) = A12
        RI(2,2) = A22
        RI(3,2) = A32

        RI(1,3) = A13
        RI(2,3) = A23
        RI(3,3) = A33

C     COULD DEFINE STRESS-DEPENDENT GROWTH IN PRINCIPAL STRESS DIRECTIONS
C     *BUT* NEED TO CORRECT AN WHEN INT PTS FACING OPPOSITE DIRECTIONS
C     ELSE IF(TIME(2).GE.KSTEPG) THEN
C
C       RI(1,1) = AN(1,1) !MAX EIGENVECTOR
C       RI(2,1) = AN(1,2) !MAX EIGENVECTOR
C       RI(3,1) = AN(1,3) !MAX EIGENVECTOR
C
C       RI(1,2) = AN(2,1) !MIN EIGENVECTOR
C       RI(2,2) = AN(2,2) !MIN EIGENVECTOR
C       RI(3,2) = AN(2,3) !MIN EIGENVECTOR
C
C       RI(1,3) = AN(3,1) !MID EIGENVECTOR
```

```
C       RI(2,3) = AN(3,2) !MID EIGENVECTOR
C       RI(3,3) = AN(3,3) !MID EIGENVECTOR
C
C     END IF

      CALL TRMAT(RI,RIT)
      CALL MULMAT(RI,DFGRD1,F1)
      CALL MULMAT(F1,RIT,F2)
C
C GROWTH
C
      IF(TIME(2).LE.KSTEPG) THEN
        IF(CT.LE.T0) THEN
          AG1 = 1.D0
          AG2 = 1.D0
          AG3 = 1.D0
        END IF
        IF(CT.GT.TMAX) THEN
          AG1 = AG1T
          AG2 = AG2T
          AG3 = AG3T
        END IF
        IF(CT.GT.T0.AND.CT.LE.TMAX) THEN
          AG1 = 1.D0 + (AG1T - 1.D0)*(CT - T0)/(TMAX - T0)
          AG2 = 1.D0 + (AG2T - 1.D0)*(CT - T0)/(TMAX - T0)
          AG3 = 1.D0 + (AG3T - 1.D0)*(CT - T0)/(TMAX - T0)
        END IF
      ELSE IF(TIME(2).GT.KSTEPG) THEN !STRESS-DEPENDENT GROWTH
        IF(CT.LE.T0) THEN
          AG1 = AG1T
          AG2 = AG2T
          AG3 = AG3T
        END IF
        IF(CT.GT.KSTEPG.AND.CT.LE.KENDG) THEN
            IF (KSG3.GE.0.) THEN
             KAG1T = (KACONSTANT*KSG1+KGBASE)
     1          * (1. - KBMP) !NO GROWTH IF BMP
     3          * (1. - KR1*KSHH) * KFGF
            ELSE
             KAG1T = 0.
            END IF
            IF (KSG3.GE.0.) THEN
             KAG2T = (KACONSTANT*KSG2+KGBASE)
     1          * (1. - KBMP) !NO GROWTH IF BMP
     3          * (1. - KR1*KSHH) * KFGF
            ELSE
             KAG2T = 0.
            END IF
             KAG3T = (KBCONSTANT)
     1          * (1. - KRP) !NO THICKENING AT ROOFPLATE
        AG1 = STATEV(1) * (1 + KAG1T*DTIME)
        AG2 = STATEV(2) * (1 + KAG2T*DTIME)
        AG3 = STATEV(3) * (1 + KAG3T*DTIME)
```

```
      END IF
      IF(CT.GT.KENDG) THEN
      AG1 = STATEV(1)
      AG2 = STATEV(2)
      AG3 = STATEV(3)
      END IF
    END IF

    GI(1,1) = 1.D0/AG1
    GI(2,2) = 1.D0/AG2
    GI(3,3) = 1.D0/AG3
    GI(1,2) = 0.D0
    GI(1,3) = 0.D0
    GI(2,3) = 0.D0
    GI(2,1) = 0.D0
    GI(3,1) = 0.D0
    GI(3,2) = 0.D0

C Remove growth part
    CALL MULMAT(F2, GI, FE)

C
C VOLUMETRIC CONSTANTS
C
C DUDJ = dU/dJ, D2UDJ2 = (d/dJ)(dU/dJ)
    CALL DETMAT(FE,AJ1)
    DUDJ = (-(1/AJ1) + AJ1)/KD1
    D2UDJ2 = (1 + AJ1**(-2))/KD1

C
C DISTORTIONAL DEFORMATION GRADIENT
C
    DO K1=1,3
      DO K2=1,3
        FBAR1(K1,K2) = (AJ1**(-1.D0/3.D0))*FE(K1,K2)
      END DO
    END DO

C
C DISTORTIONAL STRAIN COMPONENTS
C
    CALL TRMAT(FBAR1, FBAR1T)
    CALL MULMAT(FBAR1T, FBAR1, CBAR1)
    Ebar1 = (CBAR1(1,1) - 1.D0)/2.D0
    Ebar2 = (CBAR1(2,2) - 1.D0)/2.D0
    Ebar3 = (CBAR1(3,3) - 1.D0)/2.D0
    Ebar4 = CBAR1(1,2)/2.D0
    Ebar5 = CBAR1(1,3)/2.D0
    Ebar6 = CBAR1(2,3)/2.D0

C Anisotropy Constant
    AQ = b1111*Ebar1*Ebar1 + b1122*Ebar1*Ebar2 +
   1 b1133*Ebar1*Ebar3 +
```

```
     1 b1112*Ebar1*Ebar4 + b1113*Ebar1*Ebar5 + b1123*Ebar1*Ebar6 +
     2 b2222*Ebar2*Ebar2 + b2233*Ebar2*Ebar3 + b2212*Ebar2*Ebar4 +
     3 b2213*Ebar2*Ebar5 + b2223*Ebar2*Ebar6 + b3333*Ebar3*Ebar3 +
     4 b3312*Ebar3*Ebar4 + b3313*Ebar3*Ebar5 + b3323*Ebar3*Ebar6 +
     5 b1212*Ebar4*Ebar4 + b1213*Ebar4*Ebar5 + b1223*Ebar4*Ebar6 +
     6 b1313*Ebar5*Ebar5 + b1323*Ebar5*Ebar6 + b2323*Ebar6*Ebar5

C
C CAUCHY STRESS
C
C DWDE = dW/dE
      DWDE(1,1) = 2.*KC1
      DWDE(1,2) = 0
      DWDE(1,3) = 0
      DWDE(2,1) = 0
      DWDE(2,2) = 2.*KC1
      DWDE(2,3) = 0
      DWDE(3,1) = 0
      DWDE(3,2) = 0
      DWDE(3,3) = 2.*KC1

      CALL MULMAT(FBAR1, DWDE, S1)
      CALL MULMAT(S1, FBAR1T, S2)
      CALL DEV(S2, S3)

      DO K1=1,3
        DO K2=1,3
          S4(K1,K2) = S3(K1,K2)/AJ1 + DUDJ*DI(K1,K2)
          S4A(K1,K2) = S3(K1,K2)/AJ1
        END DO
      END DO

C Rotate stresses back to global system
      CALL MULMAT(RIT,S4,S5)
      CALL MULMAT(S5,RI,S6)

      STRESS(1) = S6(1,1)
      STRESS(2) = S6(2,2)
      STRESS(3) = S6(3,3)
      STRESS(4) = S6(1,2)
      STRESS(5) = S6(1,3)
      STRESS(6) = S6(2,3)

C
C DDSDDE
C
C D2WDE2 = d2Wbar/(dEbar)-dyad-(dEbar)
      D2WDE2(1,1,1,1) = 0
      D2WDE2(1,1,1,2) = 0
      D2WDE2(1,1,1,3) = 0
      D2WDE2(1,1,2,1) = 0
      D2WDE2(1,1,2,2) = 0
      D2WDE2(1,1,2,3) = 0
```

D2WDE2(1,1,3,1) = 0
D2WDE2(1,1,3,2) = 0
D2WDE2(1,1,3,3) = 0
D2WDE2(1,2,1,1) = 0
D2WDE2(1,2,1,2) = 0
D2WDE2(1,2,1,3) = 0
D2WDE2(1,2,2,1) = 0
D2WDE2(1,2,2,2) = 0
D2WDE2(1,2,2,3) = 0
D2WDE2(1,2,3,1) = 0
D2WDE2(1,2,3,2) = 0
D2WDE2(1,2,3,3) = 0
D2WDE2(1,3,1,1) = 0
D2WDE2(1,3,1,2) = 0
D2WDE2(1,3,1,3) = 0
D2WDE2(1,3,2,1) = 0
D2WDE2(1,3,2,2) = 0
D2WDE2(1,3,2,3) = 0
D2WDE2(1,3,3,1) = 0
D2WDE2(1,3,3,2) = 0
D2WDE2(1,3,3,3) = 0
D2WDE2(2,1,1,1) = 0
D2WDE2(2,1,1,2) = 0
D2WDE2(2,1,1,3) = 0
D2WDE2(2,1,2,1) = 0
D2WDE2(2,1,2,2) = 0
D2WDE2(2,1,2,3) = 0
D2WDE2(2,1,3,1) = 0
D2WDE2(2,1,3,2) = 0
D2WDE2(2,1,3,3) = 0
D2WDE2(2,2,1,1) = 0
D2WDE2(2,2,1,2) = 0
D2WDE2(2,2,1,3) = 0
D2WDE2(2,2,2,1) = 0
D2WDE2(2,2,2,2) = 0
D2WDE2(2,2,2,3) = 0
D2WDE2(2,2,3,1) = 0
D2WDE2(2,2,3,2) = 0
D2WDE2(2,2,3,3) = 0
D2WDE2(2,3,1,1) = 0
D2WDE2(2,3,1,2) = 0
D2WDE2(2,3,1,3) = 0
D2WDE2(2,3,2,1) = 0
D2WDE2(2,3,2,2) = 0
D2WDE2(2,3,2,3) = 0
D2WDE2(2,3,3,1) = 0
D2WDE2(2,3,3,2) = 0
D2WDE2(2,3,3,3) = 0
D2WDE2(3,1,1,1) = 0
D2WDE2(3,1,1,2) = 0
D2WDE2(3,1,1,3) = 0
D2WDE2(3,1,2,1) = 0
D2WDE2(3,1,2,2) = 0

```
      D2WDE2(3,1,2,3) = 0
      D2WDE2(3,1,3,1) = 0
      D2WDE2(3,1,3,2) = 0
      D2WDE2(3,1,3,3) = 0
      D2WDE2(3,2,1,1) = 0
      D2WDE2(3,2,1,2) = 0
      D2WDE2(3,2,1,3) = 0
      D2WDE2(3,2,2,1) = 0
      D2WDE2(3,2,2,2) = 0
      D2WDE2(3,2,2,3) = 0
      D2WDE2(3,2,3,1) = 0
      D2WDE2(3,2,3,2) = 0
      D2WDE2(3,2,3,3) = 0
      D2WDE2(3,3,1,1) = 0
      D2WDE2(3,3,1,2) = 0
      D2WDE2(3,3,1,3) = 0
      D2WDE2(3,3,2,1) = 0
      D2WDE2(3,3,2,2) = 0
      D2WDE2(3,3,2,3) = 0
      D2WDE2(3,3,3,1) = 0
      D2WDE2(3,3,3,2) = 0
      D2WDE2(3,3,3,3) = 0

C
C TENSOR OF ELASTICITY LOOP
C
C DEVIATORIC STRESS DEVS = DEV(S4)
      CALL DEV(S4,DEVS)

C WC = D2WDE2:C
      DO K1=1,3
        DO K2=1,3
          DO K3=1,3
            DO K4=1,3
              WC(K1,K2) = WC(K1,K2) +
     1 D2WDE2(K1,K2,K3,K4)*CBAR1(K3,K4)
            END DO
          END DO
        END DO
      END DO

C FWCF1 = F.(D2WDE2:C).TRANSPOSE(F)
      CALL MULMAT(FBAR1,WC,FWC)
      CALL MULMAT(FWC,FBAR1T,FWCF1)

C FULL COMPONENT LOOP
      DO K1=1,3
        DO K2=1,3
          DO K3=1,3
            DO K4=1,3
              SUMCSP1 = 0.D0
              SUMCWC1 = 0.D0
              DO L1=1,3
```

```
              SUMCSP2 = 0.D0
              DO L2=1,3
                SUMCSP3 = 0.D0
                SUMCWC2 = 0.D0
                DO L3=1,3
                  SUMCSP4 = 0.D0
                  DO L4=1,3
                    SUMCSP4 = SUMCSP4 +
     1 D2WDE2(L1,L2,L3,L4)*FBAR1(K4,L4)
                    SUMCWC2 = SUMCWC2 +
     1 D2WDE2(L1,L2,L3,L4)*CBAR1(L3,L4)
                  END DO
                SUMCSP3 = SUMCSP3 + SUMCSP4*FBAR1(K3,L3)
                END DO
              SUMCSP2 = SUMCSP2 + SUMCSP3*FBAR1(K2,L2)
              SUMWCW1 = SUMWCW1 + SUMWCW2*CBAR1(L1,L2)
              END DO
            SUMCSP1 = SUMCSP1 + SUMCSP2*FBAR1(K1,L1)
            END DO

            CSP = SUMCSP1/AJ1
            CWC = SUMCWC1/(9.D0*AJ1)

            FWCF = DI(K1,K2)*FWCF1(K3,K4)/(3.D0*AJ1)
     1 + FWCF1(K1,K2)*DI(K3,K4)/(3.D0*AJ1)

            CS1 = (2.D0/3.D0)*(DEVS(K1,K2)*DI(K3,K4) +
     1 DI(K1,K2)*DEVS(K3,K4))

            CS2 = (2.D0/3.D0)*(S2(1,1) +
     1 S2(2,2) + S2(3,3))*(SYM(K1,K2,K3,K4) -
     2 (1.D0/3.D0)*DI(K1,K2)*DI(K3,K4))/AJ1

            U1 = DUDJ*(DI(K1,K2)*DI(K3,K4) -
     1 2.D0*SYM(K1,K2,K3,K4))

            U2 = AJ1*D2UDJ2*DI(K1,K2)*DI(K3,K4)

            DSIG = (S4(K1,K4)*DI(K2,K3) + S4(K2,K3)*DI(K1,K4) +
     1 S4(K1,K3)*DI(K2,K4) + S4(K2,K4)*DI(K1,K3))/2.D0

            CL1(K1,K2,K3,K4) = CSP + CWC - FWCF - CS1 +
     1 CS2 + U1 + U2 + DSIG

          END DO
        END DO
      END DO
    END DO

C Rotate CL back to global system
    DO K1=1,3
      DO K2=1,3
        DO K3=1,3
```

```
          DO K4=1,3
            SUM1 = 0.D0
            DO L1=1,3
              SUM2 = 0.D0
              DO L2=1,3
                SUM3 = 0.D0
                DO L3=1,3
                  SUM4 = 0.D0
                  DO L4=1,3
                    SUM4 = SUM4 + CL1(L1,L2,L3,L4)*RI(L4,K4)
                  END DO
                SUM3 = SUM3 + SUM4*RI(L3,K3)
                END DO
              SUM2 = SUM2 + SUM3*RI(L2,K2)
              END DO
            SUM1 = SUM1 + SUM2*RI(L1,K1)
            END DO

            CL2(K1,K2,K3,K4) = SUM1

          END DO
        END DO
      END DO
    END DO

C Components of DDSDDE
      DDSDDE(1,1) = CL2(1,1,1,1)
      DDSDDE(1,2) = CL2(1,1,2,2)
      DDSDDE(1,3) = CL2(1,1,3,3)
      DDSDDE(1,4) = CL2(1,1,1,2)
      DDSDDE(1,5) = CL2(1,1,1,3)
      DDSDDE(1,6) = CL2(1,1,2,3)

      DDSDDE(2,2) = CL2(2,2,2,2)
      DDSDDE(2,3) = CL2(2,2,3,3)
      DDSDDE(2,4) = CL2(2,2,1,2)
      DDSDDE(2,5) = CL2(2,2,1,3)
      DDSDDE(2,6) = CL2(2,2,2,3)

      DDSDDE(3,3) = CL2(3,3,3,3)
      DDSDDE(3,4) = CL2(3,3,1,2)
      DDSDDE(3,5) = CL2(3,3,1,3)
      DDSDDE(3,6) = CL2(3,3,2,3)

      DDSDDE(4,4) = CL2(1,2,1,2)
      DDSDDE(4,5) = CL2(1,2,1,3)
      DDSDDE(4,6) = CL2(1,2,2,3)

      DDSDDE(5,5) = CL2(1,3,1,3)
      DDSDDE(5,6) = CL2(1,3,2,3)

      DDSDDE(6,6) = CL2(2,3,2,3)
```

```
C Fill symmetric parts of DDSDDE
      DO K1=2,6
        K3 = K1-1
        DO K2=1,K3
          DDSDDE(K1,K2) = DDSDDE(K2,K1)
        END DO
      END DO
C
C SPECIFIC ELASTIC STRAIN ENERGY: SSE
C
      SSE = KC1*(0. + 2.*(Ebar1 + Ebar2 + Ebar3))

C
C ROTATIONS
C

C Use the A_ij bases in the initial increment.
C     IF(KINC.EQ.1) THEN
      IF(CT.LE.T0) THEN
        R0 = RI
C Use the updated bases in later increments.
      ELSE
        R0(1,1) = RTOTAL(NLINE,1)
        R0(2,1) = RTOTAL(NLINE,2)
        R0(3,1) = RTOTAL(NLINE,3)

        R0(1,2) = RTOTAL(NLINE,4)
        R0(2,2) = RTOTAL(NLINE,5)
        R0(3,2) = RTOTAL(NLINE,6)

        R0(1,3) = RTOTAL(NLINE,7)
        R0(2,3) = RTOTAL(NLINE,8)
        R0(3,3) = RTOTAL(NLINE,9)
      END IF
      CALL TRMAT(R0,R0T)

      CALL MULMAT(RI,DROT,DROT1) !OR NOT?
      CALL MULMAT(DROT1,RIT,DROT2) !OR NOT?
      CALL MULMAT(DROT2,RI,R) !Changed from R0 to RI
C     ^depends if NLGEOM is on or off

C Save initial total rotation
      RTOTAL(NLINE,1) = R0(1,1)
      RTOTAL(NLINE,2) = R0(2,1)
      RTOTAL(NLINE,3) = R0(3,1)

      RTOTAL(NLINE,4) = R0(1,2)
      RTOTAL(NLINE,5) = R0(2,2)
      RTOTAL(NLINE,6) = R0(3,2)

      RTOTAL(NLINE,7) = R0(1,3)
      RTOTAL(NLINE,8) = R0(2,3)
      RTOTAL(NLINE,9) = R0(3,3)
```

```
C Save incremental rotation
      DROTINC(NLINE,1) = DROT2(1,1)
      DROTINC(NLINE,2) = DROT2(2,1)
      DROTINC(NLINE,3) = DROT2(3,1)

      DROTINC(NLINE,4) = DROT2(1,2)
      DROTINC(NLINE,5) = DROT2(2,2)
      DROTINC(NLINE,6) = DROT2(3,2)

      DROTINC(NLINE,7) = DROT2(1,3)
      DROTINC(NLINE,8) = DROT2(2,3)
      DROTINC(NLINE,9) = DROT2(3,3)

C Calculate current increment total rotation transposed.
      CALL TRMAT(R,RT)

C
C CAUCHY STRESSES IN ROTATED MATERIAL DIRECTION (IF RI=MATERIAL DIRECTION)
C
      CALL MULMAT(RT,S4,SOUT1)
      CALL MULMAT(SOUT1,R,SOUT2) !ROTATE BACK TO INITIAL XYZ
      CALL MULMAT(RI,SOUT2,S4MX)
      CALL MULMAT(S4MX,RIT,S4MR) !ROTATE TO MATERIAL DIRECTIONS

      CALL TRMAT(F2,FT)
      CALL MULMAT(FT,F2,C)

      DO K1=1,3
        DO K2=1,3
          IF(K1.EQ.K2) THEN
            E1(K1,K2) = (C(K1,K2) - 1.D0)/2.D0
          ELSE
            E1(K1,K2) = C (K1,K2)/2.D0
          END IF
        END DO
      END DO

C
C LOCAL STRESSES AND GROWTH
C
      STATEV(1) = AG1 !T1 GROWTH
      STATEV(2) = AG2 !T2 GROWTH
      STATEV(3) = AG3 !N GROWTH
      STATEV(4) = S4MR(1,1)/KC1 !T1 MATERIAL STRESS
      STATEV(5) = S4MR(2,2)/KC1 !T2 MATERIAL STRESS
      STATEV(6) = S4MR(3,3)/KC1 !N MATERIAL STRESS
      STATEV(7) = S4MR(1,2)/KC1 !IN-PLANE SHEAR MATERIAL STRESS
      STATEV(8) = KC1
      STATEV(9) = (STATEV(4)+STATEV(5))/2
      STATEV(12)= KBMP
      STATEV(13)= KRP
      STATEV(14)= KFGF
```

```
c 1ST (MAX) PRINCIPAL STRESS DIRECTION COSINES
c     STATEV(7)  = AN(1,1) !X COMPONENT OF UNIT VECTOR
c     STATEV(8)  = AN(1,2) !Y COMPONENT OF UNIT VECTOR
c     STATEV(9)  = AN(1,3) !Z COMPONENT OF UNIT VECTOR
c 2ND (MIN) PRINCIPAL STRESS DIRECTION COSINES
c     STATEV(10) = AN(2,1) !X COMPONENT OF UNIT VECTOR
c     STATEV(11) = AN(2,2) !Y COMPONENT OF UNIT VECTOR
c     STATEV(12) = AN(2,3) !Z COMPONENT OF UNIT VECTOR
c 3RD (MID) PRINCIPAL STRESS DIRECTION COSINES
c     STATEV(13) = AN(3,1) !X COMPONENT OF UNIT VECTOR
c     STATEV(14) = AN(3,2) !Y COMPONENT OF UNIT VECTOR
c     STATEV(15) = AN(3,3) !Z COMPONENT OF UNIT VECTOR

C
C END UMAT
C
      RETURN
      END

C
C AUXILIARY FUNCTIONS
C
C TRMAT - Gives B, the 3x3 matrix transpose of A.
C MULMAT - Gives C the 3x3 matrix multiplication of A.B.
C MATINV - Gives B, the 3x3 matrix inverse of A.
C DETMAT - Gives the determinant of a 3x3 matrix A.
C DEV - Gives B, the 3x3 devaitoric part of 3x3 matrix A.

C
C TRMAT
C    Subroutine to transpose a 3x3 matrix A into a 3x3 matrix AT.
C INPUTS: A - 3x3 matrix.
C         AT - The 3x3 matrix transpose of A.
C
      SUBROUTINE TRMAT(A,AT)

      INCLUDE 'ABA_PARAM.INC'

      DIMENSION A(3,3), AT(3,3)

      DO K1=1,3
        DO K2=1,3
          AT(K1,K2) = A(K2,K1)
        END DO
      END DO

      RETURN
      END

C
C MULMAT
C   Subroutine which computes the matrix C = A*B,
```

```
C where C, A, and B are 3x3 matrices.
C INPUTS: A - 3x3 matrix.
C       B - 3x3 matrix.
C       C - 3x3 matrix, such that C = A*B.
C
      SUBROUTINE MULMAT(A,B,C)

      INCLUDE 'ABA_PARAM.INC'

      DIMENSION A(3,3), B(3,3), C(3,3)

      C(1,1) = A(1,1)*B(1,1) + A(1,2)*B(2,1) + A(1,3)*B(3,1)
      C(1,2) = A(1,1)*B(1,2) + A(1,2)*B(2,2) + A(1,3)*B(3,2)
      C(1,3) = A(1,1)*B(1,3) + A(1,2)*B(2,3) + A(1,3)*B(3,3)

      C(2,1) = A(2,1)*B(1,1) + A(2,2)*B(2,1) + A(2,3)*B(3,1)
      C(2,2) = A(2,1)*B(1,2) + A(2,2)*B(2,2) + A(2,3)*B(3,2)
      C(2,3) = A(2,1)*B(1,3) + A(2,2)*B(2,3) + A(2,3)*B(3,3)

      C(3,1) = A(3,1)*B(1,1) + A(3,2)*B(2,1) + A(3,3)*B(3,1)
      C(3,2) = A(3,1)*B(1,2) + A(3,2)*B(2,2) + A(3,3)*B(3,2)
      C(3,3) = A(3,1)*B(1,3) + A(3,2)*B(2,3) + A(3,3)*B(3,3)

      RETURN
      END

C
C MATINV
C   Subroutine which calculates the inverse of a 3x3 matrix.
C INPUTS: A - 3x3 initial matrix.
C       AINV - 3x3 matrix, which is the inverse of A.
C
      SUBROUTINE MATINV(A,AINV)

      INCLUDE 'ABA_PARAM.INC'

      DIMENSION A(3,3), AINV(3,3), COFA(3,3), ADJA(3,3)
C
C Compute the cofactor of A:
C
      COFA(1,1) = A(2,2)*A(3,3) - A(2,3)*A(3,2)
      COFA(1,2) = (-1.D0)*(A(2,1)*A(3,3) - A(3,1)*A(2,3))
      COFA(1,3) = A(2,1)*A(3,2) - A(2,2)*A(3,1)

      COFA(2,1) = (-1.D0)*(A(1,2)*A(3,3) - A(1,3)*A(3,2))
      COFA(2,2) = A(1,1)*A(3,3) - A(1,3)*A(3,1)
      COFA(2,3) = (-1.D0)*(A(1,1)*A(3,2) - A(1,2)*A(3,1))

      COFA(3,1) = A(1,2)*A(2,3) - A(2,2)*A(1,3)
      COFA(3,2) = (-1.D0)*(A(1,1)*A(2,3) - A(2,1)*A(1,3))
      COFA(3,3) = A(1,1)*A(2,2) - A(1,2)*A(2,1)
C
C Compute the adjoint of matrix A:
```

```
C
      DO K1=1,3
        DO K2=1,3
          ADJA(K1,K1) = COFA(K2,K1)
        END DO
      END DO
C
C Compute the determinant of A:
C
      DETA = A(1,1)*COFA(1,1) + A(1,2)*COFA(1,2) + A(1,3)*COFA(1,3)
C
C Compute the inverse of A:
C
      DO K1=1,3
        DO K2=1,3
          AINV(K1,K2) = (1.D0/DETA)*ADJA(K1,K2)
        END DO
      END DO

      RETURN
      END

C
C DETMAT
C   Subroutine to calculate the determinant of a 3x3 matrix
C INPUTS: A - 3x3 matrix.
C       DETA - determinant of A.
C
      SUBROUTINE DETMAT(A, DETA)

      INCLUDE 'ABA_PARAM.INC'

      DIMENSION A(3,3)

      DETA = A(1,1)*( A(2,2)*A(3,3) - A(2,3)*A(3,2) ) -
     1 A(1,2)*( A(2,1)*A(3,3) - A(2,3)*A(3,1) ) +
     2 A(1,3)*( A(2,1)*A(3,2) - A(2,2)*A(3,1) )

      RETURN
      END

C
C DEV
C   Subroutine to calculate the deviatoric components
C of a 3x3 matrix
C INPUTS: A - 3x3 matrix.
C       DEVA - deviatoric part of A.
C
      SUBROUTINE DEV(A, DEVA)

      INCLUDE 'ABA_PARAM.INC'

      DIMENSION A(3,3), DEVA(3,3)
```

```
      TRA = A(1,1) + A(2,2) + A(3,3)

      DO K1=1,3
        DO K2=1,3
          IF(K1.EQ.K2) THEN
            DEVA(K1,K2) = A(K1,K2) - (1.D0/3.D0)*TRA
          ELSE
            DEVA(K1,K2) = A(K1,K2)
          END IF
        END DO
      END DO

      RETURN
      END


C
C END SUBROUTINES
C
```

C.2 Strain energy minimization in MATLAB

The following code minimizes surface strain energy between two surfaces. It requires two closed surfaces (on which to minimize strain energy) as well as a spherical surface which they can be mapped to, all with the same number of vertices and connections. This code does not match landmarks, so surfaces should first be brought into approximate register for best results.

This code follows the approach outlined in Knutsen et al. (2010), replacing the steps requiring transition from MATLAB to Comsol Multiphysics (solving equations of motion). Note that this code calls other MATLAB codes developed in Knutsen et al. (2010). These can be found in Appendix 2 of Knutsen (2010). Additional codes for importing GIfTI surface files can be found at https://www.artefact.tk/software/matlab/gifti/

Relax.m

```
% POST-PROCESSING STRAIN RELAXATION CODE
% Written by Kara E Garcia and Philip V Bayly
% Based on technique by Andy K Knutsen and Philip V Bayly

% THEORY:
%
% F = H*G1*Hinv*F0
%   where H=dx/dy, G1=dy'/dy, F0=dx/dX
%
% W = mu/2*(I1st2D - 2) + kappa/2*(J + 1/J - 2)
%   where I1st2D and J are functions of F
%   = mu/2*(R + 1/R - 2) + kappa/2*(J + 1/J - 2)
%   where R=maxstretch/minstretch and J=maxstretch*minstretch
%
% Q = Hp'*P*F0'*inv(H')
%   where Pij=(W1-W2)/(Fij1-Fij2)
%
% nu*vdot(i) = dQ(i) + g(i)
%   such that the updated G1 = I + del*v

% Input: OAS (x) - Older anatomical surface (+normals)
%        YAS (X) - Younger anatomical surface (+normals)
%        OSS (y) - Older spherical surface
%        YSS (Y) - Younger spherical surface
%        Similarity function on sphere (g)
% Output: ROAS (x') - Relaxed older anatomical surface
%         ROSS (y') - Relaxed older spherical surface

%%%%%%%%%%%%%%%%%%%%%%%%%%%%%%%%%%%%%%%%%%%%%%%%%%%%%%%%%%%%%%%%%%%%%%%%%%%%%%%
% INITIAL DEFINITIONS
%%%%%%%%%%%%%%%%%%%%%%%%%%%%%%%%%%%%%%%%%%%%%%%%%%%%%%%%%%%%%%%%%%%%%%%%%%%%%%%

close all;

Wopt = 'neoalt'; %choose neo, blatzko, neoinc, or neoalt for material
kappa = 10; %bulk modulus
mu = 1; %shear modulus
PR = 0.5*(3*kappa - 2*mu) / (3*kappa + mu); %Poisson's ratio
nu = 1; %viscosity

subject = 'MSMoutput/WUNDER_ico6/caf009.R.bc';
radius = 100; %for MSM, radius always = 100mm
ptfit = 12; %number of points to fit, must be >=6 (5-6 surround each vertex)
deltat = 0.01; %initial time increment
deltaG = 0.001; %for finite difference calculation of dW/dG
itmax = 25; %number of iterations
fit_radius = 8; %for curvature calculations

viewleft = [-1 0 0]; %lateral view for left hemisphere
viewright = [1 0 0]; %lateral view for right hemisphere
viewtop = [0 0 -1]; %top view w.r.t. model
perspective = viewtop; %choose view for future plots
distaxis = [-.2,.2];

% IMPORT INITIAL SURFACES
%%%%%%%%%%%%%%%%%%%%%%%%%%%%%%%%

%Load YAS (X) from GIFTI
FV = gifti('ico4sphere.LR.reg.surf.gii');
index = FV.vertices(:,1);
figure(1)
```

```
hold on;
p = patch('Faces',FV.faces,'Vertices',FV.vertices, ...
    'FaceColor','green','EdgeColor','none');
view(perspective);axis image;grid on
title('YAS');
camlight headlight
hold off

%Load OAS (x) from GIFTI
fv = gifti('ico4pumpkin_half2.surf.gii');
index = fv.vertices(:,1);
figure(2)
hold on;
p = patch('Faces',fv.faces,'Vertices',fv.vertices, ...
    'FaceColor','green','EdgeColor','none');
view(perspective);axis image;grid on
title('OAS');
camlight headlight
hold off

%Load OSS (y) from GIFTI
sph = gifti('ico4sphere.LR.reg.surf.gii');
index = sph.vertices(:,1);
figure(3)
hold on;
p = patch('Faces',sph.faces,'Vertices',sph.vertices, ...
    'FaceColor','green','EdgeColor','none');
view(perspective);axis image;grid on
title('OSS');
camlight headlight
hold off

%Surface normals from GIFTI
NS = sph.vertices./radius;
ns = sph.vertices./radius;
nss = sph.vertices./radius;

X = [FV.vertices(:,1),FV.vertices(:,2),FV.vertices(:,3)]; %3D coords
vertices = length(FV.vertices(:,1)); %# vertices
triangles = length(FV.faces(:,1)); %# triangles
h = ((4*pi*radius^2)*2/triangles)^0.5; %average link length (OSS), mm
angle0 = (2/pi/triangles)^0.5; %average link angle (OSS), radians

% INITIALIZE MATRICES
%%%%%%%%%%%%%%%%%%%%%%%%%%%%%%%%
W0 = zeros(vertices,1);
J0 = zeros(vertices,1);
I10 = zeros(vertices,1);
lambdamax = zeros(vertices,1);
lambdamin = zeros(vertices,1);
R0 = zeros(vertices,1);
I(1,1) = 1;
I(1,2) = 0;
I(1,3) = 0;
I(2,1) = 0;
I(2,2) = 1;
I(2,3) = 0;
I(3,1) = 0;
I(3,2) = 0;
I(3,3) = 1;
Q11 = zeros(vertices,1);
Q12 = zeros(vertices,1);
Q13 = zeros(vertices,1);
Q21 = zeros(vertices,1);
Q22 = zeros(vertices,1);
```

```
Q23 = zeros(vertices,1);
Q31 = zeros(vertices,1);
Q32 = zeros(vertices,1);
Q33 = zeros(vertices,1);
g1 = zeros(vertices,1);
g2 = zeros(vertices,1);
g3 = zeros(vertices,1);
V = zeros(vertices,3);
v = zeros(vertices,3);
vs = zeros(vertices,3);
ys = zeros(vertices,3);
xp = zeros(vertices,3);
Wavg = zeros(itmax,2);

%%%%%%%%%%%%%%%%%%%%%%%%%%%%%%%%%%%%%%%%%%%%%%%%%%%%%%%%%%%%%%%%%%%%%%%%%%%%
% CALCULATIONS
%%%%%%%%%%%%%%%%%%%%%%%%%%%%%%%%%%%%%%%%%%%%%%%%%%%%%%%%%%%%%%%%%%%%%%%%%%%%
y = [sph.vertices(:,1),sph.vertices(:,2),sph.vertices(:,3)]; %3D coords

for i=1:vertices
    phicompare(i) = atan2(y(i,2),y(i,1)); %azimuth
end

figure(4)
patch('Faces',fv.faces,'Vertices',fv.vertices, ...
            'FaceVertexCData',phicompare','FaceColor','interp',...
            'EdgeColor','none');
        xlabel('x'),ylabel('y'),zlabel('z')
        view(perspective);daspect([1 1 1]),grid off
        h1 = gcf;set(h1,'color',[1 1 1]);
        colorbar; %camlight;
        colormap(gca,'lines');

t = 0; %initial time
for count=1:itmax;
    x = [fv.vertices(:,1),fv.vertices(:,2),fv.vertices(:,3)]; %3D coords
    y = [sph.vertices(:,1),sph.vertices(:,2),sph.vertices(:,3)]; %3D coords

    % Calculate F0 -> W0 -> Q
    %%%%%%%%%%%%%%%%%%%%%%%%%%%%%
    if t==0 %only find neighboring points once, then keep set
        [Hi,keep_pts]=calc_defgrad_KG(y,x,nss,ptfit); %H = dx/dy
    else
        [Hi,keep_pts]=calc_defgrad_KG(y,x,nss,ptfit,keep_pts); %H = dx/dy
    end
    [F0i,keep_pts]=calc_defgrad_KG(X,x,NS,ptfit,keep_pts); %F0 = dx/dX

    for i=1:vertices
        F0 = F0i(:,:,i);
        H = Hi(:,:,i);
        I10(i,:) = trace(F0'*F0);
        I30 = det(F0'*F0);
        J0(i,:) = I30^0.5;
        R0(i,:) = real(((I10(i,:) - 1)/J0(i,:) + ...
            sqrt(((I10(i,:) - 1)/J0(i,:))^2 - 4)) / 2);
        if J0(i,:) >= 1
            Jprime = J0(i,:);
        else
            Jprime = 1/J0(i,:);
        end
        I1st0(i,:) = I10(i,:)*I30^(-1/3);
        if strcmp(Wopt,'neo')
            %Neo-Hookean material:
            W0(i,:) = mu/2*(I1st0(i,:)-3) + kappa/2*(J0(i,:)-1)^2;
        elseif strcmp(Wopt,'neoinc')
```

```
    %Incompressible Neo-Hookean material:
    W0(i,:) = mu/2*(I10(i,:)-3); %not a good idea
elseif strcmp(Wopt,'blatzko')
    %Blatz-Ko material:
    W0(i,:) = mu/2*(I10(i,:)-3 + ...
        (1-2*PR)/PR*(J0(i,:)^(-2*PR/(1-2*PR))-1));
elseif strcmp(Wopt,'neoalt')
    %Balanced alternative Neo-Hookean material
    W0(i,:) = mu/2*((I10(i,:)-1)./J0(i,:)-2) + ...
        kappa/2*(J0(i,:)+1/J0(i,:)-2);
else
    disp('Invalid material choice')
end

% 1st PK stress: Qij=(Wt-W)/(Gijt-Gij) - finite difference method
for m=1:3
    for n=1:3
        G1 = I; G2 = I; Hp = H; %let Hprime = H since small delta
        G1(m,n) = G1(m,n) + deltaG;
        G2(m,n) = G2(m,n) - deltaG;
        F1 = Hp*G1*inv(H)*F0;
        F2 = Hp*G2*inv(H)*F0;
        I11 = trace(F1'*F1);
        I12 = trace(F2'*F2);
        I31 = det(F1'*F1);
        I32 = det(F2'*F2);
        J1 = I31^0.5;
        J2 = I32^0.5;
        if J1 >= 1
            J1prime = J1;
        else
            J1prime = 1/J1;
        end
        if J2 >= 1
            J2prime = J2;
        else
            J2prime = 1/J2;
        end
        I1st1 = I11*I31^(-1/3);
        I1st2 = I12*I32^(-1/3);
        if strcmp(Wopt,'neo')
            %Neo-Hookean material:
            W1 = mu/2*(I1st1 - 3) + kappa/2*(J1 - 1)^2;
            W2 = mu/2*(I1st2 - 3) + kappa/2*(J2 - 1)^2;
        elseif strcmp(Wopt,'neoinc')
            %Incompressible Neo-Hookean material:
            W1 = mu/2*(I11 - 3);
            W2 = mu/2*(I12 - 3);
        elseif strcmp(Wopt,'blatzko')
            %Blatz-Ko material:
        W1 = mu/2*(I11-3 + (1-2*PR)/PR*(J1^(-2*PR/(1-2*PR))-1));
        W2 = mu/2*(I12-3 + (1-2*PR)/PR*(J2^(-2*PR/(1-2*PR))-1));
        elseif strcmp(Wopt,'neoalt')
        %Balanced alternative Neo-Hookean material
        W1 = mu/2*((I11-1)/J1 - 2) + kappa/2*(J1 + 1/J1 - 2);
        W2 = mu/2*((I12-1)/J2 - 2) + kappa/2*(J2 + 1/J2 - 2);
        else
            disp('Invalid material choice')
        end

        Q(m,n) = (W1 - W2)/deltaG./J0(i,:);
    end
end

Q11(i,:) = Q(1,1);
```

```
    Q12(i,:) = Q(1,2);
    Q13(i,:) = Q(1,3);
    Q21(i,:) = Q(2,1);
    Q22(i,:) = Q(2,2);
    Q23(i,:) = Q(2,3);
    Q31(i,:) = Q(3,1);
    Q32(i,:) = Q(3,2);
    Q33(i,:) = Q(3,3);

end

if t==0
    Jmax = max(J0); Jmin = min(J0);
    I1max = max(I10); I1min = min(I10);
    I1stmax = max(I1st0); I1stmin = min(I1st0);
end

% Calculate v, constrain radial
%%%%%%%%%%%%%%%%%%%%%%%%%%%%%%%%

% Spatial derivative of Q (dQ_ij/dy_j) - polynomial fit
[dQ11d1,dQ12d2,dQ13d3,dQ21d1,dQ22d2,dQ23d3,dQ31d1,dQ32d2,dQ33d3] = ...
   calc_spatial_linear2(y,keep_pts,Q11,Q12,Q13,Q21,Q22,Q23,Q31,Q32,Q33);

vmag = h; %initialize vmag=h to start loop
%Decrease timestep if displacements are too large
while max(vmag) > 0.1*h %|| deltat > 10
    deltat = deltat/2;

    % Calculate displacement vector: nu*vdot_i = dQ_ij/dy_j + g_i
    v(:,1) = deltat/nu*(dQ11d1 + dQ12d2 + dQ13d3 + g1);
    v(:,2) = deltat/nu*(dQ21d1 + dQ22d2 + dQ23d3 + g2);
    v(:,3) = deltat/nu*(dQ31d1 + dQ32d2 + dQ33d3 + g3);

    %Convert v to spherical coordinates, remove r-displacement, return
    for i=1:vertices
        rho = sqrt(y(i,1)^2+y(i,2)^2); %cylindrical r
        theta = atan2(rho,y(i,3)); %elevation
        phi = atan2(y(i,2),y(i,1)); %azimuth
        Rsph(1,1) = sin(theta)*cos(phi);
        Rsph(1,2) = sin(theta)*sin(phi);
        Rsph(1,3) = cos(theta);
        Rsph(2,1) = cos(theta)*cos(phi);
        Rsph(2,2) = cos(theta)*sin(phi);
        Rsph(2,3) = -1*sin(theta);
        Rsph(3,1) = -1*sin(phi);
        Rsph(3,2) = cos(phi);
        Rsph(3,3) = 0;

        vs(i,:) = (Rsph*v(i,:)')';
        vs(i,1) = 0; % REMOVE RADIAL DISPLACEMENT
        v(i,:) = (inv(Rsph)*vs(i,:)')';
    end
    vmag = (v(:,1).^2 + v(:,2).^2 + v(:,3).^2).^0.5;
end

if t==0
    Wmax = max(W0);
    Wmin = min(W0);
end

if cos((count-1)*pi*2)==1
    figure

    subplot(2,2,1);
```

```
    patch('Faces',fv.faces,'Vertices',fv.vertices, ...
        'FaceVertexCData',log(J0),'FaceColor','interp',...
        'EdgeColor','none');
    str = sprintf('ln(J), t = %6.2f',t); title(str);
    xlabel('x'),ylabel('y'),zlabel('z')
    view(perspective);daspect([1 1 1]),grid off
    h1 = gcf;set(h1,'color',[1 1 1]);
    colorbar; camlight;
    colormap(gca,'jet')
    caxis(distaxis);

    subplot(2,2,2);
    patch('Faces',fv.faces,'Vertices',fv.vertices, ...
        'FaceVertexCData',log(R0),'FaceColor','interp',...
        'EdgeColor','none');
    str = sprintf('ln(R), t = %6.2f',t); title(str);
    xlabel('x'),ylabel('y'),zlabel('z')
    view(perspective);daspect([1 1 1]),grid off
    h1 = gcf;set(h1,'color',[1 1 1]);
    colorbar;
    colormap(gca,'jet')
    caxis(distaxis);

    subplot(2,2,3);
    patch('Faces',fv.faces,'Vertices',fv.vertices, ...
        'FaceVertexCData',W0,'FaceColor','interp',...
        'EdgeColor','none');
    str = sprintf('W, t = %6.2f',t); title(str);
    xlabel('x'),ylabel('y'),zlabel('z')
    view(perspective);daspect([1 1 1]),grid off
    h1 = gcf;set(h1,'color',[1 1 1]);
    colorbar;
    colormap(gca,'jet')
    caxis([0 Wmax]);

    subplot(2,2,4);
    patch('Faces',sph.faces,'Vertices',y,'FaceVertexCData',...
        W0,'FaceColor','interp','EdgeColor','none');
    title('W and future displacement (100v)');
    xlabel('x'),ylabel('y'),zlabel('z')
    view(perspective);daspect([1 1 1]),grid off
    h1 = gcf;set(h1,'color',[1 1 1]);
    colorbar; camlight;
    colormap(gca,'jet')
    caxis([0 Wmax]);
    hold on
    quiver3(y(:,1),y(:,2),y(:,3),100*v(:,1),100*v(:,2),100*v(:,3),0)
    hold off

    pause(0.1)
end


% Calculate yp, correct radial
%%%%%%%%%%%%%%%%%%%%%%%%%%%%%%%%
yp = y + v; %yp = y + displacement
V = V + v; %cumulative displacement vector

% Correct for any overshoot in radial direction
yp3D = yp; %for comparison, record y before correction
for i=1:vertices
    rho = sqrt(yp(i,1)^2+yp(i,2)^2); %cylindrical r
    theta = atan2(rho,yp(i,3)); %elevation
    phi = atan2(yp(i,2),yp(i,1)); %azimuth
    Rsph(1,1) = sin(theta)*cos(phi);
```

```
        Rsph(1,2) = sin(theta)*sin(phi);
        Rsph(1,3) = cos(theta);
        Rsph(2,1) = cos(theta)*cos(phi);
        Rsph(2,2) = cos(theta)*sin(phi);
        Rsph(2,3) = -1*sin(theta);
        Rsph(3,1) = -1*sin(phi);
        Rsph(3,2) = cos(phi);
        Rsph(3,3) = 0;

        ys(i,:) = (Rsph*yp(i,:)')';
        ys(i,1) = radius; %CRITICAL! KEEP RADIUS CONSTANT
        yp(i,:) = (inv(Rsph)*ys(i,:)')';
    end
    Vc = V + yp - yp3D; %corrected total displacement vector

    % Calculate G, Hp-->xp
    %%%%%%%%%%%%%%%%%%%%%%%%%%%%%%%%

    % Reproject vertices
    [vert,face] = project_to_surf(yp,sph);

    % Project vertices from sphere sph to deformed surface fv
    xp = surf_to_surf(sph,fv,vert,face);

    sph.vertices = yp; %make yp the new y
    nss = sph.vertices/radius; %update sphere normals - easy :)
    fv.vertices = xp; %make xp the new x

    %print timestep and new time
    t = t + deltat;
    fprintf('iteration:%1.0f \t step:%8.6f \t total time:%8.4f \n',...
        count,deltat,t)
    deltat = deltat*10;
    Wsum(count,1) = t; %time
    Wsum(count,2) = sum(W0)/vertices; %average
    Wsum(count,3) = std(W0);
    Wsum(count,4) = max(W0); %max
    Wsum(count,5) = min(W0); %min

end

figure
subplot(2,2,1); plot(Wsum(:,1),Wsum(:,2))
title('Average Strain Energy')
xlabel('time (s)')
subplot(2,2,2); plot(Wsum(:,1),Wsum(:,3))
title('Standard Deviation')
xlabel('time (s)')
subplot(2,2,3); plot(Wsum(:,1),Wsum(:,4))
title('Maximum Strain Energy')
xlabel('time (s)')
subplot(2,2,4); plot(Wsum(:,1),Wsum(:,5))
title('Minimum Strain Energy')
xlabel('time (s)')

figure
hold on;
p = patch('Faces',fv.faces,'Vertices',fv.vertices, ...
    'FaceColor','green','EdgeColor','none');
view(perspective);axis image;grid on
title('ROAS');
camlight headlight
hold off

[Curvs,Residuals,CVectors]=curv(X,NS,fit_radius);
```

```
[curvs,residuals,cvectors]=curv(x,ns,fit_radius);

figure
subplot(2,2,1)
patch('Faces',FV.faces,'Vertices',FV.vertices,'FaceVertexCData',...
    Curvs.max-curvs.max,'FaceColor','interp','EdgeColor','none');
title({'Maximum Curvature Differences'});
xlabel('x'),ylabel('y'),zlabel('z')
view(perspective);daspect([1 1 1]),grid off
h1 = gcf;set(h1,'color',[1 1 1]);
colorbar

subplot(2,2,2)
patch('Faces',FV.faces,'Vertices',FV.vertices,'FaceVertexCData',...
    Curvs.min-curvs.min,'FaceColor','interp','EdgeColor','none');
title({'Minimum Curvature Differences'});
xlabel('x'),ylabel('y'),zlabel('z')
view(perspective);daspect([1 1 1]),grid off
h1 = gcf;set(h1,'color',[1 1 1]);
colorbar

subplot(2,2,3)
patch('Faces',fv.faces,'Vertices',fv.vertices,'FaceVertexCData',...
    Curvs.max-curvs.max,'FaceColor','interp','EdgeColor','none');
title({'Maximum Curvature'});
xlabel('x'),ylabel('y'),zlabel('z')
view(perspective);daspect([1 1 1]),grid off
h1 = gcf;set(h1,'color',[1 1 1]);
colorbar

subplot(2,2,4)
patch('Faces',fv.faces,'Vertices',fv.vertices,'FaceVertexCData',...
    Curvs.min-curvs.min,'FaceColor','interp','EdgeColor','none');
title({'Minimum Curvature'});
xlabel('x'),ylabel('y'),zlabel('z')
view(perspective);daspect([1 1 1]),grid off
h1 = gcf;set(h1,'color',[1 1 1]);
colorbar


figure(44)
patch('Faces',fv.faces,'Vertices',fv.vertices, ...
            'FaceVertexCData',phicompare','FaceColor','interp',...
            'EdgeColor','none');
        xlabel('x'),ylabel('y'),zlabel('z')
        view(perspective);daspect([1 1 1]),grid off
        h1 = gcf;set(h1,'color',[1 1 1]);
        colorbar;
        colormap(gca,'lines');
```

calc_spatial_linear2.m

```
function
[out1,out2,out3,out4,out5,out6,out7,out8,out9]=calc_spatial_linear2(xyz,np,varargin)

% Written by Kara E. Garcia, Dr. Phil Bayly
% Based on template of strains.m by Andrew K Knutsen, Dr. Phil Bayly

%%%%%%%%%%%%%%%%%%%%%%%%%%%%%% Describe Code %%%%%%%%%%%%%%%%%%%%%%%%%%%%%%
% [dfxxdx,dfxydy,dfyxdx,dfyydy] = spatial_deriv(xyz,dist,fxx,fxy,fyx,fyy)
%
% Output Variables
% dfxxdx - spatial derivative of fxx wrt x, and so forth
%
% Input Variables
% xyz - Surface Coordinates
% f - matrix for which we want the spatial derivatives:
%
% USAGE EXAMPLE #1 - spatial derivative of 1st PK stress on sphere, Q
% [dQ11d1,dQ12d2,dQ13d3,dQ21d1,dQ22d2,dQ23d3,dQ31d1,dQ32d2,dQ33d3] = ...
%       spatial_deriv3D(ys,dist,Q11,Q12,Q13,Q21,Q22,Q23,Q31,Q32,Q33)
% varargin => all 9 components of input matrix (3x3)
% varargout => spatial derivatives of input matrix - only the 9 we need
%
% USAGE EXAMPLE #2 - spatial derivative of vector function, v
% [dv1d1,dv1d2,dv1d3,dv2d1,dv2d2,dv3d3,dv3d1,dv3d2,dv3d3] = ...
%       spatial_deriv3D(ys,dist,v1,v2,v3)
% varargin => all 3 components of input vector (3x1)
% varargout => ALL spatial derivatives (9) of input vector
%
% USAGE EXAMPLE #3 - spatial derivatives of a scalar function, f(x,y,z)
% [dfdx,dfdy,dfdz] = spatial_deriv(y,dist,f)
% varargin => [f]
% varargout => [dfdx,dfdy,dfdz]

%%%%%%%%%%%%%%%%%%%%%%%%%% Define Input Variables %%%%%%%%%%%%%%%%%%%%%%%%%%

n_in = nargin;

switch n_in
    case 3
        matrix = 0; %just a function
        fxx = cell2mat(varargin(1));
        fxy = [];
        fxz = [];
        fyx = [];
        fyy = [];
        fyz = [];
        fzx = [];
        fzy = [];
        fzz = [];
    case 5
        matrix = 1; %input is 3x1 vector
        fxx = cell2mat(varargin(1));
        fxy = cell2mat(varargin(2));
        fxz = cell2mat(varargin(3));
        fyx = [];
        fyy = [];
        fyz = [];
        fzx = [];
        fzy = [];
        fzz = [];
    case 11
```

```
        matrix = 2; %input is 3x3 matrix
        fxx = cell2mat(varargin(1));
        fxy = cell2mat(varargin(2));
        fxz = cell2mat(varargin(3));
        fyx = cell2mat(varargin(4));
        fyy = cell2mat(varargin(5));
        fyz = cell2mat(varargin(6));
        fzx = cell2mat(varargin(7));
        fzy = cell2mat(varargin(8));
        fzz = cell2mat(varargin(9));
    otherwise
        disp('Wrong number of inputs')
        return
end

%%%%%% Assign Normal And Tangential Coordinates - Individual Surface %%%%%%

x = xyz(:,1); y = xyz(:,2); z = xyz(:,3);

%tic
for i=1:length(x),

    x0 = x(i); y0 = y(i); z0 = z(i);

    % Find Points in the Neighborhood
    dx = x - x0; %x-distance between each node (x) and current node (x0)
    dy = y - y0; %y-distance between each node (y) and current node (y0)
    dz = z - z0; %z-distance between each node (z) and current node (z0)
    DR = sqrt(dx.^2 + dy.^2 + dz.^2);

    keep_pts = np(i,:)';

    X = x(keep_pts); %x-coords of all points in patch
    Y = y(keep_pts); %y-coords of all points in patch
    Z = z(keep_pts); %z-coords of all points in patch

    alpha = [ones(size(X)) X Y Z];

    axx = alpha\fxx(keep_pts); %linear fit coeffs for fxx (f, fx)
    dfxxdx(i,:) = axx(2);
    dfxxdy(i,:) = axx(3);
    dfxxdz(i,:) = axx(4);

    if matrix > 0
        axy = alpha\fxy(keep_pts); %polynomial fit coeffs for fxy (fy)
        dfxydx(i,:) = axy(2);
        dfxydy(i,:) = axy(3);
        dfxydz(i,:) = axy(4);

        axz = alpha\fxz(keep_pts); %polynomial fit coeffs for fxz (fz)
        dfxzdx(i,:) = axz(2);
        dfxzdy(i,:) = axz(3);
        dfxzdz(i,:) = axz(4);
    end

    if matrix > 1
        ayx = alpha\fyx(keep_pts); %polynomial fit coeffs for fyx
        dfyxdx(i,:) = ayx(2);
        dfyxdy(i,:) = ayx(3);
        dfyxdz(i,:) = ayx(4);

        ayy = alpha\fyy(keep_pts); %polynomial fit coeffs for fyy
        dfyydx(i,:) = ayy(2);
        dfyydy(i,:) = ayy(3);
        dfyydz(i,:) = ayy(4);
```

```
        ayz = alpha\fyz(keep_pts); %polynomial fit coeffs for fyz
        dfyzdx(i,:) = ayz(2);
        dfyzdy(i,:) = ayz(3);
        dfyzdz(i,:) = ayz(4);

        azx = alpha\fzx(keep_pts); %polynomial fit coeffs for fzx
        dfzxdx(i,:) = azx(2);
        dfzxdy(i,:) = azx(3);
        dfzxdz(i,:) = azx(4);

        azy = alpha\fzy(keep_pts); %polynomial fit coeffs for fzy
        dfzydx(i,:) = azy(2);
        dfzydy(i,:) = azy(3);
        dfzydz(i,:) = azy(4);

        azz = alpha\fzz(keep_pts); %polynomial fit coeffs for fzz
        dfzzdx(i,:) = azz(2);
        dfzzdy(i,:) = azz(3);
        dfzzdz(i,:) = azz(4);
    end

%     % Progress Of Script
%     if i==round(length(x)/3)
%         disp('spatial gradient script 33% finished')
%     elseif i==round(length(x)*2/3)
%         disp('spatial gradient script 67% finished')
%     elseif i==length(x)
%         disp('spatial gradient script finished')
%     end
end

%%%%%%%%%%%%%%%%% Define Output Variables - Set varargout %%%%%%%%%%%%%%%%%

if matrix < 2
    out1 = dfxxdx;
    out2 = dfxxdy;
    out3 = dfxxdz;
    if matrix > 0
        out4 = dfxydx;
        out5 = dfxydy;
        out6 = dfxydz;
        out7 = dfxzdx;
        out8 = dfxzdy;
        out9 = dfxzdz;
    end
elseif matrix == 2
    out1 = dfxxdx;
    out2 = dfyxdy;
    out3 = dfzxdz;
    out4 = dfxydx;
    out5 = dfyydy;
    out6 = dfzydz;
    out7 = dfxzdx;
    out8 = dfyzdy;
    out9 = dfzzdz;
end
```

calc_defgrad_KG.m

```
function [F,np]=calc_defgrad_KG(XYZ,xyz,NS,ptfit,varargin)

% Written by Andy K Knutsen, Dr. Phil Bayly
% For use with IntraSubject Surface Registration (ISSR)
% Modified by Kara E Garcia for use with relax.m

%%%%%%%%%%%%%%%%%%%%%%%%%%%%%%%%%%%%%%%%%%%%%%%%%%%%%%%%%%%%%%%%%%%%%%%%%%%%%%%
%%%                                Description                                 %%%
%%%%%%%%%%%%%%%%%%%%%%%%%%%%%%%%%%%%%%%%%%%%%%%%%%%%%%%%%%%%%%%%%%%%%%%%%%%%%%%

% F = calc_deformation_gradient(XYZ,xyz,NS,dist)

% This function calculates the deformation gradient (or Jacobian) between
% two surfaces with a point-to-point correspondence.  We model local
% geometry as a second order polynomial, solving for the coefficients in
% the least squares sense.  The method is described in more detail in

% Filas B, Knutsen AK, Bayly PV, Taber LT. "A new method for measuring
% deformation of folding surfaces during morphogenesis." J. Biomech Engr.
% 2008: vol. 130

%%%%%%%%%%%%%%%%%%%%%%%%%%%%%%%%%%%%%%%%%%%%%%%%%%%%%%%%%%%%%%%%%%%%%%%%%%%%%%%
%%%                                Variables                                   %%%
%%%%%%%%%%%%%%%%%%%%%%%%%%%%%%%%%%%%%%%%%%%%%%%%%%%%%%%%%%%%%%%%%%%%%%%%%%%%%%%

% Input variables
% XYZ - Reference surface coordinates: [X Y Z]
% xyz - Deformed surface coordinates: [x y z]
% NS - Reference surface normal vectors: [NX NY NZ]
% dist - radius of points for local fit

% Output variables
% F - Calculated deformation gradient
% np - Points used to describe the local patch at each coordinate

%%%%%%%%%%%%%%%%%%%%%%%%%%%%%%%%%%%%%%%%%%%%%%%%%%%%%%%%%%%%%%%%%%%%%%%%%%%%%%%
%%%                          Define Input Variables                          %%%%
%%%%%%%%%%%%%%%%%%%%%%%%%%%%%%%%%%%%%%%%%%%%%%%%%%%%%%%%%%%%%%%%%%%%%%%%%%%%%%%

warning off all

% Normalize Surface Normal Vectors
Mag = sqrt(NS(:,1).^2+ NS(:,2).^2+NS(:,3).^2);
NS = [NS(:,1)./Mag NS(:,2)./Mag NS(:,3)./Mag];

XS=XYZ(:,1);YS=XYZ(:,2);ZS=XYZ(:,3);

F = zeros(3,3,length(XYZ));
np = zeros(length(XYZ),1);

%%%%%%%%%%%%%%%%%%%%%%%%%%%%%%%%%%%%%%%%%%%%%%%%%%%%%%%%%%%%%%%%%%%%%%%%%%%%%%%
%%%    Assign Normal And Tangential Coordinates - Individual Surface    %%%
%%%%%%%%%%%%%%%%%%%%%%%%%%%%%%%%%%%%%%%%%%%%%%%%%%%%%%%%%%%%%%%%%%%%%%%%%%%%%%%
n_in = nargin;

if n_in == 5
    np = cell2mat(varargin(1));
else
    np = [];
end
```

```
tic

for i=1:length(XS),

    % Make Unit Normal And Tangents,
    X0 = XYZ(i,1);Y0 = XYZ(i,2);Z0 = XYZ(i,3);
    x0 = xyz(i,1);y0 = xyz(i,2);z0 = xyz(i,3);

    e_N=NS(i,:)';

    imax = find(abs(e_N)==max(abs(e_N)),1,'first');
    switch imax
        case 1
            mag1=sqrt(e_N(3)^2+e_N(2)^2);
            if mag1==0,e_T1=[0;0;1];
            else e_T1 = [0;-e_N(3);e_N(2)]/mag1;
            end
        case 2
            mag2=sqrt(e_N(3)^2+e_N(1)^2);
            if mag2==0,e_T1=[0;0;1];
            else e_T1 = [-e_N(3);0;e_N(1)]/mag2;
            end
        case 3
            mag3=sqrt(e_N(1)^2+e_N(2)^2);
            if mag3==0,e_T1=[1;0;0];
            else e_T1 = [-e_N(2);e_N(1);0]/mag3;
            end
    end;
    e_T2 = cross(e_N,e_T1);

    % Reject Pts With Normals In Opposite Direction (Opposing Faces)
    dir_chk = e_N'*NS';

    if n_in == 5
            keep_pts = np(i,:)';
    else
            DX=XS-X0;DY=YS-Y0;DZ=ZS-Z0;
            DR = sqrt(DX.^2+DY.^2+DZ.^2)';
            [dr,ix] = sort(DR);
            keep_pts = ix(1:ptfit);
            np(i,:) = keep_pts;
    end

        XX=XS(keep_pts);YY=YS(keep_pts);ZZ=ZS(keep_pts);

        uno = zeros(length(keep_pts),1);
        DXYZ = [XX-X0,YY-Y0,ZZ-Z0];

        % Tangential And Normal Components - Individual Surface
        T1 = (e_T1'*DXYZ')';T2 = (e_T2'*DXYZ')';N = (e_N'*DXYZ')';

        %%%%%% Assign Normal And Tangential Coordinates - Atlas Surface %%%%%%%

        % fit curves for deformed vertices
        x = xyz(keep_pts,1);y = xyz(keep_pts,2);z = xyz(keep_pts,3);

        dxyz = [x-x0,y-y0,z-z0]; % diff b/w def coords and pt of interest
        t1 = (e_T1'*dxyz')';t2 = (e_T2'*dxyz')';n = (e_N'*dxyz')';

        %%%%%%%%%%%%%%%%%%%%%%%%%%%%%% Model Surface %%%%%%%%%%%%%%%%%%%%%%%%%%%%%

        % Fitting Polynomial
        alpha = [uno T1 T2 (1/2)*T1.^2 (1/2)*T2.^2 T1.*T2];
```

```
        % Coefficients For Fit N=N(T1,T2),t1=t1(T1,T2),t2=t2(T1,T2),n=n(T1,T2)
        a = alpha\N;b = alpha\t1;c = alpha\t2;d = alpha\n;

        % compute derivatives N,t1,t2,n wrt T1 and T2 at (T10,T20)
        dNdT1 = a(2);
        dNdT2 = a(3);
        dt1dT1 = b(2);
        dt1dT2 = b(3);
        dt2dT1 = c(2);
        dt2dT2 = c(3);
        dndT1 = d(2);
        dndT2 = d(3);

        % Describe Transformation Matrix
        T_mat = [e_T1 e_T2 e_N]';

        %%%%%%%%%%%%%%%%%%%%%%%%%% Calculate Strain %%%%%%%%%%%%%%%%%%%%%%%%%%

        % Calculate Base Vectors
        G1 = [1,0,dNdT1];
        G2 = [0,1,dNdT2];

        % Calculate New Normal Vector From G1 x G2
        G3 = cross(G1,G2);
        G3 = G3./sqrt(dot(G3,G3));

        % Compute Contravariant Components For Undeformed Base Vectors
        G = [G1' G2' G3'];

        G_cont = inv(G)';

        % Calculate Deformed Base Vectors
        g1 = [dt1dT1 dt2dT1 dndT1];
        g2 = [dt1dT2 dt2dT2 dndT2];

        g3 = cross(g1,g2);
        g3 = g3./sqrt(dot(g3,g3));

        g = [g1' g2' g3'];

        % Calculate Deformation Matrix
        f = g*G_cont';

%         F(:,:,i) = f;

        % Rotate F into Cartesian coord space
        F(:,:,i) = inv(T_mat)*f*inv(T_mat)';

end

toc

%%%%%%%%%%%%%%%%%%%%%%%%%%%%%%%%%%%%%%%%%%%%%%%%%%%%%%%%%%%%%%%%%%%%%%%%%%%%
%%%                                End Code                                 %%%
%%%%%%%%%%%%%%%%%%%%%%%%%%%%%%%%%%%%%%%%%%%%%%%%%%%%%%%%%%%%%%%%%%%%%%%%%%%%
```

pumpkingii.m

```
% Written by Kara E. Garcia, Dr. Phil Bayly
% Starting from a spherical surface, deforms surface into various shapes

close all; clear all

FV = gifti('ico4sphere.LR.reg.surf.gii');

figure
hold on;
p = patch('Faces',FV.faces,'Vertices',FV.vertices, ...
    'FaceColor','green','EdgeColor','none');
view(3);axis image;grid on
title('YAS');
camlight headlight
hold off

yp = [FV.vertices(:,1),FV.vertices(:,2),FV.vertices(:,3)]; %3D coords
vertices = length(FV.vertices(:,1)); %# vertices

for i=1:vertices
    rho = sqrt(yp(i,1)^2+yp(i,2)^2); %cylindrical r
    radius = sqrt(yp(i,1)^2+yp(i,2)^2+yp(i,3)^2); %spherical r
    theta = atan2(rho,yp(i,3)); %elevation
    phi = atan2(yp(i,2),yp(i,1)); %azimuth
    Rsph(1,1) = sin(theta)*cos(phi);
    Rsph(1,2) = sin(theta)*sin(phi);
    Rsph(1,3) = cos(theta);
    Rsph(2,1) = cos(theta)*cos(phi);
    Rsph(2,2) = cos(theta)*sin(phi);
    Rsph(2,3) = -1*sin(theta);
    Rsph(3,1) = -1*sin(phi);
    Rsph(3,2) = cos(phi);
    Rsph(3,3) = 0;

    ys(i,:) = (Rsph*yp(i,:)')';
    %ys(i,1) = 1.1*radius + 10*sin(4*phi)*sin(theta);
    %ys(i,1) = 1.1*radius + 10*sin(4*(phi+pi/8))*sin(theta);
    %ys(i,1) = 0.9*(1.1*radius + 10*sin(4*phi)*sin(theta));
    if phi>0
        ys(i,1) = 0.85*(1.1*radius + 20*sin(7*phi)*sin(theta));
    else
        ys(i,1) = 0.85*(1.1*radius);
    end
    yp(i,:) = (inv(Rsph)*ys(i,:)')';
end

fv = FV;
fv.vertices(:,1)=yp(:,1);
fv.vertices(:,2)=yp(:,2);
fv.vertices(:,3)=yp(:,3);

figure
hold on;
p =
patch('Faces',fv.faces,'Vertices',fv.vertices,'FaceColor','green','EdgeColor','none');
view(3);axis image;grid on
title('OAS')
camlight headlight

save(fv,'ico4pumpkin_half2.surf.gii','ASCII');
```

Bibliography

D. S. Adams, R. Keller, and M. A. R. Koehl. The mechanics of notochord elongation, straightening and stiffening in the embryo of xenopus laevis. *Development*, 110:115–130, 1990.

T. Aegerter-Wilmsen, C. M. Aegerter, E. Hafen, and K. Basler. Model for the regulation of size in the wing imaginal disc of drosophila. *Mechanisms of development*, 124(4):318–326, 2007.

U. Agero, J. A. Glazier, and M. Hosek. Bulk elastic properties of chicken embryos during somitogenesis. *BioMedical Engineering Online*, 9(19), 2010. doi: 10.1186/1475-925X-9-19.

A. Alansary, B. Kainz, M. Rajchl, M. Murgasova, M. Damodaram, D. F. Lloyd, A. Davidson, S. G. McDonagh, M. Rutherford, J. V. Hajnal, et al. Pvr: Patch-to-volume reconstruction for large area motion correction of fetal mri. *arXiv preprint arXiv:1611.07289*, 2016.

P. W. Alford, A. P. Nesmith, J. N. Seywerd, A. Grosberg, and K. K. Parker. Vascular smooth muscle contractility depends on cell shape. *Integrative Biology*, 3(11):1063–1070, 2011.

M. I. Alonso, A. Gato, J. A. Moro, and E. Barbosa. Disruption of proteoglycans in neural tube fluid by beta-d-xyloside (bdx) alters brain enlargement in chick embryos. *The Anatomical Record 12*, 252(4):499–508, 1998.

M. I. Alonso, J. Moro, P. Martin, E. Barbosa, and A. Gato. Enzymatic digestion of neural tube fluid proteoglycans leads to brain growth disruption. *European Journal of Anatomy*, 4(3):161–167, 2000.

R. Ananthakrishnan, J. Guck, F. Wottawah, S. Schinkinger, B. Lincoln, M. Romeyke, T. Moon, and J. Ks. Quantifying the contribution of actin networks to the elastic strength of fibroblasts. *Journal of Theoretical Biology*, 242(2):502 – 516, 2006. ISSN 0022-5193. doi: http://dx.doi.org/10.1016/j.jtbi.2006.03.021.

A. V. Bakin, A. Safina, C. Rinehart, C. Daroqui, H. Darbary, and D. M. Helfman. A critical role of tropomyosins in tgf- regulation of the actin cytoskeleton and cell motility in epithelial cells. *Molecular Biology of the Cell*, 15(10):4682–4694, Oct. 2004.

G. Ball, P. Aljabar, S. Zebari, N. Tusor, T. Arichi, N. Merchant, E. C. Robinson, E. Ogundipe, D. Rueckert, A. D. Edwards, et al. Rich-club organization of the newborn human brain. *Proceedings of the National Academy of Sciences*, 111(20):7456–7461, 2014.

S. M. Bardet, J. L. Ferran, L. Sanchez-Arrones, and L. Puelles. Ontogenetic expression of sonic hedgehog in the chicken subpallium. *Frontiers in neuroanatomy*, 4, 2010.

A. J. Barkovich, R. Guerrini, R. I. Kuzniecky, G. D. Jackson, and W. B. Dobyns. A developmental and genetic classification for malformations of cortical development: update 2012. *Brain*, 135(5):1348–1369, 2012.

M. Barr, J. W. Hanson, K. Currey, S. Sharp, H. Toriello, R. D. Schmickel, and G. N. Wilson. Holoprosencephaly in infants of diabetic mothers. *The Journal of pediatrics*, 102 (4):565–568, 1983.

P. Bayly, R. Okamoto, G. Xu, Y. Shi, and L. Taber. A cortical folding model incorporating stress-dependent growth explains gyral wavelengths and stress patterns in the developing brain. *Physical biology*, 10(1):016005, 2013.

W. M. Bement, P. Forscher, and M. S. Mooseker. A novel cytoskeletal structure involved in purse string wound closure and cell polarity maintenance. *The Journal of cell biology*, 121 (3):565–578, 1993.

P. M. Bendix, G. H. Koenderink, D. Cuvelier, Z. Dogic, B. N. Koeleman, W. M. Brieher, C. M. Field, L. Mahadevan, and D. A. Weitz. A quantitative analysis of contractility in active cytoskeletal protein networks. *Biophysical Journal*, 94(8):3126 – 3136, 2008. ISSN 0006-3495. doi: http://dx.doi.org/10.1529/biophysj.107.117960.

G. W. Brodland and D. A. Clausi. Cytoskeletal mechanics of neurulation: insights obtained from computer simulations. *Biochemistry and cell biology*, 73(7-8):545–553, 1995.

C. Bührer, I. Grimmer, B. Metze, and M. Obladen. The crib (clinical risk index for babies) score and neurodevelopmental impairment at one year corrected age in very low birth weight infants. *Intensive care medicine*, 26(3):325–329, 2000.

D. R. Burgess. Reactivation of intestinal epithelial cell brush border motility: Atp-dependent contraction via a terminal web contractile ring. *The Journal of cell biology*, 95(3):853–863, 1982.

S. Chabert and L. A. Taber. Intramyocardial pressure measurements in the stage 18 embryonic chick heart. *American Journal of Physiology-Heart and Circulatory Physiology*, 282 (4):H1248–H1254, 2002.

S. C. Chapman, J. Collignon, G. C. Schoenwolf, and A. Lumsden. Improved method for chick whole-embryo culture using a filter paper carrier. *Developmental Dynamics*, 220: 284–289, 2001.

S. Chatelin, A. Constantinesco, and R. Willinger. Fifty years of brain tissue mechanical testing: from in vitro to in vivo investigations. *Biorheology*, 47(5-6):255–276, 2010.

L. S. Chaturvedi, H. M. Marsh, and M. D. Basson. Src and focal adhesion kinase mediate mechanical strain-induced proliferation and erk1/2 phosphorylation in human h441 pulmonary epithelial cells. *American Journal of Physiology-Cell Physiology*, 292(5):C1701–C1713, 2007.

X. Chen and G. W. Brodland. Multi-scale finite element modeling allows the mechanics of amphibian neurulation to be elucidated. *Physical Biology*, 5(1):015003, 2008.

Y. Chen, G. Wang, X.-y. Wang, Z.-l. Ma, Y.-p. Chen, M. Chuai, K. von Websky, B. Hocher, and X. Yang. Effects of high salt-exposure on the development of retina and lens in 5.5-day chick embryo. *Cellular Physiology and Biochemistry*, 34(3):804–817, 2014.

A. Chenn and C. A. Walsh. Regulation of cerebral cortical size by control of cell cycle exit in neural precursors. *Science*, 297(5580):365–369, 2002.

Y. Choe, K. S. Zarbalis, and S. J. Pleasure. Neural crest-derived mesenchymal cells require wnt signaling for their development and drive invagination of the telencephalic midline. *PloS one*, 9(2):e86025, 2014.

M. M. A. E. Claessens, M. Bathe, E. Frey, and A. R. Bausch. Actin-binding proteins sensitively mediate f-actin bundle stiffness. *Nature Materials*, 5:748–753, Sept. 2006.

D. A. Clausi and G. W. Brodland. Mechanical evaluation of theories of neurulation using computer simulations. *Development*, 118(3):1013–1023, 1993.

C. Clouchoux, D. Kudelski, A. Gholipour, S. K. Warfield, S. Viseur, M. Bouyssi-Kobar, J.-L. Mari, A. C. Evans, A. J. Du Plessis, and C. Limperopoulos. Quantitative in vivo mri measurement of cortical development in the fetus. *Brain Structure and Function*, 217 (1):127–139, 2012.

I. Cobos, K. Shimamura, J. L. Rubenstein, S. Martnez, and L. Puelles. Fate map of the avian anterior forebrain at the four-somite stage, based on the analysis of quailchick chimeras. *Developmental Biology*, 239(1):46 – 67, 2001. ISSN 0012-1606. doi: http://dx.doi.org/10.1006/dbio.2001.0423.

J.-F. Colas and G. C. Schoenwolf. Towards a cellular and molecular understanding of neurulation. *Developmental dynamics*, 221(2):117–145, 2001.

S. C. Cowin. Strain or deformation rate dependent finite growth in soft tissues. *Journal of biomechanics*, 29(5):647–649, 1996.

J. Cox, A. P. Jackson, J. Bond, and C. G. Woods. What primary microcephaly can tell us about brain growth. *Trends in Molecular Medicine*, 12(8):358 – 366, 2006. ISSN 1471-4914. doi: http://dx.doi.org/10.1016/j.molmed.2006.06.006.

P. Crossley, S. Martinez, Y. Ohkubo, and J. Rubenstein. Coordinate expression of fgf8, otx2, bmp4, and shh in the rostral prosencephalon during development of the telencephalic and optic vesicles. *Neuroscience*, 108(2):183–206, 2001.

H. Darijani and R. Naghdabadi. Hyperelastic materials behavior modeling using consistent strain energy density functions. *Acta mechanica*, 213(3):235–254, 2010.

S. Datar and R. R. Bhonde. Shell-less chick embryo culture as an alternative in vitro model to investigate glucose-induced malformations in mammalian embryos. *The Review of Diabetic Studies*, 2(4):221, 2005.

L. Davidson and R. Keller. Neural tube closure in xenopus laevis involves medial migration, directed protrusive activity, cell intercalation and convergent extension. *Development*, 126 (20):4547–4556, 1999.

C. de Juan Romero, C. Bruder, U. Tomasello, J. M. Sanz-Anquela, and V. Borrell. Discrete domains of gene expression in germinal layers distinguish the development of gyrencephaly. *The EMBO journal*, 34(14):1859–1874, 2015.

M. E. Desmond and A. G. Jacobson. Embryonic brain enlargement requires cerebrospinal fluid pressure. *Developmental Biology*, 57:188–198, Jan. 1977.

M. E. Desmond, M. L. Levitan, and A. R. Haas. Internal luminal pressure during early chick embryonic brain growth: Descriptive and empirical observations. *Anatomical Record Part A: Discoveries in Molecular, Cellular, and Evolutionary Biology*, 285(2):737–747, 2005. doi: 10.1002/ar.a.20211.

M. E. Desmond, J. Knepper, A. Dibenedetto, E. Malaugh, S. Callejo, R. Carretero, M.-I. Alonso, and A. Gato. Focal adhesion kinase as a mechanotransducer during rapid brain growth of the chick embryo. *Int J Dev biol*, 58:35–43, 2014.

C. Doğanlı, H. C. Beck, A. B. Ribera, C. Oxvig, and K. Lykke-Hartmann. α3na+/k+-atpase deficiency causes brain ventricle dilation and abrupt embryonic motility in zebrafish. *Journal of Biological Chemistry*, 288(13):8862–8874, 2013.

J. Dubois, M. Benders, A. Cachia, F. Lazeyras, R. Ha-Vinh Leuchter, S. Sizonenko, C. Borradori-Tolsa, J. Mangin, and P. S. Hüppi. Mapping the early cortical folding process in the preterm newborn brain. *Cerebral Cortex*, 18(6):1444–1454, 2007.

S. Durrleman, M. Prastawa, N. Charon, J. R. Korenberg, S. Joshi, G. Gerig, and A. Trouvé. Morphometry of anatomical shape complexes with dense deformations and sparse parameters. *NeuroImage*, 101:35–49, 2014.

S. J. England, G. B. Blanchard, L. Mahadevan, and R. J. Adams. A dynamic fate map of the forebrain shows how vertebrate eyes form and explains two causes of cyclopia. *Development*, 133(23):4613–4617, 2006. ISSN 0950-1991. doi: 10.1242/dev.02678.

A. W. Feinberg, P. W. Alford, H. Jin, C. M. Ripplinger, A. A. Werdich, S. P. Sheehy, A. Grosberg, and K. K. Parker. Controlling the contractile strength of engineered cardiac muscle by hierarchal tissue architecture. *Biomaterials*, 33(23):5732–5741, 2012.

M. Fernandes, G. Gutin, H. Alcorn, S. K. McConnell, and J. M. Hébert. Mutations in the bmp pathway in mice support the existence of two molecular classes of holoprosencephaly. *Development*, 134(21):3789–3794, 2007.

B. A. Filas, P. V. Bayly, and L. A. Taber. Mechanical stress as a regulator of cytoskeletal contractility and nuclear shape in embryonic epithelia. *Annals of biomedical engineering*, 39(1):443–454, 2011.

B. A. Filas, A. Oltean, S. Majidi, P. V. Bayly, D. C. Beebe, and L. A. Taber. Regional differences in actomyosin contraction shape the primary vesicles in the embryonic chicken brain. *Physical Biology*, 9(6):066007, Nov. 2012. doi: 10.1088/1478-3975/9/6/066007.

B. Fischl. Freesurfer. *Neuroimage*, 62(2):774–781, 2012.

J. L. Fish, C. Dehay, H. Kennedy, and W. B. Huttner. Making bigger brains–the evolution of neural-progenitor-cell division. *Journal of cell science*, 121(17):2783–2793, 2008.

M. Folgueira, P. Bayley, P. Navratilova, T. S. Becker, S. W. Wilson, and J. D. W. Clarke. Morphogenesis underlying the development of the everted teleost telencephalon. *Neural Development*, 7(32), 2012.

S. Fujime and S. Ishiwata. Dynamic study of f-actin by quasielastic scattering of laser light. *Journal of molecular biology*, 62(1):251–265, 1971.

S. Fujita. Synthetico-analytic approach to mechanism of shaping of the brain through simulation with 3d computer graphics. *Science on Form", ed. by S. Ishizuka, KTK, Tokyo*, pages 339–352, 1986.

Y. Furuta, D. W. Piston, and B. Hogan. Bone morphogenetic proteins (bmps) as regulators of dorsal forebrain development. *Development*, 124(11):2203–2212, 1997.

K. E. Garcia, R. J. Okamoto, P. V. Bayly, and L. A. Taber. Contraction and stress-dependent growth shape the forebrain of the early chicken embryo. *Journal of the mechanical behavior of biomedical materials*, 65:383–397, 2017.

M. L. Gardel, J. H. Shin, F. C. macKintosh, L. Mahadevan, P. Matsudaira, and D. A. Weitz. Elastic behavior of cross-linked and bundled actin networks. *Science*, 304:1301–1305, May 2004.

M. F. Glasser, S. N. Sotiropoulos, J. A. Wilson, T. S. Coalson, B. Fischl, J. L. Andersson, J. Xu, S. Jbabdi, M. Webster, J. R. Polimeni, et al. The minimal preprocessing pipelines for the human connectome project. *Neuroimage*, 80:105–124, 2013.

M. F. Glasser, T. S. Coalson, E. C. Robinson, C. D. Hacker, J. Harwell, E. Yacoub, K. Ugurbil, J. Andersson, C. F. Beckmann, M. Jenkinson, et al. A multi-modal parcellation of human cerebral cortex. *Nature*, 536(7615):171–178, 2016a.

M. F. Glasser, S. M. Smith, D. S. Marcus, J. L. Andersson, E. J. Auerbach, T. E. Behrens, T. S. Coalson, M. P. Harms, M. Jenkinson, S. Moeller, et al. The human connectome project's neuroimaging approach. *Nature Neuroscience*, 19(9):1175–1187, 2016b.

G. R. Goodrum and A. G. Jacobson. Cephalic flexure formation in the chick embryo. *Journal of Experimental Zoology*, 216:399–408, 1981.

P. W. Gunning, G. Schevzov, A. J. Kee, and E. C. Hardeman. Tropomyosin isoforms: divining rods for actin cytoskeleton function. *Trends in Cell Biology*, 15(6):333 – 341, 2005. ISSN 0962-8924. doi: http://dx.doi.org/10.1016/j.tcb.2005.04.007.

S. Gupta and J. Sen. Retinoic acid signaling regulates development of the dorsal forebrain midline and the choroid plexus in the chick. *Development*, 142(7):1293–1298, 2015.

S. Gupta and J. Sen. Roof plate mediated morphogenesis of the forebrain: New players join the game. *Developmental biology*, 413(2):145–152, 2016.

S. Guthrie, M. Butcher, and A. Lumsden. Patterns of cell division and interkinetic nuclear migration in the chick embryo hindbrain. *Journal of Neurobiology*, 22(7):742–754, 1991.

J. H. Gutzman and H. Sive. Epithelial relaxation mediated by the myosin phosphatase regulator mypt1 is required for brain ventricle lumen expansion and hindbrain morphogenesis. *Development*, 137(5):795–804, 2010.

J. H. Gutzman, E. G. Graeden, L. A. Lowery, H. S. Holley, and H. Sive. Formation of the zebrafish midbrain–hindbrain boundary constriction requires laminin-dependent basal constriction. *Mechanisms of development*, 125(11):974–983, 2008.

B. K. Hall. *Evolutionary developmental biology*. Springer Science & Business Media, 2012.

V. Hamburger and H. L. Hamilton. A series of normal stages in the development of the chick embryo. *Journal of Morphology*, 88:49–92, 1951.

A. Y. Hardan, R. J. Jou, M. S. Keshavan, R. Varma, and N. J. Minshew. Increased frontal cortical folding in autism: a preliminary mri study. *Psychiatry Research: Neuroimaging*, 131(3):263–268, 2004.

M. D. Hens and D. W. DeSimone. Molecular analysis and developmental expression of the focal adhesion kinase pp125fak in xenopus laevis. *Developmental biology*, 170(2):274–288, 1995.

C. J. Herrick. The morphology of the forebrain in amphibia and reptilia. *Journal of comparative Neurology and Psychology*, 20(5):413–547, 1910.

C. C. Hilgetag and H. Barbas. Developmental mechanics of the primate cerebral cortex. *Anatomy and embryology*, 210(5-6):411–417, 2005.

J. Hill, D. Dierker, J. Neil, T. Inder, A. Knutsen, J. Harwell, T. Coalson, and D. Van Essen. A surface-based analysis of hemispheric asymmetries and folding of cerebral cortex in term-born human infants. *Journal of Neuroscience*, 30(6):2268–2276, 2010a.

J. Hill, T. Inder, J. Neil, D. Dierker, J. Harwell, and D. Van Essen. Similar patterns of cortical expansion during human development and evolution. *Proceedings of the National Academy of Sciences*, 107(29):13135–13140, 2010b.

H. S. Hosseini, D. C. Beebe, and L. A. Taber. Mechanical effects of the surface ectoderm on optic vesicle morphogenesis in the chick embryo. *Journal of biomechanics*, 47(16): 3837–3846, 2014.

H. S. Hosseini, K. E. Garcia, and L. A. Taber. A new hypothesis for foregut and heart tube formation based on differential growth and actomyosin contraction. *Development*, pages dev–145193, 2017.

X. Huang, Y. Litingtung, and C. Chiang. Ectopic sonic hedgehog signaling impairs telencephalic dorsal midline development: implication for human holoprosencephaly. *Human molecular genetics*, 16(12):1454–1468, 2007a.

X. Huang, Y. Litingtung, and C. Chiang. Region-specific requirement for cholesterol modification of sonic hedgehog in patterning the telencephalon and spinal cord. *Development*, 134(11):2095–2105, 2007b.

L. Hufnagel, A. A. Teleman, H. Rouault, S. M. Cohen, and B. I. Shraiman. On the mechanism of wing size determination in fly development. *Proceedings of the National Academy of Sciences*, 104(10):3835–3840, 2007.

T. E. Inder, S. K. Warfield, H. Wang, P. S. Hüppi, and J. J. Volpe. Abnormal cerebral structure is present at term in premature infants. *Pediatrics*, 115(2):286–294, 2005.

T. Inoue, S. Nakamura, and N. Osumi. Fate mapping of the mouse prosencephalic neural plate. *Developmental Biology*, 219(2):373 – 383, 2000. ISSN 0012-1606. doi: http://dx.doi.org/10.1006/dbio.2000.9616.

I. Jasiuk, J. Chen, and M. Thorpe. Elastic moduli of two dimensional materials with polygonal and elliptical holes. *Appl. Mech. Rev*, 47(1):18–28, 1994.

R. Jelinek and T. Pexieder. The pressure of encephalic fluid in chick embryos between the 2nd and 6th day of incubation. *Physiologica Bohemoslov*, 17:297–305, 1968.

B. Kainz, A. Alansary, C. Malamateniou, K. Keraudren, M. Rutherford, J. V. Hajnal, and D. Rueckert. Flexible reconstruction and correction of unpredictable motion from stacks of 2d images. In *International Conference on Medical Image Computing and Computer-Assisted Intervention*, pages 555–562. Springer, 2015.

K. Kasza, G. Koenderink, Y. Lin, C. Broedersz, W. Messner, F. Nakamura, T. Stossel, F. MacKintosh, and D. Weitz. Nonlinear elasticity of stiff biopolymers connected by flexible linkers. *Physical Review E*, 79(4):041928, 2009.

H. Kidokoro, P. J. Anderson, L. W. Doyle, L. J. Woodward, J. J. Neil, and T. E. Inder. Brain injury and altered brain growth in preterm infants: predictors and prognosis. *Pediatrics*, pages peds–2013, 2014.

H. Y. Kim, V. D. Varner, and C. M. Nelson. Apical constriction initiates new bud formation during monopodial branching of the embryonic chicken lung. *Development*, 140:3146–3155, May 2013.

A. K. Knutsen. *Magnetic resonance imaging and surface-based analysis techniques to quantify growth of the developing brain*. Washington University in St. Louis, 2010.

A. K. Knutsen, Y. V. Chang, C. M. Grimm, L. Phan, L. A. Taber, and P. V. Bayly. A new method to measure cortical growth in the developing brain. *Journal of biomechanical engineering*, 132(10):101004, 2010.

A. K. Knutsen, C. D. Kroenke, Y. V. Chang, L. A. Taber, and P. V. Bayly. Spatial and temporal variations of cortical growth during gyrogenesis in the developing ferret brain. *Cerebral Cortex*, 23(2):488–498, 2012.

E. Kocsis, B. L. Trus, C. J. Steer, M. E. Bisher, and A. C. Steven. Image averaging of flexible fibrous macromolecules: the clathrin triskelion has an elastic proximal segment. *Journal of structural biology*, 107(1):6–14, 1991.

D. Konno, G. Shioi, A. Shitamukai, A. Mori, H. Kiyonari, T. Miyata, and F. Matsuzaki. Neuroepithelial progenitors undergo lgn-dependent planar divisions to maintain self-renewability during mammalian neurogenesis. *Nature cell biology*, 10(1):93–101, 2008.

A. Kriegstein, S. Noctor, and V. Martínez-Cerdeño. Patterns of neural stem and progenitor cell division may underlie evolutionary cortical expansion. *Nature Reviews Neuroscience*, 7(11):883–890, 2006.

M. Kuklisova-Murgasova, G. Quaghebeur, M. A. Rutherford, J. V. Hajnal, and J. A. Schnabel. Reconstruction of fetal brain mri with intensity matching and complete outlier removal. *Medical image analysis*, 16(8):1550–1564, 2012.

P. G. Layer and O. Sporns. Spatiotemporal relationship of embryonic cholinesterases with cell proliferation in chicken brain and eye. *Proceedings of the National Academy of Sciences*, 84:284–288, Jan. 1987.

P. G. Layer, S. Rommel, H. Bulthoff, and R. Hengstenberg. Independent spatial waves of biochemical differentiation along the surface of chicken brain as revealed by the sequential expression of acetylcholinesterase. *Cell and Tissue Research*, 251(3):587–595, Mar. 1988.

S. Lehoux, B. Esposito, R. Merval, and A. Tedgui. Differential regulation of vascular focal adhesion kinase by steady stretch and pulsatility. *Circulation*, 111(5):643–649, 2005.

E. Leoncini, G. Baranello, I. M. Orioli, G. Annerén, M. Bakker, F. Bianchi, C. Bower, M. A. Canfield, E. E. Castilla, G. Cocchi, et al. Frequency of holoprosencephaly in the international clearinghouse birth defects surveillance systems: searching for population variations. *Birth Defects Research Part A: Clinical and Molecular Teratology*, 82(8):585–591, 2008.

G. Li, L. Wang, F. Shi, A. E. Lyall, M. Ahn, Z. Peng, H. Zhu, W. Lin, J. H. Gilmore, and D. Shen. Cortical thickness and surface area in neonates at high risk for schizophrenia. *Brain structure & function*, 221(1):447, 2016.

J. J. Lin, N. Salamon, A. D. Lee, R. A. Dutton, J. A. Geaga, K. M. Hayashi, E. Luders, A. W. Toga, J. Engel Jr, and P. M. Thompson. Reduced neocortical thickness and complexity mapped in mesial temporal lobe epilepsy with hippocampal sclerosis. *Cerebral cortex*, 17 (9):2007–2018, 2006.

Z. Q. Liu. Scale space approach to directional analysis of images. *Applied Optics*, 30(11): 1369–1373, 1991.

L. A. Lowery and H. Sive. Initial formation of zebrafish brain ventricles occurs independently of circulation and requires the nagie oko and snakehead/atp1a1a. 1 gene products. *Development*, 132(9):2057–2067, 2005.

L. A. Lowery and H. Sive. Totally tubular: the mystery behind function and origin of the brain ventricular system. *Bioessays*, 31(4):446–458, Apr. 2009.

L. Lu, S. J. Oswald, H. Ngu, and F. C.-P. Yin. Mechanical properties of actin stress fibers in living cells. *Biophysical Journal*, 95(12):6060 – 6071, 2008. ISSN 0006-3495. doi: http://dx.doi.org/10.1529/biophysj.108.133462.

A. E. Lyall, F. Shi, X. Geng, S. Woolson, G. Li, L. Wang, R. M. Hamer, D. Shen, and J. H. Gilmore. Dynamic development of regional cortical thickness and surface area in early childhood. *Cerebral cortex*, 25(8):2204–2212, 2014.

X. Ma, J. Bao, and R. S. Adelstein. Loss of cell adhesion causes hydrocephalus in nonmuscle myosin ii-b–ablated and mutated mice. *Molecular biology of the cell*, 18(6):2305–2312, 2007.

T. Mammoto and D. E. Ingber. Mechanical control of tissue and organ development. *Development*, 137(9):1407–1420, 2010.

D. S. Marcus, J. Harwell, T. Olsen, M. Hodge, M. F. Glasser, F. Prior, M. Jenkinson, T. Laumann, S. W. Curtiss, and D. C. Van Essen. Informatics and data mining tools and strategies for the human connectome project. *Frontiers in neuroinformatics*, 5, 2011.

J. P. Marquez. Fourier analysis and automated measurement of cell and fiber angular orientation distributions. *International journal of solids and structures*, 43(21):6413–6423, 2006.

A. C. Martin. Pulsation and stabilization: contractile forces that underlie morphogenesis. *Developmental biology*, 341(1):114–125, 2010.

A. C. Martin, M. Kaschube, and E. F. Wieschaus. Pulsed contractions of an actin-myosin network drive apical constriction. *Nature*, 257:495–499, Jan. 2009. doi: 10.1038/nature07522.

E. Matsunaga and K. Shiota. Holoprosencephaly in human embryos: epidemiologic studies of 150 cases. *Teratology*, 16(3):261–272, 1977.

P. Moeskops, M. J. Benders, K. J. Kersbergen, F. Groenendaal, L. S. de Vries, M. A. Viergever, and I. Išgum. Development of cortical morphology evaluated with longitudinal mr brain images of preterm infants. *PloS one*, 10(7):e0131552, 2015.

E. S. Monuki. The morphogen signaling network in forebrain development and holoprosencephaly. *Journal of Neuropathology & Experimental Neurology*, 66(7):566–575, 2007.

G. M. Morriss-Kay, F. Tuckett, and M. Solursh. The effects of streptomyces hyaluronidase on tissue organization and cell cycle time in rat embryos. *Development*, 98(1):59–70, 1986.

P. Mukherjee, K. Gill, R. G. Henry, S. C. Partridge, S. Veeraraghavan, H. Jin, Y. Lu, S. P. Miller, D. M. Ferriero, D. B. Vigneron, et al. Comparing microstructural and macrostructural development of the cerebral cortex in premature newborns: diffusion tensor imaging versus cortical gyration. *Neuroimage*, 27(3):579–586, 2005.

M. Murrell, P. W. Oakes, M. Lenz, and M. L. Gardel. Forcing cells into shape: the mechanics of actomyosin contractility. *Nature Reviews Molecular Cell Biology*, 16(8):486–498, 2015.

H. Nakajima and T. Tanoue. Epithelial cell shape is regulated by lulu proteins via myosin-ii. *Journal of Cell Science*, 123:555–566, 2010. doi: 10.1242/jcs.057752.

K. Nicholson-Flynn, S. E. Hitchcock-DeGregori, and P. Levitt. Restricted expression of the actin-regulatory protein, tropomyosin, defines distinct boundaries, evaginating neuroepithelium, and choroid plexus forerunners during early cns development. *Journal of Neuroscience*, 16(21):6853–6863, 1996.

K. Nonomura, Y. Yamaguchi, M. Hamachi, M. Koike, Y. Uchiyama, K. Nakazato, A. Mochizuki, A. Sakaue-Sawano, A. Miyawaki, H. Yoshida, et al. Local apoptosis modulates early mammalian brain development through the elimination of morphogen-producing cells. *Developmental cell*, 27(6):621–634, 2013.

Y. Ohkubo, C. Chiang, and J. Rubenstein. Coordinate regulation and synergistic actions of bmp4, shh and fgf8 in the rostral prosencephalon regulate morphogenesis of the telencephalic and optic vesicles. *Neuroscience*, 111(1):1–17, 2002.

A. Oltean, J. Huang, D. C. Beebe, and L. A. Taber. Tissue growth constrained by extracellular matrix drives invagination during optic cup morphogenesis. *Biomechanics and modeling in mechanobiology*, 15(6):1405–1421, 2016.

E. Orasanu, A. Melbourne, M. J. Cardoso, H. Lomabert, G. S. Kendall, N. J. Robertson, N. Marlow, and S. Ourselin. Cortical folding of the preterm brain: a longitudinal analysis of extremely preterm born neonates using spectral matching. *Brain and behavior*, 6(8), 2016.

A. Petryk, D. Graf, and R. Marcucio. Holoprosencephaly: signaling interactions between the brain and the face, the environment and the genes, and the phenotypic variability in animal models and humans. *Wiley Interdisciplinary Reviews: Developmental Biology*, 4 (1):17–32, 2015.

A. S. Pikalow, M. E. Flynn, and R. L. Searls. Development of cranial flexure and rathke's pouch in the chick embryo. *The Anatomical Record*, 238:407–414, 1994.

S. Preibisch, S. Saalfeld, and P. Tomancak. Globally optimal stitching of tiled 3d microscopic image acquisitions. *Bioinformatics*, 25(11):1463–1465, 2009.

L. Puelles and J. L. R. Rubenstein. Ra new scenario of hypothalamic organization: rationale of new hypotheses introduced in the updated prosomeric model. *Frontiers in Neuroanatomy*, 9(27), Mar. 2015. doi: 10.3389/fnana.2015.00027.

L. Puelles, M. M. de-la Torre M., S. Bardet, and J. L. R. Rubenstein. *The Mouse Nervous System*. Elsevier-Academic Press, San Diego, California, 2012.

G. Qiu and T. Pence. Remarks on the behavior of simple directionally reinforced incompressible nonlinearly elastic solids. *Journal of Elasticity*, 49(1):1–30, 1997. ISSN 0374-3535. doi: 10.1023/A:1007410321319.

R. Raghavan, W. Lawton, S. Ranjan, and R. Viswanathan. A continuum mechanics-based model for cortical growth. *Journal of Theoretical Biology*, 187(2):285–296, 1997.

V. Rajagopalan, J. Scott, P. A. Habas, K. Kim, J. Corbett-Detig, F. Rousseau, A. J. Barkovich, O. A. Glenn, and C. Studholme. Local tissue growth patterns underlying normal fetal human brain gyrification quantified in utero. *Journal of Neuroscience*, 31(8): 2878–2887, 2011.

A. Ramasubramanian, N. L. Nerurkar, K. H. Achtien, B. A. Filas, D. A. Voronov, and L. A. Taber. On modeling morphogenesis of the looping heart following mechanical perturbations. *Journal of biomechanical engineering*, 130(6):061018, 2008.

A. Ramasubramanian, Q. B. Chu-Lagraff, T. Buma, K. T. Chico, M. E. Carnes, K. R. Burnett, S. A. Bradner, and S. S. Gordon. On the role of intrinsic and extrinsic forces in early cardiac s-looping. *Developmental Dynamics*, 242(7):801–816, 2013.

M. Rauzi, U. Krzic, T. E. Saunders, M. Krajnc, P. Ziherl, L. Hufnagel, and M. Leptin. Embryo-scale tissue mechanics during drosophila gastrulation movements. *Nature communications*, 6, 2015.

H. J. Ray and L. Niswander. Mechanisms of tissue fusion during development. *Development*, 139(10):1701–1711, 2012.

I. Reillo, C. de Juan Romero, M. Á. García-Cabezas, and V. Borrell. A role for intermediate radial glia in the tangential expansion of the mammalian cerebral cortex. *Cerebral Cortex*, 21(7):1674–1694, 2010.

I. Rekik, G. Li, W. Lin, and D. Shen. Predicting infant cortical surface development using a 4d varifold-based learning framework and local topography-based shape morphing. *Medical image analysis*, 28:1–12, 2016.

M. Reuter, N. J. Schmansky, H. D. Rosas, and B. Fischl. Within-subject template estimation for unbiased longitudinal image analysis. *Neuroimage*, 61(4):1402–1418, 2012.

D. P. Richman, R. M. Stewart, J. Hutchinson, and V. Caviness. Mechanical mode of brain convolutional development. *Science*, 189:18–21, 1975.

E. C. Robinson, S. Jbabdi, M. F. Glasser, J. Andersson, G. C. Burgess, M. P. Harms, S. M. Smith, D. C. Van Essen, and M. Jenkinson. Msm: a new flexible framework for multimodal surface matching. *Neuroimage*, 100:414–426, 2014.

E. C. Robinson, K. Garcia, M. F. Glasser, Z. Chen, T. S. Coalson, A. Makropoulos, J. Bozek, R. Wright, A. Schuh, M. Webster, et al. Multimodal surface matching with higher-order smoothness constraints. *NeuroImage*, 2017.

E. K. Rodriguez, A. Hoger, and A. D. McCulloch. Stress-dependent finite growth in soft elastic tissues. *Journal of biomechanics*, 27(4):455–467, 1994.

F. Rousseau, O. A. Glenn, B. Iordanova, C. Rodriguez-Carranza, D. B. Vigneron, J. A. Barkovich, and C. Studholme. Registration-based approach for reconstruction of high-resolution in utero fetal mr brain images. *Academic radiology*, 13(9):1072–1081, 2006.

G. Salbreux, G. Charras, and E. Paluch. Actin cortex mechanics and cellular morphogenesis. *Trends in Cell Biology*, 22(10):536 – 545, 2012. ISSN 0962-8924. doi: http://dx.doi.org/10.1016/j.tcb.2012.07.001.

T. Savin, N. A. Kurpios, A. E. Shyer, P. Florescu, H. Liang, L. Mahadevan, and C. J. Tabin. On the growth and form of the gut. *Nature*, 476(7358):57–62, 2011.

J. Schindelin, I. Arganda-Carreras, E. Frise, V. Kaynig, M. Longair, T. Pietzsch, S. Preibisch, C. Rueden, S. Saalfeld, B. Schmid, et al. Fiji: an open-source platform for biological-image analysis. *Nature methods*, 9(7):676–682, 2012.

C. A. Schneider, W. S. Rasband, K. W. Eliceiri, et al. Nih image to imagej: 25 years of image analysis. *Nat methods*, 9(7):671–675, 2012.

Y. Shi, J. Yao, G. Xu, and L. A. Taber. Bending of the looping heart: differential growth revisited. *Journal of biomechanical engineering*, 136(8):081002, 2014.

T. Shimogori, V. Banuchi, H. Y. Ng, J. B. Strauss, and E. A. Grove. Embryonic signaling centers expressing bmp, wnt and fgf proteins interact to pattern the cerebral cortex. *Development*, 131(22):5639–5647, 2004.

J. S. Shimony, C. D. Smyser, G. Wideman, D. Alexopoulos, J. Hill, J. Harwell, D. Dierker, D. C. Van Essen, T. E. Inder, and J. J. Neil. Comparison of cortical folding measures for evaluation of developing human brain. *Neuroimage*, 125:780–790, 2016.

I. Smart and G. McSherry. Gyrus formation in the cerebral cortex in the ferret. i. description of the external changes. *Journal of anatomy*, 146:141, 1986.

E. E. Storm, S. Garel, U. Borello, J. M. Hebert, S. Martinez, S. K. McConnell, G. R. Martin, and J. L. Rubenstein. Dose-dependent functions of fgf8 in regulating telencephalic patterning centers. *Development*, 133(9):1831–1844, 2006.

S. J. Streichan, C. R. Hoerner, T. Schneidt, D. Holzer, and L. Hufnagel. Spatial constraints control cell proliferation in tissues. *Proceedings of the National Academy of Sciences*, 111 (15):5586–5591, 2014.

J. Stricker, T. Falzone, and M. Gardel. Mechanics of the f-actin cytoskeleton. *Journal of Biomechanics*, 43:9–14, Jan. 2010.

B. E. Sumpio, A. J. Banes, L. G. Levin, and G. J. Jr. Mechanical stress stimulates aortic endothelial cells to proliferate. *Journal of Vascular Surgery*, 6(3):252 – 256, 1987. ISSN 0741-5214. doi: http://dx.doi.org/10.1016/0741-5214(87)90037-1.

T. M. Svitkina, Y. A. Rovensky, A. D. Bershadsky, and J. M. Vasiliev. Transverse pattern of microfilament bundles induced in epitheliocytes by cylindrical substrata. *Journal of Cell Science*, 108(2):735–745, Feb. 1995.

L. A. Taber. *Nonlinear theory of elasticity: applications in biomechanics*. World Scientific Publishing Company Incorporated, 2004.

L. A. Taber. Toward a unified theory for morphomechanics. *Philosophical Transactions of the Royal Society A*, 367(1902):3555–3583, Aug. 2009.

L. A. Taber and R. Perucchio. Modeling heart development. *Journal of Elasticity*, 61: 165–197, Oct. 2000.

T. Takamatsu and S. Fujita. Growth of notochord and formation of cranial and mesencephalic flexures in the chicken embryo. *Development, Growth and Differentiation*, 29(5):497–502, 1987.

T. Tallinen, J. Y. Chung, J. S. Biggins, and L. Mahadevan. Gyrification from constrained cortical expansion. *Proceedings of the National Academy of Sciences*, 111(35):12667–12672, 2014.

T. Tallinen, J. Y. Chung, F. Rousseau, N. Girard, J. Lefèvre, and L. Mahadevan. On the growth and form of cortical convolutions. *Nature Physics*, 2016.

D. W. Thompson et al. On growth and form. *On growth and form.*, 1942.

J.-Y. Tinevez, U. Schulze, G. Salbreux, J. Roensch, J.-F. Joanny, and E. Paluch. Role of cortical tension in bleb growth. *Proceedings of the National Academy of Sciences*, 106(44): 18581–18586, 2009. doi: 10.1073/pnas.0903353106.

T. Tong, I. Aganj, T. Ge, J. R. Polimeni, and B. Fischl. Functional density and edge maps: Characterizing functional architecture in individuals and improving cross-subject registration. *NeuroImage*, 158:346–355, 2017.

R. Toro and Y. Burnod. A morphogenetic model for the development of cortical convolutions. *Cerebral cortex*, 15(12):1900–1913, 2005.

R. Toyoda, S. Assimacopoulos, J. Wilcoxon, A. Taylor, P. Feldman, A. Suzuki-Hirano, T. Shimogori, and E. A. Grove. Fgf8 acts as a classic diffusible morphogen to pattern the neocortex. *Development*, 137(20):3439–3448, 2010.

A. N. Tullio, P. C. Bridgman, N. J. Tresser, C.-C. Chan, M. A. Conti, R. S. Adelstein, and Y. Hara. Structural abnormalities develop in the brain after ablation of the gene encoding nonmuscle myosin ii-b heavy chain. *Journal of Comparative Neurology*, 433(1): 62–74, 2001.

D. C. Van Essen. A tension-based theory of morphogenesis and compact wiring in the central nervous system. *Nature*, 385(6614):313, 1997.

D. C. Van Essen, H. A. Drury, J. Dickson, J. Harwell, D. Hanlon, and C. H. Anderson. An integrated software suite for surface-based analyses of cerebral cortex. *Journal of the American Medical Informatics Association*, 8(5):443–459, 2001.

E. Ventsel and T. Krauthammer. *Thin plates and shells: theory: analysis, and applications*. CRC press, 2001.

D. A. Voronov and L. A. Taber. Cardiac looping in experimental conditions: effects of extraembryonic forces. *Developmental dynamics*, 224(4):413–421, 2002.

J. L. Walker, A. K. Fournier, and R. K. Assoian. Regulation of growth factor signaling and cell cycle progression by cell adhesion and adhesion-dependent changes in cellular tension. *Cytokine & growth factor reviews*, 16(4):395–405, 2005.

J. H.-C. Wang and B. P. Thampatty. An introductory review of cell mechanobiology. *Biomechanics and modeling in mechanobiology*, 5(1):1–16, 2006.

X. Wang, C. Studholme, P. L. Grigsby, A. E. Frias, V. C. C. Carlson, and C. D. Kroenke. Folding, but not surface area expansion, is associated with cellular morphological maturation in the fetal cerebral cortex. *Journal of Neuroscience*, 37(8):1971–1983, 2017.

M. Warren, K. Puskarczyk, and S. C. Chapman. Chick embryo proliferation studies using edu labeling. *Developmental Dynamics*, 238(4):944–949, 2009.

J. Weickenmeier, R. de Rooij, S. Budday, P. Steinmann, T. Ovaert, and E. Kuhl. Brain stiffness increases with myelin content. *Acta biomaterialia*, 42:265–272, 2016.

T. Weikert, R. G. Rathjen, and P. G. Layer. Developmental maps of acetylcholinesterase and g4-antigen of the early chicken brain: Long-distance tracts originate from ache-producing cell bodies. *Journal of Neurobiology*, 21(3):482–498, 1990.

A. M. Winkler, G. R. Ridgway, M. A. Webster, S. M. Smith, and T. E. Nichols. Permutation inference for the general linear model. *Neuroimage*, 92:381–397, 2014.

S. Withington, R. Beddington, and J. Cooke. Foregut endoderm is required at head process stages for anteriormost neural patterning in chick. *Development*, 128(3):309–320, 2001.

T. P. Wyatt, A. R. Harris, M. Lam, Q. Cheng, J. Bellis, A. Dimitracopoulos, A. J. Kabla, G. T. Charras, and B. Baum. Emergence of homeostatic epithelial packing and stress dissipation through divisions oriented along the long cell axis. *Proceedings of the National Academy of Sciences*, 112(18):5726–5731, 2015.

G. Xu, P. S. Kemp, J. A. Hwu, A. M. Beagley, P. V. Bayly, and L. A. Taber. Opening angles and material properties of the early embryonic chick brain. *Journal of Biomechanical Engineering*, 132(1):011005, 2010a.

G. Xu, A. K. Knutsen, K. Dikranian, C. D. Kroenke, P. V. Bayly, and L. A. Taber. Axons pull on the brain, but tension does not drive cortical folding. *Journal of biomechanical engineering*, 132(7):071013, 2010b.

B. T. Yeo, M. R. Sabuncu, T. Vercauteren, N. Ayache, B. Fischl, and P. Golland. Spherical demons: fast diffeomorphic landmark-free surface registration. *IEEE transactions on medical imaging*, 29(3):650–668, 2010.

H. G. Yevick, G. Duclos, I. Bonnet, and P. Silberzan. Architecture and migration of an epithelium on a cylindrical wire. *Proceedings of the National Academy of Sciences*, 112 (19):5944–5949, Apr. 2015.

S. Yoo, Y. Kim, H. Lee, S. Park, and S. Park. A gene trap knockout of the tiam-1 protein results in malformation of the early embryonic brain. *Molecules and Cells*, 34(1):103–108, July 2012.

J. M. Young, J. Yao, A. Ramasubramanian, L. A. Taber, and R. Perucchio. Automatic generation of user material subroutines for biomechanical growth analysis. *Journal of Biomechanical Engineering*, 132:104505, Oct. 2010.

E. A. Zamir, V. Srinivasan, R. Perucchio, and L. A. Taber. Mechanical asymmetry in the embryonic chick heart during looping. *Annals of biomedical engineering*, 31(11):1327–1336, 2003.

J. Zhou, H. Y. Kim, and L. A. Davidson. Actomyosin stiffens the vertebrate embryo during crucial stages of elongation and neural tube closure. *Development*, 136(4):677–688, 2009. ISSN 0950-1991. doi: 10.1242/dev.026211.

Vita

Kara E. Garcia

Degrees

Ph.D. Biomedical Engineering, December 2017
M.Eng. Mechanical Engineering, May 2015
B.S. with Distinction, Biomedical Engineering, May 2012

Professional Societies

Tau Beta Pi Engineering Honors Fraternity
Alpha Eta Mu Beta Biomedical Engineering Honors Society
Organization for Human Brain Mapping

Extracurricular Activities

Co-Director of Mentoring, Young Scientist Program (2014–2016)
Consultant, Biotechnology and Life Science Advising Group (2016)
Translation Team, Sling Health (2015)
BME Graduate Student Advisory Board (2014–2015)

Doctoral Honors and Awards

National Institutes of Health Pre-doctoral Training Fellowship (2014)
National Science Foundation GRFP Honorable Mention (2014)
National Science Foundation OHBM Travel Award (2016)
SB^{3}C Student Paper Competition, 2nd Place (2015)

Peer-Reviewed Publications

Garcia K. E., Okamoto R. J., Bayly P. V., Taber L. A. (2016) Contraction and stress-dependent growth shape the forebrain of the early chicken embryo. *Journal of the Mechanical Behavior of Biomedical Materials*.

Hosseini H. S., Garcia K. E., Taber L. A. (2017) A new hypothesis for foregut and heart tube formation based on differential growth and actomyosin contraction. *Development*.

Robinson E. C., Garcia K. E., Glasser M. F., Chen Z., Coalson T. S., Makropoulos A., Bozek J., Wright R., Schuh A., Webster M., Hutter J., Price A., Cordero Grande L., Hughes E., Tusor N., Bayly P. V., Van Essen D. C., Smith S. M., Edwards A. D., Hajnal J., Jenkenson

M., Glocker B., Rueckert D. (2017) Multimodal Surface Matching with higher order smoothness constraints. *Neuroimage*.

Submitted Manuscripts

Garcia K. E., Robinson E. C., Alexopoulos D., Dierker D. L., Glasser M. F., Coalson T. S., Ortinau C. M., Rueckert D. R., Taber L. A., Van Essen D. C., Rogers C. E., Smyser C. D., Bayly P. V. Dynamic patterns of cortical expansion during folding of the preterm human brain.

December 2017